Title

Reverse Osmosis and Ultrafiltration Membrane Surface Nano-Structuring with Tethered Hydrophilic Polymer Layers for Seawater Desalination

Author

Kim, Soomin

Publication Date

2020

UNIVERSITY OF CALIFORNIA

Los Angeles

Reverse Osmosis and Ultrafiltration Membrane Surface Nano-Structuring with Tethered Hydrophilic Polymer Layers for Seawater Desalination

A dissertation submitted in partial satisfaction of the

requirements for the degree of Doctor of Philosophy

in Chemical Engineering

by

Soomin Kim

2020

ABSTRACT OF THE DISSERTATION

Tailoring performance of polymeric membranes

by membrane surface nano-structuring

with tethered hydrophilic polymer layers

by

Soomin Kim

Doctor of Philosophy in Chemical Engineering

University of California, Los Angeles, 2020

Professor Yoram Cohen, Chair

A systematic investigation of membrane surface nano-structuring (SNS) with surface tethered hydrophilic polymer layers was conducted in order to mitigate fouling of reverse osmosis (RO) and ultrafiltration (UF) membranes and tune membrane performance in seawater desalination. Surface tethered hydrophilic polymer (i.e., polyacrylic acid (PAA)) layers were synthesized onto base polysulfone (PSf) UF and polyamide (PA) thin film composite (TFC) RO membranes via membrane surface activation with an atmospheric pressure plasma (APP), followed by graft polymerization (GP) of acrylic acid. Both APP surface activation and GP conditions impacted the structure of the synthesized tethered PAA layers and RO membrane desalination performance. Detailed characterization of tethered PAA chain extension length via atomic force microscopy (AFM) based force spectroscopy (FS) revealed that the number average molecular weight of the

synthesized tethered PAA chains was estimated to be in the range of ~13,000–35,000 with chain-chain separation of 1.5–2.4 nm. Extension of the tethered PAA chains in DI water was significantly greater in DI water than in high salinity aqueous environment. UF fouling stress tests with alginic acid in high salinity water and post-cleaning with non-saline water demonstrated permeability restoration of up to 90–100% for a surface nano-structured (SNS)-PAA-PSf membrane relative to 50–70% for the native PSf membrane. Synthesized SNS-PAA-PA BWRO and SWRO membranes having water and salt permeability coefficient in the range of 2.3 – 3.4 $L \cdot m^{-2} \cdot h^{-1} \cdot bar^{-1}$ and 0.15 – 0.54 $L \cdot m^{-2} \cdot h^{-1}$ revealed that membrane surface structuring with a tethered PAA layer enabled tuning membrane performance (in terms of L_p and B) to achieve water/salt selectivity (evaluated as L_p:B ratio) that was significantly higher (by up to 56%) relative to the base PA membranes. It was demonstrated that, depending on APP surface activation and GP conditions, PA TFC membranes could be tuned to have essentially the same salt rejection over a wide permeability range or a given permeability over a range of salt rejection. It was also shown that membrane performance could be achieved that overcomes the permeability-selectivity trade-off. Lastly, the present study developed an approach to scale up the APP surface activation and GP process by performing membrane surface nano-structuring for large PA TFC flat sheet membranes that are suitable for fabricating 2.5" x 21" spiral wound RO elements.

The dissertation of Soomin Kim is approved.

Panagiotis Christofides

Jenn-Ming Yang

Yoram Cohen, Committee Chair

University of California, Los Angeles

2020

To my parents.

TABLE OF CONTENTS

LIST OF FIGURES

LIST OF TABLES

ACKNOWLEDGEMENTS

I would like to acknowledge and express my deepest gratitude to my Ph.D. advisor, Professor Yoram Cohen, for his invaluable guidance, mentorship, and support. I am grateful to Professor Cohen for initiating my pursuit of becoming a better scientific researcher and writer. My success on this journey would not have been possible without the tireless and constant support of Professor Cohen. I want to extend special thanks to Dr. Anditya Rahardianto for his research guidance, and for frequently going above and beyond in providing advice and support. Most of all, I am very thankful for his mentoring and friendship. I also want to thank the current and past Prof. Cohen's research group members: Dr. Muhammad Bilal, Yian Chen, Dr. Jin Yong Choi, Yeunha Kim, Dr. Tae Lee, Dr. John Thompson, and Dr. Shangwen Zha for their friendship and help with various aspects of my research. I want to thank Dr. Adam Stieg and Dr. Shivani Sharma for guidance and assistance with AFM and Toray Membrane USA and Surfx Technologies for their support and collaboration. I am very grateful to have so much love and support from my family and my best friend, Quincy Chuck, whom I look forward to spending my life with. I appreciate Quincy's generous help in writing and proofreading the manuscript.

VITA

2010	B.S., Chemical Engineering University of California, Los Angeles
2013	M.S., Chemical Engineering University of California, Los Angeles
2013 – 2017	Teaching Assistant Department of Chemical and Biomolecular Engineering University of California, Los Angeles

PUBLICATIONS

S. Kim, Y. Chen, A. Rahardianto, and Y. Cohen, Scale-up of membrane surface nano-structuring for production of spiral wound RO elements, *Journal of Membrane Science*, ***In Preparation*** (2020).

S. Kim, A. Rahardianto, J.S. Walker, T. Wolf, K. Coleman, and Y. Cohen, Upgrading polyamide TFC BWRO and SWRO membranes to higher SWRO membrane performance via surface nano-structuring with tethered poly(acrylic acid), *Journal of Membrane Science* 597 (2020) 117736.

S. Kim, K.J. Moses, S. Sharma, M. Bilal, and Y. Cohen, Surface characterization data for tethered polyacrylic acid layers synthesized on polysulfone surfaces, *Data in Brief*, 23C (2019) 103747.

S. Kim, Y. Cohen, K.J. Moses, S. Sharma, and M. Bilal, Polysulfone surface nano-structured with tethered polyacrylic acid, *Applied Surface Science* 470 (2019) 411-422.

K.J. Moses, **S. Kim**, M. Bilal, and Y. Cohen, Tethered hydrophilic polymers layers on a polyamide surface, *Journal of Applied Polymer Science* 135 (2018) 46843.

J. Thompson, A. Rahardianto, **S. Kim**, M. Bilal, R. Breckenridge, and Y. Cohen, Real-time direct detection of silica scaling on RO membranes, *Journal of Membrane Science* 528 (2017) 346-358.

CONFERENCE PRESENTATIONS

S. Kim, Y. Cohen, Y. Chen, A. Rahardianto, and S. Zha, Surface Nano-structuring with Hydrophilic Polymer Brush Layers for Tailored Performance of Fouling Resistant RO and UF Membranes, 2018 AIChE Annual Meeting, Oct. 28 – Nov. 2, 2018, Pittsburgh, PA.

S. Zha, **S. Kim**, A. Rahardianto, and Y. Cohen, Scale-up of Synthesis Seawater Reverse Osmosis Membranes with Surface Nano-Structured Hydrophilic Polymer Brush Layers, 2018 North American Membrane Society (NAMS) Annual Meeting, June 9 – 13, 2018, Lexington, KY.

S. Kim, J. Zhang, A. Rahardianto, and Y. Cohen, Scale-up of RO and UF Membrane Surface Nano-Structuring with Hydrophilic Polymer Brush Layers: Evaluation of Uniformity of Membrane Performance, 2017 AIChE Annual Meeting, Oct. 29 – Nov. 3, 2017, Minneapolis, MN.

S. Kim, J. Zhang, A. Rahardianto, and Y. Cohen, Synthesis Scale-up of High Performance UF Membranes with Responsive Hydrophilic Brush Layers, 11th International Congress on Membranes and Membrane Processes (ICOM), Jul. 29 – Aug. 4, 2017, San Francisco, CA.

S. Kim and Y. Cohen, Surface Characterization of Membrane Surfaces Nanostructured with Tethered Hydrophilic Polymers, 2016 AIChE Annual Meeting, Nov. 13 – 18, 2016, San Francisco, CA.

S. Kim and Y. Cohen, Surface Characterization of Membrane Surfaces Nanostructured with Tethered Hydrophilic Polymers, 2016 North American Membrane Society (NAMS) Annual Meeting, May 21 – 25, 2016, Bellevue, WA.

S. Kim, Kari J. Moses (Varin), and Y. Cohen, Surface Nano-Structuring of Polysulfone UF Membrane Surfaces, 2015 AIChE Annual Meeting, Nov. 8 – 13, 2015, Salt Lake City, UT.

Kari J. Moses, **S. Kim**, and Y. Cohen, Impact of Hydrophilic Polymer Brush Layers on Biofouling Resistance of Polyamide Reverse Osmosis Membranes, 2015 North American Membrane Society (NAMS) Annual Meeting, May 30 – June 3, 2015, Boston, MA.

S. Kim and Y. Cohen, Surface Nano-Structuring with Polymer Brush Layers for Fouling Resistant UF Membranes, 248th American Chemical Society (ACS) National Meeting, Aug. 10 – 14, 2014, San Francisco, CA.

Chapter 1. Introduction

1.1 Background

About two thirds of the global population live in highly water stressed areas, and the number of people affected by intense water scarcity is projected to increase globally in the next few decades [1]. Given the abundance of seawater, seawater desalination is the most promising approach to provide a stable water supply to support the growing freshwater demand. Reverse osmosis (RO) has become the most dominant desalination technology, replacing traditional thermal desalination processes such as multi-stage flash evaporation (MSF) and multiple effect distillation (MED), which require higher energy consumption than RO. As of 2016, seawater desalination accounts for 59% of the global desalination capacity, of which 65% is accounted for by RO [2], and reliance on seawater RO (SWRO) desalination for production of freshwater is projected to increase [3].

In order to maintain optimal productivity of SWRO desalination plants, efficient and reliable RO feed pretreatment approaches are required to remove suspended particulates and organic and biological matters to avoid or minimize RO membrane fouling and ensure stable, long-term performance of RO membrane elements [4, 5]. Current conventional RO feeds often undergo chemical pretreatment (e.g., coagulation, flocculation) and dissolved air flotation (DAF) in conjunction with double media filtration (DMF) to remove a portion of the organic and inorganic particulate and colloidal matter present in the raw feed water, followed by cartridge filtration (with mesh size of 5 – 10 microns) to protect RO membranes against surface fouling [5, 6]. While conventional pretreatment may be sufficient for beach well sources where concentration of suspended solids is low and feed water quality is consistent [7], it is often insufficient for treating seawater due to possible variability in water quality (e.g., storm events, algal blooms, etc.), which

can cause significant fluctuation in the RO feed quality. This can cause severe RO membrane fouling. Given the above, RO membranes with conventional pretreatment systems typically require high chemical dosing for frequent membrane cleaning and membrane replacement in order to ensure an efficient RO desalination process. Moreover, conventional pretreatment (i.e., DMF) has a low removal efficiency for particles smaller than 10 – 15 microns, and it is difficult to achieve a silt density index (SDI_{15}) lower than 3.0, which is recommended for typical RO membranes [6]. In recent years, ultrafiltration (UF) has become a preferred pretreatment to RO in seawater desalination due to its effective removal of suspended particles (>0.01 – 0.02 μm) and thus production of consistent quality RO feed water [8, 9].

Currently, the majority of RO and UF membranes are made of polymers due to their ease of manufacture, inexpensive cost relative to ceramic counterparts, and the wide variability of barrier structures and properties that can be designed with polymeric materials [10, 11]. The polyamide (PA) based thin film composite (TFC) membrane, which was first developed by Cadotte in the 1970s [12], is still the primary RO membrane used in the RO desalination industry. Commercial UF membranes are typically synthesized with polysulfone (PSf) or polyethersulfone (PES). However, a major disadvantage of the above polymers is that their hydrophobic nature leads to adsorption of organic and biological matters (e.g., protein, polysaccharides, bacteria) on the membrane surfaces which causes membrane fouling that reduces membrane productivity. Membrane fouling poses a significant challenge for SWRO plants to maintain the same membrane productivity level due to (a) requirements of higher operating pressures (thus higher energy consumption), and (b) increased frequency of membrane cleaning and/or membrane replacement. The above increases plant operation and maintenance costs [13]. In UF operation, permeate flux can decline rapidly due to accumulation of rejected particulates on the membrane surface, which

then need to be removed regularly by a physical cleaning process (e.g., backwashing), or even chemical cleaning, in order to restore membrane permeability. Therefore, in addition to fouling reduction, effective membrane cleaning is also particularly important for UF membranes in order to maintain optimal productivity.

Another challenge that confronts current seawater RO desalination is the relatively higher energy consumption (compared to RO desalting brackish water) due to high osmotic feed pressures that require correspondingly high RO operating pressures (typically ≥ 700 psi) [3]. In that regard, improving PA TFC SWRO membrane performance (by reducing salt permeability and/or increasing water permeability) could reduce energy consumption by allowing RO system operation at a lower hydraulic pressure while achieving the same productivity at the same or higher quality (i.e., lower total dissolved solids (TDS) of product water (**Figure 1-1**). However, PA TFC membranes have been shown to display a trade-off between water permeability and water/salt selectivity (i.e., increased membrane permeability increases salt permeability and vice versa) (**Figure 1-1**) and overcoming this trade-off barrier is a challenging task [14].

In recent years, surface tethered hydrophilic polymer layers, synthesized via atmospheric pressure plasma-induced graft polymerization (APPIGP) approach, have been shown to be effective for reducing RO membrane fouling. In APPIGP, a base membrane surface is exposed to an atmospheric pressure plasma (APP) to generate surface initiation sites. Subsequent exposure of the activated membrane surface to a vinyl monomer solution enables free radical graft polymerization of vinyl monomers from the anchoring active sites at the membrane surface. APP operates in ambient air, unlike low pressure plasma that requires high vacuum chambers which limits the size of the treatable substrate. Thus, APPIGP approach can be easily scaled up to treat the large membrane surface areas required for production of commercial-scale RO membrane

elements (e.g., spiral wound membrane elements). It was shown that the surface anchored polymer chains, synthesized via the APPIGP approach, significantly reduce propensities for mineral scaling and biofouling of PA TFC RO membranes [15-17] due to: (a) increased membrane surface hydrophilicity, and (b) partial mobility (due to Brownian motion) of the free portion of the anchored chains. Moreover, previous studies have shown that synthesis of surface tethered hydrophilic polymer layers onto loose PA TFC membranes (which can be regarded as a nanofiltration membrane) can significantly increase membrane salt rejection to a level comparable to commercial brackish water RO (BWRO) membranes, while having ~2 – 3 times greater water permeability.

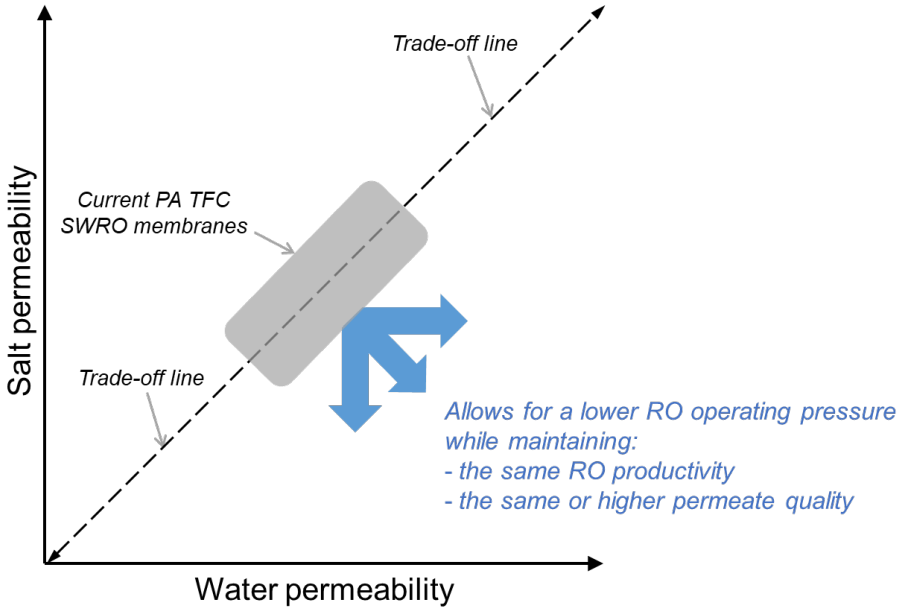

Figure 1-1. Illustration of the trade-off relation between water permeability and salt permeability of PA TFC SWRO membranes and the benefits of overcoming the trade-off.

The results of previous studies suggest that surface tethered hydrophilic polymer layers, synthesized via the APPIGP approach, could also be effective for mitigation of RO and UF membrane fouling in seawater desalination. In seawater desalination in which the membrane

surface is exposed to a highly saline feed water (~33,000 – 42,000 mg/L TDS) [2], a salt-responsive polymer layer can be utilized to improve membrane cleaning effectiveness. For example, tethered polymer chains that collapse when exposed to a high salinity water (due to the charge screening effect), but swell/extend in low salinity water [18, 19] can aid in foulant removal. Improving membrane cleaning effectiveness is particularly important for UF membranes that are routinely cleaned via backwash cycles to minimize irreversible membrane fouling [4]. Thus, the present research investigated the utility of salt-responsive tethered polymer layers for improving cleaning efficiency and reducing fouling of UF membranes. In case of SWRO membranes, it is critical to achieve the high level of salt rejection required for production of fresh water (TDS < 500 mg/L). Thus, a systematic investigation was performed in order to elucidate the effect and utility of tethered polymer layer synthesis conditions (i.e., APP treatment and graft polymerization conditions) and base PA TFC membrane type on: (a) RO desalination performance, (b) fouling propensity and mitigation, and (c) improved membrane cleaning. Lastly, the scale-up potential of the APPIGP approach was demonstrated by synthesis of surface nano-structured PA TFC membrane sheets that are sufficiently large for fabrication of commercial-scale spiral wound RO elements.

1.2 Problem Statement

Desalting seawater via RO with UF for RO freed pretreatment is a promising solution alleviating, in part, the global water scarcity problem. However, RO and UF membrane fouling is a major challenge in the operation of seawater desalination plants by increasing the cost of water production. Moreover, UF membranes typically foul even more rapidly relative to RO membranes. Therefore, UF membranes need to be cleaned via backwash at regular intervals. UF membrane backwash cycles can be effective in removing the foulant layer accumulated on the membrane surface, but the gradual buildup of foulants that cannot be completely reversed via backwash (i.e., irreversible fouling) necessitates more aggressive means (chemical cleaning). In that regard, improving UF backwash efficiency is also critical for stable, long-term UF operation, in addition to aiding in the reduction of RO membrane fouling. Development of a high performance SWRO membrane (that has a low salt permeability and high water permeability) could potentially also increase SWRO desalination process efficiency by enabling production of a higher quality of product water (lower TDS) at a lower energy cost. Accordingly, in the present study the above challenges were addressed by synthesizing SWRO and UF membranes of low fouling propensity via membrane surface nano-structuring with tethered hydrophilic polymer layers. The above approach was explored in order to: (a) increase the cleaning efficiency of UF membranes, and (b) develop high performance PA TFC SWRO membranes of lower fouling propensity, higher cleaning effectiveness, and desalination performance exceeding that of current commercial SWRO membranes.

1.3 Objectives of the Dissertation

The present dissertation research aimed to evaluate the utility of surface tethered hydrophilic polymer layers for improving membrane cleaning effectiveness and tailoring the performance of RO and UF membranes. Moreover, the research also explored the potential for scaling up the surface tethered polymer layer synthesis approach (atmospheric pressure plasma-induced graft polymerization (APPIGP)) for production of commercial scale spiral-wound RO elements. Accordingly, the specific research objectives were as follows:

1. Investigate the fundamentals of surface tethered polymer layer structures (chain size distribution and chain grafting density) by characterizing the polymer layer structure and tethered polymer chain swellability in aqueous environments.
2. Investigate and establish relationships between tethered polymer layer characteristics and RO membrane desalination performance in terms of water and salt permeability coefficients.
3. Evaluate utility of the salt-responsive surface tethered polymer layers for mitigating membrane fouling and improving membrane cleaning efficiency.
4. Develop an engineering approach to scale-up surface membrane nano-structuring to the level that allows the synthesis of commercial-scale spiral-wound membrane elements for water desalination.

1.4 Approach

In the present work, surface tethered poly(acrylic acid) (PAA) layers, synthesized via atmospheric pressure plasma-induced graft polymerization (APPIGP) approach, were investigated with respect to their surface properties and utility for enhancing the performance of polysulfone (PSf) UF and polyamide (PA) thin film composite (TFC) RO membranes. A systematic study was conducted to evaluate the impact of APP surface activation and graft polymerization conditions on the resulting tethered PAA layer characteristics and RO membrane desalination performance. In the above part of the study small membrane coupons (i.e., 4.45 cm-diameter disks of PSf UF membranes and rectangular (11.2 cm x 5.6 cm) samples of PA TFC membranes) were utilized for evaluating membrane performance with laboratory-scale stirred membrane cell and plate-and-frame crossflow membrane cell, respectively. After confirming the SNS-PAA-PA membrane performance with small membrane coupons, the APPIGP process was scaled up to fabricate SNS-PAA-PA membrane sheets of sufficiently large size (30” x 24”) for the fabrication of 2.5” x 21” spiral wound RO elements. An overview of this dissertation research is outlined in **Figure 1-2**.

The evaluation of salt-responsive swelling of surface tethered PAA layers and the utility of the PAA layers for improving UF membrane backwash efficiency are described in **Chapter 3**. Surface tethered PAA layers were synthesized onto polysulfone (PSf) films (spin-cast onto silicon wafers) via APPIGP approach. Impact of APP surface activation and graft polymerization conditions on the resulting tethered PAA layer surface characteristics (i.e., surface hydrophilicity, surface roughness, chain length distributions, and layer thickness) were evaluated via various surface characterization techniques including contact angles measurement, atomic force microscopy, and focused ion beam – scanning microscopy. The swellability condition of the tethered hydrophilic PAA layers was then quantified in saline solutions and fresh water.

The tuning of seawater reverse osmosis (SWRO) membrane performance via surface nano-structuring (SNS) of PA TFC base membranes with tethered PAA layers is detailed in **Chapter 4**. The base PA TFC membrane was activated by treatment with an impinging APP stream, followed by aqueous phase free-radical surface graft polymerization of acrylic acid (AA). The impact of APP surface activation and AA graft polymerization conditions was then investigated with respect to the path for tuning the SNS-PAA-PA performance (in terms of water and salt permeability coefficients) and also upgrading BWRO to SWRO membrane performance.

Membrane fouling studies conducted for selected SNS-PAA-PSf UF and SNS-PAA-PA RO membranes are detailed in **Chapter 5**. The efficiency of membrane cleaning with non-saline water was evaluated for the SNS-PAA-PSf membrane (synthesized at selected synthesis conditions in **Chapter 3**) via UF fouling stress tests with alginic acid in a high salinity water (35 g/L NaCl) and subsequently performing backwash of the fouled membranes with deionized water. Membrane fouling stress test with bovine serum albumin (BSA) was conducted for a selected SNS-PAA-PA membrane (**Chapter 4**), and membrane cleaning effectiveness was also evaluated for the tethered PAA layer grafted on the PA membrane surface by flushing the BSA fouled membrane with DI water.

In **Chapter 6** details are provided regarding the approach to scale up the APPIGP process. Membrane surface nano-structuring was carried out for PA TFC flat sheet membranes that are sufficiently large for fabricating 2.5" x 21" spiral wound RO elements. Additional details of the scaled up APP surface activation approach and a reactor suitable for graft polymerization of 30" x 24" base PA membranes sheets are described, along with the protocols for carrying out the scaled-up membrane nano-structuring, are provided in **Appendix A.3**.

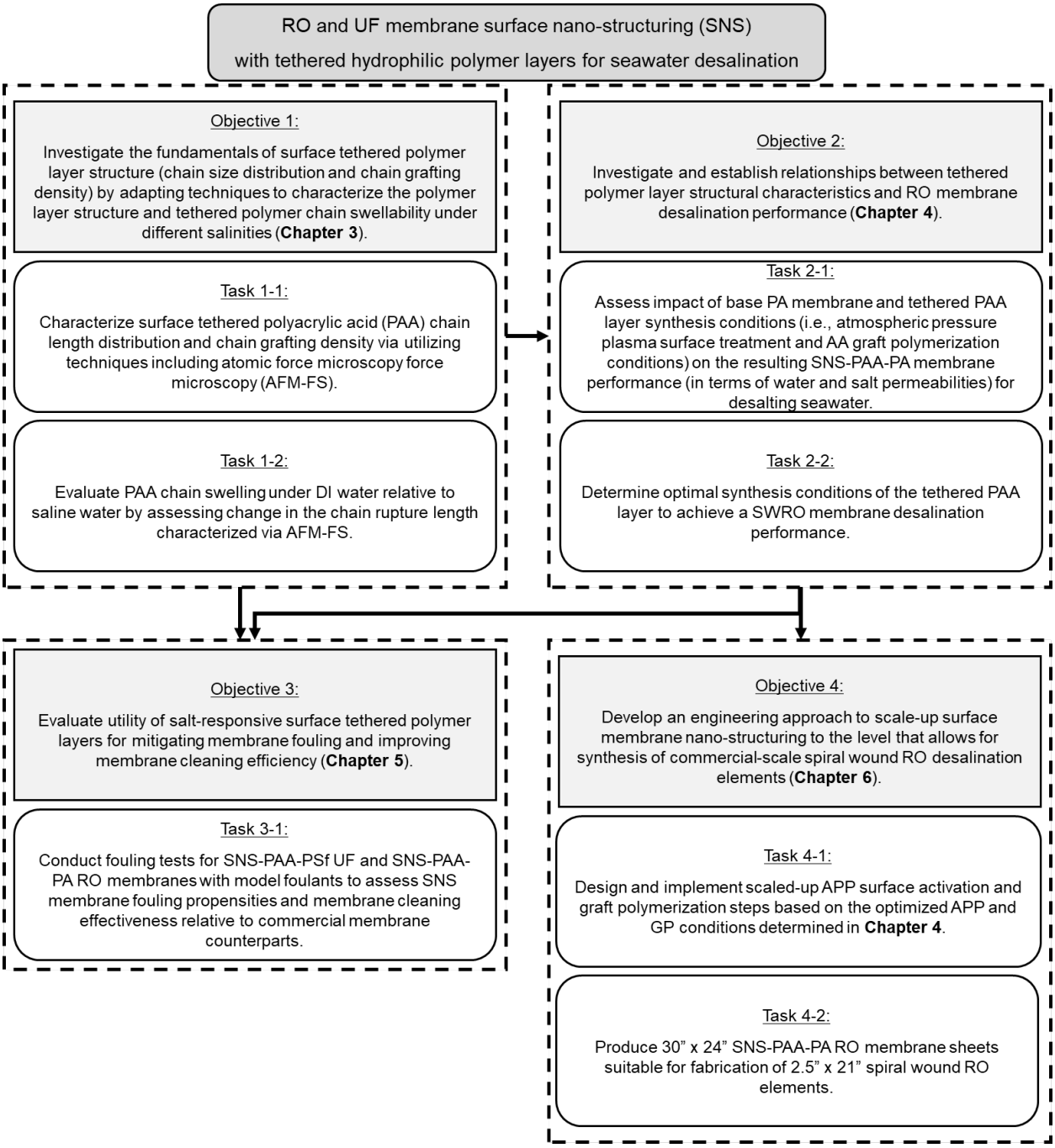

Figure 1-2. Research flowchart outlining each chapter of the dissertation.

Chapter 2. Literature Review

2.1 Ultrafiltration

2.1.1 Significance of UF as pretreatment to SWRO desalination

Ultrafiltration (UF) is a membrane filtration process that operates at relatively low transmembrane pressure (TMP) of typically less than 100 to 200 kPa [20, 21]. UF membranes have screening pore sizes ranging from approximately 1 – 100 nanometers [22, 23] and can be used to reject dissolved macromolecules, bacteria, and viruses from solutions [23] and are widely used for drinking water production and wastewater treatment [21, 23-25]. Also, UF is widely used to filter biological solutions in various industrial applications such as concentration and purification of enzymes and antibiotics in the pharmaceutical industry and dairy and beverage processing in the food industry [26-28].

In recent years, low pressure membrane (LPM) processes such as microfiltration (MF) and ultrafiltration (UF) have become preferred pretreatments to RO in seawater desalination as well as in wastewater treatment due to their effective removal of suspended particles and production of consistent quality RO feed water regardless of influent water quality [8]. While MF membranes can provide a physical barrier for particles larger than 0.1 – 10 μm, UF membranes can remove solutes of sizes that are an order of magnitude smaller than MF (0.01 – 0.1 μm) including all suspended particles as well as some dissolved compounds (e.g., proteins, inorganic colloids, bacteria) [23]. While both MF and UF can remove waterborne pathogens such as protozoan cysts (e.g., *Giardia*, *Cryptosporidium*) as well as bacteria (e.g., *E. Coli*), UF can provide more effective virus removal than MF due to its smaller pore size.

Retention of microorganisms is expressed in Log Removal Value (LRV), which is defined as [29]:

$$\mathrm{LRV} = \log_{10}\left(\frac{C_f}{C_p}\right) \tag{1.1}$$

where C_f and C_p are the concentrations of the pathogen or microorganism in the feed and permeate streams, respectively. Both MF and UF have comparable log removals of protozoan cysts and bacteria greater than 4.5 (>99.99%) [30]. Viruses are much smaller than protozoan cysts and bacteria with typical size ranges from 0.005 to 0.1 microns, which is comparable to the entire range of UF and the lower end of MF pore sizes [31]. Thus, reported virus removal values range widely (approximately 0.5 to 6.5 LRV) for MF/UF membranes depending on the size of virus and membrane MWCO or pore size [31]. However, in general, UF membranes have much higher log removal of viruses compared to MF membranes [32]. Typical removal efficiency of a virus (MS-2 bacteriophage) of 0.024 micron size for UF membranes (pore size range of 0.0025 – 0.01 micron) is within LRV of 2.9 – 7.9, while MF membranes of smaller pore size range (0.1 – 0.2 micron) can achieve LRV of up to ~4.3 [31]. Because of the high degree of pathogen removal required to meet current regulatory standards, UF can be used as a standalone membrane for treating surface water and groundwater for drinking water production or used as a pretreatment to RO when treating wastewater and brackish or seawaters [30, 33, 34]. While it is unlikely for viruses to pass through an RO membrane, it is possible for virus leakage to occur due to membrane integrity breaches caused by various factors including manufacturing defects, insufficient/improper pretreatment, chemical attacks (e.g., oxidation), faulty installation and maintenance, and failure of assembly components (e.g., O-rings, glue strips, or permeate seals) [29, 35]. Hence, another incentive for UF as RO pretreatment is to provide a double barrier for the removal of viruses and cysts of *Giardia* and *Cryptosporidium* [36]. UF pretreatment can significantly reduce biofouling of RO membranes [33] and also lead to decreased use of chemical disinfection agents (e.g., chlorine,

chloroamine, ozone) and consequently reduce the presence of harmful halogenated organic compounds which can form as byproducts of disinfection when organic material is present in the feed water [36, 37].

2.1.2 UF membrane fouling

Polysulfone (PSf) membranes are one of the most widely utilized membrane materials in MF/UF membranes because of their relatively high tolerance to pH (pH 2-13) and temperature (up to about 75°C) as well as resistance to oxidants (e.g., chlorine) [30]. In addition to PSf, polyethersulfone (PES) and poly(vinylidene difluoride) (PVDF) are two other popular polymers used for fabrication of commercially available UF membranes, which can be made in various element configurations including hollow fibers, tubular, spiral wound, and flat plate [27, 28]. Among them, hollow fiber membrane elements are most widely used in water and wastewater treatment applications due to their low energy cost and small footprint [34]. However, a major problem in UF technology is membrane fouling, promoted by the hydrophobic nature of the UF polymeric materials that leads to non-specific surface adsorption/deposition of rejected organic and biological matters on the membrane surface and inside pores; hence, increased hydraulic resistance that leads to higher operating pressure and operating costs.

UF membrane fouling can occur via various mechanisms including pore blocking and cake or gel layer formation as depicted in **Figure 2-1**. UF permeate flux can be described by a Darcy's law type equation:

$$J = \frac{\Delta P}{\mu\left(R_m + R_p + R_c\right)} \tag{2.1}$$

where J is the permeate flux (m/s), ΔP is the transmembrane pressure (Pa), μ is the solvent viscosity (Pa·s), R_m is the membrane hydraulic resistance (m^{-1}), R_p is resistance due to membrane pore blockage, and R_c is the resistance due to a cake or gel layer due to accumulation of rejected colloidal and macromolecular material on the membrane surface.

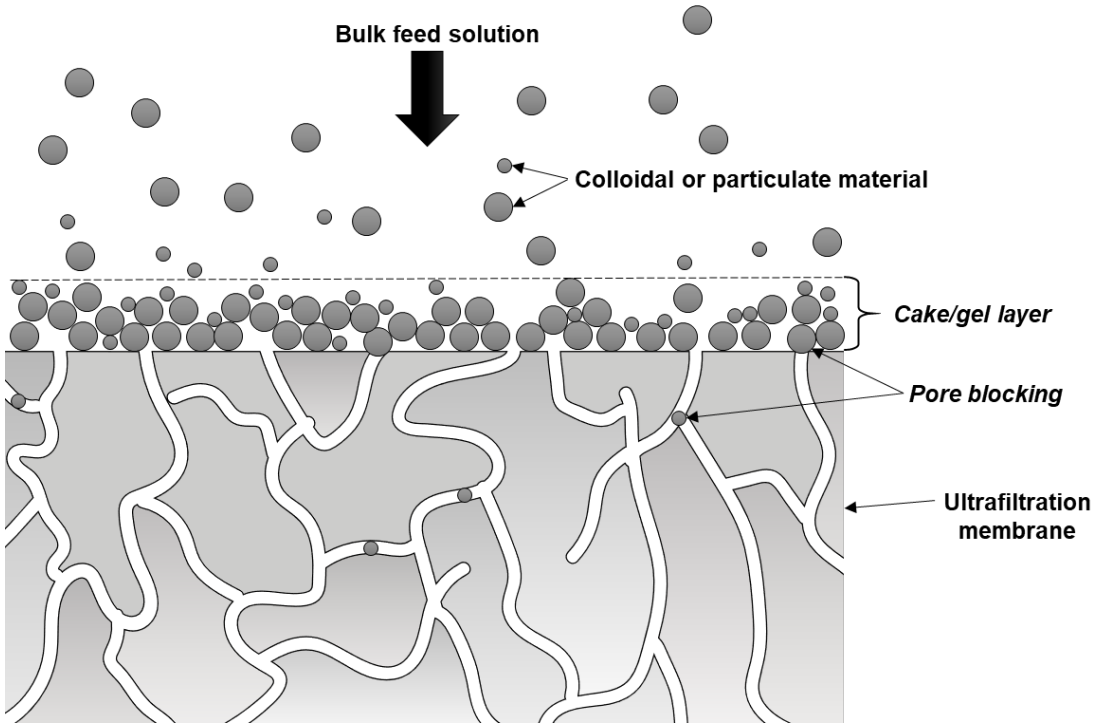

Figure 2-1. Illustration of UF membrane fouling via cake layer formation and pore blocking mechanisms.

It is noted that large-scale UF is typically operated in dead-end filtration at a constant flux mode. Therefore, transmembrane pressure applied to maintain a constant flux is increased over time due to membrane fouling (**Figure 2-2**). In order to restore permeate flux and maintain optimal productivity, UF membranes are periodically cleaned via backwashing, which is performed by flushing with freshwater (usually UF or RO permeate) from the permeate to the feed side for a short period, which is typically on the order of ~30 s up to several minutes [4] (**Figure 2-2**). Backwash is an effective means of physically removing the loosely bound foulant

layer deposited on the UF membrane surface. Foulants that cannot be removed by backwashing lead to accumulation of hydraulic resistance such as in the case shown in **Figure 2-3** and must be removed by more aggressive chemical cleaning cycles.

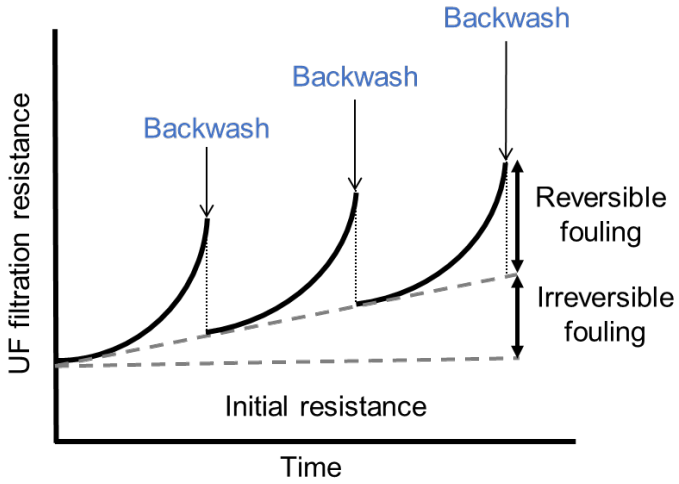

Figure 2-2. Impact of UF membrane fouling and backwash cycles on the UF resistance.

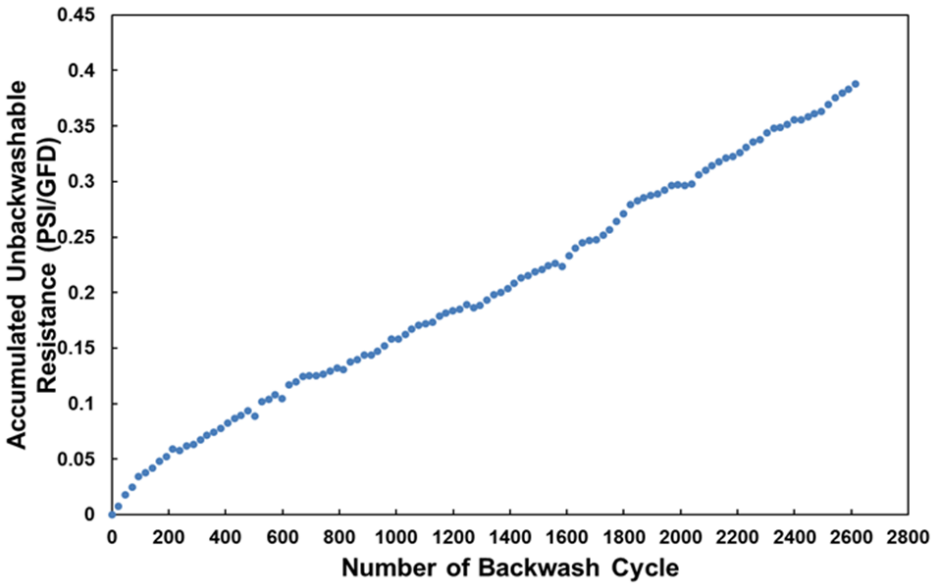

Figure 2-3. Accumulated irreversible (unbackwashable) hydraulic resistance over 2600 backwashing cycles (equivalent to ~30 days) for a hollow fiber UF module in CoM2RO (integrated UF/RO desalination system) treating raw seawater feed in US Naval Base at Port Hueneme, California. Filtration flux: 42-45 $L \cdot m^{-2} \cdot h^{-1}$, coagulant dose: 3.18-4.17 mg/L Fe^{3+}, filtration duration per cycle: 30-45 min, backwash flux: 162 $L \cdot m^{-2} \cdot h^{-1}$, backwash duration: 70s w/ RO permeate + 240s w/ RO concentrate [38].

In surface water treatments, organic fouling of UF membranes by natural organic matter (NOM) has been reported as the major contributor for the loss of membrane permeability. NOM represents organic compounds of a wide range of sizes and composed of humic and non-humic substances [39]. While humic substances (i.e. humic and fulvic acids) have high aromaticity and are hydrophobic, non-humic substances (e.g. amino acids, polysaccharides, protein, etc.) are generally hydrophilic and composed of more aliphatic molecules. Many studies have suggested that the humic fractions of NOM is the major contributor to irreversible membrane fouling. However, recent studies reported that non-humic, hydrophilic fractions of NOM that have polysaccharide-like characters can cause more severe fouling by adsorption within the membrane pore structure [40]. Biofouling of UF membranes is another problem encountered in surface water and wastewater treatments. Biofouling is caused by adhesion of micro-organisms to membrane surfaces, which can lead to the formation of a gel layer called biofilm through cell multiplication [30, 41]. UF membranes used in membrane bioreactors (MBRs) are susceptible to biological fouling, and numerous studies identified extracellular polymeric substances (EPS) as the major cause of fouling in MBRs [42].

2.2 Reverse Osmosis

2.2.1 Water and salt transport in RO membranes

Reverse osmosis (RO) desalination separates water from a saline feed solution by applying an external pressure that is greater than the osmotic pressure (which causes flow of water to the feed-side of a RO membrane) across a semi-permeable membrane. RO desalination is typically operated in a crossflow filtration mode in which a saline feed solution flows tangentially across the feed-side of the membrane surface. High pressure applied at the feed-side of the membrane surface forces the solution through the membrane, which selectively permeates water (**Figure 2-4**). Buildup of rejected salt ions near and at the feed-side of the membrane surface leads to concentration polarization, which increases the feed-side osmotic pressure, and thus decreases the net driving pressure. The osmotic pressure increases in the direction of the feed flow (x-direction) due to permeation of water through the membrane which then results in an axial increase of salt concentration in the bulk feed. Therefore, permeate flux correspondingly decreases along the same direction.

Concentration polarization is typically analyzed by the classical Film Theory, which assumes fluid flow in one dimension (x-direction in **Figure 2-1**) and a fully-developed concentration boundary layer [43]. The degree of concentration polarization may be assessed by concentration polarization modulus (*CP*), which can be related to salt concentration at the feed-side of the membrane surface (C_m) relative to the bulk solution (C_b):

$$CP = \frac{C_m - C_p}{C_b - C_p} = \exp\left(\frac{J_v}{k}\right) \tag{2.2}$$

in which C_p is the permeate salt concentration, J_v is the volumetric permeate flux, and k is the salt mass transfer coefficient defined as:

$$k = \frac{D}{\delta} \tag{2.3}$$

where D is the salt diffusion coefficient, and δ is thickness of a boundary layer. Efficiency of RO membranes for removing salts is often quantified in terms of the observed (R_o) or intrinsic (R_i) salt rejection:

$$R_o = 1 - \frac{C_p}{C_b} \tag{2.4}$$

$$R_i = 1 - \frac{C_p}{C_m} \tag{2.5}$$

However, the above parameters are highly dependent on RO operating conditions (e.g., feed pressure, feed solution salinity, permeate flux); thus, comparison of the performance of different RO membranes solely in terms of the above parameters is not definitive.

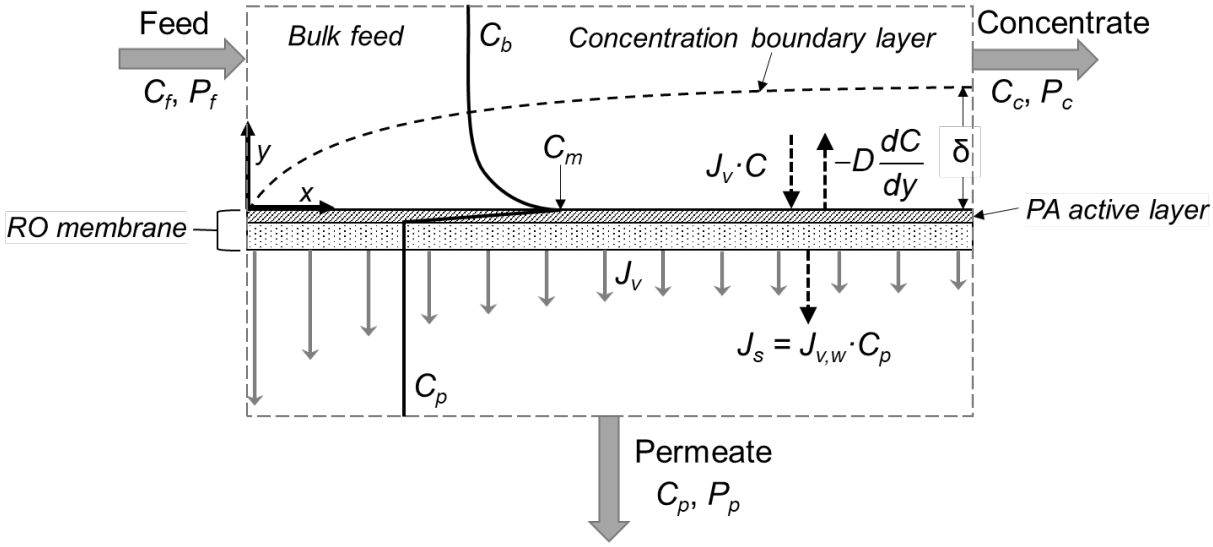

Figure 2-4. Schematic representation of concentration polarization in a crossflow RO membrane channel. Black solid line shows salt concentration profile, black dotted arrows indicate directions of salt fluxes, and gray arrows show direction of permeate fluxes. C_f, C_b, C_c, and C_p are concentration of salt in the feed water, bulk of the solution, concentrate, and permeate. C_m is the salt concentration at the membrane surface. J_v is the volumetric permeate flux, J_s is the salt flux, D is the salt diffusivity in water, dC/dy is the salt concentration driving force in the y-direction. P_f, P_c, and P_p are pressures of the feed, concentrate, and permeate streams.

Transport of water and salt ions through highly selective nonporous membranes (such as PA TFC SWRO membranes where salt transport essentially occurs primarily via diffusion) is adequately described by the solution-diffusion model [44], whereby the volumetric water flux (J_v) and salt flux (J_s) across a RO membrane are expressed as [45]:

$$J_v = L_p\left(\Delta P - \Delta\pi_m\right) \tag{2-6}$$

$$J_s = C_p J_v = B\left(C_m - C_p\right) \tag{2-7}$$

in which L_p and B are the water salt permeability coefficient, respectively, ΔP is the transmembrane pressure, $\Delta\pi_m$ is the osmotic pressure difference between the membrane surface at the feed and permeate sides, respectively. RO membrane desalination performance is often quantified by L_p and B, which are influenced by the properties of the PA active layer such as layer thickness and free volume (**Section 2.2.3**).

2.2.2 Polyamide (PA) thin film composite (TFC) membrane

RO technology utilizes semi-permeable membranes that allow for permeation of water while rejecting dissolved salts in feed water. Currently, RO processes predominantly utilize polyamide (PA) based thin film composite (TFC) membranes, which consist of three layers (**Figure 2-5**). The top layer is an ultrathin PA active layer (100 – 200 nm) [46] and is formed via polycondensation reaction of diamine and acyl chloride [47] on top of a microporous membrane support layer that is typically made of polysulfone (30 – 50 μm). The PA active layer dictates the membrane water and salt permeabilities, while the underlying microporous membrane support provides mechanical stability as well as high water flux. The bottom layer is a nonwoven or woven polyester fabric layer (100 – 200 μm), which provides additional mechanical strength [48].

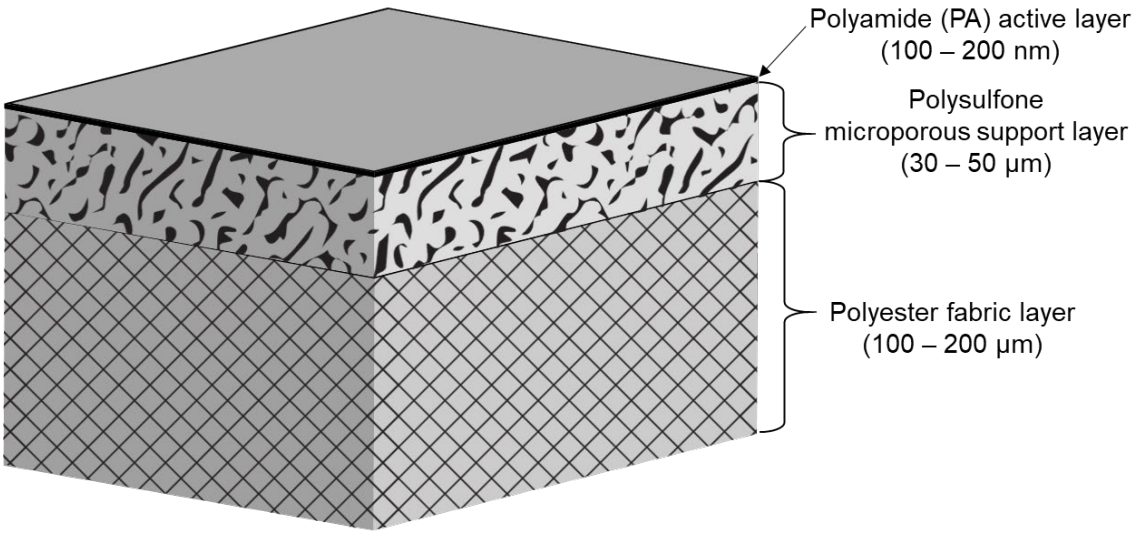

Figure 2-5. Illustration of a polyamide (PA) thin film composite (TFC) membrane.

2.2.3 Water permeability and water/salt selectivity trade-off

According to the solution-diffusion model, water permeability (P_w) and salt permeability (P_s) of a PA TFC membrane can be expressed as follows [45]:

$$P_w = D_w K_w \tag{2.8}$$

$$P_s = D_s K_s \tag{2.9}$$

where D_w and D_s are the diffusion coefficients of water and salt in the PA active layer, respectively, and K_w and K_s are the partition coefficients (solubility) of water and salt between the saline solution and the PA active layer. Accordingly, water/salt selectivity can be expressed by the ratio of P_w and P_s (i.e., P_w/P_s). The water permeability coefficient, L_p, and salt permeability coefficient, B, which were defined in Eq. 2-6 and 2-7, respectively, can be related to P_w and P_s by the following relations:

$$L_p = \frac{P_w}{l} \cdot \frac{V_w}{RT} \tag{2.10}$$

$$B = \frac{P_w}{l} \tag{2.11}$$

where l is the active layer thickness, V_m is the partial molar volume of water, R is the universal gas constant, and T is the absolute temperature. It is noted that P_w and P_s are intrinsic material properties of the PA active layer, unlike L_p and B that depend on the active layer thickness as shown in Eq. 2-10 and 2-11. However, accurate determination of the PA active layer is a challenging task. Thus, L_p and B are used more frequently in place of P_w and P_s to quantify the PA TFC membrane desalination performance. Consequently, water/salt selectivity of a PA TFC membrane is often quantified by the ratio of L_p and B (i.e., L_p/B).

For RO desalination applications, it is desirable to have membranes with high water permeability and high water/salt selectivity. However, PA TFC membranes display a trade-off between water permeability and water/salt selectivity [49-51]. It has been shown that the above trade-off behavior is attributed to the fact that the structural properties of PA active layers (e.g., layer thickness, free volume) which allow for high water permeability also lead to a high level of salt permeation through the membrane (lower salt retention ability) [52]. For example, a greater water permeation rate can be achieved by reducing the PA active layer thickness, which is obvious from Eq. 2-10. Recent analysis of commercial PA TFC membranes via positron annihilation lifetime spectroscopy (PALS) have shown that PA active layers contain sub-nanometer scale free volume cavities (~0.2 – 0.3 nm in radius) that strongly influence both water and salt transport in the membranes [46, 49, 53]. In general, reducing free volume in the PA active layer is expected to decrease water and salt permeabilities; however, membrane permeability can also be impacted by size and spatial distributions as well as total number of such cavity sites that constitute the free volume within the PA active layer.

The surface properties of PA active layers (e.g., surface hydrophilicity, charge density, roughness) have also been shown to have a measurable impact on RO membrane desalination performance. For example, increasing surface hydrophilicity has been linked to increased membrane water permeability via increased water sorption in the PA active layers [54]. However, increased water sorption in the PA layer has been associated with increased free volume in the layer, which can in turn also increase salt permeability [55]. It has been shown that increasing surface roughness of PA active layers may be a contributing factor to increased water permeability by providing a higher effective membrane surface area for water permeation or via a thinner active layer that provides a shorter diffusion path in the active layer [56].

In order to overcome the RO membrane performance trade-off, various means have been proposed to tailor the PA selective layer characteristics (e.g., thickness, extent of crosslinking) as well as the resulting membrane surface properties (e.g., roughness, hydrophilicity). It was demonstrated that PA TFC membrane desalination performance could be tuned by: optimizing the conventional PA selective layer synthesis conditions (e.g., solvent type, reaction temperature, use of additives) and the post-synthesis curing conditions [57, 58], tuning the porosity/structure of the porous support layer [59], or employing alternative PA selective layer synthesis methods (e.g., molecular layer-by-layer assembly [60]).

In recent years, it has been suggested that membrane surface modification, which is a popular approach primarily employed for membrane fouling reduction, can also be used to tune the performance of polyamide desalination membranes [61-63].

2.2.4 Polyamide interfacial polymerization

The conventional PA TFC membrane fabrication method, first developed by Cadotte [12], involves synthesis of an ultra-thin polyamide selective layer via interfacial polymerization of diamine and acyl chloride monomers *in situ* at the surface of a microporous polymer support layer (usually a polysulfone or polyethersulfone ultrafiltration membrane) [64, 65]. The surface of a microporous support layer is first coated with a layer of an aqueous solution of diamine (typically *m*-phenylenediamine or MPD), which penetrates into the underlying porous support layer to some degree. The MPD layer is subsequently contacted with an acyl chloride (typically trimesoyl chloride, TMC) solution in an organic phase (usually hexane) to initiate the interfacial polymerization [64] (**Figure 2-6**). The low solubility of acyl chlorides in water and fairly good solubility of MPD in organic solvents lead to the diffusion of the MPD monomers from the aqueous phase to the organic phase where polymerization is initiated near the water/organic interface [66]. It has been shown that the interfacial polymerization conditions (e.g., monomer concentration, organic solvent type, solvent temperature, polymerization time) and post membrane curing conditions can significantly impact the resulting PA active layer structure (e.g., thickness and degree of cross-linking) and the membrane desalination performance [64, 67, 68].

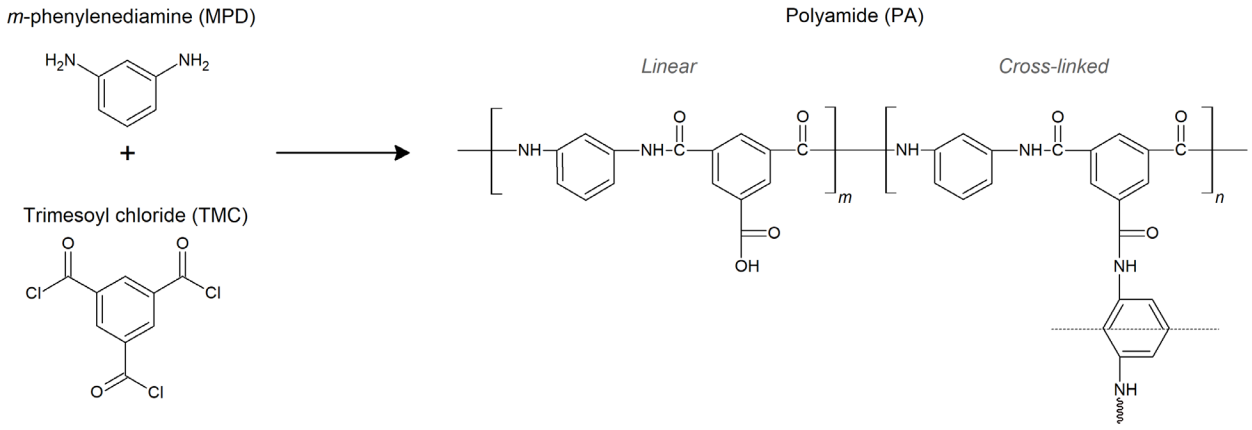

Figure 2-6. Synthesis of an aromatic polyamide (PA) selective layer via interfacial polymerization of *m*-phenylenediamine (MPD) and trimesoyl chloride (TMC).

2.3 Seawater Reverse Osmosis (SWRO) Membrane Fouling

In seawater RO desalination, membrane biofouling mitigation is a major challenge [69]. Biofouling is caused by the surface adhesion of micro-organisms (e.g., bacteria and algae) that leads to the formation of a biofilm [30, 41]. Biofilms are highly undesirable because they can be difficult to remove once they are formed even via disinfection or chemical cleaning [70]. The process of biofilm development on a membrane surface initiates by the surface attachment of organic polymers and colloids present in natural water that forms a conditioning film (composed of polysaccharides, proteins, lipids, nucleic acids, and humic and fulvic acids) that promotes surface attachment of microbial cells [71]. The surface attached microbial cells grow and produce extracellular polymeric substances (EPS), which strongly bind the cells to the membrane surface [41]. Subsequent microbial proliferation and EPS secretion leads to the formation of a mature biofilm on the membrane surface. In recent years, it has been suggested that the transparent exopolymer particles (TEP) are the major constituents of the initial conditioning film on the membrane surface and play a significant role in both initiation and development of a biofilm. TEP are clear, gel-like polysaccharides (0.4 – 300 μm) that exist as free-floating particles that are ubiquitous in marine and freshwater environments [71]. It was suggested that more effective removal of TEP can be achieved by utilizing UF as a SWRO pretreatment (compared to the conventional pretreatment methods such as DMF [71]. However, UF does not provide 100% retention of TEP, therefore, TEP in the UF permeate can cause membrane fouling in the downstream RO process. Therefore, it is critical to also reduce RO membrane fouling propensity, which can be accomplished by membrane surface modification.

2.4 The Impact of PA Surface Modification on RO Desalination Performance

In recent years, it has been suggested that membrane surface modification, a popular approach primarily employed for membrane fouling reduction, can also be used to tune PA TFC membrane desalination performance [61-63]. For example, affixing a hydrophilic polymer layer to a PA TFC membrane surface, which can be accomplished via various means including coating (via physical adsorption) [72], polymer grafting ("grafting to"), can be effective at reducing membrane fouling. In some cases, the hydrophilic polymer layers can also be used to increase salt rejection but at the cost of reduced water permeability. However, as reviewed in **Section 2.4.1-2.4.5**, the impact of PA TFC membrane surface modification on membrane desalination performance (typically evaluated in terms of water permeability coefficient (L_p) and nominal salt rejection) can vary significantly depending on the surface modification method and its specific application conditions. **Section 2.4.1-2.4.5** provide a review of various membrane modification approaches: (1) coating, (2) layer-by-layer, (3) initiated chemical vapor deposition, (4) polymer grating, and (5) graft polymerization.

2.4.1 Coating (physical adsorption)

Surface attachment of a layer of hydrophilic material (usually polymer) via non-covalent interactions (e.g., van der Waals, hydrogen bonding, electrostatic interactions) is the most commonly reported membrane surface modification approach to reduce the fouling propensity of PA TFC membranes [72-82]. Synthesis of such surface coating layers can be accomplished by either immersing a membrane in a polymer solution for a prescribed period (e.g., dip-coating) [79] or by drawdown coating the membrane surface with a layer of polymer solution using a device such as a wet film applicator [74]. Subsequently, the wet polymer layer on the membrane surface

is typically cured to evaporate the solvent, and, in some cases, to also thermally induce cross-linking of polymer chains and form a solid continuous polymer film on the membrane surface. For example, surfaces of commercial PA TFC BWRO (Hydranautics ESPA1 and ESPA3) and SWRO (Hydranautics SWC4) membranes were coated with a 0.3 μm-thick layer of PEBAX® 1657 (a hydrophilic block copolymer of nylon-6 and poly(ethylene glycol)) via dip-coating and subsequently cured at 60°C [73]. It was reported that the resulting PEBAX surface coating layers reduced fouling of SWC4 and ESPA1 membranes due to oil/surfactant/water emulsions over 106 days. For example, the cumulative permeate volume over 100 days of the oil/surfactant/water emulsion was 47% greater for the PEBAX coated SWC4 membrane than for the native SWC4 membrane. However, the fouling test of the native (base) membrane was conducted at an initial permeate flux that was greater than for the PEBAX coated membranes. Therefore, the initial fouling rate of the base membrane was greater than the PEBAX coated membranes, and hence the claim that the PEBAX coated membranes had a lower fouling propensity based on the above tests is misleading. It was also reported that the block copolymer layers significantly reduced L_p (evaluated with DI water) of ESPA1 (from 6.8 $L \cdot m^{-2} \cdot h^{-1} \cdot bar^{-1}$ to 1.8 $L \cdot m^{-2} \cdot h^{-1} \cdot bar^{-1}$) and ESPA3 (from 5.8 $L \cdot m^{-2} \cdot h^{-1} \cdot bar^{-1}$ to 1.1 $L \cdot m^{-2} \cdot h^{-1} \cdot bar^{-1}$) membranes by ~74% and ~81%, respectively. The authors attributed the significant reductions in L_p of the above membranes to the PEBAX polymer chains plugging "porous" regions of the PA selective layers of the base membranes. It was also reported that the PEBAX coating layer increased salt rejection (evaluated with a feed water containing 1,500 mg/L NaCl at ΔP = 11.3 bar) of the ESPA1 membrane from 97.8% to 99%, while the same coating layer resulted in a slight reduction in the salt rejection for the ESPA3 membrane (from 97.4% to 97%). However, no explanation was given for the difference in the salt

rejection changes for the above two membranes, and the stability of the PEBAX coating was not reported.

In order to increase stability of the physically coated polymer layers on the membrane surface, glutaraldehyde (GA) was utilized in a number of studies to cross-link surface adsorbed polymer layers [79, 80, 82]. For example, sericin, a water-soluble protein that has polar side groups (i.e., hydroxyl, carboxyl, and amino), was adsorbed (primarily via hydrogen bonding) onto the surface of a PA TFC membrane (supplied by the Development Center of Water Treatment Technology in Hangzhou, China) via dip-coating, followed by *in situ* cross-linking with GA [79]. Membrane fouling tests conducted at the same initial permeate flux and crossflow velocity showed that the sericin coated membrane had a lower permeate flux reduction (~23%) relative to the base PA membrane (~42%) after 100 h of BSA solution filtration (100 mg/L BSA aqueous solution at pH 6.8). Moreover, the sericin surface coating was reported to be stable over 300 h of saline water (500 mg/L NaCl feed water at ΔP = 5 bar) filtration period by maintaining membrane salt rejection in the range of 98.5 – 98.9% and the permeate flux in the range of 25.5 – 26.5 $L \cdot m^{-2} \cdot h^{-1}$. The sericin coating layers resulted in a 7 – 22% reduction of the base PA membrane L_p (L_p^{Base} = 6.5 $L \cdot m^{-2} \cdot h^{-1} \cdot bar^{-1}$) while increasing salt rejection from 97.6% to 98.2 – 98.5% (tested with 500 mg/L NaCl feed water at ΔP = 5 bar). It was also reported that the sericin coating layers reduced membrane salt permeability coefficient (B) by ~31 – 49% relative to the base membrane (B^{Base} = 0.75 $L \cdot m^{-2} \cdot h^{-1}$). However, the membrane B values were evaluated based on the feed water concentration (C_f) instead of the salt concentration at the membrane surface (C_m) (Eq. 2-7 in **Section 2.2.1**). Therefore, the reported membrane B values, which were evaluated at different permeate fluxes (different CP levels), and thus may deviate significantly from the actual salt permeability coefficient.

In another study, a (low energy) BWRO membrane (Dow Filmtec LC LE) surface was modified by dip-coating a layer of a random terpolymer, poly(methylacryloxyethyldimethyl benzyl ammonium chloride-*r*-acrylamide-*r*-2-hydroxyethyl methacrylate (P(MDBAC-*r*-Am-*r*-HEMA)) and GA, which was subsequently cross-linked by curing the terpolymer and GA coated membrane at 50°C for 2 h [80]. The terpolymer modified membranes had ~48 – 60% reduced L_p (reduced from 5.0 to 2.0 – 2.6 $L \cdot m^{-2} \cdot h^{-1} \cdot bar^{-1}$) and increased salt rejection (98.6 – 99.1%) relative to the base membrane (98.1%) when tested with low salinity feed water (2,000 mg/L NaCl) at ΔP = 15 bar. When compared to a standard commercial BWRO membrane (Dow Filmtec BW30), the modified membranes had similar or ~4 – 26% lower L_p but achieved greater salt rejection (98.6 – 99.1%) than the BW30 membrane (L_p = 2.7 $L \cdot m^{-2} \cdot h^{-1} \cdot bar^{-1}$, salt rejection = 98.5%). The study tested chlorine resistance of the terpolymer coated membranes with an aqueous feed solution of 500 ppm sodium hypochlorite (NaOCl). The chlorine tolerance limit was defined as the NaOCl exposure time at which a significant drop (≥ 10%) in salt rejection was observed due to membrane oxidation/degradation). It was reported that the chlorine tolerance limit for the terpolymer coated membrane was much greater (23,000 ppm·h) relative to the base (6,000 ppm·h) and BW30 (10,000 ppm·h) membranes. It was also reported that the terpolymer coated membrane maintained the same initial permeate flux after alternate filtration cycles of a BSA solution (i.e., 100 mg/L BSA in 2,000 mg/L NaCl aqueous solution, pH 4.7) and saline water (2,000 mg/L NaCl aqueous solution) over 30 hours. However, the base and BW30 membranes lost 20% of their initial permeate fluxes. It is noted that the above tests were conducted at the same transmembrane pressure of 15 bar, and thus performed at different initial fluxes (given that the tested membranes were reported to have a significantly lower L_p relative to the base membrane).

Cross-linked polymer coating layers were also prepared on a commercial SWRO membrane (CSM SHN) surface by immersing the membrane in aqueous solutions of homopolymers of hydroxyl poly(oxyethylene) methacrylate (HPOEM) and carboxylated polyethyleneimine (PEI), respectively, followed by exposing the polymer coated membrane surface to GA to cross-link the polymer layers on the membrane surface [82]. Membrane performance, evaluated with a feed water containing 32,000 mg/L NaCl and 70 mg/L $CaCl_2$ at 55.2 bar, indicated that the HPOEM homopolymer and carboxylated PEI coating resulted in membranes that had L_p lower by 8% (0.54 $L \cdot m^{-2} \cdot h^{-1} \cdot bar^{-1}$) or higher by 2% (0.60 $L \cdot m^{-2} \cdot h^{-1} \cdot bar^{-1}$), respectively, relative to the base membrane (0.59 $L \cdot m^{-2} \cdot h^{-1} \cdot bar^{-1}$). Nominal salt rejection was either slightly increased to 99.3% or decreased to 99.1% after coating with a HPOEM polymer or carboxylated PEI layer, respectively, relative to the base membrane salt rejection of 99.2%. Both HPOEM homopolymer and carboxylated PEI coating layers reduced fouling due to alginic acid and bovine serum albumin relative to the base membrane due to their amphiphilic and zwitterionic properties. For example, fouling tests with a BSA solution (100 mg/L alginic acid in 32,000 mg/L NaCl and 70 mg/L $CaCl_2$ aqueous solution at pH 8) were conducted for the above polymer coated and base membranes at initial permeate fluxes in the range of 29.9 – 32.3 $L \cdot m^{-2} \cdot h^{-1}$. After 20 h of alginic acid solution filtration, permeate flux reduction (relative to the initial flux) for the PEI-COOH coated membrane was ~9%; this was slightly lower relative to the flux reduction observed for the HPOEM coated and base membranes (both reduced by ~15%). However, long term stability of the cross-linked polymer coating layers on the PA membrane surfaces was not reported by the above study.

One of the most popular coating materials used for membrane surface modification is poly(vinyl alcohol) (PVA). PVA coating layers were shown to be effective for increasing

hydrophilicity of PA TFC membranes and mitigating membrane fouling. It has been suggested that membrane manufacturers also utilized PVA as surface coating layers for commercial PA TFC RO membranes in some cases [83]. It was shown that the structure of surface coated PVA films may be affected by the humidity to which the film is exposed to during the post-modification membrane curing step, which can also have an impact on the performance of PA membranes. For example, a solution containing PVA cross-linked with GA (PVA-GA) was allowed to contact the active side of a laboratory synthesized base PA membrane, followed by curing the solution coated membrane at 60°C for 10 min at two different relative humidity levels (30% or 90%) to form a PVA-GA layer on the membrane surface [72]. Membrane performance tests (performed with 32.8 g/L aqueous NaCl solution at 55 bar) revealed that the PVA-GA layer (prepared from 0.3% PVA-GA solution), cured at a relative humidity level of 90%, resulted in ~18% L_p reduction (from 0.93 $L \cdot m^{-2} \cdot h^{-1} \cdot bar^{-1}$ to 0.76 $L \cdot m^{-2} \cdot h^{-1} \cdot bar^{-1}$) and 0.2% salt rejection increase (99.4% to 99.6%), relative to the base PA membrane. In contrast, curing of the same coating layer (prepared from the same PVA-GA concentrated solution) at a relative humidity of 30% resulted in a significantly greater (~76%) L_p reduction (from 0.93 $L \cdot m^{-2} \cdot h^{-1} \cdot bar^{-1}$ to 0.22 $L \cdot m^{-2} \cdot h^{-1} \cdot bar^{-1}$), while salt rejection was decreased by 1.2% (99.4% to 98.2%) relative to the base PA membrane. The above was attributed to the low relative humidity resulting in the crystalline structure in the PVA-GA film relative to the amorphous structure characterized for the film cured in a high humidity environment (inferred from wide angle X-ray diffraction analysis). The study also reported reduced B values for the PVA coated membranes (by up to ~67%) relative to the base PA membrane (B = 0.31 $L \cdot m^{-2} \cdot h^{-1}$). However, it is noted that the salt permeability coefficients for different membranes were evaluated at a fixed ΔP of 55 bar; thus, the above comparisons were not at the same permeate flux (or the CP level) for all membranes, and in fact some of the PVA coated membranes had significantly

lower L_p (by as much as 76%) relative to the base membrane. Membrane fouling tests were performed with an aqueous solution of 32,800 mg/L NaCl containing 150 mg/L of dodecyl trimethyl ammonium bromide (DTAB) as a model foulant. It was reported that after performing two cycles of the DTBA solution filtration (8 hours), followed by flushing the membrane with a DTBA-free NaCl (32,800 mg/L) solution (4 hours), the PVA coated membranes maintained a higher permeate flux (~81 – 83%) relative to the base membrane (72%). However, again, the above comparisons were not conducted at the same initial permeate flux. It is noted that the selected PVA coated membranes for the fouling studies had ~22 – 34% reduced L_p relative to the base membranes; thus their initial permeate fluxes in the fouling study, conducted at a fixed ΔP = 55 bar, was lower relative to the base membrane.

In another study, a low-energy BWRO membrane (Dow Filmtec LE) surface was coated with three types of aqueous solutions containing either PVA, polyhexamethylene guanidine hydrochloride (PHMG) or a mixture of the two polymers using a wet film applicator [78]. The polymer coated membranes were then cured at 110°C for 2 min to evaporate the water and form cross-linked polymer layers on the membrane surface. Performance evaluation of polymer coated membranes (with a feed water containing 584 mg/L NaCl at ΔP = 27.6 bar) indicated that the PHMG layer reduced the base membrane L_p (L_p^{Base} ~4.4 $L \cdot m^{-2} \cdot h^{-1} \cdot bar^{-1}$) most significantly (~83%) and reduced salt rejection to the greatest degree (i.e., reduced from 97.2% for the base membrane to 91.6%). Membranes with PVA-PHMG surface coating layers, prepared from solutions containing a mixture of PVA and PHMG in ratios of 99:1 and 95:5, had 45% and 62% reduced L_p and increased or decreased salt rejections of 98.2% and 95.8%, respectively, relative to the base membrane (97.2%). Among the four types of polymer layers, the PVA coating layer reduced L_p by the least amount (~15%), while increasing salt rejection to 98.5% (from 97.2% for the base

membrane). It is noted that the study also reported salt permeability coefficients for the above polymer coated membranes, which were ~34 – 56% reduced relative to the base membrane (3.47 $L \cdot m^{-2} \cdot h^{-1}$). However, salt permeability coefficients were not evaluated at the same permeate flux. The study also reported that all three types of polymer coatings on the LE membranes reduced surface attachment of bacteria (*Pseudomonas aeruginosa*); however, PHMG, which is an antimicrobial polymer, was shown to be the most effective of the above surface modifiers for reducing bacterial surface attachment. For example, the PHMG coating layer reduced surface attachment of *Pseudomonas aeruginosa* (evaluated after immersing membranes in a bacterial suspension at room temperature for a day) by ~53%.

The hydrogel coating layers were also shown to be effective at reducing membrane fouling due to oil/surfactant. For example, various types of poly(ethylene glycol) based hydrogels were synthesized onto a BWRO membrane (GE Osmonics AG) surface with either acrylic acid (AA), 2-hydroxyethyl acrylate (HEA), or poly(ethylene glycol) acrylate (PEGA) with a cross-linker (i.e., poly(ethylene glycol) diacrylate (PEGDA)) [74]. The base AG membrane surfaces were coated with an aqueous monomer solution (containing either AA, HEA, or PEGA with PEGDA and photoinitiator (1-hydroxycyclohexyl phenyl ketone)) and subsequently underwent UV-initiated polymerization to form a hydrogel surface layer. It was reported that salt rejection (evaluated with 2,000 mg/L NaCl feed water at 15.5 bar) of the above hydrogel modified membranes was greater (99.1 – 99.3%) relative to relative to the base membrane (99.0%), while DI water permeance was reduced by ~36 – 42%. Fouling tests conducted with a cationic surfactant, DTAB, showed that the hydrogel layer coated membranes maintained a higher percentage of the initial permeate flux (36 – 43%) after 24 h filtration of a DTAB solution (200 ppm DTAB in 2,000 mg/L NaCl feed water) relative to the base membrane (30%). However, in these tests the initial permeate flux of the base

membrane was greater than the hydrogel coated membranes by up to a factor of 1.5. Again, indicating that the comparison was deficient.

It is noted that polyamide membrane surfaces are inherently negatively charged due to the carboxylic acid groups produced via hydrolysis of the acyl chlorides during polymerization step forming the active polymer layer [54]. Thus, cationic polymers may be adsorbed onto a PA membrane surface via electrostatic attraction, forming a more robust surface coating layer than coating layers affixed onto a membrane surface via van der Waals interactions. For example, a layer of a cationic phosphorylcholine polymer, poly[2-methacryloyloxyethyl phosphorylcholine (MPC)-*co*-2-aminoethylmethacrylate (AEMA)] (p(MPC-*co*-AEMA)), was adsorbed onto an ultralow pressure RO membrane (Nitto Denko ES20) surface via electrostatic interactions (i.e., between cationic amino groups of p(MPC-*co*-AEMA) and the anionic carboxyl groups present on polyamide membrane surface) [81]. The phosphorylcholine polymer layer was reported to reduce bacteria surface attachment, quantified after immersion of the membranes in a bacteria suspension (*Sphingomonas paucimobilis* as a model strain of Gram-negative bacteria) at 30°C for 24 h. It was reported that the maximum thickness of the surface attached bacteria film (quantified via bacteria staining and observed via a confocal laser scanning microscopy) was ~48% less than for the p(MPC-*co*-AEMA) coated membrane relative to the base membrane. In addition, it was reported that nominal salt rejection was increased from 94.7% to 96.9% at the cost of a ~24% L_p reduction (tested with 500 mg/L NaCl feed water at 7.5 bar).

In order to increase electrostatic attraction between a cationic biopolymer (i.e., chitosan) and the RO membrane surface, a laboratory synthesized PA TFC membrane (that had performance comparable to that of a commercial NF/ULPRO membrane) was first exposed to chlorine to increase the negative charge on the membrane surface [76]. It is noted that extensive exposure to

chlorination may result in oxidation of polyamide and cause membrane degradation that increases water permeability and salt passage [84]. However, it was shown that surface treatment with chlorine at mild conditions (e.g., a low chlorine concentration and short exposure period) may be utilized to increase membrane permeability (while minimizing loss of membrane selectivity) to partly compensate for the loss in membrane permeability due to subsequently coated surface polymer layers. It was reported that chlorination of the base PA membrane at the optimized conditions (exposure to a 200 mg/L sodium hypochlorite (NaClO) solution for 2 min) increased L_p by ~16% and decreased salt rejection from 91.0% to 88.7% (evaluated with a feed water containing 1,500 mg/L NaCl at 8 bar). The chlorine treated base PA membranes were then exposed to a chitosan solution (1,000 mg/L) for 30 min to deposit a chitosan layer on the membrane surface. It was reported that the L_p for the chitosan layer modified membranes was reduced by ~7% relative to the chlorine treated base membrane; but it was ~8% greater relative to the native base PA membrane (i.e., prior to chlorination). Moreover, the chitosan coated PA membrane achieved a higher level of salt rejection (94.5%) relative to the base PA membrane before (91.0%) and after chlorination (88.7%).

Changes in the performance of PA TFC membranes due to surface adsorbed coating layers reported in the literature are summarized in **Table 2.1**. Surface adsorbed coating layers typically resulted in L_p reduction relative to the base PA membrane, which can be quite significant in some cases (up to 83%), while it was accompanied by a rise in salt rejection. Simultaneous increase in L_p and salt rejection were also reported for the chitosan coated PA membranes [76], however, as is discussed in **Section 2.4.6**, salt rejection of membranes evaluated at different permeate flux values can lead to under or overestimation of membrane salt rejection. Membrane salt permeability coefficient was also reported in a number of studies [72, 79]; however, it was evaluated at different

permeate flux levels, thus the above comparison between membranes is questionable. Moreover, due to the noncovalent nature of interactions between the polymers and the membrane surface (e.g., van der Waals, electrostatic, hydrogen bonding interactions), such polymer films are generally considered to be less stable relative to covalently attached counterparts [85].

Table 2-1. Change in PA TFC membrane performance due to membrane surface modification by coating (physical adsorption).

Ref	Membrane surface modification method	Base PA TFC membrane[a]	Feed water; filtration mode[b]	ΔP (bar)[c]	L_p ($L \cdot m^{-2} \cdot h^{-1} \cdot bar^{-1}$)[d]		% Change in L_p[e]	R_o (%)[f]		Change in R_o (%)[g]	Comment
					Base	*Modified*		*Base*	*Modified*		
[73]	Surface coating with a PEBAX® 1657 layer via dip-coating, followed by curing at 60°C	Hydranautics ESPA1 (BWRO)	1,500 mg/L NaCl (21.5°C); crossflow	11.3	6.8[h]	1.8[h]	-74%	97.8	99.0	+1.2	All three base membranes were coated with a layer of PEBAX® 1657 at the same coating condition[(1)]
		Hydranautics ESPA3 (BWRO)			5.8[h]	1.1[h]	-81%	97.4	97.0	-0.4	
		Hydranautics SWC4 (SWRO)			0.9[h]	0.6[h]	-29%				
[79]	Surface coating of a sericin layer via dip-coating, followed by cross-linking with GA[(2)]	PA TFC membrane supplied by Development Center of Water Treatment Technology in Hangzhou, China	500 mg/L NaCl (25°C, pH 6.8); crossflow	5	6.5	6.0	-7%	97.6	98.2	+0.6	50 mg/L sericin[(3)]
						5.5	-16%		98.5	+0.9	100 mg/L sericin[(3)]
						5.0	-22%		98.4	+0.8	200 mg/L sericin[(3)]
[80]	Surface coating of a hydrophilic terpolymer P(MDBAC-r-Am-r-HEMA)[(4)] layer via dip-coating, followed by cross-linking with GA[(2)]	Dow Filmtec LC LE (BWRO)	2,000 mg/L NaCl (25°C, pH 7); crossflow	15	5.0	2.0	-60%	98.1	98.6	+0.5	200 mg/L terpolymer[(5)]
						2.3	-53%		98.7	+0.6	500 mg/L terpolymer[(5)]
						2.6	-48%		98.8	+0.7	1,000 mg/L terpolymer[(5)]
						2.4	-52%		98.9	+0.8	3,000 mg/L terpolymer[(5)]
						2.1	-59%		99.1	+1.0	10,000 mg/L terpolymer[(5)]
		Dow Filmtec BW30 (BWRO)			2.7			98.5			Membrane used for comparison
[82]	Surface coating of a HPOEM[(6)] homopolymer or carboxylated PEI[(7)] layer via dip-coating, followed by cross-linking with GA[(2)]	Toray SHN (SWRO)	32,000 mg/L NaCl + 70 mg/L $CaCl_2$ (25°C, pH 8); crossflow	55.2	0.6	0.5	-8%	99.2	99.3	+0.1	HPOEM[(6)]
						0.6	+2%		99.1	-0.1	Carboxylated PEI[(7)]
[72]	Membrane active side coating with solution containing pre-crosslinked PVA[(8)] with GA[(2)], followed by curing (60°C) to solidify the PVA[(8)]	Laboratory synthesized PA based TFC membrane	32,800 mg/L NaCl (25°C); crossflow	55	0.9	0.3	-66%	99.4	98.5	-0.9	[PVA]=0.1%, RH=30%[(9)]
						0.2	-76%		98.2	-1.2	[PVA]=0.3%, RH=30%[(9)]
						0.8	-12%		99.5	+0.1	[PVA]=0.1%, RH=90%[(9)]
						0.8	-18%		99.6	+0.2	[PVA]=0.3%, RH=90%[(9)]
						0.7	-24%		99.7	+0.3	[PVA]=0.5%, RH=90%[(9)]
						0.6	-33%		99.7	+0.3	[PVA]=1.0%, RH=90%[(9)]
						1.0	+6%		99.5	+0.1	[PVA]=0.1%, RH=90%[(9),(10)]

	film on the membrane surface	Dow Filmtec SW30HRLE (SWRO)			0.8			99.4			Membrane used for comparison
[78]	Surface coating of a PVA[8], PHMG[11] or PVA:PHMG layer via dip-coating, followed by curing at 110°C	Dow Filmtec LE-400 (BWRO)	584 mg/L NaCl (23°C); crossflow	27.6	4.4	3.7	-15%	97.2	98.5	+1.3	PVA[12]
						2.4	-45%		98.2	+1.0	PVA:PHMG (99:1)[12]
						1.7	-62%		95.8	-1.4	PVA:PHMG (95:5)[12]
						0.8	-83%		91.6	-5.6	PHMG[12]
[74]	Drawdown coating of an aqueous monomer solution containing PEGDA[13], HPK[14] and either AA[15], HEA[16], or PEGA[17] followed by surface exposure to UV to initiate polymerization to form a hydrogel layer	GE Osmonics AG (BWRO)	2,000 mg/L NaCl (25°C, pH 6.5 – 7.5); crossflow	15.5	4.5[h]	2.6[h]	-43%	99.0	99.3	+0.3	PEGDA[18]
						2.7[h]	-40%		99.1	+0.1	AA:PEGDA (50:50) [18]
						2.8[h]	-37%		99.2	+0.2	HEA: PEGDA (50:50) [18]
						2.9[h]	-36%		99.2	+0.2	PEGA:PEGDA (50:50) [18]
[81]	Surface coating of a p(MPC-co-AEMA)[19] layer via dip-coating	Nitto Denko ES20 (ULPRO)	500 mg/L NaCl; crossflow	7.5	5.5	4.2	-24%	94.7	96.9	+2.2	
[76]	Membrane exposure to chlorine, followed by coating a positively charged chitosan layer	PA TFC membrane supplied by Hangzhou Tianchuang Environmental Technology Co., LTD.	1,500 mg/L NaCl; crossflow	8	6.3	6.8	+8%	91.0	94.5	+3.5	2 min chlorination, 1,000 mg/L chitosan[20]
						7.2	+15%		95.4	+4.4	5 min chlorination, 1,000 mg/L chitosan[20]
						7.1	+12%		95.7	+4.7	5 min chlorination, 2,000 mg/L chitosan[20]

[a] Commercial or laboratory synthesized PA TFC membranes used as base membranes for surface modification

[b] Feed water condition and filtration mode used to evaluate the membrane L_p and R_o

[c] Transmembrane pressure used to evaluate the membrane L_p and R_o

[d] Water permeability coefficient, L_p, defined as $L_p = J_v/(\Delta P - \Delta\pi_m)$ where J_v is volumetric permeate flux and $\Delta\pi_m$ is the osmotic pressure difference between the membrane surface at the feed and permeate sides.

[e] Percentage change in L_p relative to base membrane defined as $\Delta L_p = \left[\left(L_p^{Modified} - L_p^{Base}\right)/L_p^{Base}\right]\cdot 100\%$

[f] Percent observed (nominal) salt rejection defined as $R_o = \left(1 - C_p/C_f\right)\cdot 100\%$

[g] Change in the percent salt rejection R_o relative to base membrane defined as $\Delta R_o = R_o^{Modified} - R_o^{Base}$

[h] L_p was evaluated with deionized water.

[1] PEBAX® 1657 is a hydrophilic block copolymer of nylon-6 and polyethylene glycol.
[2] GA = glutaraldehyde
[3] Sericin is a water-soluble globular protein that has polar side groups such as hydroxyl, carboxyl and amino groups. Base membranes were immersed in the aqueous solution (25°C) of sericin at the indicated concentrations (50 – 200 mg/L) for 5 min, followed by removing the excess solution from the membrane surface. Then, the membrane surface was exposed to an aqueous solution (25°C) containing 0.2% (w/v) glutaraldehyde and 0.1% (w/v) sulfuric acid for 5 min and the excess solution was removed from the membrane surface. Lastly, the membranes were cured at 40°C for 5 min and rinsed with deionized water.
[4] P(MDBAC-*r*-Am-*r*-HEMA) is a random terpolymer synthesized via free radical copolymerization of methylacryloxyethyldimethyl benzyl ammonium chloride (MDBAC), acrylamide (Am), and 2-hydroxyethyl methacrylate (HEMA) carried out in dimethyl sulfone (DMSO).
[5] Membranes were modified by immersing in a solution of P(MDBAC-r-Am-r-HEMA) at the indicated concentrations (200 – 10,000 mg/L) and GA (0.3 wt%) for 2 min, then the P(MDBAC-r-Am-r-HEMA) and GA adsorbed on the membrane surface was cross-linked at 50°C for 2 h.
[6] HPOEM = hydroxy poly(oxyethylene) methacrylate; The base SWRO membrane was immersed in a solution of laboratory synthesized HPOEM homopolymer (M_n 15,200 and M_w 38,600) for 1 min, and the excess solution was removed from the surface using a rubber roller. Then, the HPOEM coated SWRO membranes were exposed to an aqueous GA solution (0.01 wt%) for 30 s to affix the coating layer on the membrane surface.
[7] PEI = poly(ethyleneimine); The base SWRO membranes were immersed in an aqueous solution of PEI (0.1 wt%) for 1 min, followed by removal of excess solution from the membrane surface using a rubber roller. Then, the membranes were exposed to an aqueous GA solution (0.01 wt%) at pH 9 for 30 s to form cross-linked polymer layers on the membrane surface. Finally, the membranes were immersed in an aqueous bromoacetic acid (0.1 wt%) in the presence of potassium hydroxide (0.08 wt%) at 30°C for 10 h to form carboxyl end groups from the reaction between the PEI amine groups and bromoacetic acid.
[8] PVA = poly(vinylalcohol)
[9] PVA layers were casted onto base PA membrane surfaces by exposing the PA membrane active side to an aqueous PVA solution (PVA concentration, [PVA], of 0.1 wt% or 0.3 wt%) containing GA for 3 min, followed by draining of the excess PVA solution from the membrane surface and curing the PVA coated membranes at 60°C for 10 min at a fixed relative humidity (RH) or 30% or 90%.
[10] Following the membrane active surface exposure to the PVA solution (0.1 wt%) containing GA for 3 min, the membrane sample was rinsed with deionized water extensively prior to curing at 60°C and RH=90%.
[11] PHMG = polyhexamethylene guanidine hydrochloride
[12] Membrane sample was drawdown coated with a 4 μm-thick film of an aqueous solution of PVA (2 wt%), PVA:PHMG (2 wt%, ratios of PVA and PHMG are 99:1 or 95:5), or PHMG (2 wt%) via a wet film applicator. Subsequently, the wet film coated membranes were cured at 110°C for 2 min to evaporate the water and induce thermal cross-linking of the polymers to increase the film stability.
[13] PEGDA = poly(ethylene glycol) diacrylate, M_w: 698 g/mol
[14] HPK = 1-hydroxycyclohexyl phenyl ketone, a photoinitiator
[15] AA = Acrylic acid
[16] HEA = 2-hydroxyethyl acrylate
[17] PEGA = poly(ethylene glycol) acrylate, M_w: 380 g/mol
[18] Pre-polymerization mixtures containing 50 mol% cross-linker (PEGDA) and 50 mol% monomer (AA, HEA, or PEGA) were prepared with 1 wt% (based on total cross-linker and monomer content) photoinitiator (HPK). The base membranes were drawdown coated with the above pre-polymerization mixture using a wet film applicator and exposed to UV light for 90 s at an intensity of 3,000 μW/cm^2 to initiate polymerization of the coating layer.
[19] p(MPC-co-AEMA) = poly[2-methacryloyloxyethyl phosphorylcholine (MPC)-co-2-aminoethylmethacrylate (AEMA)], a cationic phosphorylcholine polymer; The base membrane was immersed in an aqueous solution of 0.1 wt% p(MPC-co-AEMA) polymer for 3 h in a refrigerator and rinsed with an aqueous solution of 3.5 wt% NaCl for 1 h.
[20] The base membranes were immersed in dilute aqueous solutions of sodium hypochlorite (NaClO concentration of 200 mg/L) for up to 20 minutes at 19°C and pH 5.5 (in order to oxidize PA membrane surface and generate negatively charged surface groups on the membrane surface), followed by rinsing with deionized water. Subsequently, the active sides of the chlorine-treated base membranes were exposed to a chitosan solution (1000 mg/L or 2000 mg/L chitosan in a dilute acetic acid solution) at 19°C for 30 min to allow for the chitosan (which exist as positively charged chitosanium in acidic solutions) to adsorb onto the membrane surface (via electrostatic interaction), followed by rinsing with deionized water.

2.4.2 Layer-by-layer (LbL) assembly

In layer-by-layer (LbL) assembly, oppositely charged materials (e.g., polyelectrolyte, nanoparticle, etc.) are alternatively deposited onto a substrate surface to form a multilayered film. Since the surface of polyamide active layers of TFC NF/RO membranes are anionic (due to carboxylic acid groups [86]), a cationic film is typically first deposited onto the native PA membrane surface. For example, an ultralow pressure RO membrane (Nitto Denko ES20) surface was modified by first depositing a cationic poly(allylamine hydrochloride) (PAH) layer, followed by surface deposition of an anionic poly(sodium 4-styrenesulfonate) (PSS) layer. It was shown that the surface charge of a LbL film is determined by the charge of the last deposited layer and thus can be controlled by the number of surface deposited layers [87]. Moreover, it was reported that increasing the number of bilayers (i.e., a pair of cationic and anionic layers) monotonously decreased L_p while increasing salt rejection. Membrane performance testing (with 500 mg/L feed concentration at ΔP = 7.5 bar) showed that increasing the number of PAH/PSS bilayers up to 6 led to increased salt rejection from 98.3% up to 99.3%, while L_p was reduced by up to ~48% (reduced from 4.7 to 2.5 $L \cdot m^{-2} \cdot h^{-1} \cdot bar^{-1}$).

Change in the RO membrane performance was also reported for a BWRO membrane (CSM RE4021-TE), which was coated with anionic polyacrylic acid (PAA) and cationic tobramycin (TOB) layers via LbL assembly [88]. It was reported that three bilayers of PAA/TOB resulted in increased salt rejection from 99.2% to 99.5% and increased L_p by ~17% (3.0 to 3.5 $L \cdot m^{-2} \cdot h^{-1} \cdot bar^{-1}$) relative to the base BWRO membrane (2,000 mg/L NaCl feed concentration at ΔP = 15.5 bar). Increasing the number of bilayers from three to ten resulted in a ~21% reduction in L_p (3.5 to 2.8 $L \cdot m^{-2} \cdot h^{-1} \cdot bar^{-1}$); however, salt rejection was not further increased from 99.5%. It was also reported that TOB, which is an aminoglycoside antibiotic, increased the mortality of *E. Coli* and *B. Subtilis*

significantly to 99.6 – 100% relative to the base BWRO membrane (10 – 15%). Moreover, the surface deposited PAA-TOB LbL films increased membrane fouling resistance to BSA and alginic acid. It was reported that after 3 cycles of foulant solution filtration (each cycle consisted of filtration of a foulant solution (100 ppm BSA or alginic acid + 2,000 mg/L NaCl) for 4 hours, followed by 1 hour of DI water flushing) the LbL film (with 3 PAA-TOB bilayers) modified membranes retained 75% of its initial permeate flux, while the native BWRO membrane only retained 38 – 49% of the initial membrane permeate flux.

The LbL assembly technique was also utilized to deposit alternating layers of anionic and cationic nanoparticles (LUDOX® HS-30 and CL-30 colloidal silica; nominal diameters of 12 nm and 22 nm, respectively) onto a commercial NF membrane (Dow Filmtec NF270) [89]. The NF270 membrane had a water permeability coefficient of ~10.8 $L \cdot m^{-2} \cdot h^{-1} \cdot bar^{-1}$ and salt rejection of ~31% when evaluated with 150 mg/L NaCl concentration feed water at ΔP = 17.2 bar. It was reported that even a single layer of either anionic or cationic silica nanoparticles deposited onto the base NF membrane greatly reduced the water permeability coefficient (~57%) and increased the salt rejection significantly to ~52%. Deposition of one or two nanoparticle bilayers resulted in greater degrees of L_p reduction by ~61% and ~68%, respectively, relative to the base NF membrane, but salt rejection remained the same as for the single nanoparticle layer coated membrane (~51 – 52%). Increasing the number of bilayers to 4 further reduced L_p (~76%) relative to the base NF membrane; however, salt rejection achieved with the membranes coated with 4 bilayers was ~47%, which was slightly lower than that for the membranes coated with ≤ 2 bilayers. However, stability of the nanoparticle bilayers was not investigated in the above study.

In another study, layers of polyethyleneimine (PEI) coated copper nanoparticles (PEI-CuNPs) and polyacrylic acid (PAA) were deposited onto a commercial SWRO membrane (Toray

UTC-82V) via spray- and spin-assisted LbL assembly [90]. It was reported that surface deposition of 10 bilayers of PEI-CuNPs/PAA onto the base SWRO membrane resulted in L_p (evaluated with DI water) reduced by ~13% (reduced from 1.59 to 1.38 $L \cdot m^{-2} \cdot h^{-1} \cdot bar^{-1}$), while salt rejection (evaluated with 2,922 mg/L NaCl concentration feed water and ΔP = 27.6 bar) was not changed due to the LbL film. The LbL film was shown to also reduce biofouling propensity of the base membrane due to the antimicrobial property of the copper nanoparticles deposited onto the membrane surface. Permeate flux reduction (relative to the initial permeate flux), following a 24 h period of bacterial solution filtration, for the LbL film (10 bilayers of PEI-CuNPs/PAA) coated and the native SWRO base membranes was 43% and 66%, respectively. However, it was reported that the surface deposited copper nanoparticles embedded in the LbL films were nearly depleted from the membrane surface after just 7 days of immersion in a 32 g/L NaCl solution. Therefore, the LbL films need to be re-deposited frequently and do not provide a practical solution to mitigate membrane fouling.

NF/RO membrane performance changes due to various types of LbL films reported in the literature are summarized in **Table 2.2**. In general, increasing number of bilayers deposited onto a membrane surface led to increased surface film thickness and hydraulic resistance, hence reduced water permeability. Salt rejection, however, did not monotonously increase with increasing number of bilayers. In most cases, salt rejection of LbL modified membrane increased relative to the base membrane, and it seems that there was an optimal number of bilayers at which the membrane salt rejection was maximized.

Table 2-2. Change in PA TFC membrane performance due to membrane surface modification by layer-by-layer (LbL) assembly.

Ref	Surface modification method	Base PA TFC membrane[a]	Feed water; filtration mode[b]	ΔP (bar)[c]	L_p (L·m^{-2}·h^{-1}·bar^{-1})[d]		% Change in L_p[e]	R_o (%)[f]		Change in R_o (%)[g]	Comment
					Base	*Modified*		*Base*	*Modified*		
[87]	Surface deposition of PAH[(1)] and PSS[(2)] layers via LbL assembly	Nitto Denko ES20 (ULPRO)	500 mg/L NaCl; crossflow	7.5	4.7	2.5	-48%	98.3	99.3	+1.1	6 bilayers of PAH/PSS[(3)]
[88]	Surface deposition of PAA[(4)] and TOB[(5)] layers via LbL assembly	CSM RE4021-TE (BWRO)	2,000 mg/L NaCl (25°C); crossflow	15.5	3.0	3.5	+17%	99.2	99.5	+0.3	3 bilayers of PAA/TOB[(6)]
[89]	Surface deposition of anionic (Ludox HS-30) and cationic (Ludox CL-30) colloidal silica nanoparticles[(7)] via LbL assembly	Dow Filmtec NF270 (NF)	150 mg/L NaCl; dead-end	17.2	10.8	~4.7	-57%	~31	~52	+21	a single layer of either PAA or TOB[(8),(9)]
						~4.2	-61%		~51	+20	1 bilayer of PAA/TOB[(8)]
						~3.5	-68%		~52	+21	2 bilayers of PAA/TOB[(8)]
						~2.6	-76%		~47	+16	4 bilayers of anionic and cationic nanoparticles[(8)]
[90]	Surface deposition of PEI-CuNPs[(10)] and PAA[(4)] layers via LbL assembly	Toray UTC-82C (SWRO)	2,922 mg/L NaCl (20°C); crossflow	27.6	1.6	1.4	-13%			No change	10 bilayers of PEI-CuNPs/PAA[(11)]

[a] Commercial or laboratory synthesized PA TFC membranes used as base membranes for surface modification

[b] Feed water condition and filtration mode used to evaluate the membrane L_p and R_o

[c] Transmembrane pressure used to evaluate the membrane L_p and R_o

[d] Water permeability coefficient, L_p, defined as $L_p = J_v/(\Delta P - \Delta\pi_m)$ where J_v is volumetric permeate flux and $\Delta\pi_m$ is the osmotic pressure difference between the membrane surface at the feed and permeate sides.

[e] Percentage change in L_p relative to base membrane defined as $\Delta L_p = \left[\left(L_p^{Modified} - L_p^{Base}\right)/L_p^{Base}\right]\cdot 100\%$

[f] Percent observed (nominal) salt rejection defined as $R_o = \left(1 - C_p/C_f\right)\cdot 100\%$

[g] Change in the percent salt rejection R_o relative to base membrane defined as $\Delta R_o = R_o^{Modified} - R_o^{Base}$

---

(1) PAH = poly(allylamine hydrochloride), a cationic polyelectrolyte

(2) PSS = poly(sodium 4-styrenesulfonate), an anionic polyelectrolyte

(3) Surface deposition of PAH and PSS layers performed by utilizing a cross-flow membrane cell. The base membrane surface was exposed to PAH and PSS solutions (10 g/L PAH or PSS in a 10 mM Tris buffer solution containing 1 M NaCl at pH 7) alternatively (for 30 min each). After deposition of each layer, the membrane surface was rinsed with deionized water for 5 minutes. The maximum number of PAH/PSS bilayers deposited is the study was 6.

(4) PAA = poly(acrylic acid), an anionic polyelectrolyte

(5) TOB = tobramycin, an aminoglycoside antibiotic

(6) The active side of the base membrane was first exposed to a 0.5 mg/L TOB solution for 15 min, followed by rinsing with deionized water. Then, the membrane active side was exposed to 1 mg/L PAA solution for 15 min, followed by rinsing with deionized water. The above two steps were repeated up to 5 times to acquire 10 bilayers of TOB/PAA. After surface deposition of the bilayers, the bilayers were cross-linked by immersing the membrane in a solution containing 5 mg/L EDC and 4.5 mg/L NHS for 12 h. The membranes were then subsequently rinsed with deionized water.

(7) Anionic Ludox HS-30 and cationic Ludox CL-30 colloidal silica nanoparticles had nominal diameters of 12 nm and 22 nm, respectively.

[8] The base membranes were immersed in aqueous nanoparticle solutions (0.03 wt%, pH 3) for 10 min, followed by two deionized water rinses, each lasted for 2 min. The step was repeated to acquire 1, 2, and 4 bilayers (each bilayer consists of one cationic and one anionic nanoparticle layers).
[9] A single layer of either anionic Ludox HS-30 or catinic Ludox CL-30 nanoparticle
[10] Positively charged poly(ethyleneimine) (PEI) coated copper nanoparticles (PEI-CuNPs) were synthesized in the study.
[11] The spray- and spin-assisted PEI-CuNPs/PAA LbL coating process was performed by spinning the base membrane (using a spin-coater) samples at 2,000 rpm while alternatively spraying solutions of positively charged PEI-CuNPs (pH 8.3) and negatively charged PAA (1 g/L, pH 3) onto the membrane surface at 2.1 bar. Between each layer deposition, the base membrane was rinsed with deionized water for 3 s and air-dried for 10 s (via spinning the membrane sample). The above steps were repeated to obtain a desired number of PEI-CuNPs/PAA bilayers.

2.4.3 Initiated chemical vapor deposition (iCVD)

A hydrophilic polymer film may be deposited onto a membrane surface via initiated chemical vapor deposition (iCVD) technique [91]. In iCVD, vinyl monomers and initiators in a vapor phase are deposited and polymerized (via free radical polymerization) simultaneously onto a substrate surface [91]. Polymerization is initiated by using chemical initiators such as tert-butyl peroxide, which thermally dissociate into radicals (upon passing through a heated filament at 200 – 360°C in the reactor) that can initiate the polymerization from the surface adsorbed monomers [91]. In the iCVD process, polymerization can proceed at a relatively low substrate surface temperature (i.e., 20 – 30°C) [92-96] and without any solvent and thus should maintain the integrity of the polyamide membrane [97]. Moreover, the technique allows for precise control of the deposited polymer film thickness in the order of a tenth to a hundredth nanometers [97]. However, it was reported that deposited polymer films of thickness below 20 nm do not form robust coating layers and could not withstand high feed pressures ($\Delta P \geq 48.3$ bar), as evidenced by gradually increased permeate flux during filtration tests of the polymer film coated polyamide RO membranes [93].

The iCVD technique can be applied to any type of substrate; however, in some cases, an adhesion layer is required to prevent delamination of surface deposited polymer films from the polyamide membrane surface. For example, prior to iCVD deposition of a copolymer (2-(dimethylamino)ethyl methacrylate (DMAEMA) and ethylene glycol diacrylate (EGDA)) layer, maleic anhydride (MA) was covalently anchored to a commercial BWRO membrane (Koch TFC-HR) via reaction between the anhydride and amide functional groups present in the RO membrane surface [92]. The subsequently deposited p(DMAEMA-*co*-EGDA) copolymer layer was covalently bonded to the MA groups on the membrane surface, thus forming a robust copolymer

layer that resisted delamination from the membrane surface. The copolymer layer was subsequently treated with 1,3-propanesulfone to obtain zwitterionic sulfobetaine surface functional groups. It was reported that the zwitterionic functionalized p(DMAEMA-*co*-EGDA) film effectively reduced surface attachment of *Escherichia coli* cells. It was also reported that surface deposition of the zwitterionic copolymer film (30 nm in thickness) reduced L_p of the TFC-HR membrane by ~17% (reduced from 5.3 to 4.4 $L \cdot m^{-2} \cdot h^{-1} \cdot bar^{-1}$) and also reduced salt rejection from 97% to 95% (tested with 2,000 mg/L NaCl feed water at ΔP = 20.7 bar).

Other types of zwitterionic and amphiphilic copolymer films synthesized onto commercial PA TFC membranes via the iCVD technique were also reported to reduce membrane biofouling [93, 95-97]. In the above studies, the thickness of the surface deposited polymer films was in the range of 20 – 40 nm, which was deemed to be optimal due to the low impact on water permeability (~10 – 20% reduction relative to the base membrane; **Table 2.3**) [93-95, 97]. Salt rejection, on the other hand, increased or remained the same after surface deposition of the polymer films via iCVD. For example, an amphiphilic polymer film, synthesized by copolymerization of a hydrophilic monomer, hydroxyethyl methacrylate (HEMA), and a hydrophobic monomer, perfluorodecyl acrylate (PFA), via the iCVD technique, was also shown to be effective for reducing surface adhesion of *Escherichia coli* [93]. It was reported that surface deposition of the amphiphilic copolymer p(HEMA-*co*-PFA) film (~20 nm thickness) onto a BWRO membrane (Koch TFC-HR) reduced L_p (evaluated with DI water) by ~10% (reduced from 3.5 to 3.2 $L \cdot m^{-2} \cdot h^{-1} \cdot bar^{-1}$), while salt rejection remained at the same level of 98% (evaluated with 12,000 mg/L NaCl feed water at ΔP = 48.3 bar). Surface deposition of the same film (~20 nm thickness) via iCVD onto SWRO membranes (Dow Filmtec SW30HR, GE AD, and Toray UTC80B) also resulted in a similar degree of reduction in L_p (~8 – 11%), while salt rejection (evaluated with 2,000 mg/L NaCl feed

water at ΔP = 50 bar) was either decreased (99.5% to 99.3% for SW30HR) or increased (99.2% to 99.4% for AD and 99.3% to 99.7% for UTC80B), depending on the base membrane [94].

In other studies, polymerization of 4-vinylpyridine (4-VP) was carried out via iCVD with a cross-linker, ethylene glycol diacrylate (EGDA) or divinylbenzene (DVB), in order to increase the mechanical stability of the resulting copolymer (i.e., p(4-VP-*co*-EGDA) or p(4-VP-*co*-DVB), respectively) film formed onto the BWRO membrane (Koch TFC-HR) surface [95-97]. The resulting copolymers were reacted with 3-bromopropionic acid or 1,3-propanesultone at the solid-gas interface to form zwitterionic surface functional groups (carboxybetaine or sulfobetaine, respectively) [95-97]. It was reported that both carboxybetaine and sulfobetaine functionalized p(4-VP-*co*-EGDA) copolymer films (38 nm and 35 nm in thickness, respectively) were effective for lowering surface attachment of bacteria cells (*Escherichia coli* and *Pseudomonas aeruginosa*) and increasing salt rejection of the base membrane (Koch TFC-HR) from 96.0 – 96.1% to 97.6 – 97.9% (evaluated with feed water containing 2,000 mg/L NaCl at ΔP = 20.7 bar) while reducing L_p (evaluated with DI water) by ~17 – 19% (reduced from ~2.2 to ~1.8 $L \cdot m^{-2} \cdot h^{-1} \cdot bar^{-1}$) [95, 96]. However, for the case of desalting a high salinity feed water (i.e., 35,000 mg/L NaCl at ΔP = 48.3 bar), surface modification of the same base membrane with a sulfobetaine functionalized p(4-VP-*co*-DVB) copolymer film (30 nm in thickness) did not improve salt rejection (remained at ~92%) and reduced L_p by ~19% (reduced from 0.48 to 0.39 $L \cdot m^{-2} \cdot h^{-1} \cdot bar^{-1}$) [97].

Reports of PA TFC membrane surface modification via iCVD indicate that the approach is suitable for depositing nano-scale polymer films that can mitigate bacterial surface attachment and have a relatively moderate to low impact on the base membrane water permeability (**Table 2.3**) compared to all other membrane surface modification approaches. However, scale up of the iCVD approach for commercial-scale membrane applications is likely to be difficult given the

requirement of a vacuum chamber (≤ 107 Pa) [93, 97], which would limit the treatable membrane surface area.

Table 2-3. Change in PA TFC membrane performance due to membrane surface modification by iCVD.

Ref	Surface modification technique	Base PA TFC membrane[a]	Feed water; filtration mode[b]	ΔP (bar)[c]	L_p (L·m^{-2}·h^{-1}·bar^{-1})[d]		% Change in L_p[e]	R_o (%)[f]		Change in R_o (%)[g]	Comment
					Base	*Modified*		*Base*	*Modified*		
[92]	Surface deposition of a p(DMAEMA-*co*-EGDMA) film via iCVD, followed by surface treatment with 1,3-propanesultone to form zwitterionic sulfobetaine surface functional groups[(1)]	Koch TFC-HR (BWRO)	2,000 mg/L NaCl; crossflow	20.7	5.3	4.4	-17%	97.0	95.0	-2.0	30 nm thick film[(2)]
[93]	Surface deposition of a p(HEMA-*co*-PFA) film via iCVD[(3)]	Koch TFC-HR (BWRO)	12,000 mg/L NaCl (25°C); crossflow	48.3	3.5[h]	3.2[h]	-10%	98.0	98.0	No change	20 nm thick film[(4)]
[94]	Surface deposition of a p(HEMA-co-PFA) film by via iCVD[(5)]	Dow Filmtec SW30HR (SWRO)	2,000 mg/L NaCl (25°C, pH 6); crossflow	50	0.74	0.68	-8%	99.5	99.3	-0.2%	20 nm thick film[(4)]
		GE Osmonics AD (SWRO)			0.50	0.45	-10%	99.2	99.4	+0.2%	
		Toray UTC80B (SWRO)			0.94	0.84	-11%	99.3	99.7	+0.4%	
[95]	Surface deposition of a p(4VP-*co*-EGDA) film via iCVD, followed by surface treatment with 3-bromopropionic acid to form zwitterionic carboxybetaine surface functional groups[(6)]	Koch TFC-HR (BWRO)	2,000 mg/L NaCl (21°C); crossflow	20.7	2.20[h]	1.82[h]	-17%	96.0	97.9	+1.9	38 nm thick film[(7)]
[96]	Surface deposition of a p(4VP-*co*-EGDA) film via iCVD, followed by surface treatment with 1,3-propanesultone to form zwitterionic sulfobetaine surface functional groups[(8)]	Koch TFC-HR (BWRO)	2,000 mg/L NaCl; crossflow	20.7	2.16[h]	1.76[h]	-19%	96.1	97.6	+1.5	35 nm thick film[(9)]
[97]	Surface deposition of a p(4VP-*co*-DVB) film via iCVD, followed by surface treatment with 1,3-propanesultone to form zwitterionic sulfobetaine surface functional groups[(10)]	Koch TFC-HR (BWRO)	35,000 mg/L NaCl; dead-end	48.3	0.48	0.39	-19%	92.0	92.0	No change	30 nm thick film[(11)]

[a] Commercial or laboratory synthesized PA TFC membranes used as base membranes for surface modification

[b] Feed water condition and filtration mode used to evaluate the membrane L_p and R_o

[c] Transmembrane pressure used to evaluate the membrane L_p and R_o

[d] Water permeability coefficient, L_p, defined as $L_p = J_v / (\Delta P - \Delta \pi_m)$ where J_v is volumetric permeate flux and $\Delta\pi_m$ is the osmotic pressure difference between the membrane surface at the feed and permeate sides.

[e] Percentage change in L_p relative to base membrane defined as $\Delta L_p = \left[\left(L_p^{Modified} - L_p^{Base}\right)/L_p^{Base}\right]\cdot 100\%$

[f] Percent observed (nominal) salt rejection defined as $R_o = \left(1 - C_p/C_f\right)\cdot 100\%$

[g] Change in the percent salt rejection R_o relative to base membrane defined as $\Delta R_o = R_o^{Modified} - R_o^{Base}$

[h] L_p was evaluated with deionized water.

---

(1) The base membrane was first treated with maleic anhydride, which was covalently bonded to the base membrane surface. The surface grafted MA was critical for preventing delamination of the subsequently deposited zwitterionic films when placed in water. The MA grafted base membrane surface was deposited with a random copolymer p(DMAEMA-*co*-EGDMA) film via iCVD during which tert-butyl peroxide (initiator) and monomers, 2-(dimethylamino)ethyl methacrylate (DMAEMA) and ethylene glycol dimethacrylate (EGDMA), were delivered into the reactor where the copolymer film was deposited at a filament temperature of 250°C and a stage temperature of 20°C. Total pressure in the vacuum chamber was maintained at ~29 Pa. Following the film deposition, the p(DMAEMA-*co*-EGDMA) film surface was exposed to 1,3-propane sultone vapor to form sulfobetaine zwitterionic groups on the membrane surface.

(2) The reported performance is for the base membrane that was modified with a p(DMAEMA-*co*-EGDMA) film of a final film thickness of 30 nm (after treatment with 1,3-propane sultone).

(3) The base membrane was modified by depositing with a random amphiphilic copolymer p(HEMA-*co*-PFA) film via iCVD. The p(HEMA-*co*-PFA) film was deposited by delivering tert-buryl peroxide (initiator), a hydrophilic monomer (2-hydroxyethyl methacrylate (HEMA)), and a hydrophobic monomer (perfluorodecyl acryate (PFA)) to the iCVD reactor at the total pressure of 27 Pa, while maintaining the filament and stage temperatures at 210°C and 30°C, respectively.

(4) The reported performance is for the base membrane that was modified with a 20-nm thick p(HEMA-*co*-PFA) film.

(5) The base membrane was deposited with a random amphiphilic copolymer p(HEMA-*co*-PFA) film via iCVD. The p(HEMA-*co*-PFA) film was deposited by delivering tert-buryl peroxide (initiator), a hydrophilic monomer (2-hydroxyethyl methacrylate (HEMA)), and a hydrophobic monomer (perfluorodecyl acryate (PFA)) to the iCVD reactor at the total pressure of 27 Pa, while maintaining the filament and stage temperatures at 220°C and 30°C, respectively.

(6) A random copolymer p(4-VP-*co*-EGDA) film deposition onto the base membrane surface via iCVD was performed by delivering tert-buryl peroxide (initiator), 4-vinylpyridine (4-VP), and ethylene glycol diacrylate (EGDA) to the iCVD reactor where temperatures of the filament and substrate were maintained at 200°C and 20°C, respectively, and the total pressure was maintained at 60 Pa. Subsequently, the deposited copolymer was exposed to 3-bromopropionic acid vapor to form zwitterionic carboxybetaine surface groups.

(7) The reported performance is for the base membrane that was modified with a p(4-VP-*co*-EGDA) film of a final film thickness of 38 nm (after treatment with 3-bromopropionic acid).

(8) A random copolymer p(4-VP-*co*-EGDA) film deposition onto the base membrane surface via iCVD was performed by delivering tert-buryl peroxide (initiator), 4-vinylpyridine (4-VP), and ethylene glycol diacrylate (EGDA) to the iCVD reactor where temperatures of the filament and substrate were maintained at 220°C and 20°C, respectively, and the total pressure was maintained at 60 Pa. Subsequently, the deposited copolymer was exposed to 1,3-propane sultone vapor to form zwitterionic sulfobetaine surface groups.

(9) The reported performance is for the base membrane that was modified with a p(4-VP-*co*-EGDA) film of a final film thickness of 35 nm (after treatment with 1,3-propane sultone).

(10) A random copolymer p(4VP-*co*-DVB) film deposition onto the base membrane surface via iCVD was performed by delivering tert-buryl peroxide (initiator), 4-vinylpyridine (4-VP), and divinylbenzene (DVB) to the iCVD reactor where temperatures of the filament and substrate were maintained at 250°C and 20°C, respectively, and the total pressure was maintained at 107 Pa. Subsequently, the deposited copolymer was exposed to 1,3-propane sultone vapor to form zwitterionic sulfobetaine surface groups.

(11) The reported performance is for the base membrane that was modified with a p(4-VP-*co*-DVB) film of a final film thickness of 30 nm (after treatment with 1,3-propane sultone).

2.4.4 Polymer grafting ("Grafting to")

In polymer grafting, preformed polymer chains are covalently attached to a membrane surface via a reaction between the polymer chain ends and the membrane surface. For example, polyamide active layer surfaces of TFC NF/RO membranes contain free carboxylic acid and primary amine groups that may be used to react with epoxy end groups of poly(ethylene glycol) diglycidyl ether (PEGDE) [98]. Commercial BWRO (Dow XLE) and NF (Dow NF90) membranes were grafted with PEGDE by exposing active sides of the membranes to 1% w/w or 15% w/w aqueous PEGDE (MW 200 or 1,000) solutions at 40°C for 10 minutes. Membrane performance evaluation (with 2,000 mg/L NaCl feed water at ΔP = 10.3 bar) revealed that PEGDE (MW 200) grafted XLE membranes had 15 – 31% lower L_p and intrinsic salt rejection (99.1 – 99.3%) that was similar or higher relative to the base XLE membrane (L_p^{XLE} ~ 6.9 $L \cdot m^{-2} \cdot h^{-1} \cdot bar^{-1}$, intrinsic salt rejection = 99.1%). Surface modification with a higher molecular weight PEGDE (MW 1,000) resulted in increased reductions of L_p (37 – 44%) relative to the base XLE membrane and correspondingly higher intrinsic salt rejection (99.4 – 99.5%), which was attributed to the longer PEGDE chains sealing surface defects present on the native base membrane surface more effectively than the shorter chains. When the same PEGDE (MW 1,000) molecules were grafted onto a NF base membrane (NF90), reduction in L_p (45 – 48%) the increase in intrinsic salt rejection (increased from 97.8% to 98.8%) relative to the base membrane (L_p^{NF} ~ 9.0 $L \cdot m^{-2} \cdot h^{-1} \cdot bar^{-1}$, intrinsic salt rejection = 97.8%) was more substantial compared to the PEGDE modified XLE membranes. It was conjectured that NF90, being a nanofiltration membrane, has more surface defects than the XLE BWRO membrane. Therefore, it was suggested that water permeability reduction due to plugging of base membrane surface defects by the surface grafted PEGDE chains was more significant for the NF90 than for the XLE membrane.

It is noted that the polyamide active layer surface also contains acyl chlorides (which is the precursor to carboxylic acids), which can be used to covalently anchor hydrophilic molecules that contain either a hydroxyl or amine end group [99, 100]. It was shown that 3-Monomethylol-5,5-dimethylhydantoin (MDMH), a hydantoin derivative, can be anchored to a PA membrane surface via reaction between a hydroxyl end group in MDMH and either the acyl chloride or carboxylic acid groups present on the PA active layer surface [100]. In the study, a laboratory synthesized PA TFC membrane surfaces were exposed to an aqueous solution containing MDMH of varying concentrations (2 – 20 wt%) at 40°C for 5 min, followed by curing at a high temperature (103°C) for 10 min [100]. Membrane performance evaluation (with 2,000 mg/L NaCl feed water at ΔP = 15 bar) revealed that surface grafting of MDMH onto the base PA membrane resulted in ~16 – 43% increased L_p (increased from 5.5 to 6.3 – 7.5 $L \cdot m^{-2} \cdot h^{-1} \cdot bar^{-1}$) but at reduced nominal salt rejection (reduced from 95.6% to 91.8 – 94.3%). It was reported that MDMH grafted membranes exhibited a higher resistance to chlorine oxidation relative to the base membrane. Exposing the MDMH grafted membranes to 2,000 ppm·h of chlorine (at pH 4) led to 9 – 26% L_p increase and 2.8 – 4.7% lower salt rejection. The same chlorine exposure resulted in a greater increase in L_p (~39%) and correspondingly greater reduction of salt rejection (by ~7%) due to membrane degradation associated with membrane oxidation by chlorine. Antimicrobial property of the surface grafted MDMH layers was tested by immersing chlorine treated membranes (exposed to 500 ppm·h at pH 4) in an *E. coli* suspension and incubating the solution at 37°C for 48 hours. After 48 h exposure to the microbial cells, permeate flux of the base membrane was reduced by ~25%, whereas the MDMH grafted membrane flux was reduced slightly lower by ~13 – 22. However, the bacteria fouling tests for the above membranes were conducted at different initial permeate flux values.

Covalent tethering of hydrophilic macromolecules on a PA membrane surface is also

possible by utilizing a mediating chemical compound that allows for a coupling reaction between a functional group present on the polyamide surface and a chemical modifier. For example, primary amines ($R–NH_2$) such as imidazolidinyl urea, poly(ethyleneimine), poly(vinylamine), and polyether diamines (JEFFAMINE® ED series) have been grafted onto PA membrane surfaces via carbodiimide-mediated coupling reaction [101-104]. A water soluble carbodiimide compound such as 1-ethyl-3-(3-dimethylaminopropyl) carbodiimide hydrochloride (EDC) can be employed to convert carboxylic acids that are inherently present on PA membrane surface to *O*-acylisourea ester intermediates (**Figure 2-7**). The *O*-acylisourea ester intermediate is then displaced by a nucleophile attack by a primary amine to form a surface amide group [105, 106]. However, the *O*-acrylisourea is highly unstable in aqueous solutions and rapidly undergoes hydrolysis or rearrange to form the more stable *N*-acylurea, thus resulting in a low yield of the coupling reaction [105, 106]. It was reported that the reaction yield can be significantly increased by use of *N*-hydroxysuccinimide (NHS) (or its derivative N-hydroxysulfosuccinimide) in conjunction with EDC to convert the *O*-acylisourea intermediate to form a more stable NHS ester intermediate, which hydrolyzes slowly relative to rate at which it reacts with a primary amine (**Figure 2-7**) [105, 106].

The above approach (i.e., carbodiimide-mediated coupling reaction) was utilized to graft imidazolidinyl urea (IU) and polyethyleneimine (PEI) onto an ultralow pressure RO membrane (CSM RE4021-TL) [101, 102]. Surface grafting of IU and PEI (MW 70,000) both resulted in a similar degree of L_p reduction (~25%) relative to the base membrane (~6.3 – 6.8 $L \cdot m^{-2} \cdot h^{-1} \cdot bar^{-1}$). However, the PEI grafted membrane had a higher salt rejection (~98.1%) than the IU grafted membrane (96.9%), which had a lower salt rejection than the base membrane (~97.0 – 97.1%) (both L_p and salt rejection were evaluated with 2,000 mg/L NaCl feed water at ΔP = 15.5 bar). It

was reported that the surface grafted IU layer significantly reduced membrane biofouling propensity and also reduced the PA active layer degradation by chlorine [101]. It was reported that the surface grafted PEI layers reduced membrane fouling by positively charged model foulants (i.e., lysozyme, dodecyl trimethyl ammonium chloride (DTAC), and cetyl trimethyl ammonium chloride (CTAC)) [102]. For example, filtration of feed solutions containing 1,000 mg/L lysozyme and 2000 mg/L NaCl at pH 4 – 10 for 500 min resulted in 20 – 39% flux reduction for the PEI grafted membranes, whereas the permeate flux of the base membrane was reduced by 41 – 60%. The above was partly attributed to a positively charged PEI surface layer, which effectively reduced attachment of the above foulants by electrostatic repulsion over a wider range of pH compared to the base PA membrane (the surface grafted PEI layer increased the isoelectric point of the base membrane from 3.1 to ~8). However, in the above fouling tests, the initial permeate flux of the base membrane was ~28% higher relative to the initial permeate flux of the PEI grafted membrane. Therefore, the assertion of inferiority of the base membrane is questionable.

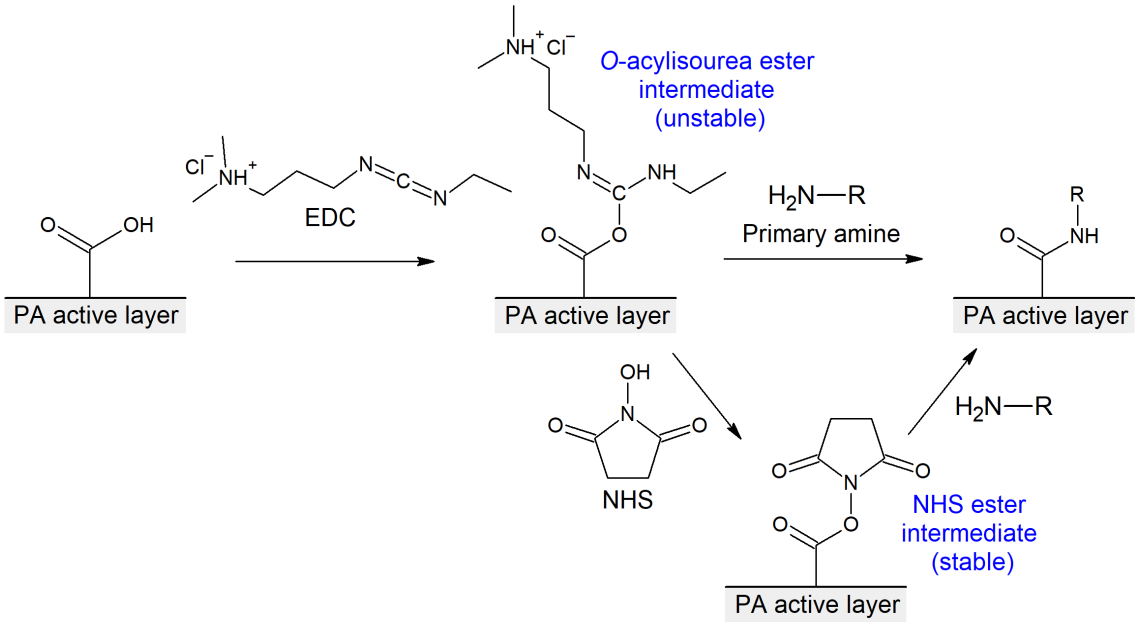

Figure 2-7. 1-Ethyl-3-(3-dimethylaminopropyl) carbodiimide hydrochloride (EDC) mediated coupling reaction between carboxylic acid of a polyamide active layer surface and a primary amine modifier with facilitated by use of *N*-hydroxysuccinimide (NHS) (side reactions and byproducts are not shown).

Glutaraldehyde was utilized as a mediating compound for surface grafting of polyvinyl alcohol (PVA) onto a commercial PA TFC ULPRO membrane (supplied by Hangzhou Tianchuang Environmental Technology Co., LTD) [107]. Glutaraldehyde, which possesses two aldehyde end groups, was grafted onto the PA membrane surface via reaction between one of the aldehyde groups in the GA and the amide or free primary amines present on the PA membrane surface [107]. Subsequently, PVA chains (M_W ~22,000) were covalently tethered to the PA membrane surface via a reaction between the hydroxyl PVA groups and free ends of surface tethered GA molecules with aldehyde groups. The resulting PVA modified membranes L_p in the range of 5.4 – 5.9 $L \cdot m^{-2} \cdot h^{-1} \cdot bar^{-1}$, which was 4% lower or 4 – 11% greater than the base PA membrane (5.6 $L \cdot m^{-2} \cdot h^{-1} \cdot bar^{-1}$), while salt rejection increased up to 98.5% from 98.1% for the base PA membrane (tested with feed water containing 500 mg/L NaCl at ΔP = 5 bar). The PVA grafted membrane had a lower fouling propensity to various types of model foulants including bovine serum albumin (BSA), sodium dodecyl sulfate (SDS), and dodecyltrimethyl ammonium bromide (DTAB). Following the filtration of the foulant solutions (containing either 100 mg/L BSA, 200 mg/L SDS, or 10 mg/L DTAB) for up to 40 hours, permeate flux of the PVA grafted membranes was reduced by ~19 – 33%, whereas ~27 – 54% permeate flux decline was observed for the native ULPRO membrane. It was also reported that membrane cleaning of the fouled membranes via DI water flushing for 60 minutes (at a crossflow velocity of 20 cm/s) achieved permeability recovery for the PVA grafted membranes (79 – 93%), which was greater than for the native membrane (59 – 82%).

In another study, the same research group modified the ULPRO base membrane (supplied by Hangzhou Tianchuang Environmental Technology Co., LTD) by surface grafting PVA chains using potassium persulfate ($K_2S_2O_8$) as a thermal initiator [108]. The base membrane surface was coated with a layer of an aqueous solution containing PVA (M_w ~22,000) and $K_2S_2O_8$ and then

subsequently heated to 60°C for 2 minutes. Upon heating to 60°C the potassium persulfate is expected to dissociate to generate sulfate radicals ($\cdot SO_4^-$), which can abstract hydrogen atoms from PA surface and PVA to generate free radicals. Subsequent combination of the free radicals generated on the PA membrane surface and PVA macroradicals were reasoned to lead to grafting of PVA chains onto the PA membrane surface [108]. The PVA grafted membranes (via potassium persulfate initiation) were also tested with 500 mg/L NaCl solution at ΔP = 5 bar and shown to achieve ~3 – 12% reduced L_p (5.3 – 5.8 $L \cdot m^{-2} \cdot h^{-1} \cdot bar^{-1}$) and increased salt rejection (98.6 – 98.9%) relative to the base membrane (L_p^{Base} ~6 $L \cdot m^{-2} \cdot h^{-1} \cdot bar^{-1}$, R_o^{Base} = 98.3%).

Gamma radiation has been utilized to graft preformed polyvinylpyrrolidone (PVP) chains onto a laboratory synthesized PA TFC membrane surface [62]. In this approach, the PA membrane surface was first covered with a layer of aqueous solution of PVP (M_w of 8,000, 24,000, or 58,000), followed by surface irradiation with gamma rays under nitrogen. Gamma irradiation of the aqueous polymer solution causes radiolysis of water and produces OH radicals that can abstract hydrogen atoms from PVP in the solution [109]. The resulting PVP macroradicals attack the underlying PA membrane surface and can be covalently bond to the surface. It was shown that the PVP grafted membrane performance may be tuned by the polymer grafting conditions including the concentration of PVP in the aqueous solution, PVP molecular weight, and gamma ray dose. Membrane performance evaluation (with feed water containing 2,000 mg/L NaCl at ΔP = 15.5 bar) indicated that PVP surface grafting could achieve a significant increase in salt rejection from 97.2% to 99.4%, while reducing L_p by only 2% (reduced from 1.9 to 1.8 $L \cdot m^{-2} \cdot h^{-1} \cdot bar^{-1}$).

Change in the PA TFC membrane performance due to polymer grafting reported in the current literature is summarized in **Table 2.4**. The impact of the grafted polymer chains on the membrane surface vary significantly depending on the approach utilized for polymer grafting. It

is noted that polymer grafting approach typically yields a low surface chain density due to steric hindrance. Thus, when a high surface density is important, which is the case for generating fouling-resistant membrane surfaces, graft polymerization is preferred over polymer grafting.

Table 2-4. Change in PA TFC membrane performance due to membrane surface modification by polymer grafting ("grafting to").

Ref	Surface modification method	Base PA TFC membrane[a]	Feed water; filtration mode[b]	ΔP (bar)[c]	L_p (L·m^{-2}·h^{-1}·bar^{-1})[d]		% Change in L_p[e]	R_o (%)[f]		Change in R_o (%)[g]	Comment
					Base	*Modified*		*Base*	*Modified*		
[98]	Surface grafting of poly(ethylene glycol) diglycidyl ether PEGDE[(1)]	Dow Filmtec XLE (BWRO)	2,000 mg/L NaCl (25°C, pH 8); crossflow	10.3	6.9	5.8	-15%	99.1	99.1	+0.0	1% w/w PEGDE, MW 200[(2)]
						4.8	-31%		99.3	+0.2	15% w/w PEGDE, MW 200[(2)]
						4.4	-37%		99.4	+0.3	1% w/w PEGDE, MW 1,000[(2)]
						3.9	-44%		99.5	+0.4	15% w/w PEGDE, MW 1,000[(2)]
		Dow Filmtec NF90 (NF)			9.0	5.0	-45%	97.8	98.8	+1.0	1% w/w PEGDE, MW 1,000[(2)]
						4.7	-48%		98.8	+1.0	15% w/w PEGDE, MW 1,000[(2)]
[100]	Surface grafting of 3-monomethylol-5,5-dimethylhydantoin (MDMH)[(3)]	Laboratory-made PA TFC membrane	2,000 mg/L NaCl (25°C); crossflow	15	5.5	6.3	+16%	95.6	94.3	-1.3	modified w/ 2 wt% MDMH[(4)]
						7.5	+43%		91.8	-3.8	modified w/ 20 wt% MDMH[(4)]
[101]	Carbodiimide-mediated grafting of imidazolidinyl urea[(5)]	CSM RE4021-TL (ULPRO)	2,000 mg/L NaCl (25°C); crossflow	15.5	6.8	5.1	-25%	97.1	96.9	-0.2	
[102]	Carbodiimide-mediated grafting of poly(ethyleneimine) (PEI)[(6)]	CSM RE4021-TL (ULPRO)	2,000 mg/L NaCl (25°C)	15.5	6.3	4.7	-25%	97.0	98.1	+1.1	PEI, MW 70,000[(7)]
[103]	Carboiimide-mediated grafting of poly(vinylamine) (PVAm)[(8)]	CSM RE4021-TE (ULPRO)	2,000 mg/L NaCl (25°C, pH 7); crossflow	15.5	4.7	4.5	-4%	97.9	97.9	+0.1	0.05 w/v% PVAm[(8)]
						4.2	-10%		97.8	-0.1	0.10 w/v% PVAm[(8)]
						4.1	-12%		98.4	+0.5	0.20 w/v% PVAm[(8)]
						3.7	-22%		98.2	+0.4	0.25 w/v% PVAm[(8)]
[104]	Carbodiimide-mediated grafting of PEG derivatives[(9)]	Hangzhou Beidouxing Membrane Co., Ltd.	1,500 mg/L NaCl (25°C); crossflow	10.5	4.8[h]	3.0[h]	-36%	96.7	96.4	-0.3	Jeffamine ED600[(9)]
						3.4[h]	-28%		96.5	-0.2	Jeffamine ED2001[(9)]
[107]	Surface grafting of poly(vinyl alcohol) (PVA) via glutaraldehyde[(10)]	Hangzhou Tianchuang Environmental Technology Co., LTD. (ULPRO)	500 mg/L NaCl (25°C, pH 7); crossflow	5	5.6	5.9	+5%	98.1	98.3	+0.2	[PVA] = 50 mg/L[(10)]
						6.2	+11%		98.5	+0.4	[PVA] = 100 mg/L[(10)]
						5.7	+4%		98.5	+0.4	[PVA] = 150 mg/L[(10)]
						5.4	-4%		98.4	+0.4	[PVA] = 200 mg/L[(10)]
[108]	Surface grafting of poly(vinyl alcohol) (PVA) via using a thermal initiator ($K_2S_2O_8$) [(11)]	Hangzhou Tianchuang Environmental Technology Co., LTD. (ULPRO)	500 mg/L NaCl (25°C, pH 7); crossflow	5	6.0	5.8	-3%	98.3	98.9	+0.6	[PVA] = 100 mg/L[(11)]
						5.6	-7%		98.8	+0.5	[PVA] = 300 mg/L[(11)]
						5.4	-10%		98.7	+0.4	[PVA] = 500 mg/L[(11)]
						5.3	-12%		98.6	+0.3	[PVA] = 1000 mg/L[(11)]

[62]	Surface grafting of poly(vinyl alcohol) (PVA) via gamma irradiation[12]	Laboratory synthesized PA TFC membrane	2,000 mg/L NaCl (25°C); crossflow	15.5	1.9	1.8	-2%	97.2	99.4	+2.2%	2 w/v% PVP (MW 58,000) and 20 kGy radiation dose[13]

[a] Commercial or laboratory synthesized PA TFC membranes used as base membranes for surface modification

[b] Feed water condition and filtration mode used to evaluate the membrane L_p and R_o

[c] Transmembrane pressure used to evaluate the membrane L_p and R_o

[d] Water permeability coefficient, L_p, defined as $L_p = J_v / (\Delta P - \Delta \pi_m)$ where J_v is volumetric permeate flux and $\Delta\pi_m$ is the osmotic pressure difference between the membrane surface at the feed and permeate sides.

[e] Percentage change in L_p relative to base membrane defined as $\Delta L_p = \left[\left(L_p^{Modified} - L_p^{Base} \right) / L_p^{Base} \right] \cdot 100\%$

[f] Percent observed (nominal) salt rejection defined as $R_o = \left(1 - C_p / C_f\right) \cdot 100\%$

[g] Change in the percent salt rejection R_o relative to base membrane defined as $\Delta R_o = R_o^{Modified} - R_o^{Base}$

[h] L_p was evaluated with deionized water.

---

[1] The base membranes were modified by exposing the active side of the membranes to aqueous solutions (40°C) of poly(ethylene glycol) diglycidyl ether (PEGDE) for 10 min, followed by rinsing with deionized water and a 25 vol% isopropyl solution.

[2] The reported performance is for the membrane that was modified with a 1% w/w or 15% w/w PEGDE solution prepared with PEGDE that has PEG MW of 200 or 1,000.

[3] 3-monomethylol-5,5-dimethylhydantoin (MDMH) solutions were prepared with 2-20 wt% MDMH, 0.1 wt% sodium dodecyl sulfate, and 3 wt% tives triethyl amine in deionized water and the solution pH was adjusted to 9.5 using (+)-10-camphorsulfonic acid. The active sides of the base membranes were exposed to the MDMH solutions (40°C) for 5 min, followed by draining of the excess solution. The membranes were then cured at 103°C for 10 min.

[4] The reported performance is for the base membrane that was modified with 2 or 20 wt% MDMH solution.

[5] The active side of the base membrane was first exposed to a *N*-(3-dimethylaminopropyl)-*N*-ethylcarbodiimide hydrochloride (EDC·HCl) solution for 10 min, and *N*-hydroxysuccinimide (NHS) was added to the EDC·HCl solution. The membrane surface was exposed to the solution containing EDC·HCl and NHS in a dark place at room temperature for 16 h, prior to addition of a 5 wt% ethylenediamine (EDA) solution to the solution containing EDC·HCl and NHS. Subsequently, the membrane surface was exposed to an aqueous solution containing 5 wt% imidazolidinyl urea (IU), EDC·HCl, and NHS for 12 h and then rinsed with deionized water.

[6] The active side of the base membrane was first exposed to an EDC·HCl solution for 10 min, and NHS was added to the EDC·HCl solution. After 15 minutes of membrane surface exposure to a solution containing EDC·HCl and NHS, an aqueous solution containing 5 wt% poly(ethyleneimine) (PEI) of MW in the range of 600-70,000 was added to the solution containing EDC·HCl and NHS. The membrane exposed to the solution was placed in a dark room at the room temperature for 12 h, followed by rinsing with deionized water.

[7] The reported performance is for the base membrane that was modified with PEI of MW 70,000.

[8] The base membranes were modified using the same procedures as [5],[6]. Poly(vinylamine) (PVAm) was grafted onto the base membrane surface in the presence of EDC·HCl and NHS for 4 hours, followed by rinsing the membranes with deionized water. Aqueous PVAm solutions (PVAm concentration in the range of 0.05-0.25 w/v%) were utilized in polymer grafting reactions.

[9] The poly(ethylene glycol) (PEG) derivatives with amine end groups, Jeffamine ED600 and Jeffamine ED2001, were grafted onto the base membrane surface via the carboiimide-induced method. The base membranes were immersed in 0.1 wt% EDC aqueous solution at 4°C for 3 h, followed by rinsing with deionized water. The membranes were then placed in an aqueous solution containing ED600 or ED2001 at 4°C for 24 h and rinsed with deionized water afterwards.

[10] The base membranes were sequentially treated with an aqueous solution of glutaraldehyde (GA) and an aqueous poly(vinyl alcohol) (PVA) solution. First, the base membrane surface was exposed to a 0.04 wt% GA aqueous solution (25°C, pH 3) for 5 min, and the excess solution was drained from the membrane surface afterwards. Subsequently, the membranes were rinsed with deionized water and dried in air to rid of moisture from the membrane surface. The GA-coated membrane surface was then exposed to an aqueous PVA solution (PVA concentration in the range of 50-200 mg/L, 25°C, pH 3) for 2 min, followed by draining of the excess solution and membrane surface drying under heated air flow (50°C).

[11] The active side of the base membranes were exposed to an aqueous solution (25°C, pH 7.6) containing 1 wt% potassium persulfate ($K_2S_2O_8$) and PVA (MW 22,000; concentration in the range of 100-1,000 mg/L) for 2 min, followed by draining of the excess solution and air drying the membrane sample at the room temperature. Subsequently, the membrane surface was dried under hot air flow (60°C) for 2 min.
[12] The active sides of the base membranes were exposed to an aqueous poly(vinylalcohol) (PVA) solution (MW 8,000, 24,000, or 58,000; concentration up to 5 w/v%) in a glass radiation tube. The membrane and grafting solution were degassed and irradiated by γ-ray at the radiation dose (up to 100 kGy).
[13] The reported performance is for the base membrane that was modified with a 2 w/v% PVP (MW 58,000) solution and 20 kGy irradiation dose.

2.4.5 Graft polymerization ("Grafting from")

In graft polymerization, end-tethered polymer chains are grown from surface initiation sites via sequential monomer addition, thus enabling a high surface chain density. Surface initiation sites (e.g., free radical, peroxide, etc.) on a polyamide membrane can be generated by surface activation via a chemical initiator (e.g., redox [110], thermal [111] or atom transfer radical polymerization (ATRP) [112]), UV irradiation [113] or low pressure plasma (LPP) [114]. Among the above, redox-initiated free radical graft polymerization has been most frequently utilized to graft tethered hydrophilic polymer layers on a polyamide membrane surface [110, 115-119]. Typical redox system utilized to generate surface initiation sites (radicals) on PA membrane surfaces consist of potassium persulfate ($K_2S_2O_8$) paired with either sodium metabisulfite ($Na_2S_2O_5$) [115, 116, 118], sodium bisulfate ($NaHSO_3$) [119], or potassium metabisulfite ($K_2S_2O_5$) [61, 110]. In the earliest study, methacrylic acid (MA) and poly(ethylene glycol) methacrylate (PEG-MA) were grafted onto two types of commercial BWRO membranes (Hydranautics CPA2 and Dow BW30) using a $K_2S_2O_8/Na_2S_2O_5$ redox pair [116]. Surface-initiated graft polymerization reactions were carried out by immersing the base membrane samples in aqueous MA (10%) and PEG-MA (16%) solutions containing the redox initiators for periods of 10 – 60 minutes and 15 – 30 minutes, respectively. Membrane performance evaluation (with feed water containing 1,500 mg/L NaCl at ΔP = 15.5 bar) showed that the MA surface graft polymerization reduced the base membrane water permeability coefficient (L_p^{CPA2} = 2.3 $L \cdot m^{-2} \cdot h^{-1} \cdot bar^{-1}$) by ~9 – 36%, and that increasing the reaction time of MA graft polymerization led to a greater reduction in L_p. Graft polymerization of PEG-MA onto BW30 base membrane (L_p^{BW30} = 2.7 $L \cdot m^{-2} \cdot h^{-1} \cdot bar^{-1}$) led to a relatively small reduction in L_p (~5%). Graft polymerization of MA and PEG-MA also impacted

salt rejection of the base membranes, which either increased (from 95.5% to 96.9 – 98% for CPA2) or decreased (from 94.8% to 94.2 – 94.6% for BW30) to various degrees (**Table 2-5**).

In recent years, there has been growing interest in utilizing surface tethered zwitterionic polymer layers due to their effectiveness for reducing membrane fouling [115, 119]. For example, a low pressure PA TFC RO membrane (CSM RE4021-TE) was modified by redox-initiated graft polymerization of N,N'-dimethylaminoethyl methacrylate (DMAEMA) using a $K_2S_2O_8/Na_2S_2O_5$ redox pair, followed by surface quarternization reaction with 3-bromopropionic acid to obtain zwitterionic poly(carboxybetaine methacrylate) (PCBMA) chains grafted onto the membrane surface [115]. It was reported that the permeate flux decline after 4 hour filtration of BSA and LYS solutions (1,000 mg/L BSA or LYS + 2,000 mg/L NaCl at pH 6.8) was reduced by only ≤ 10% due to the surface grafted PCBMA layer (evaluated at the same initial flux as the base membrane). However, permeate flux recovery after membrane cleaning with DI water flushing (for 30 minutes) for the PCBMA grafted membranes was 92 – 95%, whereas only 71 – 74% of initial permeate flux could be recovered for the base membrane after the DI water flushing. It was also reported that the surface grafted PCBMA layer increased the base membrane L_p (4.7 $L \cdot m^{-2} \cdot h^{-1} \cdot bar^{-1}$) by 23% while maintaining salt rejection at 97.9% (evaluated with feed water containing 2,000 mg/L NaCl at ΔP = 15 bar).

It has been shown that surface tethered zwitterionic polymers, such as poly (4-(2-sulfoethyl)-1-(4-vinylbenzyl) pyridinium betaine) (PSVBP), which exhibit increased swelling with increased salt concentration, could allow for improve membrane cleaning by flushing with a solution of salinity higher than that of the raw feed water being treated [119]. For example, surface tethered PSVBP chains synthesized onto a PA TFC brackish water RO (BWRO) membrane (Dow Filmtec XLE) surface, via redox-initiated graft polymerization increased salt rejection from 98.0%

up to 99.6% but at the cost of ~23% permeate flux reduction (reduced from 6.1 to 4.7 $L \cdot m^{-2} \cdot h^{-1} \cdot bar^{-1}$) attained after a very long graft polymerization reaction period of 18 hours (membrane performance was evaluated with 2,000 mg/L NaCl feed water at ΔP = 15 bar). Membrane fouling testing with BSA showed that the surface tethered PSVBP layer did not reduce BSA fouling appreciably after filtration of a BSA solution over 100 hours (tested with a solution containing 100 mg/L BSA and 2,000 mg/L NaCl at pH 6.8). It was reported that BSA solution filtration was accompanied by ~24% and ~28% permeate flux reduction for the PSVBP grafted membrane and the native XLE membrane, respectively. Subsequent DI water flushing (for 2 hours) of the BSA fouled membranes restored the PSVBP membrane to ~83% of its initial permeability, while the DI water flushing did not recover any of the base XLE membrane permeability lost due to BSA fouling. Additional membrane cleaning (total 2 hours) with alternating cycles of DI water and saline water (1.5 M NaCl solution) flushing restored up to ~90% of the initial permeability for the PSVBP grafted membrane, while the permeability of the native XLE membrane declined further from 72% to 57% of the initial membrane permeability. The latter was attributed to dehydration of the BSA after exposure to a high salinity water that led to the aggregation and precipitation of BSA molecules and subsequent formation of a dense cake layer on the membrane surface. The above results demonstrated that the tethered PSVBP layer could be beneficial for increasing membrane cleaning efficiency. However, it is noted that the tethered PSVBP layer did not fully restore the initial membrane permeability (which remained at ~90%) even after a very long (total of 4 hours) of membrane cleaning, which would be too long of a down time for practical implementation of the approach.

A temperature-responsive polymer has also been utilized to improve RO membrane cleaning efficiency [118]. Redox-initiated graft polymerization reactions of N-

isopropylacrylamide (NIPAm) and acrylic acid (AA) were performed sequentially onto a commercial PA TFC RO membrane supplied by Development Center of Water Treatment Technology in Hangzhou, China) by exposing the membrane surface first to an aqueous NIPAM monomer solution (30°C) containing redox initiators ($K_2S_2O_8/Na_2S_2O_5$), followed by exposure to an aqueous AA monomer solution (30°C) also containing the same redox initiators. It was reported that surface grafting poly(N-isopropylacrylamide) (PNIPAm) alone resulted in salt rejection reduced from 98.2% to 96.8 – 98.0% and up to 26% increased L_p from 5.6 $L \cdot m^{-2} \cdot h^{-1} \cdot bar^{-1}$ up to 7.1 $L \cdot m^{-2} \cdot h^{-1} \cdot bar^{-1}$ (membrane performance tested with 500 mg/L NaCl feed water at ΔP = 5 bar). Subsequent grafting of poly(acrylic acid) (PAA), however, increased salt rejection up to 98.6% (which is 0.4% greater than the base membrane) while maintaining 4% increased L_p relative to the base membrane. Membrane fouling test conducted with BSA (at the same initial permeate flux) showed that after 40 h filtration of a BSA solution (200 mg/L BSA + 500 mg/L NaCl at pH 6.8) permeate fluxes of the PNIPAm and PAA grafted membrane (PA-g-NIPAm60-AA90) and the base PA membrane were reduced by ~45% and ~21%, respectively. Membrane cleaning effectiveness evaluation was conducted using the PA-g-NIPAm60-AA90 and base PA membranes that had the same permeate flux reduction (40% of initial permeate flux) due to BSA fouling. Membrane cleaning performed by membrane soaking in DI water (45°C) for 3 h, followed by DI water (25°C) flushing for 30 min showed that membrane cleaning of the NIPAm60-AA90 recovered 93% of initial membrane permeability, which was greater than the 82% permeability recovery achieved for the base PA membrane. The greater permeability recovery achieved for the NIPAm60-AA90 membrane was attributed to the PNIPAm chain segments that collapse upon heating above the lower critical solution temperature of 32°C. It was also reported that the surface grafted PNIPAm and PAA chains improved membrane resistance to chlorine. Exposure to a

sodium hypochlorite solution (1,000 mg/L NaClO at pH 7 and 25°C) for up to 5 hours resulted in salt rejection of the base membrane being significantly reduced from 98.2% to 75.8%, while salt rejection of the NIPAm60-AA90 membrane only decreased from 98.5% to 96.5%. However, given that the above approach requires two different graft polymerization reactions and a lengthy reaction period (optimal at ≥ 2.5 hours), the scalability of the approach for commercial membrane fabrication is questionable.

Improved chlorine resistance was also reported for the PA membrane surface modified with a copolymer of 3-sulphopropyl methacrylate (SPMA) and methylene-bis-acrylamide (MBA) synthesized via redox-initiated graft polymerization using a Ce(IV)/polyvinyl alcohol (PVA) redox system [117]. It was reported that Ce(IV) rapidly generates radical sites on PVA, which then initiates copolymerization of SPMA and MBA. Polymerization of SPMA in the presence of MBA (which served as a cross-linker) yielded a cross-linked copolymer layer of PVA-g-poly(SPMA-co-MBA) on the PA membrane surface. The surface grafted PVA-g-poly(SPMA-co-MBA) layer synthesized at various concentrations of PVA, SPMA, and MBA, however, resulted in salt rejection decrease from 97.0% to 94.0 – 96.0%, except for a case in which salt rejection was slightly increased to 97.5% (membrane performance evaluated with feed water containing 2,000 mg/L NaCl at ΔP = 17.2 bar). After graft polymerization the membrane L_p was reduced by up to 64% (base membrane L_p was 3.4 $L \cdot m^{-2} \cdot h^{-1} \cdot bar^{-1}$). The optimal graft polymerization reaction conditions resulted in a membrane (TFC-M1) that had a slightly increased salt rejection of 97.5% and 4% reduced L_p of 3.2 $L \cdot m^{-2} \cdot h^{-1} \cdot bar^{-1}$ relative to the base PA membrane. Also, it was shown that the surface grafted PVA-g-poly(SPMA-co-MBA) layer retarded PA membrane oxidation due to chlorine attack and the associated PA membrane degradation. Membrane exposure to 1,000 mg/L NaOCl aqueous solution led to a significant increase in permeate flux of the base membrane

by up to 4.5 times and reduced salt rejection from 97% to 30% after 6 h exposure period. The same chlorine exposure period led to 1.2 times increased permeate flux and salt rejection reduced from 96% to 65% for the TFC-M1 membrane.

It is noted that it is typically difficult to achieve a high degree of surface grafting with redox initiators due to the redox-initiation step being a slow process and which does not preferentially takes place at the membrane surface (i.e., over homopolymerization which also occurs in the solution phase) [120]. It was proposed that a higher rate of surface graft polymerization (without using a high monomer concentration) can be achieved by carrying out the polymerization reaction while the monomer solution is being filtered through the membrane [120]. Typical RO/NF membranes reject monomers and initiators, which accumulate on the membrane surface and lead to concentration polarization. The increased concentrations of monomer and initiator at the membrane surface would thus lead to the polymerization reaction taking place preferentially near the membrane surface. The technique named as concentration polarization enhanced graft polymerization was reported for surface initiated graft polymerization of [2-(methacryloyloxy)ethyl]dimethyl-(3-sulfopropyl)ammonium (SPE), sulfonated glycidyl methacrylate (GMS), and [2-(methacryloyloxy)ethyl]trimethylammonium chloride (METMAC) onto a commercial LPRO membrane (Hydranautics ESPA1) using a redox initiator pair ($K_2S_2O_8$/$K_2S_2O_5$) [110]. Membrane modification with the above polymers resulted in ~20 – 40% reduced L_p, while salt rejection (assessed with 1,500 mg/L NaCl feed water) either remained the same (95%) or increased to 96.5%. The above was attributed to the surface grafted polymer plugging of defects that are inherently present at the polyamide membrane surface.

A thermal initiator, 2,2'-azobis(isobutyramidine) dihydrochloride (AIBA), was also utilized to carry out free radical graft polymerization of 3-allyl-5,5-dimethylhydantoin (ADMH)

onto a commercial ULPRO membrane (CSM RE4021-TL) [111]. It was reported that upon exposure to chlorine, surface grafted polymers of ADMH forms surface *N*-halamine groups that exhibit antimicrobial property. Thus, it was suggested that the above polymer would also produce a surface coating layer that would protect the underlying polyamide active layer from chlorine attack. For example, chlorine exposure at 1,500 ppm·h led to 29% increase in L_p and 9% lower salt rejection for the base membrane. At the same chlorine exposure, the ADMH graft polymerized membrane had a lower L_p rise of 14% and about 4% reduced salt rejection. Following chlorine exposure, membrane biofouling propensity was tested by exposing the chlorine treated membranes to a bacterial suspension of *Escherichia coli*, followed by incubation at 37°C for 60 h. After 60 h exposure to microbial cells, the base membrane permeate flux decreased by ~31%, whereas only ~9% permeate flux reduction was observed for the ADMH polymer grafted membrane. It was reported that the resulting surface grafted polymer layer led to increased base membrane L_p (10.1 $L \cdot m^{-2} \cdot h^{-1} \cdot bar^{-1}$), which was up to 22% increase for the graft polymerization period of 100 minutes (membrane performance evaluated with feed water containing 2,000 mg/L NaCl at ΔP = 15 bar). However, the L_p increase was accompanied by 4.8% reduced salt rejection (reduced from 96.6% to 91.8% after grafting).

As shown from the above examples, free radical graft polymerization (FRGP) is a versatile polymerization approach that is applicable to various types of monomers and surface initiators. However, the main drawback of FRGP is a broad chain size or molecular weight distribution that results in highly polydisperse surface grafted polymer chains [121]. Controlled radical polymerization such as atom transfer radical polymerization (ATRP), on the other hand, enables better control over surface grafted polymer chains lengths and thus can achieve a narrower size distribution of surface grafted polymer chains than FRGP [122]. In order to carry out surface-

initiated ATRP (SI-ATRP) reaction from a polyamide membrane surface, an ATRP initiator such as 2-bromoisobutyryl bromide (BIBB) must be first immobilized onto the membrane surface [112, 123]. BIBB is typically employed because its acyl halide groups can react readily with hydroxyl and amino groups that are present on the polyamide membrane surface [123]. However, the number of hydroxyl and amino groups present on a commercial PA TFC membrane surface is typically too small to achieve a high density of surface immobilized ATRP initiators [123]. Thus, an additional step is required to increase density of hydroxyl and/or amino groups on the PA membrane surface prior to surface immobilization of ATRP initiators. For example, 3-aminopropyltrimethoxysilane (APTES) was used to generate amine groups on the surface of a commercial PA TFC ULPRO membrane (Nitto Denko ES20) to increase the density of immobilized BiBB initiators on the membrane surface [123]. Following the initiator immobilization, poly[(2-methacryloyloxy)ethyl]dimethyl[3-sulfopropyl]ammonium hydroxide (pMEDSAH) was grafted onto the membrane surface via SI-ATRP. It was reported that the pMEDSAH grafted membrane (graft polymerization period ≥ 1 h) maintained its initial permeate flux over 20 h filtration of a saline solution (0.85 wt% NaCl) containing bacteria (*Sphingomonas paucimobilis*), thus demonstrating high resistance to biofouling. In contrast, permeate flux of the base membrane dropped to below 40% of the initial permeate flux after the 20 h period of bacteria solution filtration. However, surface grafting of the pMEDSAH layer led to significant reduction of membrane L_p by ~31 – 67% relative to the base membrane (L_p^{base} ~6.7 $L \cdot m^{-2} \cdot h^{-1} \cdot bar^{-1}$), while salt rejection decreased up to 3.8% (salt rejection decreased from 97.3% to 93.5 – 96.6%) (evaluated with 500 mg/L NaCl feed water at ΔP = 7.5 bar).

In order to increase the density of ATRP initiators grafted onto the PA TFC membrane surface (laboratory synthesized), the membrane surface was first treated with diethanolamine

(DEA) to generate surface hydroxyl groups that can be utilized to immobilize BIBB initiator molecules onto the membrane surface [112]. The BIBB initiators were then used to graft poly(2-methacryloyloxyethyl phosphorylcholine) (pMPC) onto the base membrane surface via SI-ATRP [112]. It was reported that the surface grafted pMPC layer was effective for reducing bacteria (*Sphingomonas* paucimobilis) attachment to the membrane surface by ≤ 5% (by mass) relative to the base membrane surface (after filtration of the bacterial suspension for 14 h). However, the surface grafted pMPC layer led to deterioration of the base membrane performance. It was reported that surface grafting of pMPC chains resulted in reduction of the base membrane L_p by ~63% (L_p^{base} ~1.5 $L \cdot m^{-2} \cdot h^{-1} \cdot bar^{-1}$) and also significantly reduced salt rejection from ~96% to ~90% (assessed with 500 mg/L NaCl feed water at ΔP = 7.5 bar).

Examples of graft polymerization techniques for modifying PA TFC RO membrane surfaces are summarized in **Table 2.5**. In general, it can be concluded that redox-initiated graft polymerization (performed with the persulfate initiator systems) was most effective for maintaining or improving RO membrane performance. However, it is noted that when the redox initiators are present in the solution phase during graft polymerization, initiation of homopolymerization in solution dominates over membrane surface initiated graft polymerization. Thus, surface density of grafted polymer chains is typically lower compared to approaches that generate surface initiation sites directly on the membrane surface prior to the membrane exposure to monomers.

Surface initiation sites on a PA membrane surface can be also generated by surface exposure to atmospheric pressure plasma (APP). Surface activation via APP is effective in producing a high density of surface active sites, in a relatively short plasma exposure time (<< 1 min, [124, 125]), thereby enabling the formation of a high-density layer of tethered chains upon

graft polymerization [16, 126]. Previous studies on APP induced graft polymerization (APPIGP) have focused primarily on reducing membrane fouling propensity; but it has also been documented that membrane permeability and salt rejection are impacted by the base membrane choice [15-17]. Details of APPIGP approach used to synthesize tethered hydrophilic polymer layers on PA TFC membrane surfaces are provided in **Chapter 4**.

Table 2-5. Change in PA TFC membrane performance due to membrane surface modification by graft polymerization.

Ref	Surface modification technique	Base PA TFC membrane[a]	Feed water; filtration mode[b]	ΔP (bar)[c]	L_p (L·m^{-2}·h^{-1}·bar^{-1})[d]		% Change in L_p[e]	R_o (%)[f]		Change in R_o (%)[g]	Comment
					Base	*Modified*		*Base*	*Modified*		
[115]	Redox-initiated graft polymerization of DMAEMA (via $K_2S_2O_8/Na_2S_2O_5$ redox initiators), followed by surface quaternization reaction with 3-BPA to obtain PCBMA[(1)]	CSM RE4021-TE (BWRO)	2,000 mg/L NaCl (25°C); crossflow	15	4.7	5.1	+9%	97.9	98.0	+0.1	TE-PDMAEMA5 ([DMAEMA] = 0.05 M)[(2)]
						5.7	+22%		98.0	+0.1	TE-PDMAEMA10 ([DMAEMA] = 0.1 M)[(2)]
						5.3	+13%		97.8	-0.1	TE-PDMAEMA20 ([DMAEMA] = 0.2 M)[(2)]
						5.6	+19%		97.1	-0.8	TE-PDMAEMA30 ([DMAEMA] = 0.3 M)[(2)]
						5.8	+23%		97.9	No change	TE-PCBMA obtained after surface quaternization of TE-PDMAEMA10 membrane[(3)]
[116]	Redox-initiated graft polymerization of MA and PEG-MA (via $K_2S_2O_8/Na_2S_2O_5$ redox initiators)[(4)]	Hydranautics CPA2 (BWRO)	1,500 mg/L NaCl	15.5	2.3	2.1	-9%	95.5	97.5	+2.0	10% MA (10 min)[(4)]
						2.1	-9%		98.0	+2.5	10% MA (20 min)[(4)]
						1.6	-30%		97.8	+2.3	10% MA (40 min)[(4)]
						1.5	-36%		96.9	+1.4	10% MA (60 min)[(4)]
		Dow Filmtec BW30 (BWRO)			2.7	2.6	-5%	94.8	94.6	-0.2	16% PEGMA (15 min)[(4)]
						2.6	-5%		94.2	-0.6	16% PEGMA (30 min)[(4)]
[119]	Redox-initiated graft polymerization of SVBP (via $K_2S_2O_8/NaHSO_3$ redox initiators)[(5)]	Dow Filmtec XLE (BWRO)	2,000 mg/L NaCl (25°C, pH 6.8); crossflow	15	6.1	4.7	-23%	98.0	99.6	+1.6	The graft polymerization reaction was carried out for 18 h[(5)]
[117]	Redox-initiated graft co-polymerization of SPMA and MBA (via Ce(IV)/PVA redox initiators)[(6)]	Laboratory synthesized PA TFC membrane	2,000 mg/L NaCl; crossflow	17.2	3.4	3.2	-4%	97.0	97.5	+0.5	[SPMA]=20 mM, [MBA]=9.5 mM, [PVA]=10 mM[(7)]
						2.3	-32%		95.0	-2.0	[SPMA]=4 mM, [MBA]=1.9 mM, [PVA]=20 mM[(7)]
						2.6	-24%		96.0	-1.0	[SPMA]=8 mM, [MBA]=1.9 mM, [PVA]=20 mM[(7)]
						3.7	+9%		94.0	-3.0	[SPMA]=28 mM, [MBA]=13 mM, [PVA]=10 mM[(7)]
						1.2	-64%		94.0	-3.0	[SPMA]=20 mM, [MBA]=9.5 mM, [PVA]=0 mM[(7)]
[118]	Redox-initiated graft polymerization of NIPAm and AA (via $K_2S_2O_8/Na_2S_2O_5$ redox initiators)[(8)]	Development Center of Water Treatment Technology	500 mg/L NaCl (25°C, pH 7); crossflow	5	5.6	6.6	+16%	98.2	98.0	-0.2	NIPAm GP period=30 min[(9)]
						7.1	+26%		97.6	-0.6	NIPAm GP period=60 min[(9)]
						6.4	+13%		97.2	-1.0	NIPAm GP period=90 min[(9)]
						5.5	-2%		96.8	-1.4	NIPAm GP period=120 min[(9)]
						6.6	+16%		98.0	-0.2	NIPAm GP period=60 min, AA GP period=30 min[(10)]

		(Hangzhou, China)				6.1	+8%		98.3	+0.1	NIPAm GP period=60 min, AA GP period=60 min[10]
						5.8	+4%		98.6	+0.4	NIPAm GP period=60 min, AA GP period=90 min[10]
						5.4	-4%		98.8	+0.6	NIPAm GP period=60 min, AA GP period=120 min[10]
[110]	Redox-initiated concentration polarization enhanced graft polymerization of METMAC, SPE, and GMS (via $K_2S_2O_8$/$K_2S_2O_5$ redox initiators)[11]	Hydranautics ESPA1 (LPRO)	1,500 m/L NaCl; crossflow				-20% to -40%	95.0	95.0	No change	METMAC (positively charged monomer)[11]
									96.5	+1.5	SPE (zwitterionic monomer)[11]
									96.5	+1.5	GMS (negatively charged monomer)[11]
[111]	Thermal-induced graft polymerization of ADMH (via AIBA thermal initiator)[12]	CSM RE4021-TL (ULPRO)	2,000 mg/L NaCl (25°C); crossflow	15	10.1	11.1	+10%	96.6	95.8	-0.8	GP period=10 min[12]
						12.3	+22%		91.8	-4.8	GP period=100 min[12]
[123]	SI-ATRP of MEDSAH (via BIBB initiator)[13]	Nitto Denko ES20 (ULPRO)	500 mg/L NaCl; crossflow	7.5	6.7	4.7	-31%	97.3	~96.2	-1.1	GP period=10 min[13]
						4.3	-37%		~96.6	-0.7	GP period =20 min[13]
						4.1	-39%		~95.3	-2.0	GP period=30 min[13]
						3.1	-54%		~96.0	-1.3	GP period=60 min[13]
						2.2	-67%		~93.5	-3.8	GP period=120 min[13]
[112]	SI-ATRP of MPC (via BIBB initiator)[14]	Laboratory synthesized PA TFC membrane	500 mg/L NaCl	7.5	1.5	0.6	-63%	~96	~90	-6.0	GP period=120 min[14]

[a] Commercial or laboratory synthesized PA TFC membranes used as base membranes for surface modification

[b] Feed water condition and filtration mode used to evaluate the membrane L_p and R_o

[c] Transmembrane pressure used to evaluate the membrane L_p and R_o

[d] Water permeability coefficient, L_p, defined as $L_p = J_v/(\Delta P - \Delta\pi_m)$ where J_v is volumetric permeate flux and $\Delta\pi_m$ is the osmotic pressure difference between the membrane surface at the feed and permeate sides.

[e] Percentage change in L_p relative to base membrane defined as $\Delta L_p = \left[\left(L_p^{Modified} - L_p^{Base}\right)/L_p^{Base}\right]\cdot 100\%$

[f] Percent observed (nominal) salt rejection defined as $R_o = \left(1 - C_p/C_f\right)\cdot 100\%$

[g] Change in the percent salt rejection R_o relative to base membrane defined as $\Delta R_o = R_o^{Modified} - R_o^{Base}$

---

[1] The active sides of the base membranes were exposed to a solution (30°C) containing 0.05-0.3 mol/L of N,N'-dimethylaminoethyl methacrylate (DMAEMA) and the redox initiators (i.e., $K_2S_2O_8$ and $Na_2S_2O_5$) for 1 h to graft poly(DMAEMA) (PDAMEMA) chains on the membrane surface. The modified membranes were dried, and the membrane active surfaces were subsequently exposed to a solution (30°C) containing 3-bromopropionic acid (3-BPA) for 2 days to obtain surface grafted zwitterionic carboxybetaine

methacrylate (CBMA) polymer chains.
(2) The PDMAEMA grafted base TE membranes synthesized using DMAEMA solutions of concentrations 0.05 M, 0.1 M, 0.2 M, and 0.3 M were labelled as TE-PDMAEMA5, TE-PDMAEMA10, TE-PDMAEMA20, and TE-PDMAEMA30, respectively.
(3) The TE-PDMAEMA10 membrane was further modified with 3-BPA to obtain the TE-PCBMA membrane.
(4) Graft polymerization methacrylic acid (MA) and poly(ethylene glycol) methacrylate (PEGMA) carried out by immersing the base membranes in aqueous solutions of 10% MA and 16% PEGMA (10-20% monomer concentration) containing the redox initiators ($K_2S_2O_8$ and $Na_2S_2O_5$) for 10-60 min and 15-30 min, respectively.
(5) The base membranes were modified by immersion in an aqueous solution of 4-(2-sulfoethyl)-1-(4-vinylbenzyl) pyridinium betaine) (SVBP) (2 mmol L^{-1}), $K_2S_2O_8$ (1 mmol L^{-1}) and $NaHSO_3$ (1 mmol L^{-1}) at 25°C for up to 18 h. The reported performance is for the base membrane that was graft polymerized with SVBP for 18 h.
(6) The base membrane surfaces were modified via Ce(IV)-PVA redox system initiated free radical graft co-polymerization of 3-sulphopropyl methacrylate (SPMA) and methylene-bis-acrylamide (MBA). The active sides of the base membranes were exposed to aqueous solutions containing SPMA, MBA, poly(vinyl alcohol) (PVA), and ceric ammonium nitrate in HNO_3 for 15 min, followed by drying at 50°C for 10 min and rinsing with deionized water.
(7) The reported performances are for the base membranes modified with co-polymers of SPMA and MBA, synthesized at various concentrations of SPMA, MBA, and PVA as indicated in the table.
(8) Graft polymerization reactions of N-isopropylacrylamide (NIPAm) and acrylic acid (AA) were performed sequentially as follows. The base membranes were immersed in aqueous solutions (30°C) containing 2 wt% NIPAm, 0.5 wt% AA and redox initiators ($K_2S_2O_8$ and $Na_2S_2O_5$) for 30-120 min. The poly(NIPAm) (PNIPAm) grafted membranes were rinsed with deionized water for at least 12 hours and subsequently immersed in aqueous AA monomer solutions (30°C) for 30-120 min. The modified membranes were thoroughly rinsed with deionized water.
(9) The reported performances are for the base membranes modified via surface graft polymerization (GP) of NIPAm at the indicated NIPAm GP reaction periods (30-120 min).
(10) The reported performances are for the base membranes modified via surface graft polymerization of NIPAm for 60 min, followed by surface graft polymerization (GP) of AA at the indicated AA GP reaction periods (30-120 min).
(11) Surface modification of the base membranes were carried out inside a laboratory scale crossflow membrane cell where the base membrane surfaces were contacted with solutions of three monomers, [2-(methacryloyloxy)ethyl]trimethylammonium chloride (METMAC), [2-(methacryloyloxy)ethyl]dimethyl-(3-sulfopropyl)ammonium (SPE), and glycidyl methacrylate (GMA), containing $K_2S_2O_8$/$K_2S_2O_5$ redox initiators, which were delivered to the cell at 20 bar while keeping the retentate line of the membrane cell closed. The concentrations of the monomers and redox initiators and graft polymerization period employed for graft polymerization (GP) reactions of METMAC, SPE, and GMA were as follows:
GP of METMAC: [METMAC] = 30 mM, [$K_2S_2O_8$]=2 mM, [$K_2S_8O_5$]=2 mM, GP period=35 min
GP of SPE: [SPE] = 65 mM, [$K_2S_2O_8$]=2 mM, [$K_2S_8O_5$]=2 mM, GP period=60 min
GP of GMA: [GMA] = 2.5 mM, [$K_2S_2O_8$]=2 mM, [$K_2S_8O_5$]=4 mM, GP period=30 min
It is noted that the GP of GMA was followed by conversion of the epoxy groups of GMA to negatively charged sulfonate groups via reaction with 10% Na_2SO_3 in 15% aqueous isopropyl solution at 35-40°C for 12-16 h. The resulting membrane surfaces were grafted with polymers of sulfonated glycidyl methacrylate (GMS).
(12) The active side of the base membranes was exposed to an aqueous solution containing 0.02 wt% 2,2-azobis(isobutyramidine) dihydrochloride (AIBA) for 15 min, followed by surface coating with aqueous solutions of 3-allyl-5,5-dimethylhydantoin (ADMH) monomer (5 wt%). The membranes were then placed in an oven to carry out the graft polymerization reaction at 70°C for the indicated periods (10-100 min).
(13) The base membranes were modified by immersion in aqueous solutions of 3-aminopropyltrimethoxysilane (APTES) and placed in a vacuum chamber at room temperature for 10 min. Subsequently, the membranes were immersed in a hexane solution of 2-bromoisobutyryl bromide (BIBB) at room temperature for 1 min to immobilize BIBB initiator molecules on the membrane surface. The BIBB-immobilized membranes were then immersed in a mixture of 14 mL of DI water and methanol (1:1, v/v) containing 10mmol of [(2-methacryloyloxy)ethyl]dimethyl[3-sulfopropyl]ammonium hydroxide (MEDSAH) and 0.8 mmol of ascorbic acid. After bubbling the mixture with nitrogen for 10 min, 4 mL of DI water/methanol (1:1, v/v) containing 0.02 mmol of copper (II) bromide ($CuBr_2$) and 0.04 mmol of tris(2-pyridylmethyl)amine (TPMA) was added to initiate the ATRP reaction. The mixed solution was then stirred for the indicated polymerization time.
(14) The base membrane surface was first modified with diethanolamine (DEA) by immersing the membrane in an aqueous solution containing 2 wt% DEA, 2 wt% triethylamine, and 4 wt% (±)-10-camphorsulfonic acid for 5 min, then dried at 80°C for 10 min. The DEA-modified membrane was then immersed in 20 mL of a hexane solution containing 4.2 mmol of dehydrated pyridine and 4.2 mmol of 2-bromoisobutyryl bromide (BIBB) for 1h to immobilize BIBB initiators on the membrane surface. Subsequently, the BIBB-immobilized base membrane was immersed in a solution containing 18 mL of deionized water/methanol (1:4 v/v) containing 2-methacryloyloxyethyl phosphorylcholine (MPC) and bubbled with nitrogen for 15 min, followed by addition of 2 mL of deionized water/methanol (1:4, v/v) containing 0.02 mmol of 2,2′-bipyridine, 0.002 mmol of $CuBr_2$, and 0.02 mmol of ascorbic acid was added to the solution to initiate the ATRP reaction. The reaction mixture was stirred for the duration of the graft polymerization reaction period of 120 min.

2.4.6 Summary

As illustrated in the previous sections (**Sections 2.4.1-2.4.5**), impact of membrane surface modification on the PA TFC membrane performance is usually reported in terms of changes in the water permeability coefficient (or permeate flux) and nominal (observed) salt rejection of the base PA membranes before and after the surface modification. However, the nominal salt rejection (defined in **Section 2.2.1**) is not an accurate metric for comparison of membrane performance, because salt rejection can vary depending on the permeate flux (which is a function of *both* water permeability, operating pressure, and crossflow velocity). In most instances, water permeability and salt rejection are evaluated at a fixed operating pressure. However, since water permeability is generally reduced by membrane surface modification, membrane performance evaluation of the pre- and post-modification membranes at the same operating pressure leads to salt rejection of the modified membrane being evaluated at a lower permeate flux compared to the base membrane. It is noted that reducing permeate flux leads to a higher salt concentration in the permeate (C_p) due to the diffusive salt flux (J_s) across the membrane remains unchanged (i.e., $J_s = C_p J_v$) [127]. Consequently, salt rejection by the modified PA membranes would be lower (underestimated) when evaluated at a lower permeate flux relative to that of the base PA membrane (the opposite case would be overestimation of salt rejection of the modified membranes when water permeability is increased relative to the base membrane).

It is noted that PA TFC membranes are expected to display a trade-off between water permeability and water/salt selectivity (**Section 2.3.3**) [45, 128]. However, this trade-off would not be discernable when salt rejection is used instead of water/salt selectivity, and instead one would expect to see a randomized effect with respect to salt rejection when water permeability is changed. This can be indeed seen in **Figure 2-8**, which depicts results from various published

studies, and demonstrates that PA TFC membrane surface modifications lead to various changes in membrane water permeability coefficient and salt rejection, which do not display a discernable trade-off relationship. Therefore, in order to accurately determine impact of membrane surface modification on the PA TFC membrane performance, it is preferred to assess the membrane water/salt selectivity in terms of salt permeability coefficient (Eq. 2-7) as discussed for the surface nano-structured membranes developed in the current work (**Chapter 4**).

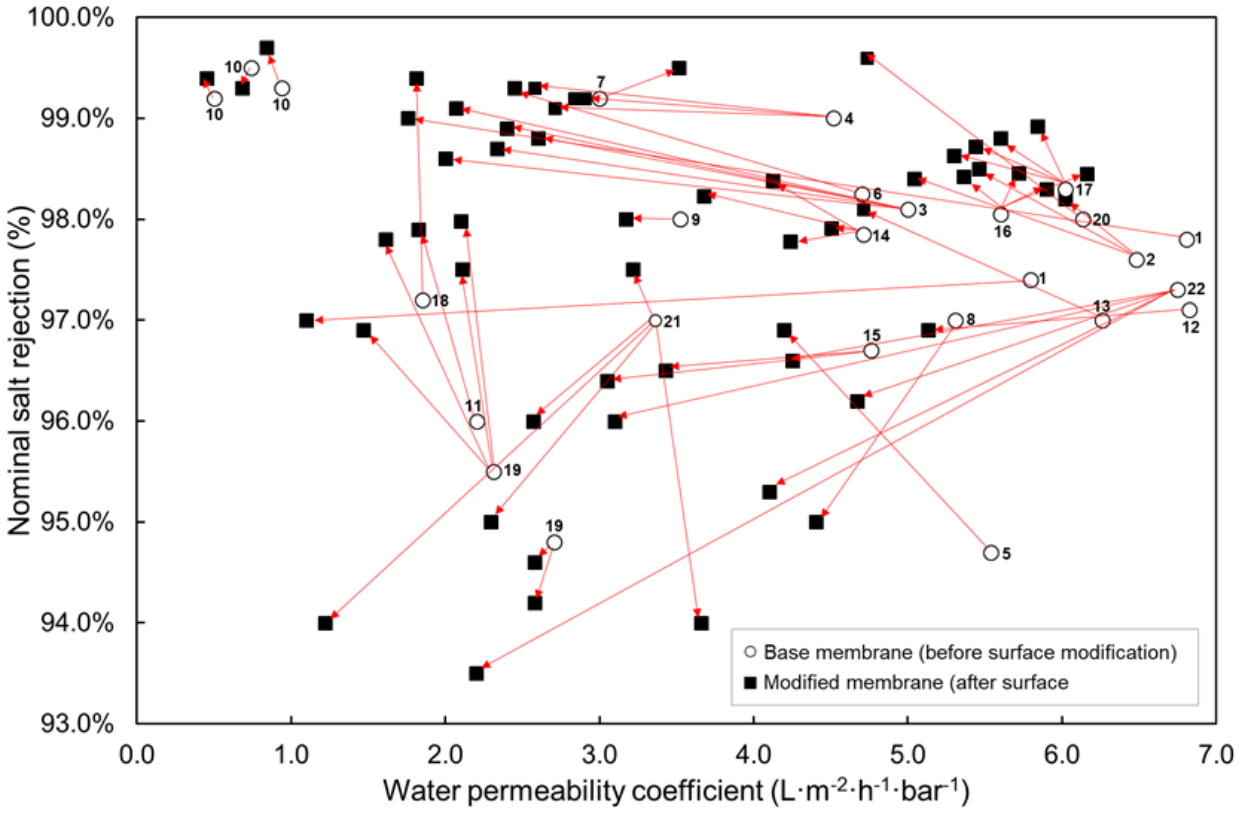

1. Louie et al., J. Membr. Sci. 280 (2006) 762-770. (coating)
2. Yu et al., Sep. Pur. Tech. 118 (2013) 285-293. (coating)
3. Ni et al., J. Membr. Sci. 451 (2014) 205-215. (coating)
4. Sagle et al., J. Membr. Sci. 240 (2009) 92-108. (coating)
5. Saeki et al., Colloids Surf., A 443 (2014) 171-176. (coating)
6. Ishigami et al., Sep. Pur. Tech. 99 (2012) 1-7. (LbL assembly)
7. Wang et al., J. Membr. Sci. 539 (2017) 403-411. (LbL assembly)
8. Yang et al., Chem. Mater. 23 (2011) 1263-1272. (iCVD)
9. Ozaydin-Ince et al., Thin Solid Films 539 (2013) 181-187. (iCVD)
10. Matin et al., Desalination 343 (2014) 128-139. (iCVD)
11. Shafi et al., Desalination 362 (2015) 93-103. (iCVD)
12. Xu et al., J. Membr. Sci. 435 (2013) 80-91. (polymer grafting)
13. Xu et al., Desalination 365 (2015) 398-406. (polymer grafting)
14. Wu et al., J. Membr. Sci. 495 (2015) 1-13. (polymer grafting)
15. Kang et al., Desalination 275 (2011) 252-259. (polymer grafting)
16. Hu et al., J. Membr. Sci. 501 (2016) 209-219. (polymer grafting)
17. Liu et al., Desalination 367 (2015) 11-20. (polymer grafting)
18. Liu et al., RSC Adv. 9 (2019) 17766. (polymer grafting)
19. Belfer et al., J. Membr. Sci. 139 (1998) 175-181. (graft polymerization)
20. Meng et al., J. Membr. Sci. 461 (2014) 123-129. (graft polymerization)
21. Rana et al., Desalination 375 (2015) 93-103. (graft polymerization)
22. Yang et al., J. Membr. Sci. 550 (2018) 332-339. (graft polymerization)

Figure 2-8. Water permeability coefficient and nominal salt rejection values for base membranes and modified membranes reported by the studies that performed various types of membrane surface modification (the arrows show the direction at which water permeability coefficient and salt rejection changed from the base membrane to the modified membrane).

Chapter 3. Polysulfone Surface Nano-Structured with Polyacrylic Acid

3.1 Overview

Tethered polymer layers are of interest in a wide range of applications (e.g., sensors [129, 130], membrane separation [131, 132], and biointerfaces [133, 134]) in which fine tuning of surface properties (e.g., wettability, friction, adhesion, attraction/repulsion to target analytes) can be achieved by the choice of the tethered polymer and the environmental conditions (e.g., pH, salinity, temperature). In particular, tethered polyelectrolyte chains have been shown to impart hydrophilic character to the surfaces of reverse osmosis (RO), nanofiltration (NF) and ultrafiltration (UF) membranes in order to reduce membrane fouling by organics, particulate and biological matter [135-137]. It has been suggested that partial mobility (due to Brownian motion) of the free portion of terminally anchored chains can be effective in reducing the ability of foulants to adhere to the surface. At the same time, the grafted polymer chains, which can extend from the membrane surface in a good solvent (e.g., water), screen the underlying membrane surface [16, 17, 138]. However, gradual permeate flux decline over time (due to buildup of a foulant layer) is inevitable and membranes need to be periodically cleaned to in order to maintain a reasonable level of productivity.

In membrane desalination applications, in which the membrane surface is exposed to saline water (e.g., seawater and brackish water), a salt-responsive tethered polymer layer could serve to both increase fouling resistance and achieve effective membrane cleaning. For example, previous studies have reported that zwitterionic polymer brush layers, which exhibit increased swelling with increased salt concentration, could allow for improved membrane cleaning by flushing with a solution of salinity higher than that of the raw feed water being treated [119, 139]. In contrast with the above, tethered polyelectrolyte layers are expected to collapse in a high salinity aqueous

environment (due to charge screening effect) [18, 19] and swell when exposed to a low ionic strength solution. Therefore, one would expect that exposing a membrane surface with a tethered polyelectrolyte layer to a water stream of salinity lower than that of the feed being desalted, would lead to swelling of the tethered polymer and thus improve membranes cleaning. The benefit of improved membrane cleaning could also be realized when tethered polyelectrolyte chains collapse upon flushing of the membrane surface with water of salinity that is higher than that of the feed. Previously, increased membrane cleaning efficiency was demonstrated for polyelectrolyte layers grafted onto polyamide membranes, whereby cleaning of a fouled membrane was achieved by flushing the membrane channel with DI water [17]. It was reported that polyamide membranes with surface tethered polymer chains could be effectively cleaned with DI water owing to swelling of these chains; however, swelling of the tethered polymer layer was not ascertained nor quantified.

In the present work, the concept of utilizing tethered polyelectrolyte layers for membrane cleaning benefits was evaluated using poly(acrylic acid) (PAA) as a model hydrophilic polymer tethered onto a polysulfone (PSf) surface. The tethered PAA chains, which has been shown to be highly effective for improving surface hydrophilicity [113, 140], have polar acid groups (i.e., carboxylic acid); thus, polymer chain swelling is affected by ionic strength and water pH [18, 141, 142]. PSf was selected as a model substrate due to both its highly hydrophobic character relative to PAA and popularity as a membrane material for synthesis of UF membranes utilized for a broad range of applications (e.g., water treatment [39], protein separation [143], and medical devices [144]). It is also noted that modification of the PSf surface with tethered hydrophilic polymers has been proposed as the means for reducing membrane fouling and improving the effectiveness of membrane cleaning [145, 146]. The polysulfone surface was activated by exposure to an impinging atmospheric plasma jet [15, 124], followed by aqueous phase free-radical surface graft

polymerization of acrylic acid (AA) [147]. The resulting tethered PAA layers were characterized with respect to their chain extension length via atomic force microscopy based force spectrocopy (AFM-FS) [148-150] conducted in DI water and 35 g/L NaCl aqueous solution (i.e., a typical salinity for seawater) to assess impact of salinity on chain swelling. Surface topography and wettability were also evaluated via AFM and contact angle measurements, respectively, under the above same solvent conditions.

3.2 Experimental

3.2.1 Materials and reagents

Prime grade 4" silicon <100> wafers were used as substrates for casting a PSf film onto which a tethered PAA layer was synthesized. Sulfuric acid (96%) and aqueous hydrogen peroxide (30%), used for silicon wafer cleaning, were purchased from KMG Electronic Chemicals, Inc. (Houston, TX). Helium (99.999%), hydrogen (99.999%), oxygen (99.999%), and nitrogen (99%) gases were obtained from Airgas (Los Angeles, CA). PSf pellets (M_w ~35,000), poly(ethyleneimine) (PEI, M_w ~750,000) solution (50 wt% in H_2O), chloroform (≥ 99.9%), acrylic acid (99%), *n*-octane (≥ 99.7%) were all obtained from Sigma-Aldrich (St. Louis, MO). Ultra-pure deionized (DI) water was produced using a Milli-Q filtration system (Millipore Corp., San Jose, CA), and 35 g/L NaCl solution was prepared with sodium chloride (≥ 99.0%; Fisher Scientific, Chino, CA) and DI water. The pH of DI water was ~6 (likely due to the presence of dissolved CO_2) as determined using a pH meter (Oakton pH 110 Meter; Cole-Parmer, Vernon Hills, IL).

3.2.2 Preparation of PSf films

In order to evaluate nano-scale changes in the surface topography due to tethered PAA layers, smooth PSf substrate films were prepared on the silicon wafers by spin-coating a solution of PSf in chloroform (790 Spinner with PWM32 controller; Headway Research Inc., Garland, TX). The silicon wafers were first cleaned in a piranha solution (a mixture of 70 vol% sulfuric acid and 30 vol% aqueous hydrogen peroxide) for 10 min at 90 – 100°C, followed by triple rinsing with DI water and drying with nitrogen. Each dried wafer was cut into approximately 1 cm x 1 cm square samples using a diamond scriber (Techni-Tool Inc., Worcester, PA). Each sample was cleaned successively with isopropanol and DI water followed by drying with nitrogen. About 0.1 mL of a 0.3 wt% aqueous solution of PEI was then used to spin-coat an adhesion layer, on the silicon surface, at 2500 rpm for 30 s. Subsequently, about 0.1 mL of a 1 wt% PSf solution in chloroform was spin-coated onto the PEI layer coated Si surface at 2500 rpm for 30 s. The PSf film samples (PSf-Si) were subsequently dried in a vacuum oven at 75°C for 48 hours prior to surface characterization.

3.2.3 Plasma surface activation and graft polymerization

The PSf substrates were treated by an impinging atmospheric pressure plasma via a cylindrical plasma jet as described elsewhere [151]. The plasma source radio frequency (RF) power output and gas flow rates to the plasma source were set via a plasma controller (Atomflo^{TM} 250; Surfx Technologies Inc., Redondo Beach, CA). Helium (He) plasma was operated at a helium flow rate of 30 L/min. Helium and hydrogen (He/H_2) and helium and oxygen (He/O_2) plasmas were generated at the same helium flow rate, but with additional 0.2 L/min of hydrogen and oxygen, respectively. The above plasmas were generated at a relatively low RF power (i.e., 60 W) to

prevent PSf surface damage. The PSf surfaces were activated via exposure to plasma over a period of 5 – 120 s. It is noted that upon surface activation with plasma, surface wettability increased (as determined via contact angle measurements) due to the increased presence of surface polar functional groups, including peroxides that are suitable for initiating graft polymerization [152]. Accordingly, increased surface wettability can serve as an indication of APP activation of the PSf surface as well as hydrophilic character imparted to the surface post graft polymerization to form the tethered PAA layer [153].

Following PSf surface activation, the PSf film substrate samples were immediately placed in glass vials containing aqueous solutions of the AA monomer. Graft polymerization was carried out at initial AA monomer concentrations ($[M]_0$) in the range of 1 – 20 vol% for 1 – 2 hours at 70°C. The above combination of monomer concentrations and grafting temperature were selected, based on initial tests, in order to minimize homopolymerization in solution. Nitrogen was injected (via a dispensing needle) at the bottom of the vials during graft polymerization to remove oxygen that can inhibit the polymerization reaction [154] and also to provide mixing (provided by the swarm of nitrogen bubbles) of the monomer solutions. Graft polymerization was terminated by quenching the reaction with copious volume of DI water before removing from the vials and subsequent additional rinsing of the substrate to remove unreacted species. The PAA grafted PSf film samples (PAA-PSf-Si) were then dried, prior to surface characterization, in vacuum for 48 hours at 40°C.

3.2.4 Surface characterization

The presence of surface grafted PAA chains on the PSf surface was confirmed by X-ray photo electron spectroscopy (XPS) performed using a Kratos Axis Ultra DLD (Kratos Analytical,

Manchester, UK) with a monochromatic Al Kα source. Survey and high-resolution C 1s spectra were obtained at a pass energy of 160 eV and 20 eV, respectively, for the native PSf-Si and PAA-PSf-Si surfaces. The C 1s spectra were deconvoluted using the hydrocarbon peak at 285 eV as described in [155].

Surface wettability of the plasma activated PSf-Si and the PAA-PSf-Si surfaces was evaluated by both the sessile drop (SD) and captive bubble (CB) contact angle measurements using an automated system (DSA20; KRÜSS GmbH, Germany). SD water contact angle measurements were taken within 2 seconds following placement of 1 µL DI water drops onto sample surfaces. The reported contact angles are averaged values based on measurements at 5 locations for each sample. CB contact angle measurements were taken for sample surfaces immersed under water at 20 – 22°C using 4 µL of air or *n*-octane bubbles [156-158]. Each sample was immersed in DI water for about 30 min prior to measuring contact angles at five different locations. The above allowed for equilibration of both swelling of the tethered polymer chains and of the vapor pressure within the air bubbles [159]. The average contact angle values for air and *n*-octane bubbles were used to determine surface free energy (γ_s, in mJ/m^2), which was expressed as the sum of contributions from dispersive (γ_s^d) and polar (γ_s^p) components ($\gamma_s = \gamma_s^d + \gamma_s^p$) as determined following the Owens, Wendt, Rabel, and Kaelble (OWRK) method [160, 161], i.e., $\gamma_l\left(1+\cos\theta\right) = 2\sqrt{\gamma_s^d \gamma_l^d} + 2\sqrt{\gamma_s^p \gamma_l^p}$ where γ_l^a, γ_l^p, and γ_l are the dispersive, polar, and total surface tension of a liquid (i.e., water or *n*-octane), respectively. The values of γ_l^d and γ_l^p were taken as the reference values for dispersive and polar surface tensions, respectively, of water and octane at 20°C [158].

Surface topography was assessed via atomic force microscopy (AFM) using a Bruker Dimension Icon Scanning Probe Microscope with a NanoScope V Controller (Bruker, Santa

Barbara, CA). AFM images were obtained in PeakForce Tapping mode, under air and liquid (i.e., DI water and 35 g/L NaCl solution) using ScanAsyst-Air and ScanAsyst-Fluid+ probes whose nominal spring constants were 0.4 N/m and 0.7 N/m, respectively, and the manufacturer reported nominal radius was 2 nm for both probes. Cantilever deflection sensitivity was determined from the slope of the noncompliance region of the cantilever deflection vs the piezo displacement curve obtained using a silicon substrate in contact mode. Spring constants of the cantilevers were determined via thermal tuning method at the room temperature (~20°C) [162]. AFM scans of size 1 μm x 1 μm were obtained with 512 x 512-pixel resolutions at scan rates of 0.5 – 0.8 Hz. Topographic images were obtained with a relatively small loading force (~500 pN) in order to minimize the deformation of surface features. It is noted that in displaying the height distributions, the feature heights for each sample were scaled to the lowest height as determined by the AFM tip. Surface roughness was quantified by the root-mean-square surface roughness (R_{rms}), which was determined from the AFM height data for each scans as $R_{rms} = \sqrt{\sum_i \left(Z_i - Z_{avg}\right)^2 \Big/ N}$, where Z_i is the height of i^{th} sample out of N total number of samples, and Z_{avg} is the mean feature height. Cross-sectional feature height profiles were produced from the Z-height data corresponding to a 1 μm-line across the topographic images.

Swelling of the surface tethered PAA chains was assessed indirectly by chain stretching, accomplished via AFM based force spectroscopy (AFM-FS; [163-165]), under different solvents (i.e., air, DI water, 35 g/L NaCl solution). Such an approach has been utilized to evaluate the impact of aqueous solution pH and ionic strength on the swelling of tethered polyelectrolytes [163, 164]. In the AFM-FS approach, stretching of the tethered chains is accomplished whereby chains are pulled away from the substrate surface by the AFM tip until the chain elastic restoring force overcomes the attractive force between the tip and chains (hence the chains "rupture" from the tip)

[148, 149]. The stretched length of the surface tethered PAA chains was estimated by the rupture length (L_R) corresponding to the tip-surface separation at which a peak in the retraction force curves was observed, due to detachment of polymer chain segment(s) from the tip [148]. The magnitude of the peak (i.e., rupture force, F_R) is indicative of the chain-tip affinity. It is expected that in a poor solvent the AFM tip will be unable to pick and pull surface grafted chains sufficiently away from the surface due to stronger interactions between neighboring chains relative to the chain-tip interaction. In contrast, in a good solvent, chain-chain interactions are less favored (due to steric and electrostatic repulsions) and hence the tethered chains are expected to be more easily picked by the tip and pulled away from the surface.

The AFM-FS was performed using a Bruker MultiMode 8-HR Scanning Probe Microscope and a PicoForce Spectroscopy Control Module (Bruker, Santa Barbara, CA). A silicon nitride probe of a nominal tip radius of 20 nm (Bruker MLCT-D) was used whose cantilever deflection sensitivity and spring constant were determined as described previously. Force measurements were taken in contact mode for the native PSf-Si and PAA-PSf-Si surfaces using a ramp size of 1 μm at a tip velocity of 500 nm/s. The maximum force applied on the sample surface prior to retraction (i.e., trigger force) was 1 nN. Approach and retraction force-distance profiles were obtained at 200 randomly selected locations over the area (i.e., ~1 cm x 1 cm) of each sample. Multiple peaks, associated with chain detachment from the AFM tip, were typically observed in the retraction force profiles. The total number of such peaks (N), with the exception of the first observed peak (see **Section 3.3**), were considered as chain pulling events. Rupture force and rupture length distributions, determined from the retraction force profiles, were then fitted with log-normal curves, and the mean rupture force ($\overline{F}_R$) and mean rupture length ($\overline{L}_R$) were taken to be the means of the log-normal fitted distributions. The rupture length determined in DI water was used to estimate an

approximate measure of the single chain molecular weight as $M_i = M_{mon} L_R / l_{mon}$ where M_{mon} is the molecular weight (72.06 g/mol) of an AA monomer, and l_{mon} is the length of a monomer unit, which was taken to be 0.25 nm based on the projected C–C bond length and angle [166-168]. Using the above data, the number and weight averaged molecular weights were calculated as $M_n = \sum_i M_i / N$ and $M_w = \sum_i M_i^2 \Big/ \sum_i M_i$, respectively, with the polydispersity index (*PDI*) defined as $PDI = M_w / M_n$. The above approach of estimating the molecular weight of tethered chains has been shown to provide a reasonable approximation [163], particularly for cases, as in the present work, where chemical de-grafting of the tethered chains is challenging.

Swelling of the grafted PAA chains was also assessed by the PAA layer equilibrium thickness (L_e), which was estimated as the tip-sample separation at which a repulsive force was first detected by AFM tip approaching the surface [148, 149]. L_e was estimated from the approach force curves (obtained in DI water and 35 g/L NaCl solution) by determining the tip-surface separation at which a significant sharp AFM tip deflection from the baseline (i.e., Force = 0) was observed [148, 149]. This was accomplished by first producing an average force curve from 200 approach curves obtained for each PAA-PSf-Si sample. Subsequently, at each tip-surface separation, the 5th percentile of the force data set (total of 200) was determined, and the equilibrium thickness was taken to be the smallest tip-surface separation at which the corresponding 5th percentile of the force data was greater than zero [169].

The PAA layer dry thickness (h) was determined from sample sectioned images obtained via Focused Ion Beam (FIB) – Scanning Electron Microscopy (SEM) (Nova 600 NanoLab DualBeam^{TM}-SEM/FIB; FEI company, Hilsboro, OR) [170]. The samples were first coated with a gold layer using a Denton Desk II Sputter Coater (Denton Vacuum, Inc., Moorestown, NJ),

followed by a thin strip of platinum coating above the cross-sectioned locations just prior to FIB sectioning. The PAA layer thickness was estimated by the difference between the film thickness measured above the silicon wafer substrate before and after surface nano-structuring with PAA. Examples of FIB-SEM images obtained for the film thickness analysis are shown in **Figure 3-1**. The grafting density (σ) of the tethered chains was estimated from $\sigma = h\rho N_A / M_n$, where ρ is the PAA bulk density (1.15 g/cm^3), N_A is Avogadro's number, and M_n is the number averaged molecular weight of the grafted PAA chains (approximated from the AFM-FS data as described previously).

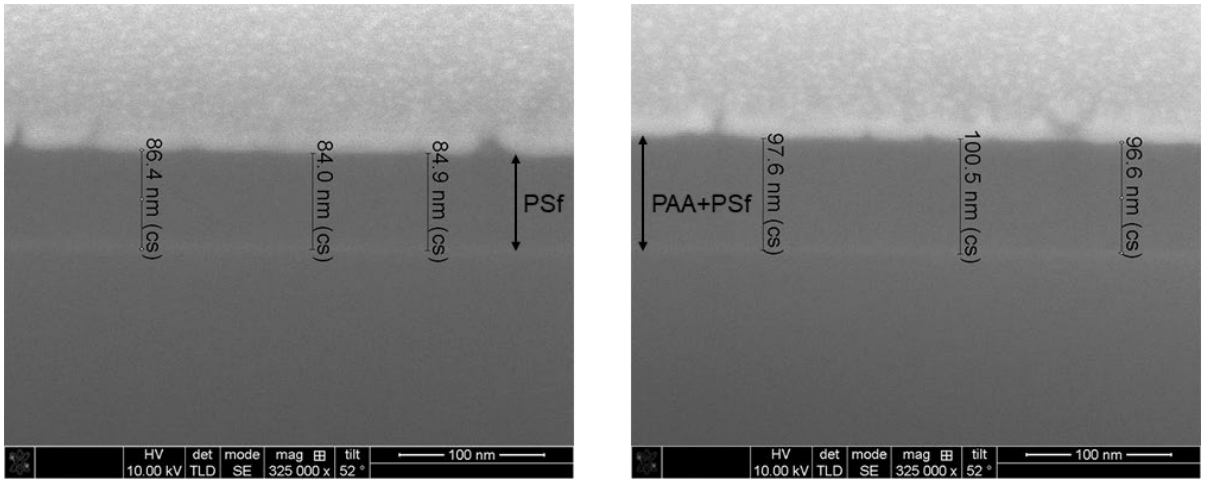

Figure 3-1. Examples of FIB-SEM images obtained for PSf-Si (left) and PAA-PSf-Si (right) (Note: the tethered PAA layer synthesized at $[M]_0$ = 20 vol% for 2 h following surface activation with He/O_2 APP) used to estimate dry thickness of the PAA layer (by subtracting thickness for the native PSf layer (left) from PAA layer grafted PSf (right)). Note: prior to FIB, a gold layer was deposited onto the samples using a Denton Desk II Sputter Coater (Denton Vacuum, Inc., Moorestown, NJ), followed by coating a thin strip of platinum above the cross-sectioned regions.

3.3 Results and Discussion

3.3.1 APP PSf surface activation and graft polymerization with acrylic acid

The effectiveness of APP for PSf surface activation by the three types of APP, He, He/H_2, and He/O_2 plasmas was assessed by the increase in surface wettability as quantified by the SD water contact angle (**Figure 3-2**). The highest water contact angle reduction was for surfaces treated with He/O_2 plasma (~74%) followed by He (~40%) and He/H_2 (~8%) plasmas, relative to the native PSf-Si surface (90 ± 2°) at the same plasma exposure time (i.e., 15 s). A series of preliminary tests of surface activation, followed by graft polymerized at $[M]_0$ = 10 vol% for 1 h (**Figure 3-3**), indicated that surface activation with the He/O_2 plasma was most effective. A plasma exposure time of 15 s was selected as being sufficiently short for effective surface activation and reasonable duration for process scale-up.

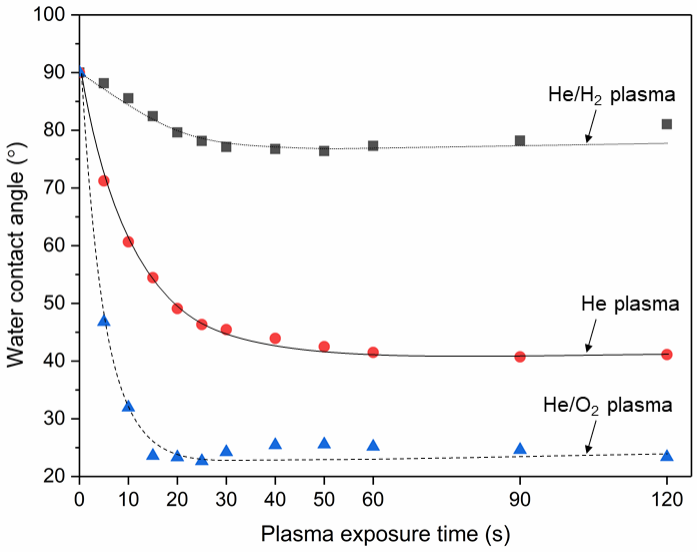

Figure 3-2. Sessile drop water contact angles for PSf-Si surface following surface activation with He/H_2, He, and He/O_2 APP at various plasma exposure times (5 – 120 s). Water contact angles increased by ~6% (83.7° to 89.0°), ~39% (54.9° to 76.3°), and ~242% (22.0° to 75.3°) after storage in ambient air for ≥ 5 days following the corresponding (15 s) PSf surface activation with He/H_2, He, and He/O_2 plasmas**.**

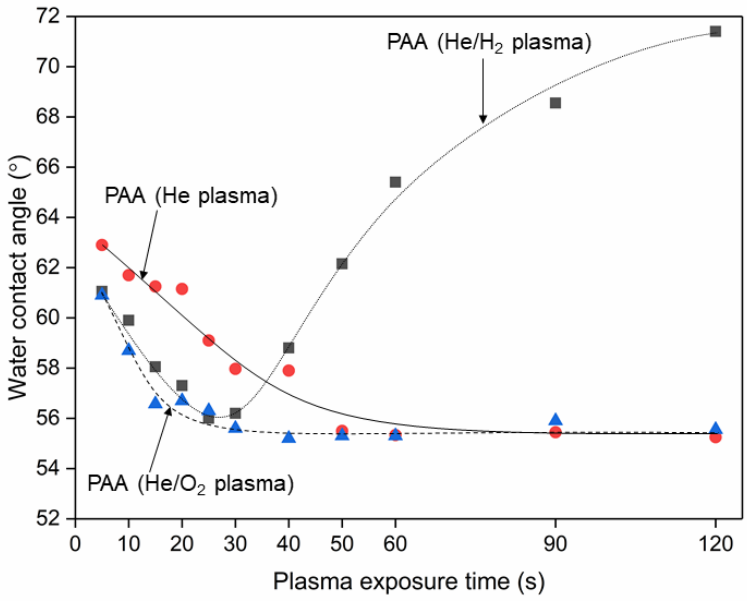

Figure 3-3. Sessile drop water contact angles for PAA-PSf-Si surfaces (graft polymerized at $[M]_0 = 10$ vol% for 1 h) following PSf surface activation with He/H_2, He, and He/O_2 APP at various plasma exposure times (5 – 120 s). Water contact angles increased by ~7% after storage in air for ≥ 5 days for the tethered PAA layers regardless of the type of APP used for surface activation prior to graft polymerization.

Previous studies have shown that the wettability of polymer surfaces achieved by plasma treatment is not permanent [171, 172]. In the current work, the SD water contact angle for the PSf surface, which was reduced by ~8 – 74% upon APP treatment (15 s exposure time), increased after 5 days of exposure to ambient air toward ~1 – 20% below the PSf water contact angle of 90°. After 1 h exposure to ambient air, the water contact angles for the He/H_2, He, and He/O_2 plasma activated PSf surfaces (15 s exposure time) increased by ~1%, ~12%, and ~94%, respectively, relative to the initial water contact angle which was taken immediately after exposure to plasma; after 5 days, the water contact angle increased to within ~1%, ~18%, and ~20% of the PSf surface contact angle (90°) for the same plasmas (i.e., He/H_2, He, and He/O_2), respectively. The PSf surface activation was fully retained for the first 20 min post-APP treatment. However, it is noted that in the present work graft polymerization was carried out within 1 minute of surface activation by APP.

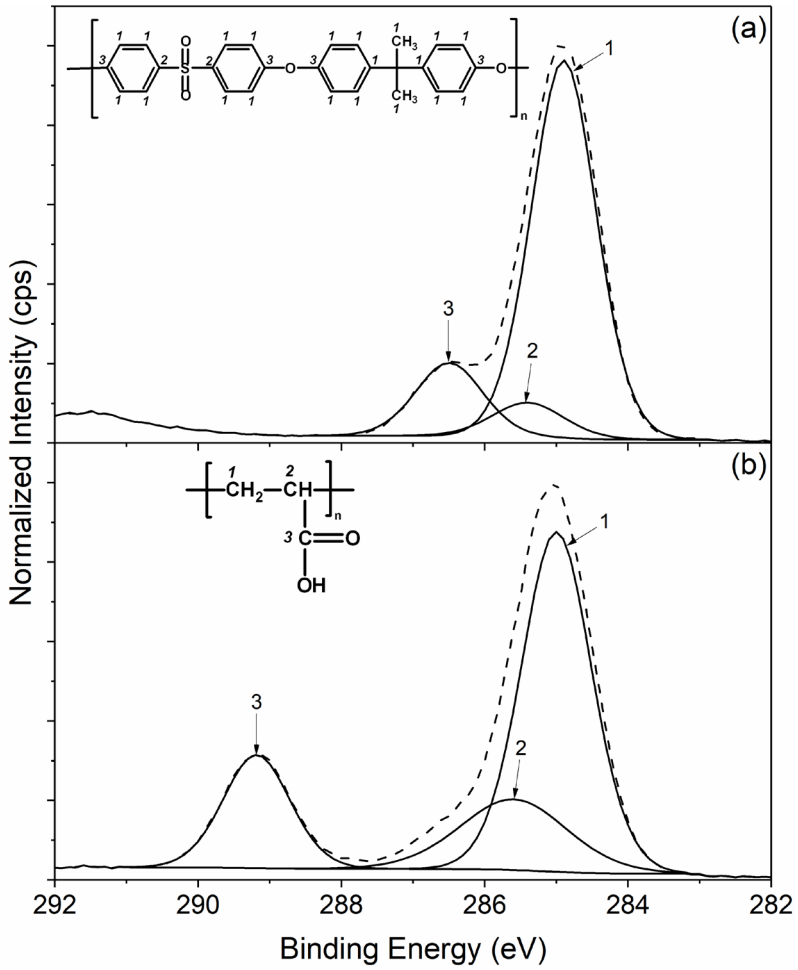

Figure 3-4. C 1s XPS spectra for (a) the native PSf-Si and (b) PSf with tethered PAA layer (PAA-PSf-Si) synthesized at $[M]_0$ = 20 vol% for 2 h onto PSf surface activated with He/O_2 plasma.

Table 3-1. Elemental surface compositions for the native PSf-Si and PAA-PSf-Si†

Surface	Carbon%	Oxygen%	Sulfur%
Native PSf	85.2	11.3	3.5
Tethered PAA layers synthesized at $[M]_0$:			
1 vol%	80.9	17.0	2.1
5 vol%	80.4	17.5	2.1
10 vol%	80.1	17.7	2.1
15 vol%	79.1	19.0	1.9
20 vol%	75.4	23.4	1.2

†AA graft polymerization was carried out for a period of 2 h following PSf surface activation by He/O_2 plasma for a period of 15 s.

Subsequent to PSf surface activation by APP, AA graft polymerization was carried out to form a tethered PAA layer. The C 1s spectrum for the native PSf surface was characterized by peaks centered at 285 eV, 285.6 eV, and 286.6 eV, which correspond to aromatic/aliphatic carbons, C–S, and C–O groups, respectively (**Figure 3-4(a)**) [153, 173]. The native PSf surface comprised mostly of carbon (85.2%), followed by oxygen (11.3%) and sulfur (3.5%). Compared to the native PSf surface, the carbon and sulfur composition for the PAA layers (grafted with $[M]_0$ = 1 – 20 vol% for 2 h) decreased to 75.4 – 80.9% and 1.2 – 2.1%, respectively, while oxygen content increased to 17.0 – 23.4% (**Table 3-1**). As shown in **Figure 3-4(b)**, for the example of PAA tethered surface synthesized at $[M]_0$ = 20 vol% for 2 h, a C 1s spectrum exhibited a clear peak at 289.2 eV associated with the carboxylic acid group [155], in addition to peaks at 285 eV and 285.4 eV, due to aliphatic carbon and C–C=O [155], respectively, thus confirming the presence of grafted PAA chains.

3.3.2 Surface topography

In order to evaluate the alteration of the PSf surface topography by the tethered PAA chains, the underlying PSf film was first examined before and after plasma surface activation. It has been reported that PSf can exhibit slight swelling in water due to its polar sulfone groups [174, 175]. Accordingly, one would expect that the native PSf surface feature height distribution (FHD), when submersed in DI water, would be somewhat broader relative to the FHD for the dry surface (in air). The above was indeed observed for the PSf-Si surface where it was also apparent that the FHD mode increased by ~5% (**Figure 3-5(a)**). Although the PSf surface roughness increased slightly when in water (R_{rms} = 0.30 nm) relative to air (R_{rms} = 0.26 nm) (**Table 3-2**), the PSf substrate can be considered to be relatively smooth in both cases (**Figure 3-6(a)**).

Upon exposure to He/O_2 plasma, the PSf surface displayed distinct globular features as observed by AFM analysis of the dry surface (**Figure 3-5(b)** and **Figure 3-6(b)**). The resulting surface roughness (R_{rms} = 1.50 nm) was about five-fold higher relative to the native PSf substrate. Observations of such globular surface features (via AFM) have been reported for a wide range of polymers (e.g., polypropylene, poly(ethylene terephthalate), polyethylene, etc.) after exposure to various types of atmospheric pressure plasmas (e.g., air, Ar, CO_2) [176-178] as well as low pressure O_2 plasma [179]. Such globular features have been attributed to the aggregation of low molecular weight oxidized materials (LMWOM) reported to be hydrophilic oligomers generated from plasma-induced surface polymer chain scission [177, 180]. It has also been reported that washing of the plasma treated polymer surfaces with water can remove loosely surface bound LMWOM owing to their solubility in water [177, 179-181]. It is noted that the type of globular surface features reported in previous studies were not observed in the AFM images obtained under water for the plasma treated PSf surface (**Figure 3-5(b)** and **Figure 3-6(b)**). When submerged in water, the He/O_2 plasma activated PSf surface had a somewhat higher surface roughness (R_{rms} = 0.43 nm) and a marginally broader FHD relative to the native PSf (R_{rms} = 0.30 nm) (**Figure 3-5**). The above results suggest that surface activation with He/O_2 plasma had minor impact on the topography of the PSf surface when submerged in water. Given the above, it is reasonable to assert that the surface features observed post-graft polymerization (**Figure 3-7**) were associated primarily with the surface grafted PAA chains.

Upon AA graft polymerization ($[M]_0$ = 1 – 20 vol% for 2 h) onto the PSf-Si surfaces that were activated with He/O_2 plasma, the surface roughness (R_{rms}) increased for both the dry substrates and when immersed in DI water by factors of ~2.2 – 3.8 and ~2.0 – 4.3, respectively, relative to the native PSf-Si substrate surface (**Table 3-2**). Graft polymerization at increasing $[M]_0$

from 1 to 20 vol% resulted in greater surface feature heights and broader FHD (**Figure 3-7**) accompanied by a surface roughness increase by factor of ~1.8 and ~2.1 for the surfaces as dry and when immersed in DI water, respectively (**Table 1**). Surface roughness of the PAA tethered surfaces immersed in water (0.61 – 1.28 nm) was about 7 – 28% higher relative to the roughness of the dry substrates (0.57 – 1.00 nm). At the same time, broader surface FHDs were revealed from AFM characterization of the surfaces in DI water relative to the dry surfaces (**Figure 3-7**), with corresponding FHD modes of 2.4 – 4.7 nm and 3.7 – 7.0 nm, respectively.

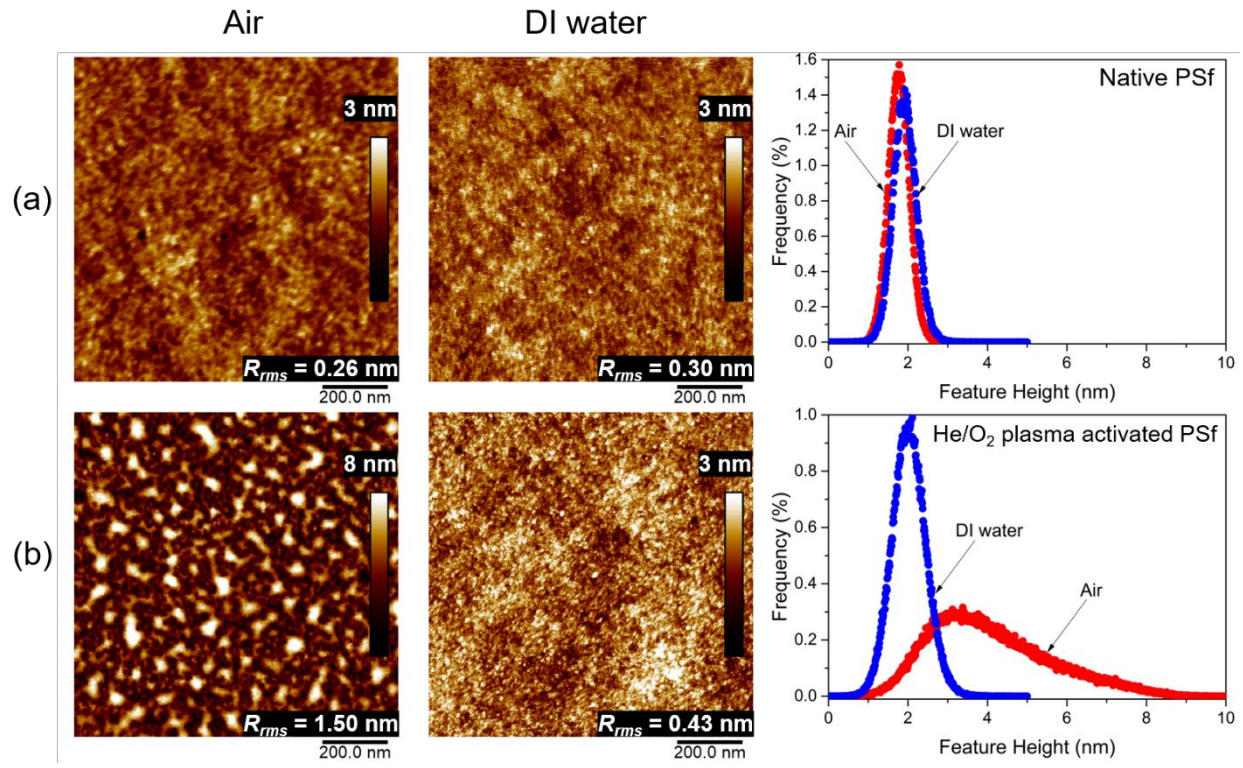

Figure 3-5. AFM 2-D images for obtained for dry substrates (in air) (left) and in DI water (middle) with the respective feature height distributions (right) for (a) native PSf-Si surface and (b) He/O_2 plasma activated PSf-Si surface.

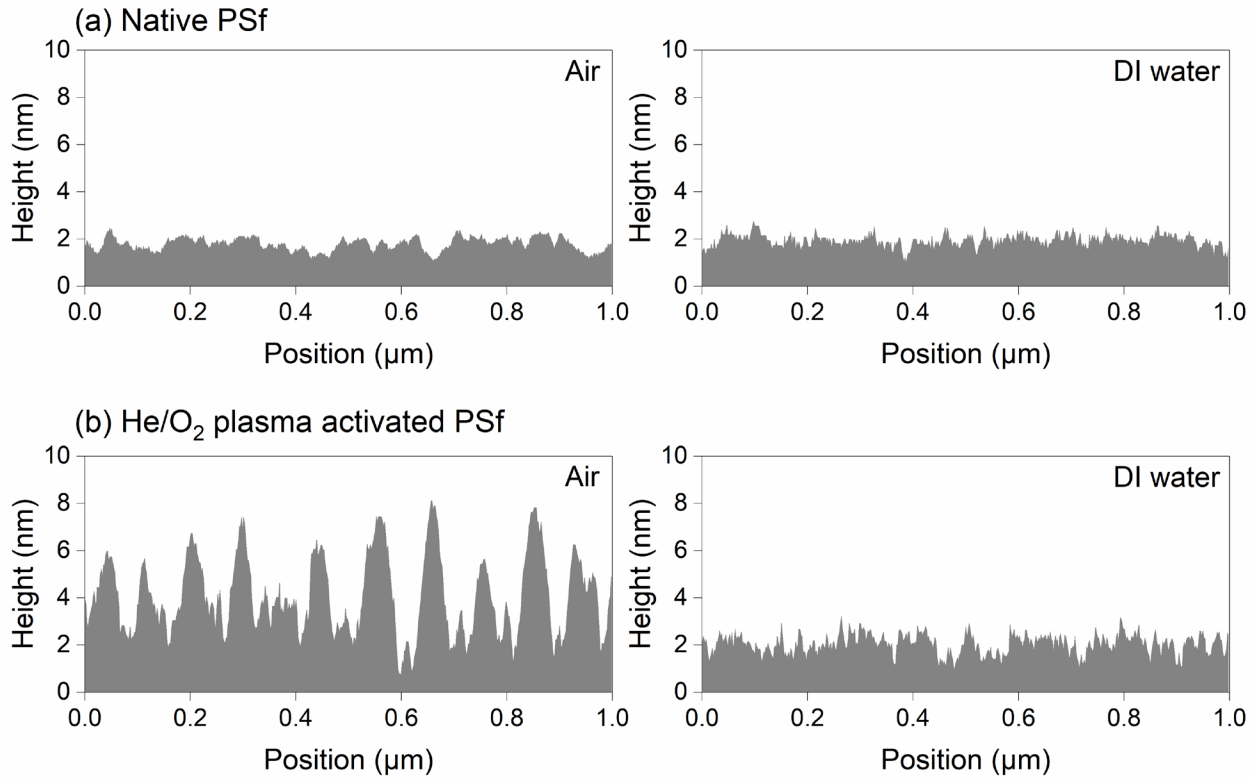

Figure 3-6. Cross-sectional AFM feature height profiles obtained for dry substrates (in air) (left) and in DI water (right) for (a) the native PSf-Si and (b) He/O_2 plasma activated PSf-Si surfaces.

Table 3-2. Surface roughness (R_{rms}) for the native PSf-Si and PAA-PSf-Si[†]

Surface	Surface roughness (R_{rms}), nm	
	in air	in DI water
Native PSf	0.26	0.30
Tethered PAA layers synthesized at $[M]_o$:		
1 vol%	0.57	0.61
5 vol%	0.64	0.75
10 vol%	0.64	0.80
15 vol%	0.72	0.91
20 vol%	1.00	1.28

[†]AA graft polymerization was carried out for a period of 2 h following PSf surface activation by He/O_2 plasma for a period of 15 s.

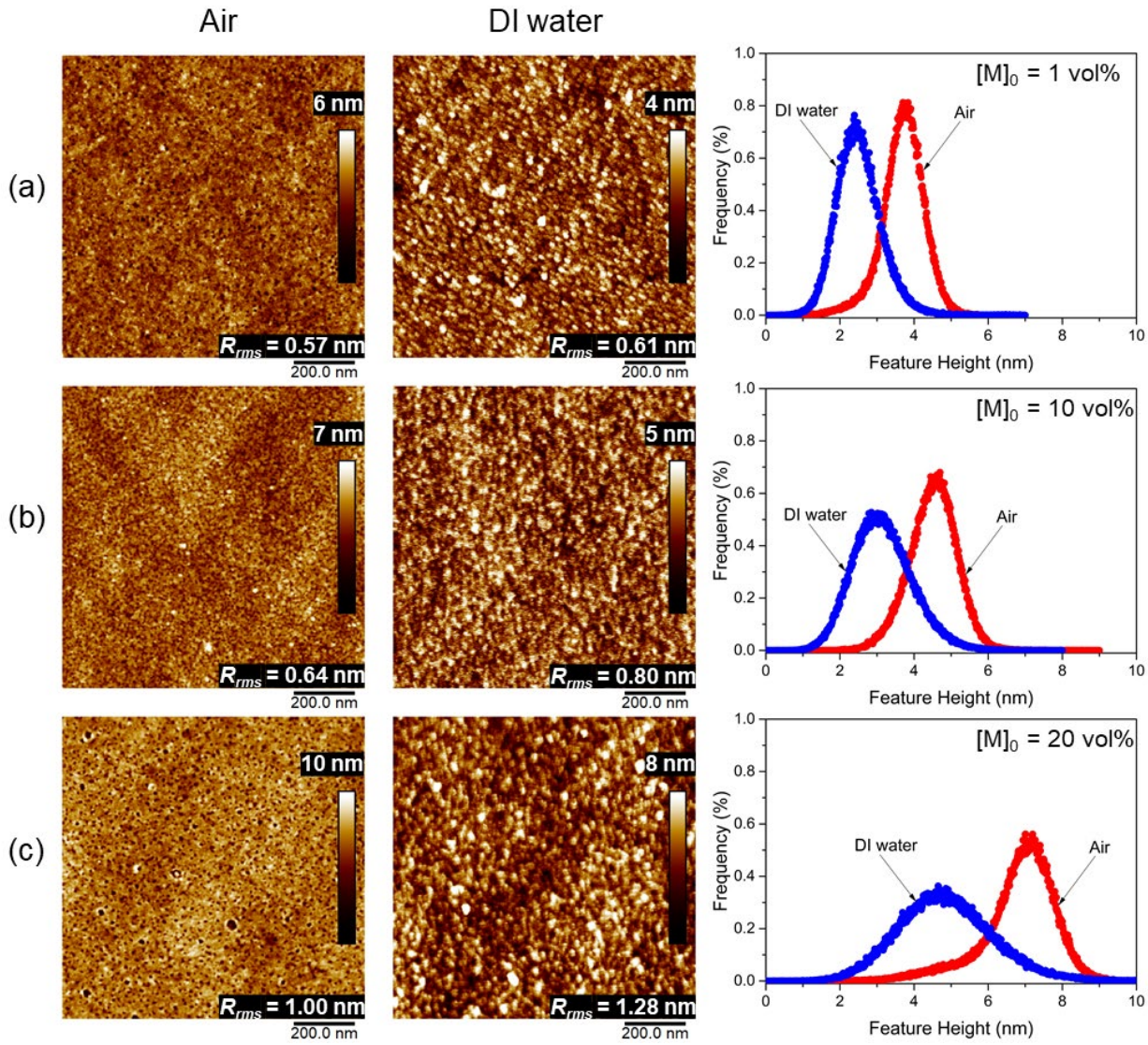

Figure 3-7. AFM 2-D images for the tethered PAA surfaces (PAA-PSf-Si) obtained for dry substrates (in air) (left) and in DI water (middle) with the respective feature height distributions (right). The tethered PAA layers were synthesized at $[M]_0$: (a) 1 vol%, (b) 10 vol%, and (c) 20 vol% for 2 h following PSf surface activation with He/O_2 APP.

Surface topography of tethered polymer layers is often reported based on AFM characterization in air, which is a poor solvent for hydrophilic polymer chains (e.g., PAA). In air the hydrophilic tethered chains are expected to collapse and aggregate (due to unfavorable interaction between the chain and solvent), forming a laterally inhomogeneous layer characterized

by “dimples” whose depth and distance between the dimples are governed by chain length and grafting density [182-184]. Indeed, cross-sectional AFM feature height profiles for the dry surfaces (i.e., in air), as shown for the example of PAA layer grafted at $[M]_0$ = 20 vol% for 2 h, exhibited dimples of widths in the range of ~2 – 20 nm (**Figure 3-8**). These separations were sufficiently wide to enable deeper penetration of the AFM tip into the tethered layer, relative to the narrower separations for the layers when swollen in water. As a consequence, the AFM determined FHD for the dry surface provides a misleading impression of higher surface feature heights relative to the swollen PAA layer in water (**Figure 3-8**). It is expected that at a high ionic strength, the PAA chains should also collapse due to charge screening which should reduce charge repulsion between the chains [185]. In contrast to the PAA layer in air, the collapsed PAA layer in aqueous 35 g/L NaCl, as shown for the example of a tethered PAA layer, grafted at $[M]_0$ = 20 vol% for 2 h, was laterally homogeneous (or dimple-free) similar to the swollen PAA layer in DI water (**Figure 3-8**); however, the feature heights were shorter and surface roughness (0.83 nm) was reduced by ~35% and ~17% relative to the PAA surface in DI water (1.28 nm) and in air (1.00 nm), respectively (**Figure 3-9**). It is noted that the laterally homogeneous structures observed for the swollen and collapsed PAA layers in water and 35 g/L NaCl solution, respectively, are consistent with findings based on coarse-grained molecular dynamics simulations of a polyelectrolyte brush in the presence of monovalent salts in a good solvent [186]. It is inferred from the above results that for applications in which tethered hydrophilic chains are exposed to water, surface topography would be more appropriately described via AFM of the liquid submerged surfaces.

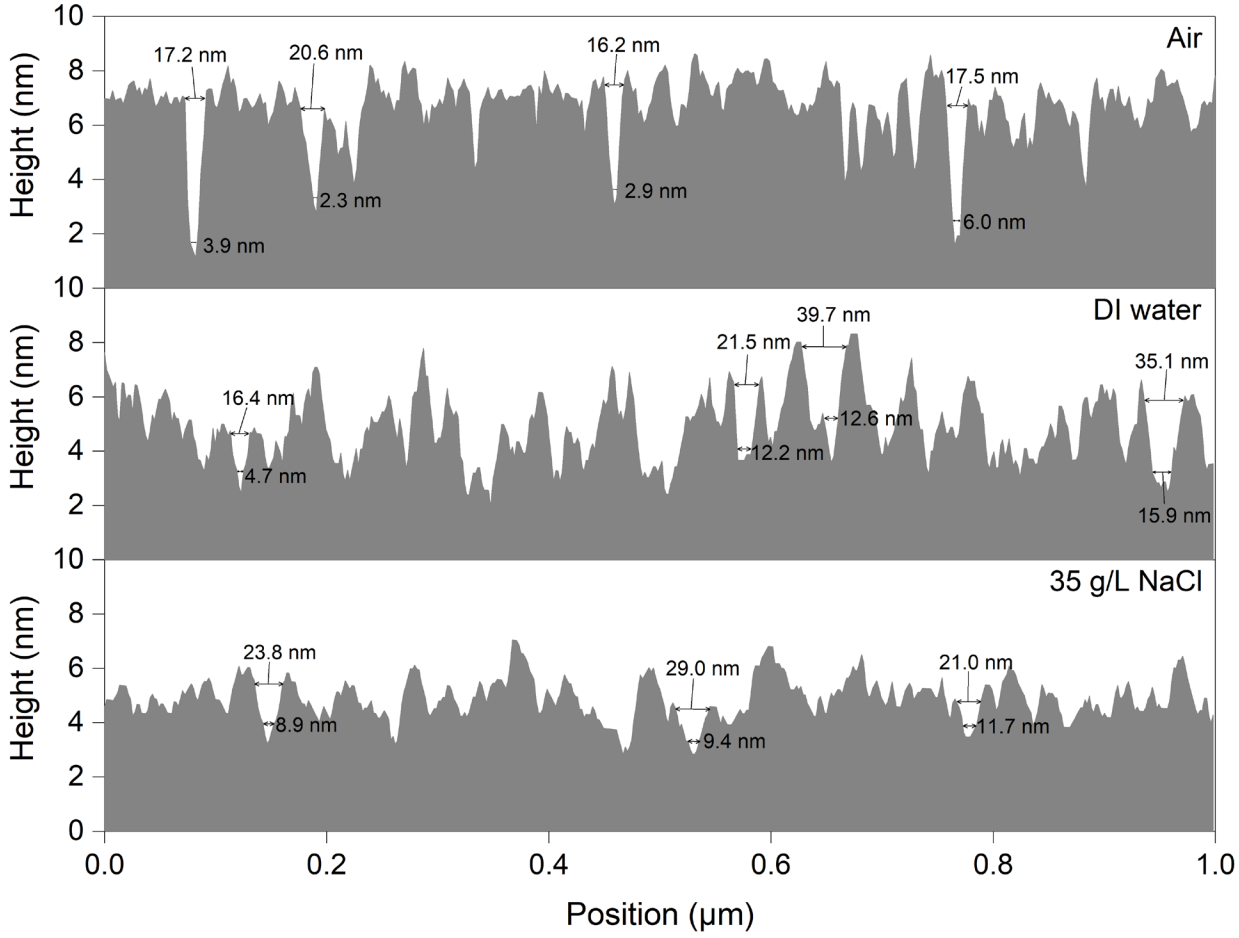

Figure 3-8. Cross-sectional AFM feature height profiles for the PAA-PSf-Si surface (tethered PAA layer synthesized at $[M]_0$ = 20 vol% for 2 h) obtained for dry substrate (in air) (top), in DI water (middle) and in 35 g/L NaCl solution (bottom). Widths of the dimples (of depth ≥ 4 nm) are indicated for the dry PAA tethered surface in air. Distance between valleys are also indicated for the tethered PAA layers in DI water and 35 g/L NaCl solution.

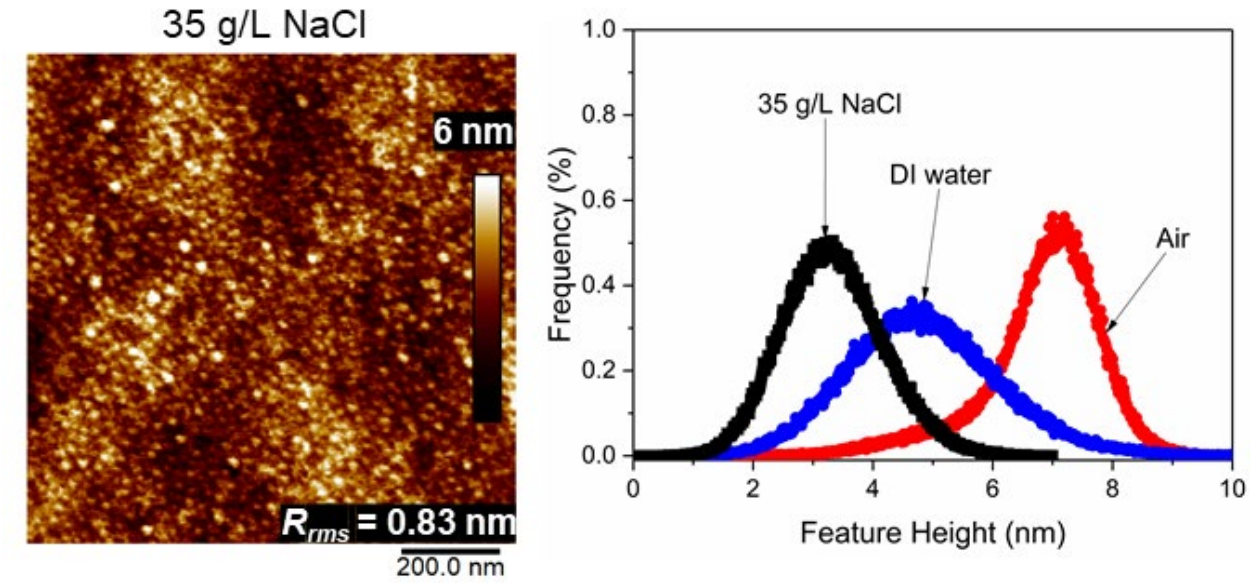

Figure 3-9. AFM 2-D image obtained in 35 g/L NaCl solution (left) and the corresponding feature height distribution (FHD) (right) for the PAA-PSf-Si (the tethered PAA layer synthesized at $[M]_0 = 20$ vol% for 2 h following surface activation with He/O_2 APP) (plotted along with the FHD for the surface as determined in DI water and air). The feature heights are scaled to the lowest height determined by the AFM tip and R_{rm} is root-mean-square surface roughness.

3.3.3 PAA chain rupture length

The PSf surface was initially examined via AFM-FS in DI water to confirm that chain pulling events (identified as peaks in the retraction force profile) were primarily due to the surface-tethered PAA chains. The tests demonstrated a surface adhesion peak of average rupture force of ~7.2 ± 2.6 nN at distances < 10 nm, while no other peak was observed at tip-surface separation > 10 nm (**Figure 3-10** and **Figure 3-11**). In comparison, typical retraction force profile for the PAA layers revealed multiple peaks due to rupture events whereby detachment of the pulled PAA chains from the tip occurred for the different PAA layers immersed in DI water (**Figure 3-12**). The first surface adhesion force peak, which was typically observed for tip separation of < 10 nm from the substrate surface, had a mean rupture force (F_R = 0.85 – 1.32 nN), which was ~2 – 4 times greater than at greater separations. Rupture events that occurred in proximity of the surface below 10 nm

may be attributed, in part, to increased tip interaction with the underlying PSf surface at such short distances [163, 187]. Therefore, the first peak in the retraction force curves was excluded for the purpose of determining the mean rupture forces and lengths for the PAA layers (**Figure 3-13**, **Figure 3-14**, **Figure 3-15**, **and Figure 3-16**) [187].

Tethered PAA layers displayed longer rupture lengths and broader distributions of rupture length that increased for PAA layers synthesized at higher initial monomer concentration ($[M]_0$). The above is consistent with the expected broad chain size distribution due to the increased rate of monomer addition to surface growing chains and chain termination by homopolymers formed in solution (**Figure 3-15**). For example, the mean rupture length ($\overline{L}_R$) for the PAA chains synthesized at $[M]_0$ = 20 vol% was 2.5 and 1.6 times larger relative to values obtained for the PAA tethered layers synthesized at $[M]_0$ of 1 vol% and 10 vol%, respectively, for a reaction time of 2 h (**Table 3-3**). Consistent with the above, the estimated number (M_n) and weight (M_w) average molecular weights of the tethered PAA chains, calculated based on the L_R values (**Section 3.2.4**), also increased with initial monomer concentration. For example, at the highest $[M]_0$ (i.e., 20 vol%) employed in the present work, M_n and M_w were approximately 2.7 and 3 times greater, respectively, relative to the corresponding values for the PAA layer synthesized at the lowest $[M]_0$ of 1 vol%. Also, the polydispersity index (*PDI*), determined based on the rupture length distribution (**Figure 3-15**), increased from 1.4 to 1.6 as the initial monomer concentration increased from 1 – 15 vol% to 20 vol%, respectively.

The PAA chain grafting densities, determined based on estimates of M_n and the dry polymer layer thickness, were in the range of 0.2 – 0.4 chains/nm^2, which is well within the range of moderate grafting densities for a polymer brush layer [188] (**Table 3-3**). It is also noted that the number of chain pulling events increased, with increasing PAA chain length and/or chain grafting

density. As shown in **Table 3-3** the total number of chain pulling events (*N*) increased by ~3.5 folds (i.e., from 170 to 593) as the initial monomer concentration ($[M]_0$) for graft polymerization rose from 1 to 20 vol%. Clearly, the initial monomer concentration for graft polymerization significantly impacts the resulting polymer chain length distribution as well as chain grafting density.

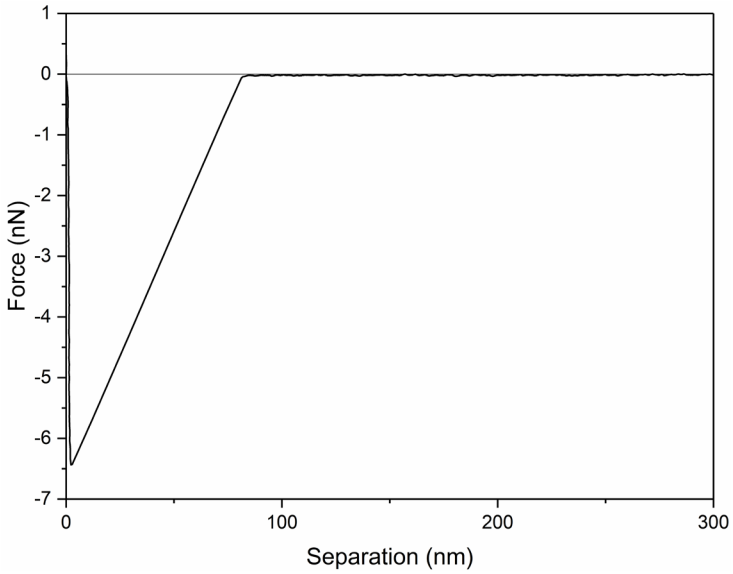

Figure 3-10. A typical retraction force curve for the native PSf-Si surface in DI water.

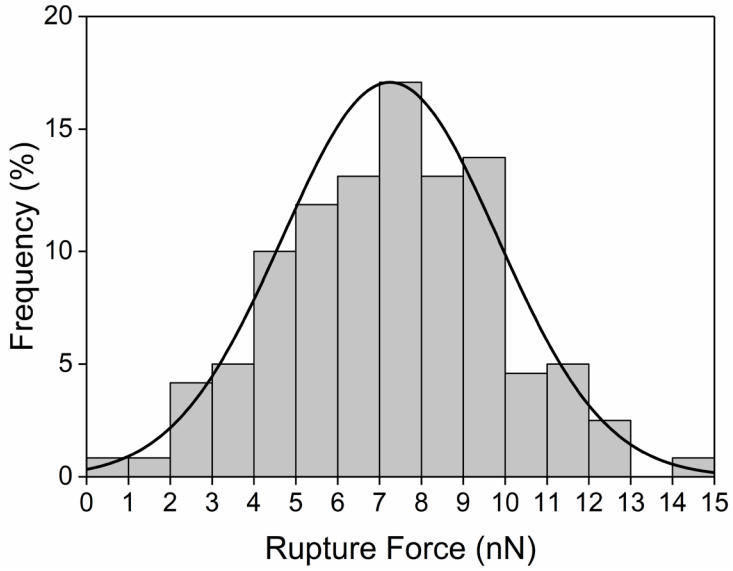

Figure 3-11. AFM-FS determined rupture force distribution for the native PSf-Si surface in DI water.

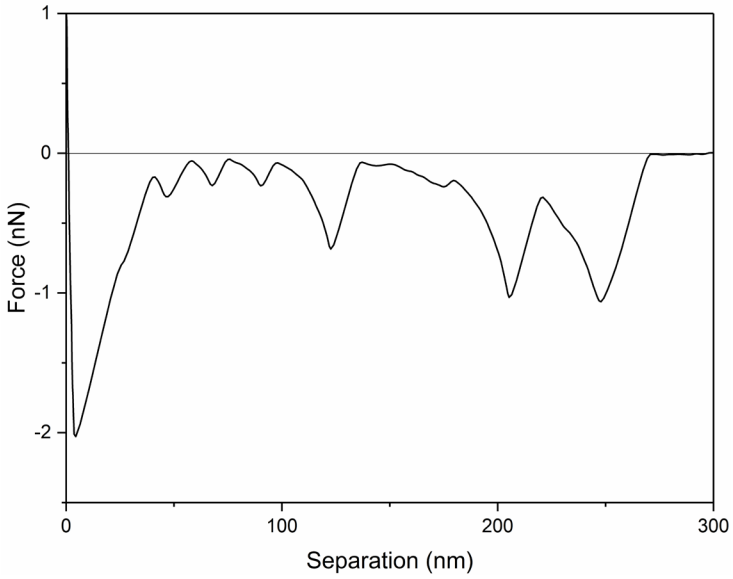

Figure 3-12. A typical retraction force curve for PSf with the tethered PAA layer (PAA-PSf-Si) in DI water. The tethered PAA layer (synthesized onto PSf activated with He/O_2 plasma) was synthesized at $[M]_0$ = 20 vol% for 2 h.

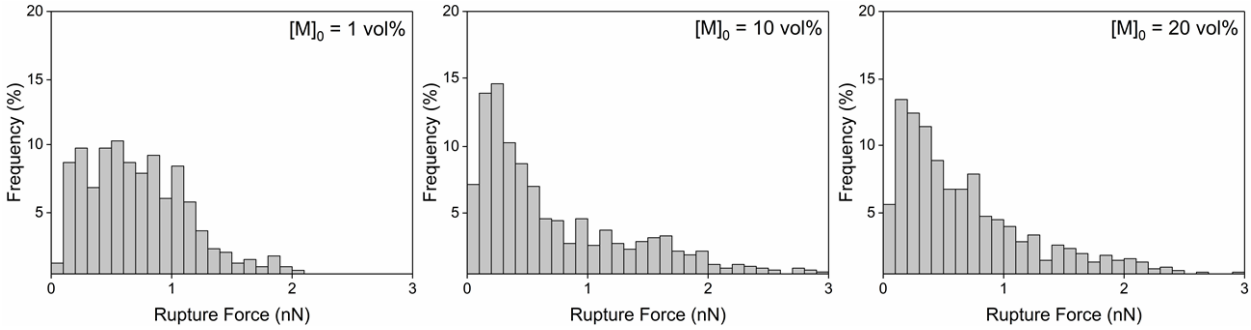

Figure 3-13. AFM-FS determined rupture force distributions (evaluated under DI water) for PAA chains synthesized at $[M]_0$ of 1 vol%, 10 vol%, and 20 vol% for 2 h (Note: the PSf surfaces were activated with He/O_2 plasma; data include the surface adhesion peaks (i.e., the first rupture event in the retraction profiles, L_R < 10 nm)).

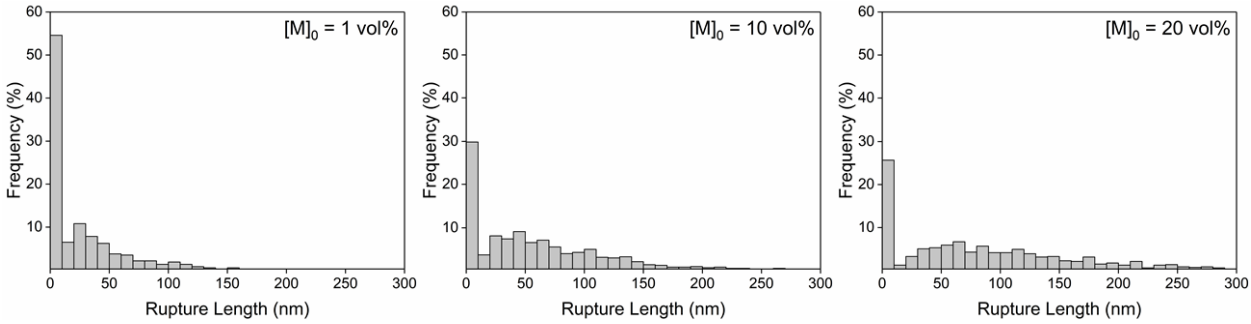

Figure 3-14. AFM-FS determined rupture length distributions (evaluated under DI water) for PAA chains synthesized at $[M]_0$ of 1 vol%, 10 vol%, and 20 vol% for 2 h (Note: the PSf surfaces were activated with He/O_2 plasma; data include the surface adhesion peaks (i.e., the first rupture event in the retraction profiles, $L_R < 10$ nm)).

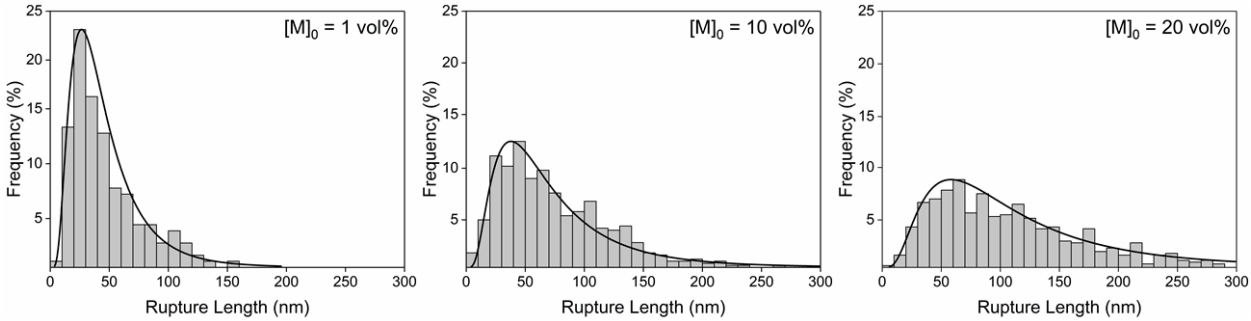

Figure 3-15. AFM-FS determined rupture length distributions (evaluated under DI water) for PAA chains synthesized at $[M]_0$ of 1%, 10%, and 20 vol% for 2 h. (Note: the PSf surfaces were activated with He/O_2 plasma; Also, the first rupture event in the retraction profiles, $L_R < 10$ nm, which is the adhesion peak, is excluded from the distributions).

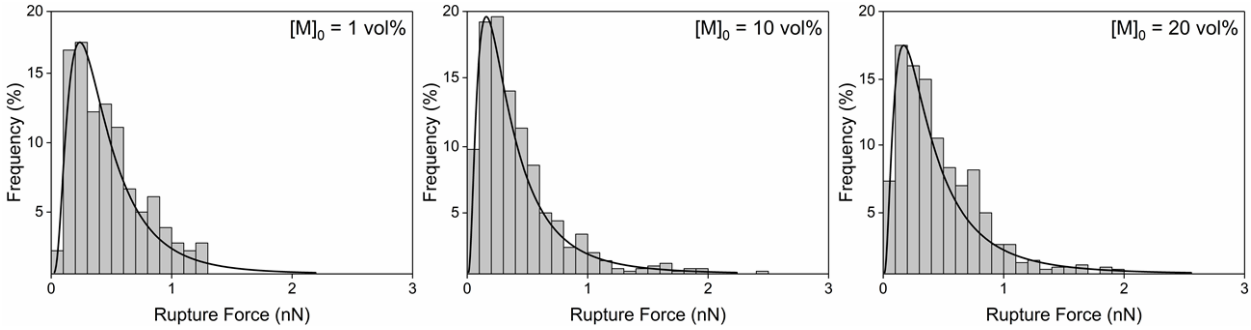

Figure 3-16. AFM-FS determined rupture force distributions (evaluated under DI water) for PAA chains synthesized at $[M]_0$ of 1%, 10%, and 20 vol% for 2 h. (Note: the PSf surfaces were activated with He/O_2 plasma; Also, the first rupture event in the retraction profiles, $L_R < 10$ nm, which is the adhesion peak, is excluded from the distributions).

Table 3-3. Characteristics of the tethered PAA layers on PSf substrate[†]

$[M]_0$ (vol%)	$\overline{F}_R$ [(a)] (nN)	$\overline{L}_R$ [(a)] (nm)	h [(b)] (nm)	L_e [(c)] (nm)	M_n [(d)] (g/mol)	M_w [(d)] (g/mol)	PDI [(d)]	N [(e)]	σ [(f)] (chains/nm^2)	d [(f)] (nm)
1	0.38	38	3.4	96	13,435	18,888	1.4	170	0.18	2.4
5	0.38	55	8.2	110	19,617	27,430	1.4	458	0.30	1.8
10	0.31	60	11.0	111	21,168	29,331	1.4	504	0.37	1.6
15	0.41	60	12.5	118	21,163	29,771	1.4	592	0.42	1.5
20	0.34	95	17.7	145	34,961	56,361	1.6	593	0.36	1.7

[†] Tethered PAA layer synthesized at $[M]_0$ = 1 – 20 vol% over 2 h graft polymerization period.
[(a)]Mean values obtained based on the log-normal fitted rupture force (F_R) and rupture length (L_R) distributions obtained in DI water; [(b)]Dry thickness (h) of the PAA layers in air determined via FIB-SEM; [(c)]Equilibrium thickness (L_e) of the PAA layers in DI water determined from AFM-FS approach curves; [(d)]Estimated number (M_n) and weight (M_w) average molecular weights and polydispersity index (PDI) of tethered PAA chains; [(e)]Total number of chain pulling events (N) encountered in the 200 retraction force profiles (Note: the first rupture event in the retraction profiles, L_R < 10 nm is excluded as it represents the adhesion peak); [(f)]PAA chain surface grafting density (σ) and average distance (d) between neighboring PAA chains (estimated as $d = \sqrt{\sigma^{-1}}$).

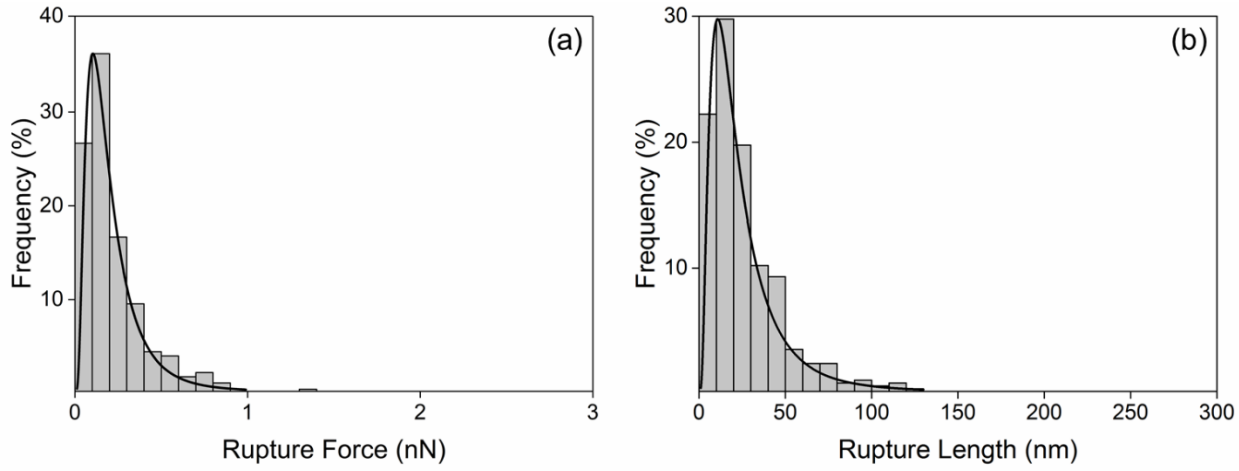

Figure 3-17. AFM-FS determined (a) rupture force and (b) rupture length distributions for tethered PAA chains (synthesized at $[M]_0$ = 20 vol% for 2 h) in 35 g/L NaCl solution. (Note: the PSf surface was activated with He/O_2 plasma; Also, the first rupture event in the retraction profiles, L_R < 10 nm, which is the adhesion peak, is excluded from the distributions).

3.3.4 PAA chain rupture force

The rupture force, which represents the affinity between the AFM tip (i.e., Si_3N_4) and PAA chains, was also examined for the PAA layers in DI water. Qualitatively similar rupture force

distributions and mean rupture forces ($\overline{F}_R$), in the range of ~0.31 – 0.38 nN, were obtained for the PAA layers synthesized at different initial monomer concentrations (**Figure 3-16** and **Table 3-3**). The above rupture force range is expected to be due to short range interactions between the PAA chains and SiN_4 tip, primarily via hydrogen bonding and van der Waals interaction in water [163]. The mean rupture forces for the PAA layers were significantly smaller relative to the expected force for a single C–C bond (~10 nN) [189]. The above indicates that the PAA chains interacted with the Si_3N_4 tip noncovalently and remained intact after the chain pulling events (i.e., no delamination).

The presence of the long-range repulsive Coulomb force between the PAA and AFM tip was also evident from the equilibrium thickness (L_e) determined from the AFM approach force profiles (**Figure 3-18**). It is noted that both the PAA chains and Si_3N_4 tip are expected to bear a slight negative charge in water near neutral pH [190, 191]. Since the Debye screening length for pure water at neutral pH is ~1 μm [192], it is reasonable to assert that long-range Coulombic repulsions between the tethered PAA chains and the AFM tip were not screened in DI water. The existence of long-range repulsive Coulomb force between the two surfaces (i.e., PAA and Si_3N_4) was evident from the equilibrium thickness (L_e), which correlated with increased rupture length obtained at higher $[M]_0$. For example, L_e in DI water increased from 96 nm to 145 nm as $[M]_0$ increased from 1 vol% to 20 vol% for the same graft polymerization time of 2 h (**Table 3-3** and **Figure 3-18**).

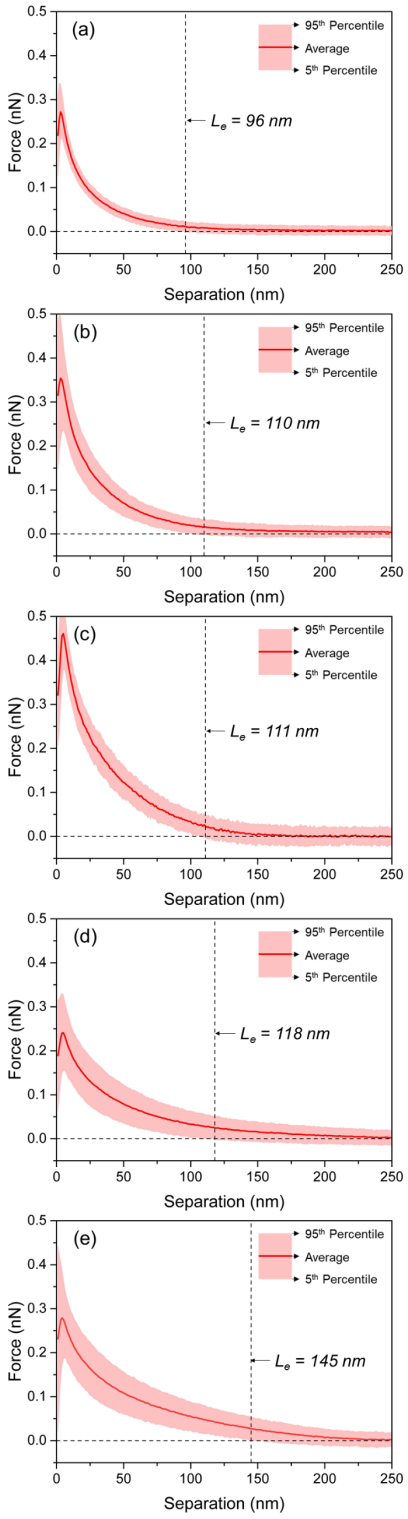

Figure 3-18. Equilibrium thickness (L_e) in DI water estimated for PSf with the tethered PAA layers (PAA-PSf-Si) synthesized at $[M]_0$: (a) 1 vol%, (b) 5 vol%, (c) 10 vol%, (d) 15 vol%, and (e) 20 vol% for a reaction period of 2 h (Note: PSf surface was activated with He/O_2 plasma).

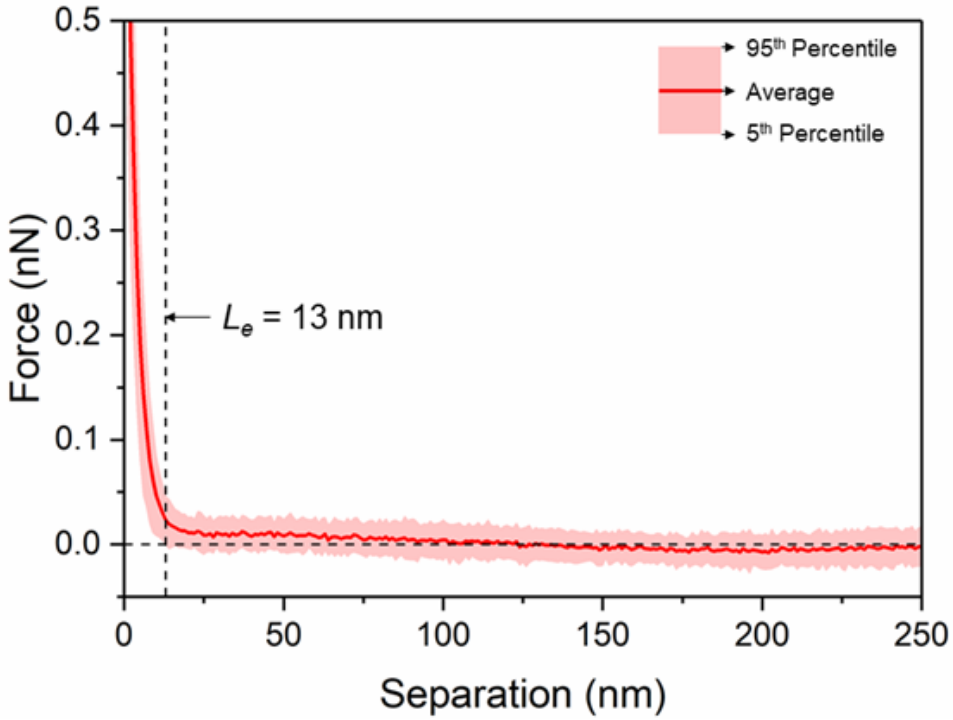

Figure 3-19. Equilibrium thickness (L_e) in saline water (35 g/L NaCl) estimated for PSf with the tethered PAA layer (PAA-PSf-Si) synthesized at $[M]_0$ = 20 vol% for a reaction period of 2 h (Note: PSf surface was activated with He/O_2 plasma).

In high salinity water such as seawater (i.e., ~35 g/L NaCl), in which the electrostatic forces are effectively screened (the Debye screening length is ~0.4 nm) [192], L_e values for the tethered PAA layers are expected to decrease relative to in DI water. Indeed, as illustrated by the example of the PAA layer grafted at $[M]_0$ = 20 vol% for 2 h (**Figure 3-19**), in 35 g/L NaCl the L_e (13 nm) was ~91% lower than in DI water (145 nm). In addition to charge screening, it is hypothesized that repulsive hydration forces would reduce PAA interaction with the Si_3N_4 tip at a short range (order of few nanometers) in the saline solution; the above is likely to be due to the presence of hydrated Na^+ near the negatively charged surfaces of the PAA layer and Si_3N_4 tip [193]. This is evident from the rupture force reduction, as shown for the example of a tethered PAA layer grafted at $[M]_0$ = 20 vol% for 2 h (**Figure 3-17(a)**), whose mean rupture force was reduced by ~50% in 35 g/L

NaCl solution relative to DI water (**Figure 3-16**). The tethered PAA chains in saline water are expected to be in a collapsed state and thus form a more rigid layer than swollen PAA chains in DI water [165]. Consequently, a reduced degree of PAA chain pulling (both number of chain pulling events and pulling distance) was expected for the collapsed relative to swollen PAA chains. Indeed, as shown in the example of **Figure 3-17(b)**, the mean rupture length and the total number of chain pulling events (N) were reduced by ~80% and ~23%, respectively, in 35 g/L NaCl solution relative to DI water (**Figure 3-15**). It is also noted that for the dry PAA layers (in air) chain pulling events were not encountered, and the retraction force profile was similar to that obtained for the native PSf surface (**Figure 3-10**); the above is possibly due to even greater interchain and intersegment interactions in air relative to those in salt water. The above results suggest that tethered PAA can be beneficial as a surface modifier for membranes (e.g., UF) used for filtration of saline water sources. Given that the tethered chains will swell in a DI water fouled membranes should be amenable to cleaning using freshwater (specifically at pH above the pK_a of PAA).

3.3.5 Surface wettability of collapsed and swollen PAA layers

Increased surface wettability, as inferred by contact angle measurements, should be expected for extended hydrophilic polymer chains in a good solvent. Indeed, the DI water (i.e., good solvent for PAA) CB contact angle for the tethered PAA decreased by ~54 – 55% relative to that of the native PSf surface (i.e., 80°). It has been reported that, at sufficiently high grafting densities, increased layer thickness or chain length one should expect the CB contact angle to be governed primarily by the chemical functionality and topography at the polymer-water interface [194, 195]. Consistent with the above, the CB contact angle (**Figure 3-20** and **Table 3-4**) was within a narrow range (36.4 – 36.9°) for the PAA layers synthesized over the range of layer

properties shown in **Table 3-3**. The increase in hydrophilicity is evident noting that the surface free energy (**Section 3.2.4**) for the PAA surfaces (59.1 – 59.3 mJ/m^2) was ~38% greater relative to the native PSf surface (42.9 mJ/m^2), and its polar component was correspondingly a factor of ~11 times greater for the PAA-PSf-Si surfaces (**Figure 3-21**). It is noted that the contact angle was ~17 – 26% higher for the dry (and thus collapsed) PAA-PSf-Si surface based on the SD relative to the CB measurements (**Figure 3-20** and **Table 3-4**). The above behavior is consistent with findings of other studies on the wetting behavior of hydrophilic tethered polymer layers [195, 196]. Given the above, it appears that the CB contact angle is more appropriate for characterizing surface hydrophilicity for applications in which the tethered polymer layer is submerged in an aqueous environment. It is noted that the CB contact angle for the PAA surfaces obtained in the salt solution (35 g/L aqueous solution) and DI water (**Table 3-6**) at pH 6 and 8 was in the range of ~29 – 38°, indicating that the surfaces remain hydrophilic in the above solvent conditions.

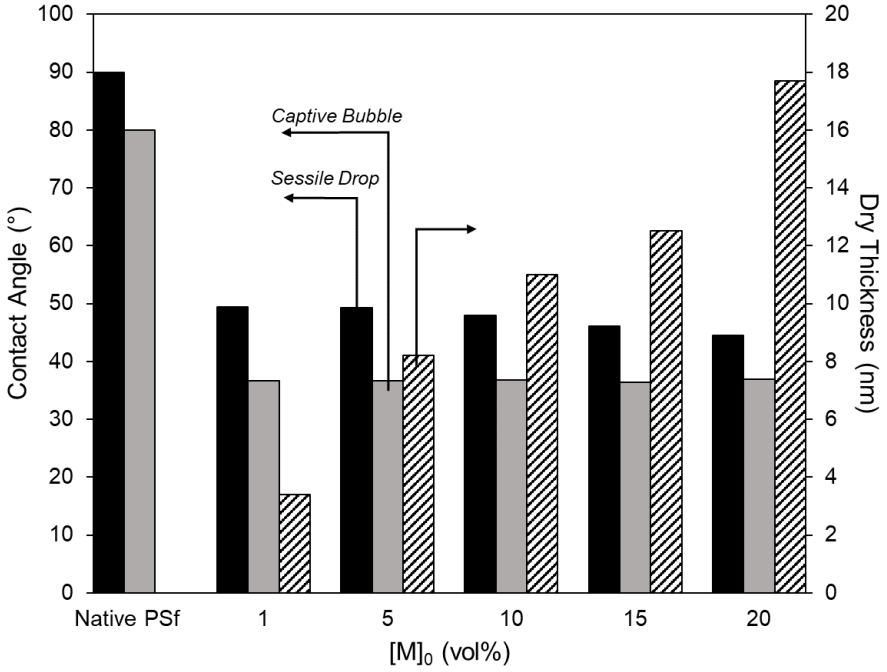

Figure 3-20. Sessile drop and captive bubble contact angles for the native PSf-Si and for PSf with the tethered PAA layer (PAA-PSf-Si) synthesized at $[M]_0$ = 1 – 20 vol% for 2 h post PSf surface activation with He/O_2 plasma. Dry thickness is also plotted for the tethered PAA layers.

Table 3-4. Sessile drop (SD) and captive bubble (CB) contact angles (CA) and surface free energy (SFE) data for the native PSf-Si and PAA-PSf-Si† surfaces.

Surface	SD CA[(a)] (°)	CB CA[(b)] (°) (air)	CB CA[(b)] (°) (octane)	γ_s^p [(c)] (mJ·m^{-2})	γ_s^d [(c)] (mJ·m^{-2})	% Polar SFE component[(c)]
Native PSf	90.0	80.0	118.5	3.5	39.4	8.1
Tethered PAA layers synthesized at $[M]_0$:						
1 vol%	49.4	36.6	42.5	38.3	20.8	64.8
5 vol%	49.3	36.6	41.7	38.7	20.4	65.5
10 vol%	47.9	36.8	43.2	38.0	21.1	64.3
15 vol%	46.1	36.4	42.7	38.2	21.1	64.4
20 vol%	44.5	36.9	43.6	37.8	21.3	63.9

†AA graft polymerization was carried out for a period of 2 h following PSf surface activation by He/O_2 plasma for a period of 15 s.
[(a)] Sessile drop contact angles measured with 1 µL DI water drops.
[(b)] Captive bubble contact angles measured with 4 µL air and octane bubbles.
[(c)] Polar (γ_s^p) and dispersive (γ_s^d) components of the surface free energy.

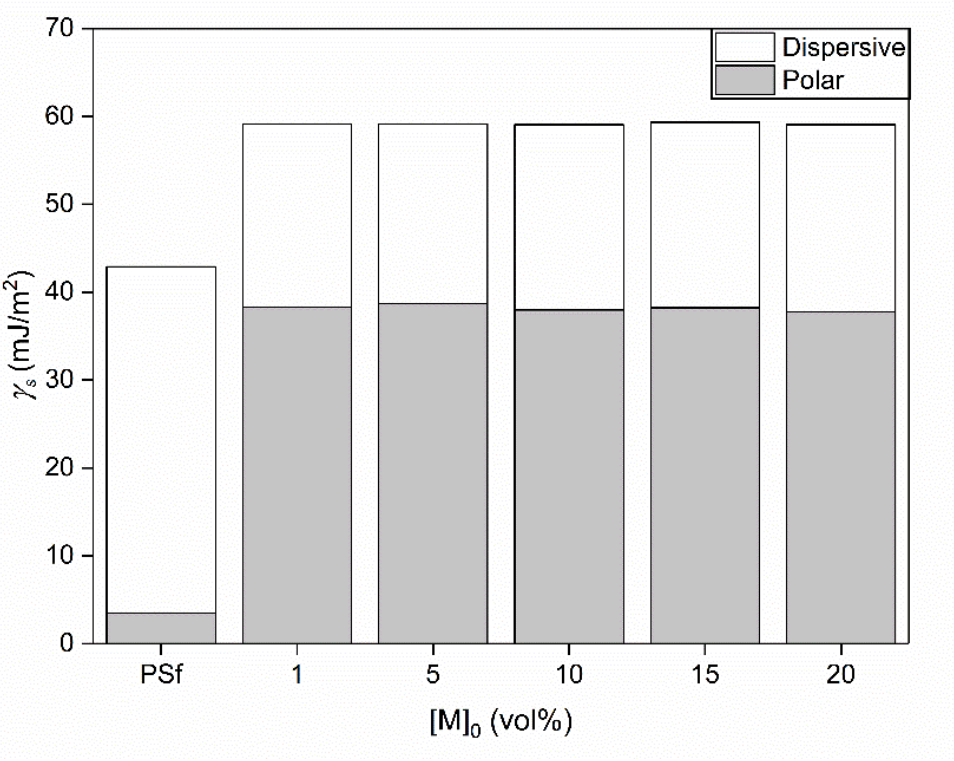

Figure 3-21. Surface free energy (γ_s) and its dispersive and polar components, for the native PSf-Si surface and the tethered PAA-PSf-Si surfaces synthesized at $[M]_0$ = 1 – 20 vol% for 2 h. γ_s was determined using the CB contact angles as determined in DI water.

Table 3-5. Captive bubble contact angles for PAA-PSf-Si (the tethered PAA layer was synthesized at $[M]_0$ = 20 vol% for 2 h post PSf activation with He/O_2 plasma) in DI water and NaCl solutions.

Solvent	Captive bubble contact angle (°)
DI water (pH 6)	38.4
DI water (pH 8)	29.7
35 g/L NaCl (pH 6)	29.3
35 g/L NaCl (pH 8)	29.1

3.4 Conclusions

The topography and potential swelling of polyacrylic acid (PAA) chains tethered onto a polysulfone (PSf) surface were assessed via AFM and AFM-FS characterization. The tethered PAA chains were synthesized via free-radical graft polymerization of acrylic acid onto PSf surfaces activated by an impinging stream of atmospheric pressure plasma. Chain extension for the PAA-PSf-Si surface in DI and high salinity (i.e., 35 g/L NaCl) water indicated that the chains were in a collapsed configuration in saline water but could be extended significantly in DI water. The estimated number-average molecular weight of the tethered chains, for the present graft polymerization conditions of $[M]_0$ = 1 – 20 vol%, was in the range of ~13,000 – 35,000 with chain-chain separation distance of 1.5 – 2.4 nm. The PAA-PSf-Si surface was hydrophilic, as assessed via contact angle measurements, in both DI and high salinity water suggesting that such layers could be of low fouling propensity when exposed to negatively charged foulants.

Chapter 4. Tailoring PA TFC RO Membrane Performance via Surface Nano-Structuring with Tethered Poly(acrylic acid) Layers

4.1 Overview

In recent years, it has been shown that hydrophilic polymers that are terminally attached to the polyamide membrane surface can be synthesized at a high degree of surface chain density via atmospheric pressure plasma (APP) surface activation which serves to induce graft polymerization using the target monomer [124, 197, 198]. Surface grafted polymer chain density and layer thickness can also be tuned by the plasma surface activation and graft polymerization conditions [197, 198], which then allows for tailoring the performance of the modified membrane. Previous studies with APP followed by graft polymerization (GP) have focused primarily on reducing membrane fouling propensity; but it has also been documented that membrane permeability and salt rejection are impacted by the base membrane choice. In previous work, a surface tethered hydrophilic polymer layer was utilized to transform the performance of a PA TFC nanofiltration (NF) base membrane into that of a brackish RO membrane. The above work demonstrated significantly lower mineral scaling propensity as well as increased biofouling resistance compared to commercial PA TFC RO membrane of the same level of salt rejection [15-17]. The PA membranes with tethered hydrophilic polymer layers had up to a factor of ~2 greater pure water permeance (determined using 500 mg/L NaCl feed water) compared to a commercial BWRO membranes of about the same rejection level (~94 – 95%). Given that chain surface density and size are affected by the plasma surface treatment and graft polymerization conditions, it is reasonable to expect that membrane performance will accordingly also be impacted. Therefore, it is of interest to investigate the degree to which fine-tuning of membrane rejection and permeability can be attained with a tethered hydrophilic polymer layer and accordingly the impact on the water

permeability and water/salt selectivity trade-off.

The present study demonstrates tuning seawater reverse osmosis (SWRO) membrane performance via surface nano-structuring (SNS) of PA TFC base membranes with tethered poly(acrylic acid) (PAA) chains. Surface nano-structuring (SNS) with a layer of PAA chains tethered onto a base PA membrane forming a SNS-PAA-PA membrane was accomplished by a two-step process [15-17, 199]. The base PA TFC membrane was first activated by treatment with an impinging APP stream, followed by aqueous phase free-radical surface graft polymerization of acrylic acid (AA). The impact of APP surface activation and graft polymerization conditions was then investigated with respect to the path for tuning the SNS-PAA-PA performance (i.e., water and salt permeability, salt rejection and water/salt selectivity) and also upgrading BWRO to SWRO membrane performance.

4.2 Experimental

4.2.1 Materials and reagents

Three types of flat sheet polyamide based TFC membranes (indicated as Base-PA1, Base-PA2 and Base-PA3 in **Table 4-1**), supplied by Toray Membrane USA Inc. (Poway, CA), were utilized as base membranes onto which tethered PAA layers were synthesized. Flat sheet membrane coupons were also extracted from a commercial spiral wound element (Dow Filmtec SW30-2514) for a baseline comparison. Helium (99.99%) and oxygen (99.999%) gases for plasma generation and treatment and nitrogen (99.5%) gas, used for drying polyamide membrane surfaces and purging monomer solutions during graft polymerization, were obtained from Airgas (Los Angeles, CA). Temperature of APP discharge was measured with a Digi-Sense thermocouple thermometer coupled with a Digi-Sense Type K High-Temperature flexible thermocouple probe

(Cole-Parmer, Vernon Hills, IL). Acrylic acid (99%) was from Sigma-Aldrich (St. Louis, MO), and sodium chloride (≥ 99.0%), glacial acetic acid (≥ 99.7% w/w) and sodium hydroxide solution (50% w/w) were obtained from Fisher Scientific (Chino, CA). Ultra-pure deionized (DI) water was produced using a Milli-Q filtration system (Millipore Corp., San Jose, CA). Solution pH was measured with an Oakton pH 110 meter (Oakton Instruments, Vernon Hills, IL).

4.2.2 Membrane surface nano-structuring with tethered poly(acrylic) acid

The base SWRO and BWRO membrane coupons (11.2 cm x 5.6 cm) were cut from rolls of flat sheet membranes using a CF042 steel rule die (Sterlitech Corp., Kent, WA) following the protocol described in **Appendix A.2.1**. Three different PA TFC membranes (**Table 4-1**) were selected as the base membranes having ~1.5 – 2.3 times greater water permeability coefficient (L_p) relative to a popular commercial membrane selected for seawater desalination (i.e., SW30 in **Table 4-1**). Prior to plasma treatment, the active membrane side of the coupons was blow dried with nitrogen in order to prevent plasma surface etching and ineffectiveness of surface activation due to surface moisture [200, 201].

Plasma surface activation was accomplished with an APP system comprised of a plasma head (producing a rectangular 79 mm x 0.4 mm plasma beam) connected to a plasma controller (Atomflo^{TM} 500) and a coolant control module (Surfx Technologies LLC, Redondo Beach, CA). The membrane coupons were affixed to a base plate, and the plasma source was translated over the membrane surface, at a speed of 100 mm/s, via an XYZ scanning robot (Surfx Technologies LLC, Redondo Beach, CA). Helium (He) plasma, which was selected for PA surface activation, was generated at He flow rate of 45 L/min and radio frequency (RF) power of 150 W. At the above RF power and over the range of plasma source-surface separation (*PSS*) distance used in the

present work (5 mm – 15 mm), the He plasma discharge temperature (at the membrane surface) was in the range of ~52 – 71°C (**Figure 4-1**). This plasma discharge temperature range is significantly lower than the reported glass transition temperature range (i.e., ~140 – 190°C [202]) of the PA layer of commercial TFC RO membranes. Therefore, it is reasonable to assert that plasma surface treatment did not lead to significant thermally-induced structural or chemical changes in the PA active layer.

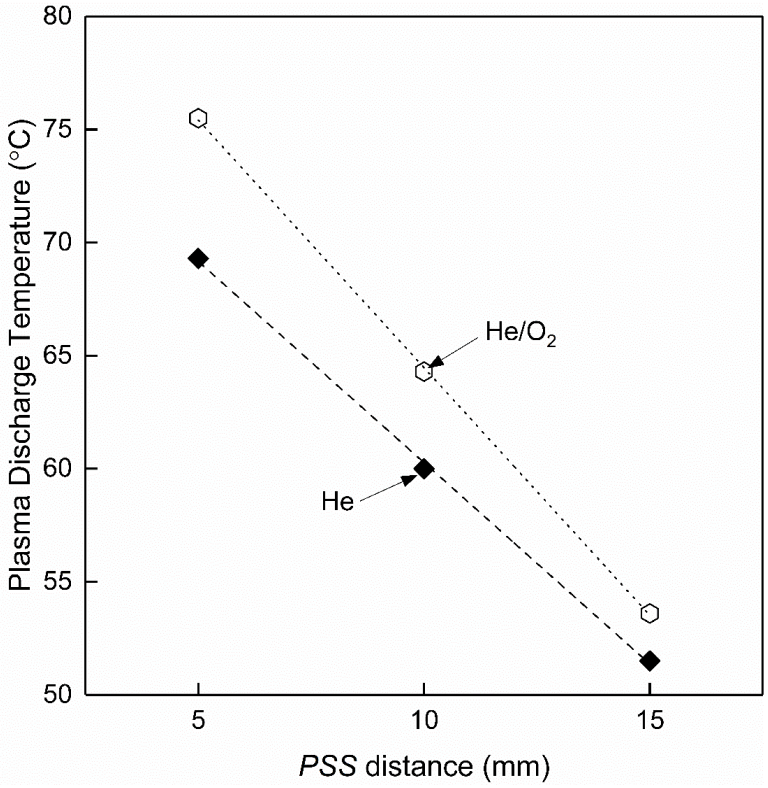

Figure 4-1. Discharge temperatures for He and He/O_2 APP at plasma source-surface separation (*PSS*) distances of 5 – 15 mm.

APP membrane surface activation effectiveness and the potential for surface etching (which can increase permeability and reduce salt rejection [203, 204]) can be affected by (a) plasma type, (b) plasma power, (c) plasma head scan speed and/or number of sequential scans which in essence dictate the exposure period and (d) the plasma source-surface separation (*PSS*)

distance. It is noted that helium and oxygen (He/O_2) plasma was also reported to be effective for polyamide surface activation [198]; however, unlike helium plasma, He/O_2 plasma led to excessive polyamide surface etching as was also confirmed in the present work (**Figure 4-2**). Therefore, in the present work helium plasma was selected for polyamide surface activation, particularly since it was shown to be effective for generating a high density of surface active sites for subsequent graft polymerization [198]. Surface treatment with a given plasma source at excessive *PSS* distance diminishes the concentrations of plasma species that reach the substrate surface, primarily due to the recombination of plasma species with the ambient air downstream of the discharge region [124, 205]; the consequence is a lower density of surface active sites for graft polymerization. Here it is noted that in previous work on APP induced AA graft polymerization, onto both polyamide and polysulfone surfaces [197, 198], effective surface activation was achieved at a *PSS* distance of 10 mm. For a given plasma type and power, the *PSS* distance and number of consecutive plasma surface treatment scans of the base membrane can markedly impact surface activation (and possibly the base membrane permeability) and thus these variables were experimentally assessed over ranges of 5 – 15 mm and 1 – 5 scans, respectively. It is noted that the plasma exposure period for a single surface treatment scan for the present plasma source head was 4 milliseconds [152] with the delay between sequential scans being in the range of ~0.3 – 1.4 seconds. Plasma surface treatment for the membrane coupons was carried out following the protocol described in **Appendix A.2.2**.

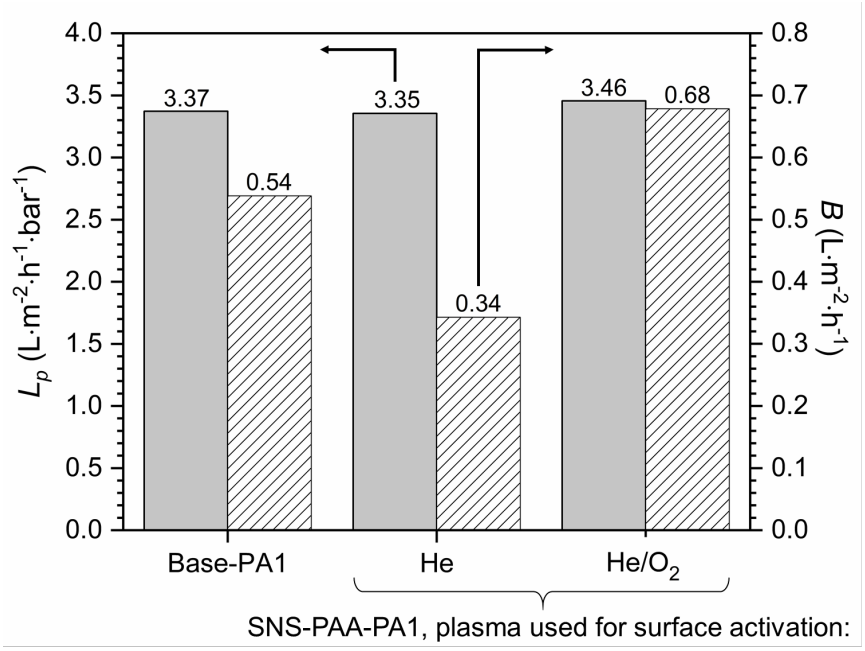

Figure 4-2. The effect of He and He/O_2 APP surface treatment (at two sequential scans at *PSS* distance of 10 mm) on water (L_p) and salt (B) permeability coefficients for SNS-PAA-PA1 membranes derived from BWRO Base-PA1 membranes via AA graft polymerization at the initial conditions of $[M]_0 = 20$ vol% and pH of 1.8 for a period of 1 h at 70°C. He and He/O_2 (90:1 v/v He:O_2 ratio) plasmas were generated at helium flow rate of 45 L/min and radio frequency power of 150 W. The SNS-PAA-PA1 membrane, which was synthesized following Base-PA1 membrane surface activation with the He/O_2 plasma, had only a 3% greater L_p but a B value that was twice that of the membrane synthesized post-surface activation with the He plasma. The B value for the SNS-PAA-PA1 that was synthesized using the He/O_2 plasma was even greater (by 26%) than that of the Base-PA1 membrane; the above result was assessed to be indicative of PA membrane surface etching due to the He/O_2 plasma surface treatment consistent with previous studies [203, 204].

Following surface plasma activation, graft polymerization of acrylic acid was carried out at an initial AA monomer concentration ($[M]_0$) of 10 – 30 vol% for a period of 1 h at 70°C. The pH of the prepared AA monomer solutions was in the range of ~1.7 – 2.0. For the current range of initial monomer concentration, the AA monomer reactivity is expected to decrease with increasing pH of the AA monomer solution above its $pK_a \sim 4$ owing to increased ionization of the monomer [206]. However, the tethered (macroradical) chains are expected to adopt a more extended conformation at increasing pH which increase the accessibility to the radical propagation site [207].

At pH < pK_a, monomer reactivity, in its unionized form, increases with decreasing pH, while the growing macroradical chains will tend toward a more collapsed configuration and thus decreased accessibility of the radical reactive sites [206]. Given the above competing effects, the potential impact of pH on graft polymerization on SNS-PAA-PA membrane performance was evaluated for graft polymerization pH range of 1.8 – 13. Adjustment of the solution pH above 1.8 (the native pH of the monomer solution) was accomplished by the addition of 50% w/w NaOH solution.

Graft polymerization was carried out immediately after plasma surface treatment of the membrane coupons following the protocol detailed in **Appendix A.2.3.** Briefly, each of the plasma treated membrane coupons was placed in a separate 235 ml monomer containing glass jar. The glass jars were then placed in a temperature-controlled water bath for the duration of graft polymerization. Nitrogen gas was injected at the bottom of the reaction vessels during graft polymerization to remove oxygen that can inhibit the polymerization reaction [154], and also to impart solution mixing (provided by a swarm of nitrogen bubbles). Graft polymerization was terminated by quenching the reaction with a copious volume of DI water after removing the coupons from the reaction mixture, followed by additional DI water rinsing. The SNS-PAA-PA membrane coupons were then stored in DI water prior to their performance characterization.

4.2.3 Membrane performance evaluation

Membrane performance was quantified with respect to the water permeability coefficient (L_p) and salt transport coefficient (B) using a laboratory plate-and-frame RO (PFRO) membrane recirculation unit, which is described in detail in **Appendix B.1**. The membranes were first compacted with DI water (20.0 ± 0.2℃) flowing through the PFRO unit at a transmembrane pressure (ΔP) of 5.9 MPa (~850 psi) for 24 hours, prior to determining the water permeability

coefficient, over a ΔP range of 3.4 – 5.9 MPa (~500 – 850 psi). Prior to determining the salt transport coefficient, the PFRO unit was operated with saline feed water (i.e., 32 g/L NaCl in DI water at 20.0 ± 0.2℃ and pH ~6.2) at 5.5 MPa (~800 psi) for 24 hours to stabilize the permeate flux and permeate conductivity.

The salt permeability coefficient was evaluated from the solution-diffusion model, i.e., $J_{v,sw}C_p = B(C_m - C_p)$, where $J_{v,sw}$ is average volumetric permeate flux of a saline solution (maintained at the same level for all membrane characterization tests), and C_p and C_m are the average salt concentrations in the permeate and at the membrane surface, respectively. The diffusive salt permeability coefficient (B) or simply the B-value as defined above, which is commonly used in the characterization of high salt rejection TFC RO membranes [14, 208, 209], is a function of the selective layer thickness and salt solubility and diffusivity in the selective layer [45]; however, the B-value can also be impacted by hydrodynamic conditions for membranes of low levels of solute rejection where convective cross-membrane salt transport can occur [210, 211]. In order to determine the B-value, C_m was determined via estimation of the concentration polarization modulus (CP) using the simple film model, i.e., $CP = \left(C_m - C_p\right)/\left(C_b - C_p\right) = \exp\left(J_{v,sw}/k\right)$, where C_b is the average salt bulk concentration. Given the low recovery in the short PFRO cell (< 1%), the bulk salinity was reasonably approximated by that of the RO feed. It is noted that the film model provides a reasonable CP estimate for the present PFRO membrane channel dimensions [212]. The average feed side mass transfer coefficient, k, for the membrane cross flow cell at a given cross flow velocity was estimated via the approach described in [43] using the following equation, $k = J_{v,sw} \cdot \ln\left[\left(\Delta P/\left(\pi_f - \pi_p\right)\right)\cdot\left(1 - J_{v,sw}/J_{v,w}\right)\right]^{-1}$, where $J_{v,w}$ is the permeate volumetric flux of pure water, and π_f and π_p are osmotic pressures of the saline feed and permeate, respectively. The

osmotic pressures were estimated, for a given salt concentration, using OLI multi-electrolyte thermodynamic simulation software. Intrinsic salt rejection ($R_i = 1 - C_p / C_m$) was determined for given measurements of C_p and estimates of C_m at $J_{v,sw}$ = 34 L·m^{-2}·h^{-1} (equivalent to 20 gal·ft^{-2}·day^{-1}) and a relatively high cross flow velocity of 49 cm/s in order to keep the *CP* modulus at or below 1.3 in the present PFRO cell. It is noted that the permeate flux was within the typical range for commercial SWRO elements (i.e., 26 – 42 L·m^{-2}·h^{-1}) at the standard testing conditions (32 g/L NaCl feed water concentration, ΔP = 5.5 MPa) [213, 214]).

4.3 Results and Discussion

4.3.1 Alteration of base membrane performance due to drying and plasma treatment

Membrane surface structuring of polyamide (PA) BWRO and SWRO membranes with tethered PAA layers was evaluated for three base membranes (**Table 4-1**) as an approach to tune membrane performance. The membrane water permeability coefficient, L_p, and salt permeability coefficient, B, for base membrane Base-PA1 were determined to be within the typical ranges for commercial BWRO membranes. Base membranes Base-PA2 and Base-PA3, which had 29% and 33% lower L_p and 61% and 72% lower B-value, respectively, relative to membrane Base-PA1, can be considered a SWRO membrane relative to current standards of commercial RO membranes.

Prior to plasma surface activation, the base membranes were dried with a nitrogen stream (**Section 4.2.2**) to avoid PA surface etching linked to surface moisture [200, 201]. However, drying of the PA membranes can lead to water permeability reduction as noted in previous studies [123, 215] which was also experienced in the present work. Indeed, once the base membranes were dried, L_p decreased by about 29% and 33% and B was reduced by about 45% and 17% for base membranes Base-PA1 and Base-PA2, respectively (**Figures 4-3 and 4-4**). Base-PA3 membrane,

which had the lowest water permeability, experienced a lower L_p reduction (21%) upon drying but essentially no change in B (**Figure 4-5**). It is postulated that the above behavior could have been due to shrinkage/collapse of the relatively lower free volume in the active layer. The reduction in B and L_p due to membrane drying was partially recovered after rewetting the membranes. In various tests, after about 6 weeks of immersion in DI water, only 16% of the lost L_p was recovered and B was increased by 39% as shown, for example in **Figure 4-6**.

Table 4-1. Performance of Base-PA, SNS-PAA-PA and SW30 membranes

	Membrane [a]	*PSS* [b] (mm)	*N* [c]	Initial AA solution pH [d]	L_p [e] ($L \cdot m^{-2} \cdot h^{-1} \cdot bar^{-1}$)	*B* [f] ($L \cdot m^{-2} \cdot h^{-1}$)	Water/salt selectivity, L_p/B (bar^{-1})	R_i [g] (%)	% Change in L_p relative to base membrane [h]	% Change in *B* relative to base membrane [h]	Change in R_i (%) relative to base membrane [h]
	Base-PA1	-	-	-	3.37	0.54	6.3	98.4	-	-	-
SNS-PAA-PA1	1	10	1	1.8	3.56	0.41	8.8	98.8	+6%	-25%	+0.4
	2	10	2	1.8	3.35	0.34	9.8	99.0	-1%	-36%	+0.6
	3	10	3	1.8	3.20	0.40	8.0	98.9	-5%	-26%	+0.4
	4	5	2	1.8	3.24	0.38	8.5	98.9	-4%	-29%	+0.5
	5	15	2	1.8	3.47	0.52	6.7	98.5	+3%	-4%	+0.1
	6	10	2	6	2.59	0.26	9.8	99.2	-23%	-51%	+0.8
	7	10	2	8	2.57	0.29	8.9	99.1	-24%	-46%	+0.7
	Base-PA2	-	-	-	2.40	0.21	11.4	99.4	-	-	-
SNS-PAA-PA2	8	10	1	1.8	1.87	0.29	6.5	99.2	-22%	+37%	-0.2
	9	10	2	1.8	1.84	0.20	9.2	99.4	-23%	-5%	0.0
	10	10	3	1.8	1.79	0.25	7.0	99.3	-26%	+21%	-0.1
	11	5	2	1.8	1.83	0.26	6.9	99.2	-24%	+25%	-0.2
	12	15	2	1.8	2.03	0.30	6.7	99.1	-16%	+44%	-0.3
	13	10	2	6	1.69	0.15	11.4	99.6	-30%	-30%	+0.2
	14	10	2	8	1.44	0.18	8.1	99.5	-40%	-16%	+0.1
	Base-PA3	-	-	-	2.25	0.15	15.0	99.6	-	-	-
SNS-PAA-PA3	15	10	1	1.8	2.60	0.41	6.4	98.8	+15%	+173%	-0.8
	16	10	2	1.8	2.53	0.31	8.2	99.1	+12%	+104%	-0.5
	17	10	3	1.8	2.51	0.41	6.1	98.8	+12%	+174%	-0.8
	18	15	2	1.8	2.50	0.33	7.5	99.0	+11%	+121%	-0.5
	19	15	2	1.8	2.85	0.51	5.6	98.5	+27%	+239%	-1.0
	20	10	2	6	1.82	0.29	6.3	99.2	-19%	+92%	-0.4
	21	10	2	8	1.58	0.32	5.0	99.1	-30%	+112%	-0.5
	SW30	-	-	-	1.46	0.27	5.4	99.2	-	-	-

[a] SNS-PAA-PA1 (#1-7), SNS-PAA-PA2 (#8-14) and SNS-PAA-PA3 (#15-21) are the surface nano-structured (SNS) membranes synthesized from base membranes Base-PA1, Base-PA2 and Base-PA3 membranes, respectively; [b] *PSS* is the separation distance between the APP plasma source and substrate surface; [c] *N* is the number of sequential plasma scans varied between 1-3 to control the plasma exposure period. Each scan was performed at a speed of 100 mm/s; [d] Graft polymerization was carried out at 70°C for 1 h with AA monomer solutions of initial monomer concentration of 20 vol%, which had a pH of ~1.8. The pH of AA solutions was raised to 6 and 8 by addition of NaOH; [e] Water permeability coefficient (L_p) was determined with DI water at 20.0 ± 0.2°C; [f] Salt (NaCl) permeability coefficient (*B*) was determined with a saline feed water (32 g/L NaCl) at 20.0 ± 0.2°C; [g] Intrinsic salt rejection ($R_i = 1\text{-}C_p/C_m$) was evaluated at $J_{v,sw}$ = 34 $L \cdot m^{-2} \cdot h^{-1}$ with a saline feed water (32 g/L NaCl) at 20.0 ± 0.2°C; [h] Percentage changes in L_p and *B* relative to base membrane defined as $\Delta L_p = \left[\left(L_p^{SNS\text{-}PAA\text{-}PA} - L_p^{Base\text{-}PA}\right)\Big/ L_p^{Base\text{-}PA}\right] \cdot 100$ and $\Delta B = \left[\left(B^{SNS\text{-}PAA\text{-}PA} - B^{Base\text{-}PA}\right)\Big/ B^{Base\text{-}PA}\right] \cdot 100$, respectively, and change in the percentage intrinsic salt rejection defined as $\Delta R_i = R_i^{SNS\text{-}PAA\text{-}PA} - R_i^{Base\text{-}PA}$.

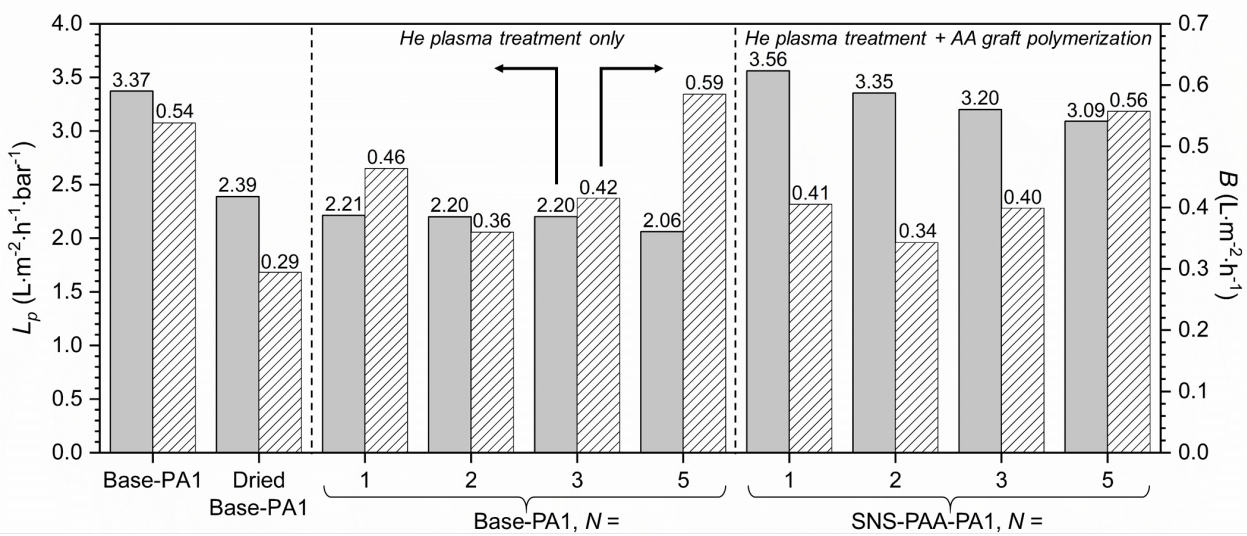

Figure 4-3. The effect of number of sequential He APP scans (N) on water (L_p) and salt (B) permeability coefficients for Base-PA1 before and after drying, after surface activation and post AA graft polymerization ($[M]_0$ = 20 vol%, pH 1.8, for 1 h reaction at 70°C). (Note: plasma treatment was performed at a *PSS* distance of 10 mm.)

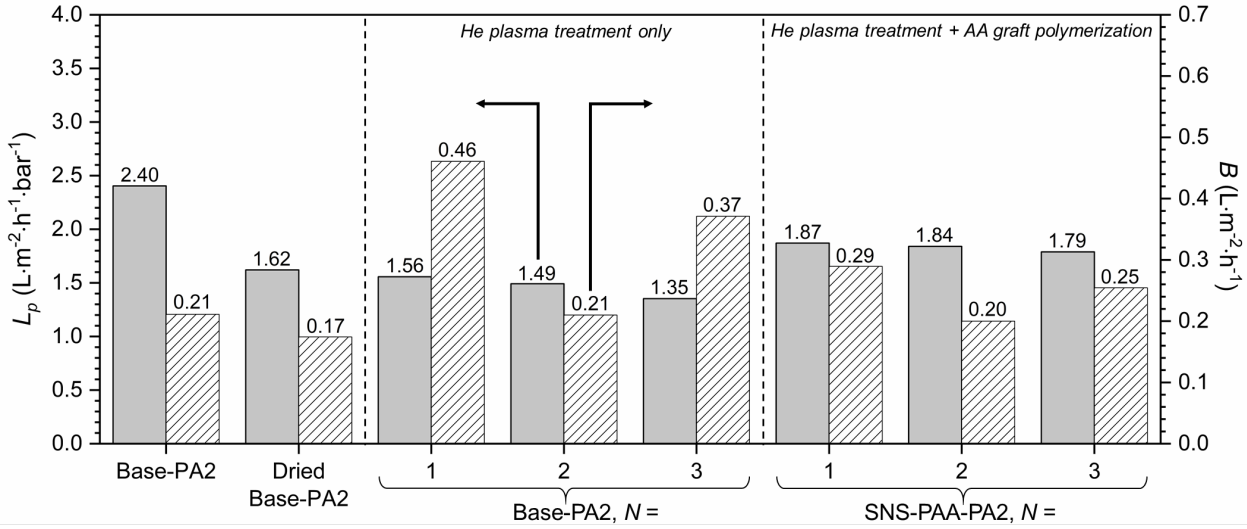

Figure 4-4. The effect of He APP surface activation at different numbers of sequential surface scans (N), at a *PSS* distance of 10 mm, on water (L_p) and salt (B) permeability coefficients for Base-PA2 before and after drying, after He APP surface treatment and post AA graft polymerized ($[M]_0$ = 20 vol%, initial monomer solution pH 1.8, reaction period of 1 h at 70°C).

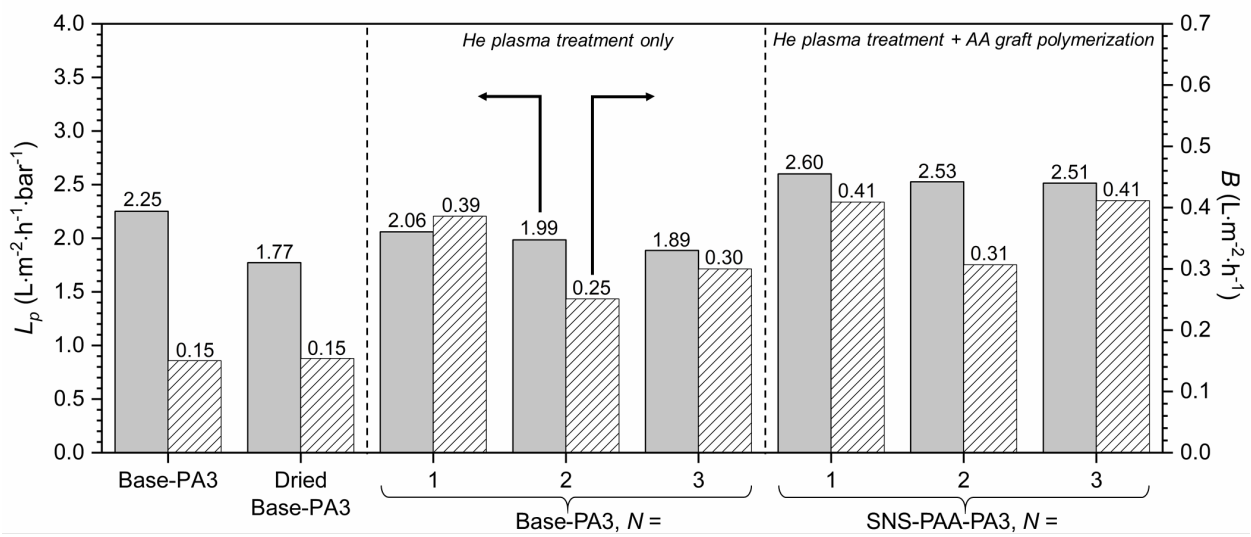

Figure 4-5. The effect of He APP surface activation at different numbers of sequential surface scans (N), at a *PSS* distance of 10 mm, on water (L_p) and salt (B) permeability coefficients for Base-PA3 before and after drying, after He APP surface treatment and post AA graft polymerized ($[M]_0$ = 20 vol%, initial monomer solution pH 1.8, reaction period of 1 h at 70°C).

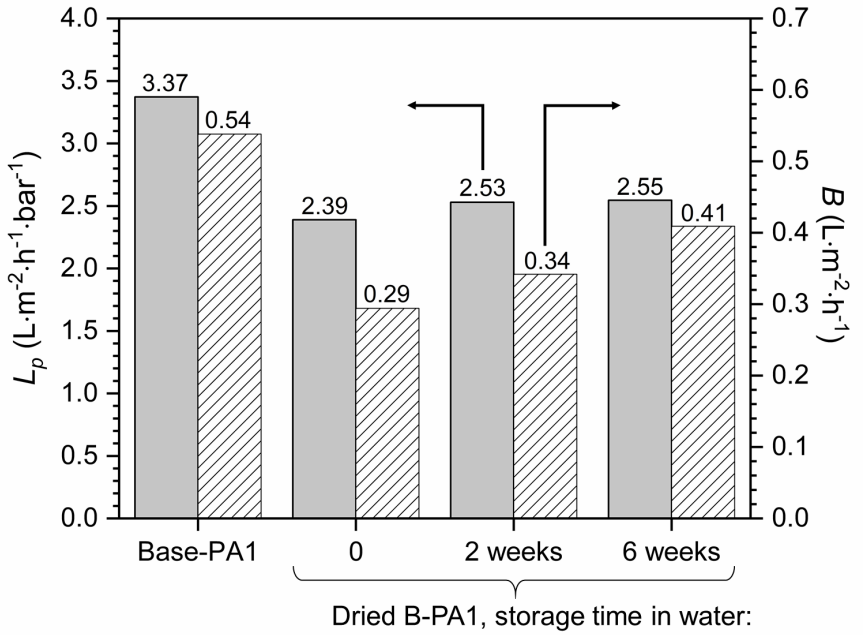

Figure 4-6. Water (L_p) and salt (B) permeability coefficients for Base-PA1 in its native state, immediately after drying with nitrogen and after storage in DI water for 2 and 6 weeks.

Plasma surface treatment of the dried membranes altered their performance (prior to graft AA polymerization) as shown in **Figures 4-3, 4-4, and 4-5** for base membranes Base-PA1, Base-PA2 and Base-PA3, respectively. As illustrated in **Figure 4-3** for base membrane Base-PA1, surface APP treatment at three or five sequential scans led to a higher *B* by 15% and 63%, respectively, whereas L_p was reduced by ≤ 6%, relative to two sequential APP scans. Similarly, surface treatment at single or triple APP scans led to increased *B*, relative to two sequential scans, by 77 – 119% and 20 – 54%, for base membranes Base-PA2 and Base-PA3, respectively; however, L_p reduction was less pronounced (≤ 9%) (**Figures 4-4 and 4-5**). It is also noted that two sequential APP surface scans of the three base membranes, at a *PSS* distance below (5 mm) and above (15 mm) the optimal distance (10 mm), resulted in higher *B* values (i.e., implying greater salt passage tendency) by 14 – 28%, 10 – 21% and 4 – 12% for Base-PA1, Base-PA2, and Base-PA3, respectively, relative to at a *PSS* distance of 10 mm, while L_p was reduced (≤ 7%) or increased (≤ 17%) at *PSS* distances of 5 mm and 15 mm, respectively (**Figures 4-7, 4-8, and 4-9**). It is emphasized that alteration of membrane performance upon APP surface treatment was not permanent. For example, after storage in DI water for a period of 6 weeks, the *B* and L_p values for the plasma treated Base-PA1 membrane (two sequential He APP scans at PSS distance of 10 mm) increased by 39% and 4%, respectively (**Figure 4-10**).

4.3.2 Performance of SNS-PAA-PA membranes

The impact of plasma surface treatment conditions on the resulting performance of SNS-PAA-PA membranes was assessed for membrane graft polymerization at an initial AA monomer concentration ($[M]_0$) of 20 vol% at 70°C for 1 h. As reported in earlier work [197, 198], at the above reaction conditions the tethered PAA chains form primarily by graft polymerization

("grafting from") rather than polymer grafting ("grafting to"). Upon AA graft polymerization, it was feasible to attain, depending on the PA base membrane performance characteristics (i.e., water and salt permeability coefficients) and plasma treatment conditions, SNS-PAA-PA membrane performance of a *B* value that was higher or lower than that of the base membranes. The lowest *B* value was attained for SNS-PAA-PA membranes derived from graft polymerization of the base PA membranes surface which was activated via two sequential APP scans at a 10 mm *PSS* distance (**Figures 4-3, 4-4, 4-5, 4-7, 4-8, and 4-9**). For example, as shown in **Figures 4-3 and 4-7**, the *B* value for the SNS-PAA-PA1 membranes was reduced by 4 – 36% relative to the Base-PA1 membrane (B = 0.54 $L \cdot m^{-2} \cdot h^{-1}$), with the exception of the case of surface activation via five sequential APP scans. However, it is noted that upon AA graft polymerization of membranes Base-PA2 and Base-PA3, which had corresponding *B* values of 61% and 72% lower than membrane Base-PA1, the *B* value for the resulting SNS-PAA-PA membranes was at about the same level or up to ~3.4 folds greater than that of the base membranes (**Figures 4-4, 4-5, 4-8, and 4-9**). It is postulated that the above behavior could have potentially resulted from plasma etching which for the tight base membranes (which have less free volume within the active layer) would lead to a greater impact on the membrane permselectivity, relative to looser membranes.

Performance of the SNS-PAA-PA membranes, derived by surface plasma activation and subsequent AA graft polymerization, can be tuned to decrease *B* (i.e., increased salt rejection) and restore or increase the hydraulic permeability relative to both the base and plasma treated membranes. Also, it is emphasized that the SNS-PAA-PA membranes were stable (i.e., with respect to both L_p and *B*) after prolonged storage in DI water as observed in the present work in performance testing over a period of up to 1 year.

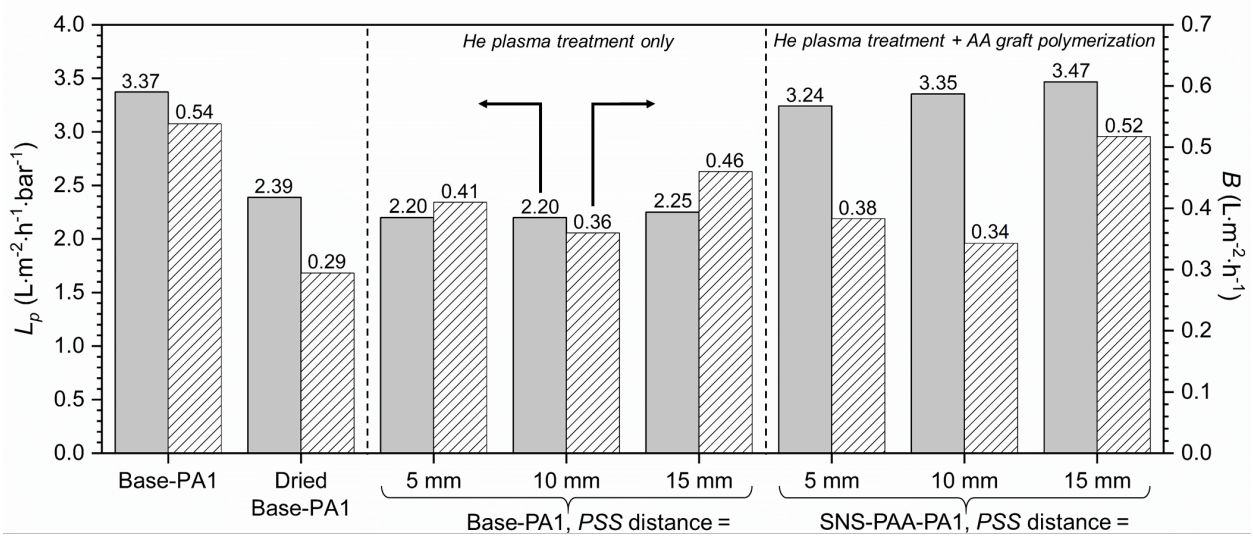

Figure 4-7. The effect of He APP membrane surface treatment at different plasma source-surface separation (*PSS*) distances on resulting water (L_p) and salt (B) permeability coefficients for Base-PA1 before and after drying, after surface activation (two sequential APP scans) and post AA graft polymerization ($[M]_0$ = 20 vol%, pH 1.8, 1 h reaction time at 70°C).

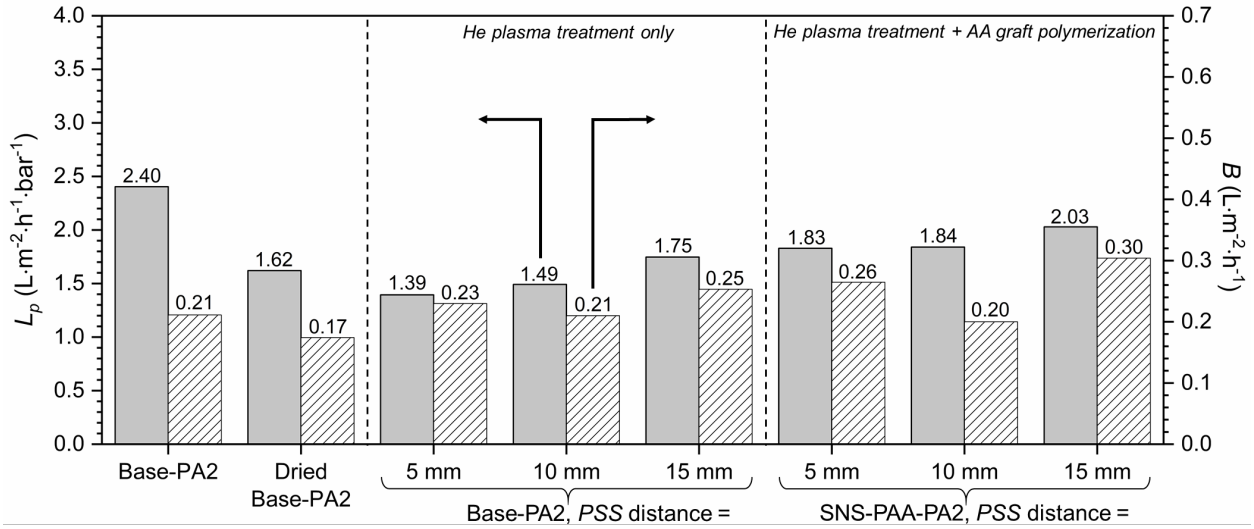

Figure 4-8. The effect of He APP surface activation at different *PSS* distances (at two sequential scans) on water (L_p) and salt (B) permeability coefficients for Base-PA2 before and after drying, after He APP surface treatment and post AA graft polymerized ($[M]_0$ = 20 vol%, initial monomer solution pH 1.8, reaction period of 1 h at 70°C).

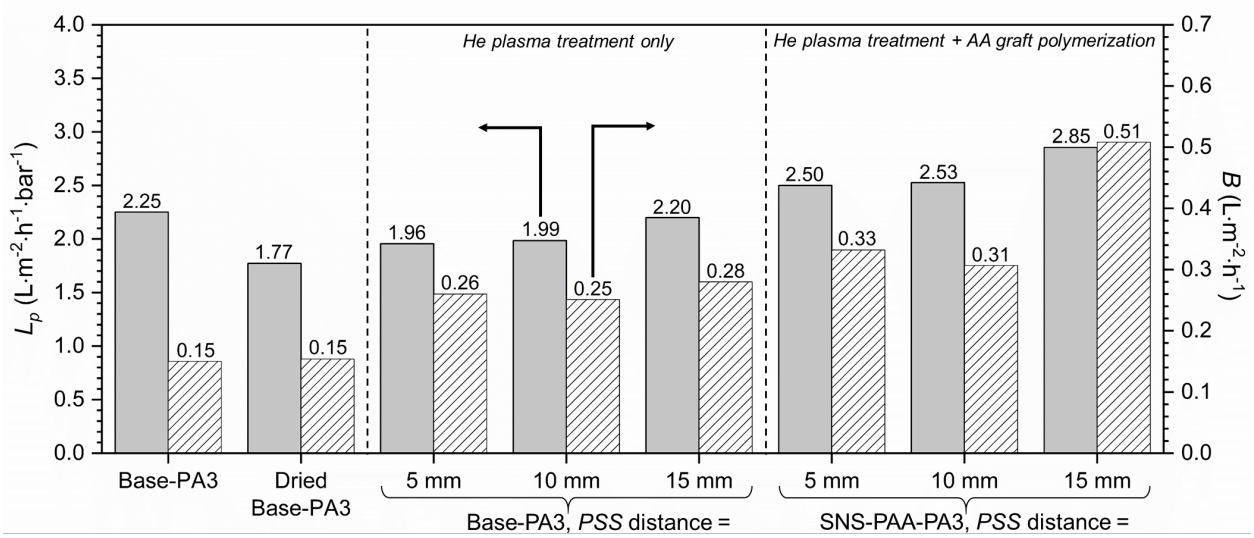

Figure 4-9. The effect of He APP surface activation at different *PSS* distances (at two sequential scans) on water (L_p) and salt (B) permeability coefficients for Base-PA3 before and after drying, after He APP surface treatment and post AA graft polymerized ($[M]_0$ = 20 vol%, initial monomer solution pH 1.8, reaction period of 1 h at 70°C).

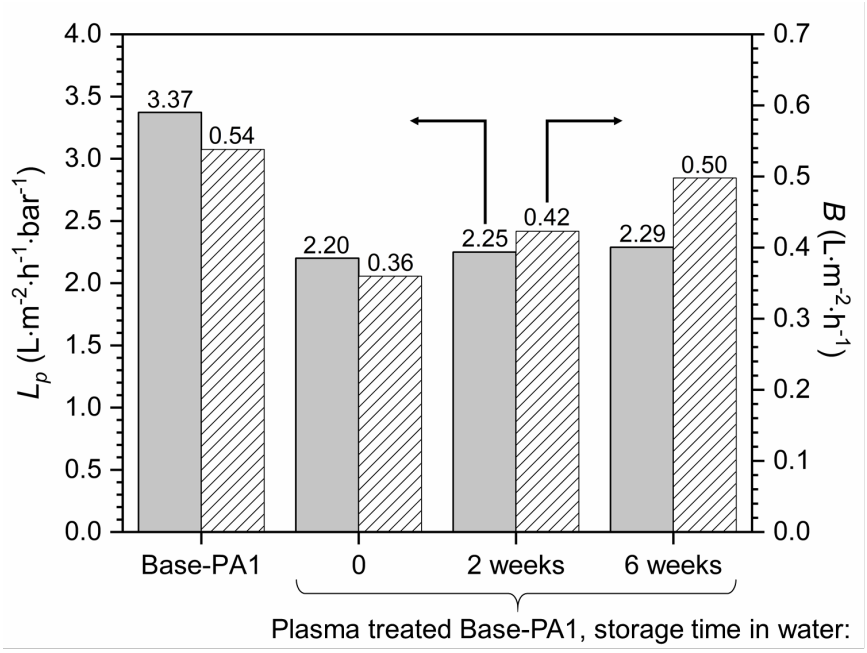

Figure 4-10. Water (L_p) and salt (B) permeability coefficients for Base-PA1 plasma treated, via two sequential He APP scans at a *PSS* distance of 10 mm, after 2 and 6 weeks of storage in DI water.

4.3.3 Effect of graft polymerization conditions on SNS-PAA-PA membrane performance

4.3.3.1 Effect of initial monomer concentration on SNS-PAA-PA membrane performance

The tethered PAA chain length (and thus the PAA layer thickness) are expected to increase as the initial monomer concentration ($[M]_0$) is increased [197]. Therefore, one should expect that both the membrane *B*-value and permeability coefficient (L_p) will be affected by $[M]_0$. Accordingly, an evaluation was carried out in which SNS-PAA-PA1 membranes were produced (using the Base-PA1 BWRO base membrane) over $[M]_0$ range of 10 – 30 vol% (**Figure 4-11**). The above monomer concentration range was reported to be effective for AA graft polymerization with the optimal value at about $[M]_0$ = 20 vol% [197, 198]. As $[M]_0$ increased from 10 vol% to 20 vol% (**Figure 4-11**) 26% reduction in *B* was observed for the SNS-PAA-PA1 membrane, while the change in L_p was negligible (2%). It is noted that, at excessive initial monomer concentrations early chain termination can take place (due to increased rates of chain transfer and combination of two propagating chains), thus resulting in reduced grafted layer thickness [124]. The above is postulated to be the cause for the significant *B* increase (82%) as membrane SNS-PAA-PA1 synthesis was at an initial monomer concentration that increased from 20 vol% to 30 vol% (**Figure 4-11**). These results illustrate that initial monomer concentration adjustment provides an additional control measure for tuning membrane salt permeability while maintaining its water permeability at the level of the base BWRO (i.e., Base-PA1) membrane (within approximately ± 2%).

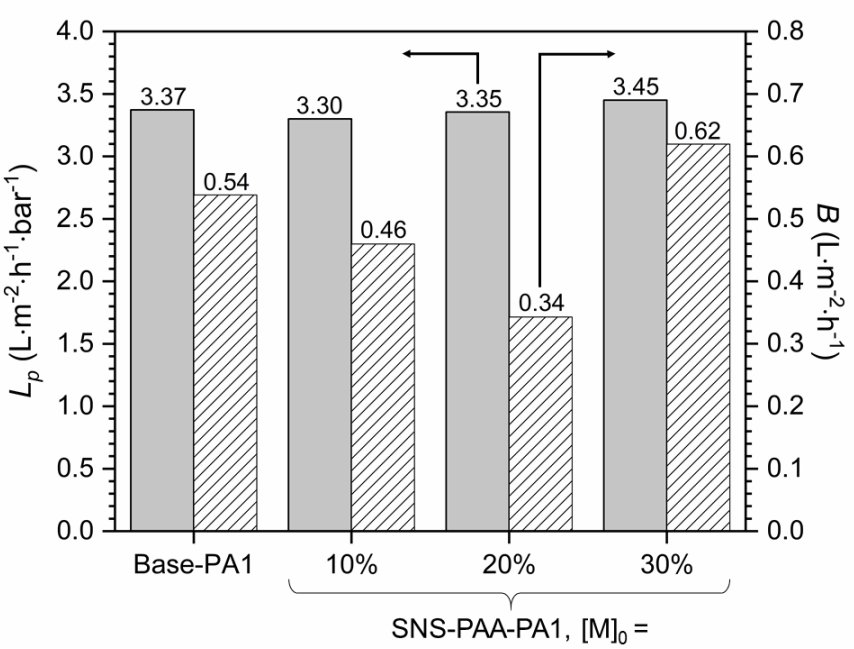

Figure 4-11. The effect of initial monomer concentration ($[M]_0$ = 10 – 30 vol%) on the water (L_p) and salt (B) permeability coefficients for SNS-PAA-PA1 membranes derived from Base-PA1, via He APP surface activation (two sequential scans and *PSS* distance of 10 mm) followed by AA graft polymerization for 1 h at 70°C and initial monomer solution pH of ~1.7 – 2.0.

4.3.3.2 Effect of initial monomer solution pH on the SNS-PAA-PA membrane performance

The pH at which AA graft polymerization is carried out can impact the AA monomer reactivity and thus the resulting tethered PAA chain lengths and SNS-PAA-PA membrane performance (**Section 4.2.2**). Indeed, AA graft polymerization which was carried out for an initial monomer solution pH range of 1.8 – 13 and $[M]_o$ = 20 vol% (following He APP treatment via 2 sequential scans at *PSS* distance of 10 mm), resulted in the lowest B (over the pH levels tested) for the SNS-PAA-PA membranes synthesized at pH of 6. For example, the SNS-PAA-PA1 membranes, which were derived via graft polymerization at pH 1.8 and 13 had L_p and B values higher by 8 – 29% and 31 – 58%, respectively, relative to the membrane prepared at pH 6 (**Figure 4-12**). SNS-PAA-PA membranes derived from base membranes Base-PA2 and Base-PA3 similarly demonstrated increased L_p and B when graft polymerization was at pH above and below

6 (**Figures 4-13 and 4-14**). Higher B and L_p values, for membrane A graft polymerization above pH 6, is postulated to be the result of a lower graft polymerization rate (**Section 4.2.2**). On the other hand, one should expect that below pH 6 monomer reactivity should increase [206], thus lowering the L_p and B for the resulting SNS-PAA-PA membranes. It is also known that acid treatment of RO membranes can lead to a rise of L_p and B [216] as observed with decreasing monomer solution pH below pH 6 (**Figures 4-12, 4-13, and 4-14**). However, it appears that AA graft polymerization, at the current reaction conditions, had a lesser impact on L_p and B relative to membrane "loosening" under the acidic reaction conditions.

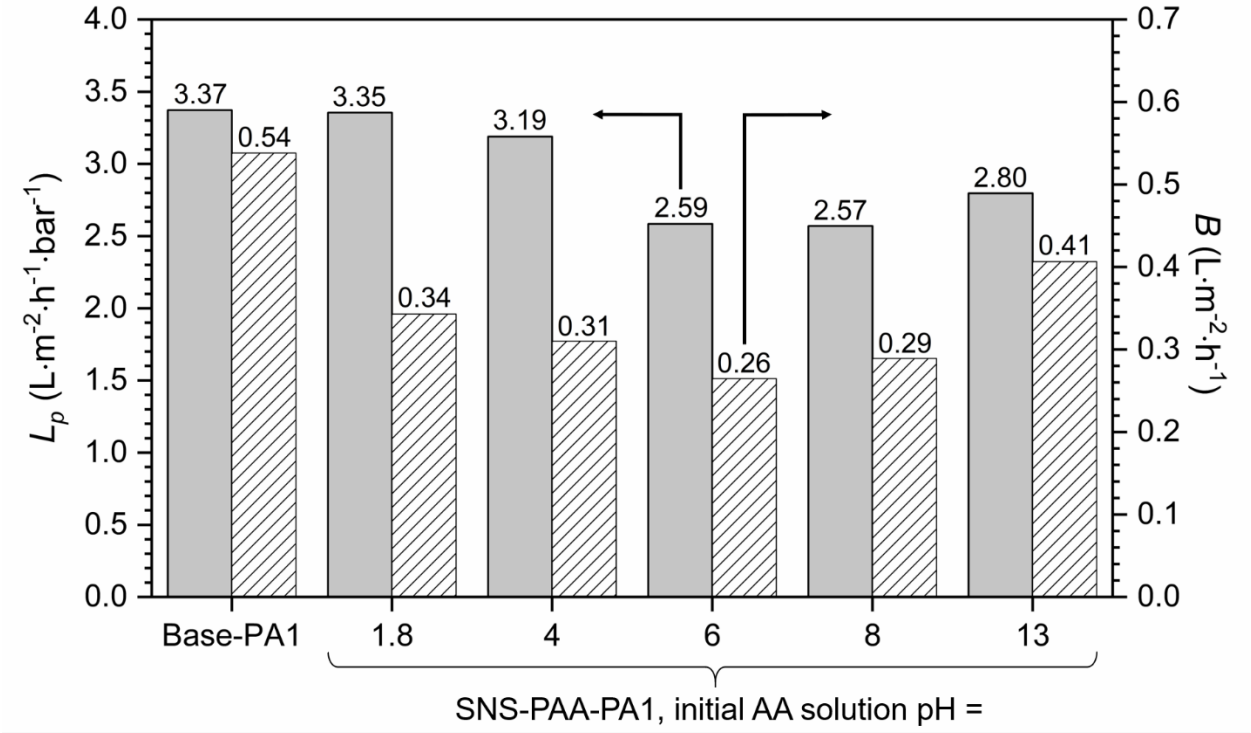

Figure 4-12. The effect of graft polymerization monomer solution initial pH (1.8 – 13) on water (L_p) and salt (B) permeability coefficients of SNS-PAA-PA1 membranes derived from Base-PA1 via He APP surface activation (two sequential scans at *PSS* distance of 10 mm) followed by AA graft polymerization at $[M]_0 = 20$ vol% for 1 h at 70°C.

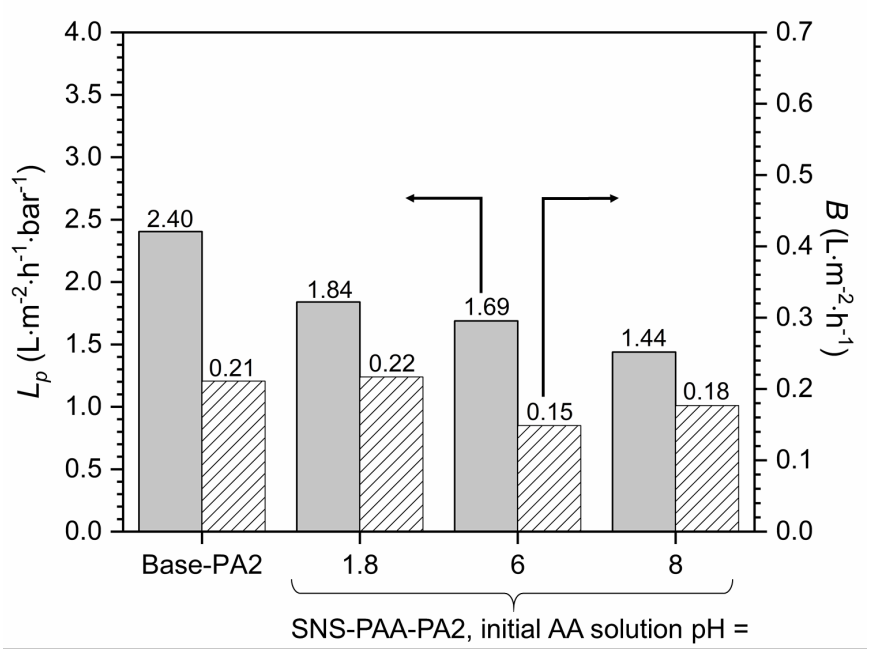

Figure 4-13. The effect of graft polymerization monomer solution initial pH (1.8 – 13) on water (L_p) and salt (B) permeability coefficients of SNS-PAA-PA2 membranes derived from Base-PA2 via He APP surface activation (two sequential scans at *PSS* distance of 10 mm) followed by AA graft polymerization at $[M]_0 = 20$ vol% for 1 h at 70°C.

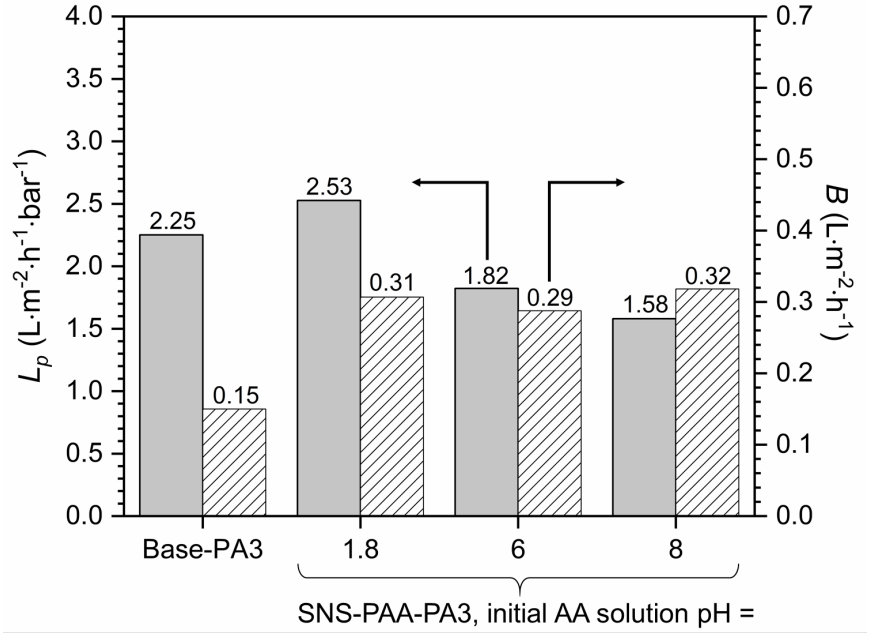

Figure 4-14. The effect of graft polymerization monomer solution initial pH (1.8 – 13) on water (L_p) and salt (B) permeability coefficients of SNS-PAA-PA3 membranes derived from Base-PA3 via He APP surface activation (two sequential scans at *PSS* distance of 10 mm) followed by AA graft polymerization at $[M]_0 = 20$ vol% for 1 h at 70°C.

4.3.4 Impact of selected base membrane on the derived SNS-PAA-PA membrane performance

Previous studies suggested that surface grafted polymers plugging of "porous" spots (which may be inherent defects or free volume sites) in the PA active layer surface is the major contribution to reduced water permeance and salt passage of such modified membranes [217, 218]. Therefore, it is expected that achieving a measurable increase of salt retention (or lower *B*), due to a surface tethered polymer layer, would be more feasible to attain for a looser PA base membrane [98, 218]. On the other hand, the relative reduction in membrane permeability, upon AA graft polymerization, should be higher for a lower permeability (i.e., tighter) relative to a looser base membrane. Therefore, a wide range of SNS-PAA-PA membrane performance (i.e., L_p and *B*) can be attained as illustrated in **Table 4-1**, depending on the selected base membrane performance for given plasma surface activation and graft polymerization conditions. For example, AA graft polymerization onto the most permeable of the base membranes (i.e., Base-PA1) resulted in the most significant reduction in *B* (up to 51%), while L_p was reduced to a lesser degree (1 – 24%) or even increased in some cases (up to 6%) (SNS-PAA-PA1, #1-7 in **Figure 4-15** and **Table 4-1**). In contrast, tethered PAA layers synthesized onto the tighter Base-PA2 membrane reduced *B* by 16 – 30%, but with a greater L_p reduction (30 – 40%) when graft polymerization was carried out at elevated pH of 6 and 8 (SNS-PAA-PA2, #13-14 in **Figure 4-15** and **Table 4-1**; see also **Section 4.3.3**). For the base membrane of the lowest L_p and *B* (Base-PA3), at the same graft polymerization conditions as for base membranes Base-PA1 and Base-PA2, the resulting SNS-PAA-PA3 membrane *B*-value increased significantly (92 – 239%) in all cases. On the other hand, L_p increased (11 – 27%) or decreased (up to 30%), relative to the base membrane (SNS-PAA-PA3, #15-21 in **Figure 4-15** and **Table 1**).

The above results suggest that while graft polymerization enables lowering the *B* value of a base membrane that already has a relatively low *B*, the trade-off is a lower water permeability coefficient. On the other hand, utilizing a sufficiently loose base membrane should allow one to increase selectivity (within a reasonable range) without sacrificing water permeability. For example, SNS-PAA-PA1 membrane #2 (**Figure 4-15** and **Table 4-1**) had a *B* value that was 37% lower relative to its base membrane, while the change in L_p was negligible (1%). However, using the same Base-PA1 membrane to attain a comparable *B* level to that of SW30 membrane, via graft polymerization, required a greater reduction in *B* (51%) and also L_p reduction (23%) relative to the base membrane. It is noted that SNS-PAA-PA1 membrane #6 (**Figure 4-15** and **Table 4-1**) had an essentially similar *B* value (0.26 $L \cdot m^{-2} \cdot h^{-1}$) and intrinsic salt rejection (R_i = 99.2%; **Figure 4-16**) as that of SW30 (i.e., within experimental uncertainty), while having nearly a factor of two greater L_p; hence, demonstrating that the tethered PAA layer can transform BWRO to SWRO membrane performance. It is noted that in order to achieve further *B* reduction relative to SW30, a tighter PA base membrane (i.e., Base-PA2) can be used. For example, synthesizing a tethered PAA layer (at the same plasma surface activation and grafting conditions as the SNS-PAA-PA1 membrane #6 (**Table 4-1**) onto the Base-PA2 membrane resulted in a SNS-PAA-PA2 membrane (#13 in **Figure 4-15** and **Table 4-1**) having 44% lower *B* and ~1.5 fold greater L_p relative to the SW30 membrane.

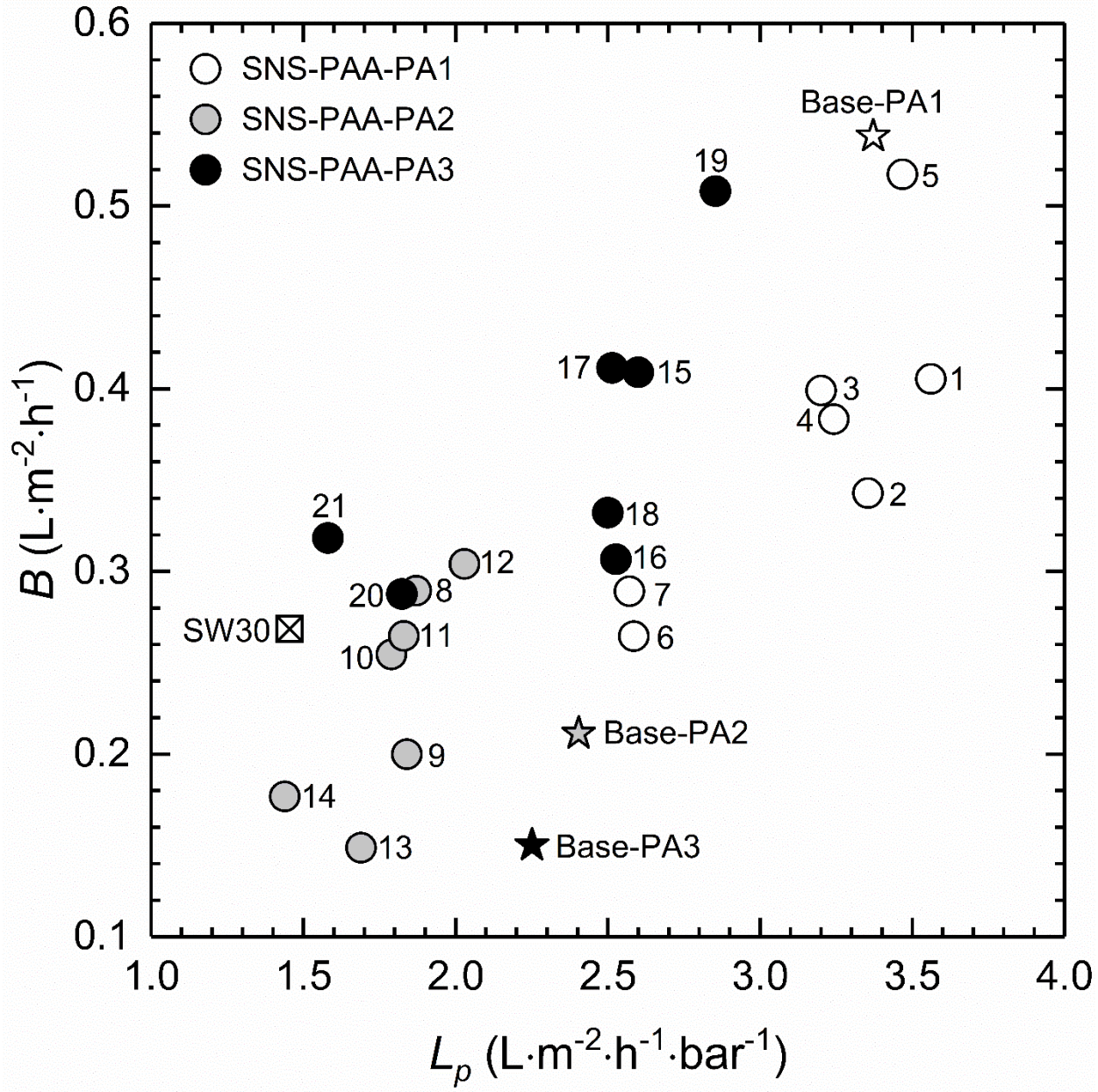

Figure 4-15. Water (L_p) and salt (B) permeability coefficients for SNS-PAA-PA membranes (SNS-PAA-PA1: #1-7, SNS-PAA-PA2: #8-14 and SNS-PAA-PA3: #15-21), the respective base polyamide membranes (Base-PA1, Base-PA2 and Base-PA3) and SW30 membrane (Dow Filmtec). (Note: The numbers next to data points correspond to the synthesis conditions listed in **Table 4-1**.)

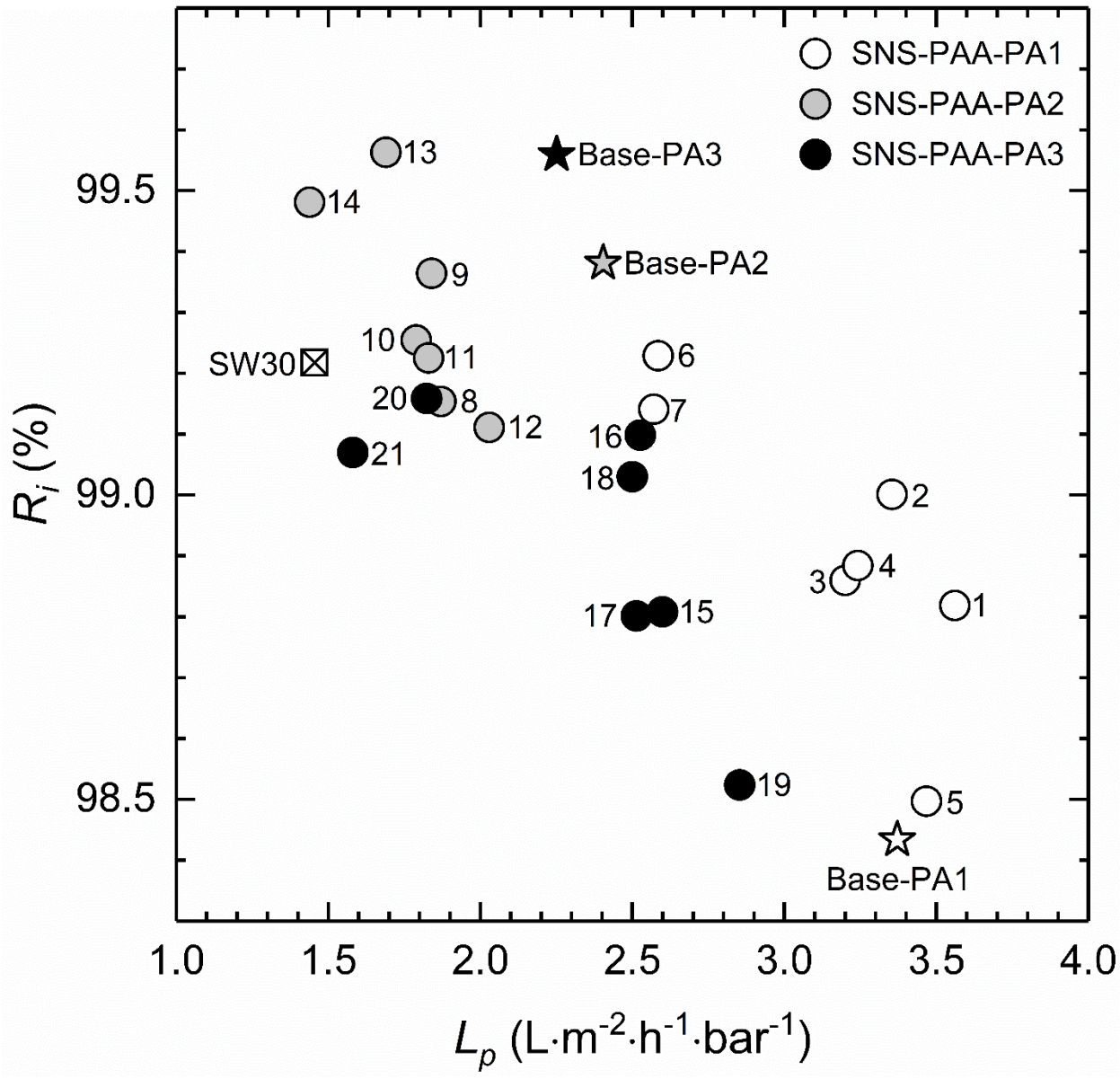

Figure 4-16. Water permeability coefficient (L_p) and intrinsic salt rejection (R_i) for SNS-PAA-PA membranes (SNS-PAA-PA1: #1-7, SNS-PAA-PA2: #8-14 and SNS-PAA-PA3: #15-21), the respective base polyamide membranes (Base-PA1, Base-PA2 and Base-PA3) and SW30 membrane (Dow FilmTec). (Note: The numbers next to data points correspond to the synthesis conditions listed in **Table 4-1**.)

4.3.5 SNS-PAA-PA membrane water/salt selectivity

Evaluation of RO membranes in terms of water permeability and water/salt selectivity has been proposed in some studies as an alternate approach of assessing progress in improving

membrane performance [45, 219]. However, for the PA TFC membranes accurate measurements of the PA active layer thickness are required (for determination of water permeability) which is a challenging task [55]. Thus, comparison of RO membrane performance is often made in terms of the correlation of water permeability coefficient (L_p is the active layer thickness normalized water permeability) with the water/salt selectivity (evaluated as L_p/B ratio) [128, 219, 220]. It is stressed that membrane water and salt permeability coefficients can vary with the specific test conditions (e.g., permeate flux, cross flow velocity, pressure, salinity, pH and temperature, and membrane conditioning) [221], which poses a challenge for comparison of membrane performance data from different studies. Nonetheless, such a comparison can be useful for assessing membrane performance if compared at the same test conditions as was the case in the present work.

As shown in the water/salt selectivity (i.e., L_p/B ratio) plot of **Figure 4-17**, increased selectivity was only achieved for the SNS-PAA-PA1 membranes for which the reduction in B was greater than the relative reduction in L_p (reduction relative to the base Base-PA1 membrane). The tethered PAA layer significantly improved the selectivity of base membrane Base-PA1 by up to 56%, with a relatively low reduction ($\leq$ 5%) of water permeability coefficient (SNS-PAA-PA1 membranes #1-5). In contrast, for the SNS-PAA-PA2 membranes the water/salt selectivity decreased by up to 41%, while higher L_p reduction, in the range of 16 – 40%, resulted relative to the Base-PA2 base membrane. It is noted that selectivity of the SNS-PAA-PA2 membranes was at best maintained at the same level as its base PA membrane; this is due to the tethered PAA layers leading to an equal or greater reduction in L_p relative to the reduction in B. The SNS-PAA-PA3 membranes suffered a significant selectivity loss as the tethered PAA layer led to increased B (by up to 249%) relative to change in L_p (decreased or increased by up to 19% and 27%, respectively).

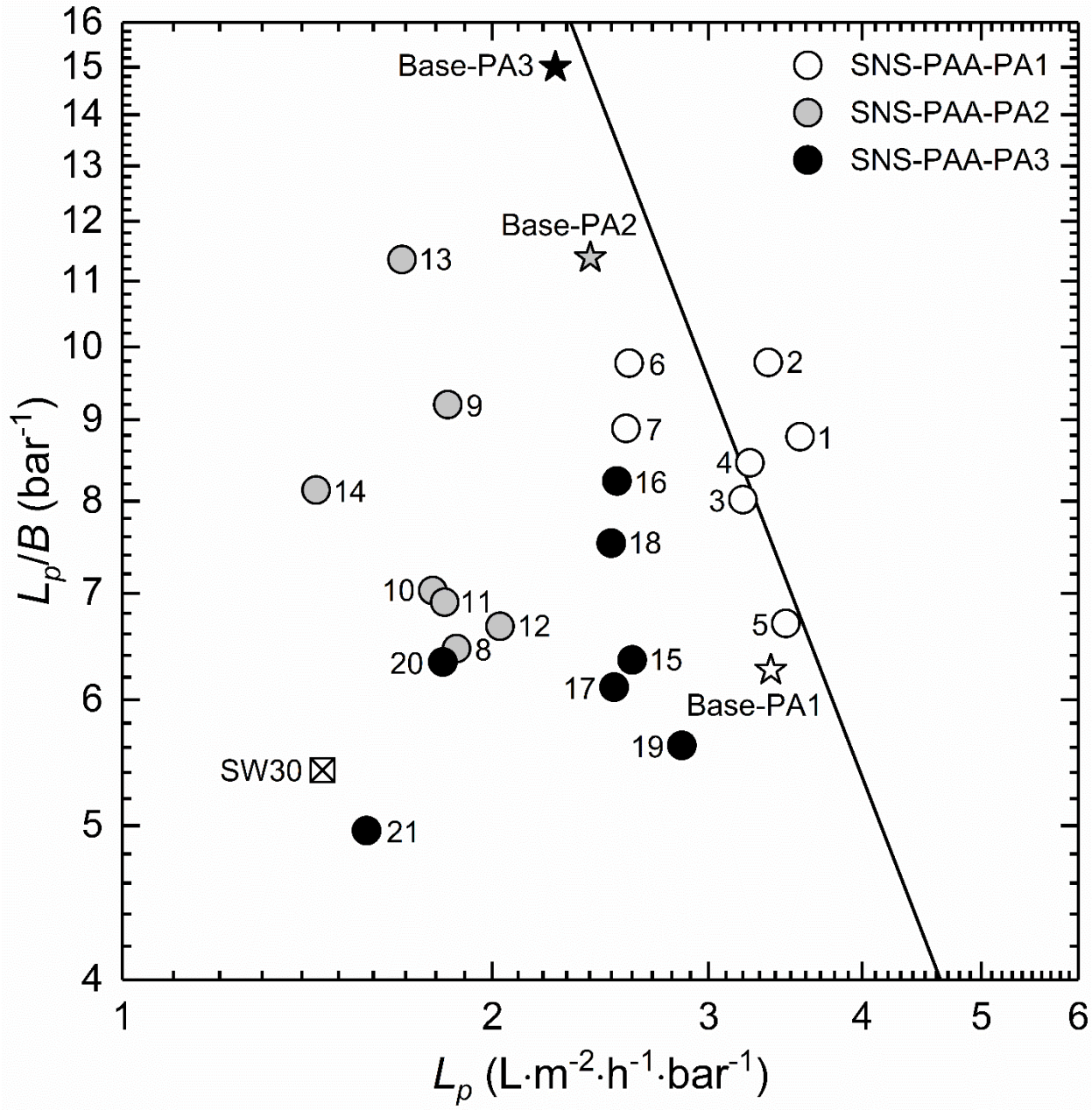

Figure 4-17. Water permeability coefficient (L_p) and water/salt selectivity (i.e., L_p/B ratio) for polyamide base membranes Base-PA1, Base-PA2 and Base-PA3 and the respective SNS-PAA-PA membranes (SNS-PAA-PA1: #1-7, SNS-PAA-PA2: #8-14 and SNS-PAA-PA3: #15-21), and the Dow Filmtec SW30 membrane. The numbers next to data points correspond to the tethered PAA layers synthesized at the conditions specified in **Table 4-1**. The black solid line is the trade-off relationship of selectivity-permeability for TFC membranes proposed in [128].

It is apparent that performance of SNS-PAA-PA membranes was consistent with the expected permeability-selectivity trade-off relationship proposed for TFC membranes [128] (displayed as a solid line in **Figure 4-17**)**.** This trade-off line (**Figure 4-17**) was proposed based on an empirical relationship between L_p and B for the SW30 membrane and hand-cast PA TFC membranes that were subjected to chlorine and alkaline treatments [14, 128]. However, the ranges of L_p and B achieved for SNS-PAA-PA membranes (**Figure 4-17**) demonstrated an ability to fine-tune RO membrane performance by tethered PAA layers synthesized through adjustments of the plasma treatment and graft polymerization conditions. As shown in **Figure 4-17**, one can derive membranes of a given selectivity but with a range of water permeability, or membranes of a given permeability with a range of selectivity.

The qualitative trends of the impact of plasma surface activation conditions (i.e., exposure time as governed by the number of scans and *PSS* distance) and graft polymerization conditions (i.e., $[M]_0$ and pH) on SNS-PAA-PA membrane performance are summarized in **Table 4-2**. A minimum B value exists with respect to all of the above parameters, while L_p can increase with increasing plasma exposure time and decreasing *PSS* distance. L_p also marginally increases with increasing initial monomer concentration and displays a minimum value with respect to initial monomer solution pH. Clearly, the path to tuning membrane performance will be specific to the APP surface activation and graft polymerization system. However, it should be expected that guidelines with respect to plasma exposure time and initial monomer concentration should be similar irrespective of the particular plasma source and vinyl monomer type.

Table 4-2. Summary of membrane surface nano-structuring conditions and impact on L_p and B of the SNS-PAA-PA membranes

Membrane surface structuring condition	L_p	B	Relevant figure(s)
Plasma exposure time	Decreases with increasing exposure time	A minimum exists	Figures 4-3, 4-4, and 4-5
Plasma source-surface-separation (*PSS*) distance	Decreases with decreasing *PSS* distance	A minimum exists	Figures 4-7, 4-8, and 4-9
Initial monomer concentration ($[M]_0$)	Marginally increases with increasing $[M]_0$	A minimum exists	Figure 4-11
Initial monomer solution pH	A minimum exists	A minimum exists	Figures 4-12, 4-13, and 4-14

4.4 Conclusions

The upgrade of thin film composite (TFC) polyamide membranes to SWRO membrane performance, via atmospheric pressure plasma (APP) induced graft polymerization (APPIGP) of acrylic acid, was investigated over a range of APP surface treatment and graft polymerization conditions. The resulting surface nano-structured (SNS) membranes featured a tethered poly(acrylic acid) (PAA) layer that altered the base BWRO membrane water (L_p) and salt (B) permeability coefficients. Base membrane exposure to plasma led to a decrease L_p for all cases, while B either increased or decreased. Upon graft polymerization, both the membrane B and L_p increased or even decreased depending on the number of surface scans and plasma source-surface separation distance in the surface activation step. Upon graft polymerization the resulting SNS membrane could be tuned to emerge with B value maintained at the level or reduced below that which is suitable for SWRO membrane performance, but with L_p level higher than SW30. Increased water/salt selectivity for the SNS-PAA-PA membranes was achieved when synthesizing

the tethered PAA layer using base PA membranes of a sufficiently high L_p and B, provided that the attained reduction in B water greater relative to the reduction in L_p.

The present work demonstrated that the same membrane surface structuring approach, which is beneficial for reducing membrane fouling propensity, can be utilized to tune membrane permeability and selectivity to the extent that one can achieve membranes that overcome the permselectivity trade-off. The highest membrane performance, imparted by the tethered PAA layer, was for membrane #13 (**Figures 4-15**) derived from the base SWRO membrane (Base-PA2) which had a B value 45% lower than for SW30, but with a L_p value 16% higher than for SW30. The highest performing SNS-PAA-PA1 membrane had a similar B and 78% greater L_p than SW30. However, the SNS-PAA-PA1 (#2) membrane, which was upgraded from the BWRO Base-PA1 membrane had performance beyond the presumed limit indicated by the trade-off line.

Chapter 5. Tethered Polyacrylic Acid Layers for Membrane Fouling Mitigation and Effective Membrane Cleaning

5.1 Overview

In RO seawater desalination, in which the membrane surface is exposed to high salinity water, surface tethered hydrophilic polymers such as poly(acrylic acid) (PAA) are expected to collapse due to charge screening effect [18, 19], while swelling in low salinity water. The collapsed chains are expected to have limited chain mobility, and the contribution of partial chain mobility to membrane fouling reduction is expected to be lower in seawater desalination applications than for lower salinity feed water (brackish water) environment. However, one would expect that swelling of the collapsed tethered PAA layer upon exposure to fresh water could be utilized to improve membrane cleaning efficiency of seawater RO membranes.

Accordingly, the present study focused on evaluating membrane fouling mitigation and membrane cleaning effectiveness achieved by surface tethered poly(acrylic acid) (PAA) layers in high salinity feed waters (i.e., 32-35 g/L NaCl aqueous solution). Ultrafiltration (UF) and reverse osmosis (RO) membrane fouling tests were conducted for tethered PAA layers synthesized polysulfone (PSf) ultrafiltration UF and polyamide (PA) thin film composite (TFC) RO membranes using alginic acid and bovine serum albumin, respectively. Alginic and bovine serum albumin are model foulants typically employed to assess potential membrane fouling in seawater desalination and associated membrane feed pretreatment [222, 223]. Following the series of UF and RO flux decline fouling tests, membrane cleaning efficacy afforded by the tethered PAA layer was evaluated by membrane flushing with deionized water.

5.2 Experimental

5.2.1 Materials and reagents

PSf flat sheet membranes having 100 kDa and 10 kDa molecular weight cutoff (MWCO) and a PA TFC flat sheet membrane (i.e., Base-PA1 in **Chapter 4**) were supplied by Toray Membrane USA Inc. (Poway, CA). A commercial spiral wound element (Dow Filmtec SW30-2514) was used to extract flat sheet SW30 membrane coupons. Helium (99.99%) and oxygen (99.999%) gases for plasma generation and treatment and nitrogen (99.5%) gas, used for drying membrane surfaces and purging monomer solutions during graft polymerization, were obtained from Airgas (Los Angeles, CA). Acrylic acid (99%), alginic acid sodium salt from brown algae, and bovine serum albumin (≥ 98%) were obtained from Sigma-Aldrich (St. Louis, MO), and sodium chloride (≥ 99.0%) and sodium hydroxide (50% w/w; Fisher Scientific, Chino, CA), which were used for preparing a saline solution and adjusting solution pH, were obtained from Fisher Scientific (Chino, CA). Solution pH was measured with an Oakton pH 110 meter (Oakton Instruments, Vernon Hills, IL). The pH of ultra-pure deionized (DI) water, which was produced using a Milli-Q filtration system (Millipore Corp., San Jose, CA), was ~6 (likely due to the presence of dissolved CO_2).

5.2.2 Synthesis of SNS-PAA-PSf UF membrane

A flat sheet PSf membrane of 100 kDa MWCO was used as a base membrane for synthesizing tethered PAA layers. The flat sheet membrane was cut into circular disks (1.75 inch in diameter) to prepare sample coupon samples, which were kept in DI water for at least a day prior to use. Prior to plasma surface activation, the membrane coupon samples were rinsed with DI water and dried with nitrogen. Plasma surface activation and graft polymerization were carried

out using the same protocols described in **Section 3.2.3**. The PSf membrane surface activation was performed by exposing the dried membrane coupon surface to the helium and oxygen (He/O_2) plasma for 15 seconds. Subsequent AA graft polymerization was carried out at initial AA monomer concentrations ($[M]_0$) of 20 vol% for 1 h at 70°C. Following graft polymerization, the PAA grafted PSf membrane samples (SNS-PAA-PSf) were rinsed with DI water and kept immersed in DI water (typically no longer than a day) prior to the ultrafiltration fouling tests.

5.2.3 Synthesis of SNS-PAA-PA RO membrane

The SNS-PAA-PA membrane selected for the fouling study was synthesized at the same condition as SNS-PAA-PA1 (#6 in **Table 4-1**; **Chapter 4**) following the plasma surface activation and graft polymerization protocols described in **Section 4.2.2**. Surface activation of the base PA membrane coupon (Base-PA1) was performed at 2 sequential plasma scans at *PSS* distance of 10 mm. Subsequently, AA graft polymerization was performed at $[M]_0$ = 20 vol% at 70°C and initial monomer solution pH of 6 for 1 h. Graft polymerization was terminated by quenching the reaction with a copious volume of DI water after removing the coupons from the reaction mixture, followed by additional DI water rinsing. The SNS-PAA-PA membrane coupons were then stored in DI water prior to the fouling test.

5.2.4 Membrane surface characterization

The presence of surface grafted PAA chains on the PA membrane surface was confirmed by X-ray photo electron spectroscopy (XPS) performed using a Kratos Axis Ultra DLD (Kratos Analytical Ltd., Manchester, UK) with a monochromatic Al Kα source. Survey spectra were obtained at a pass energy of 160 eV, and XPS data analysis was performed using CasaXPS

software (i.e., computer-aided surface analysis for X-ray photoelectron spectroscopy, Casa Software Ltd., UK).

Surface topography was assessed via atomic force microscopy (AFM) using a Bruker Dimension Icon Scanning Probe Microscope with a NanoScope V Controller (Bruker, Santa Barbara, CA). AFM images were obtained in PeakForce Tapping mode (at a loading force of 10 nN), under air using a ScanAsyst-Air probe with a nominal spring constant of 0.4 N/m. Cantilever deflection sensitivity was determined from the slope of the noncompliance region of the cantilever deflection vs. the piezo displacement curve obtained using a silicon substrate in contact mode. Spring constants of the cantilevers were determined via the thermal tuning method at room temperature (~20°C) [162]. AFM scans of 10 μm x 10 μm areas were obtained at 1024 x 1024-pixel resolution and 0.5 Hz scan rate. The distribution of feature heights for each sample was scaled to the lowest height as determined by the AFM tip. The root-mean-square surface roughness (R_{rms}) was then quantified based on AFM feature height data as, $R_{rms} = \sqrt{\sum_i \left(Z_i - Z_{avg}\right)^2 \Big/ N}$, where Z_i is the i^{th} sample height, N is total number of samples and Z_{avg} is the mean feature height.

Finally, surface wettability of the SNS-PAA-PA1, Base-PA1, and SW30 membranes that were utilized in the BSA fouling tests was assessed by contact angle measurements via an automated system (DSA20; KRÜSS GmbH, Germany). Sessile drop water contact angle measurements were taken within 2 s following placement of a 2 μL DI water drop onto the sample surface at room temperature (~22°C). The reported contact angles represent averaged values based on measurements at 5 locations for each sample.

5.2.5 UF fouling tests

Membrane fouling propensity and cleaning effectiveness of the PAA grafted PSf membrane (SNS-PAA-PSf) relative to a PSf membrane of 10 kDa MWCO (10 kDa-PSf) were evaluated in dead-end filtration mode using a stirred cell system. The stirred cell had a volume capacity of 50 mL (MilliporeSigma, Burlington, MA) and an effective membrane filtration area of 13.4 cm^2. Feed solution was delivered to the membrane cell from an 800 mL reservoir pressurized with nitrogen. Filtration experiments were performed at 20°C and the permeate flow rate was measured using a Sensirion SLI-1000 liquid flow meter (Sensirion AG, Switzerland). The clean membrane permeability ($L_{p,0}$) was determined using DI water following membrane compaction with DI water at 345 kPa (~50 psi) for 3 hours to reach a stabilized permeate flux. Subsequently, a challenge fouling test (to simulate severe organic fouling) was conducted with a high concentration (1 g/L) alginic acid solution in high salinity water (35 g/L NaCl) at pH 8 (typical pH range of seawater is ~7.5 – 8.5) [4, 222]. A fouling test was also conducted at pH 6, which is the lower limit of the typical pH range of natural waters [224, 225]. Filtration tests were carried out at an initial permeate flux of 22 $L \cdot m^{-2} \cdot h^{-1}$ (~13 $gallon \cdot ft^{-2} \cdot day^{-1}$), which is within the typical permeate flux range for UF seawater pretreatment [222], set by adjusting the feed pressure. Alginic acid concentration in the permeate was quantified by UV absorbance at 220 nm [226]. The observed alginic acid rejection was determined from $R_o = 1 - C_p / C_f$, where C_p and C_f are the alginic acid concentrations in the permeate and feed solutions, respectively. Following a 2 h filtration period, backwash was performed with DI water at twice the initial permeate flux (i.e., 44 $L \cdot m^{-2} \cdot h^{-1}$) for 2 minutes. Following backwash, the membrane permeability (L_p) was determined with DI water.

5.2.6 RO fouling tests

Membrane fouling propensity and cleaning effectiveness of the SNS-PAA-PA membranes, relative to the base membranes and the SW30 membrane, were evaluated using the PFRO system (**Appendix B.1**) with bovine serum albumin (BSA) as a model foulant. Fouling stress tests were performed with an aqueous 32 g/L NaCl solution of relatively high BSA concentration (1 g/L) at pH 6.4 and 20.0 ± 0.2°C. The PFRO channel cross flow velocity was set to 11 cm/s to establish a high initial *CP* modulus (estimated to be ~30 based on correlation provided in [227]) in order to accelerate the fouling rate over the test period. Prior to the fouling tests, the membranes were compacted and the clean membrane permeability ($L_{p,0}$) was determined with DI water, following determination of salt permeability coefficient (B) as described in **Section 4.2.3**. Subsequently the fouling tests were all conducted with the saline BSA solution, at the same initial permeate flux of 25.5 ± 0.5 $L \cdot m^{-2} \cdot h^{-1}$, over a period of 24 hours. Membrane cleaning efficiency was assessed, after each fouling test, by cleaning of the membranes with DI water (at ~22°C) at a cross flow velocity of 17 cm/s and transmembrane pressure of 1.4 MPa (~200 psi) for a period of 30 minutes. Following membrane cleaning, the water L_p was again determined with DI water.

5.3 Results and Discussion

5.3.1 UF membrane fouling and backwash efficiency

In order to assess if the tethered PAA layers can indeed improve the release of foulants from a SNS-PAA-PSf membrane, UF flux decline fouling tests were conducted using alginic acid as a model foulant in an aqueous 35 g/L NaCl solution (i.e., mimicking seawater salinity). The SNS-PAA-PSf membrane had an alginic acid retention of ~81 – 82% and water permeability coefficient of 22.1 – 24.1 $L \cdot m^{-2} \cdot h^{-1} \cdot bar^{-1}$ (**Table 5-1**). This membrane was evaluated relative to a

PSf membrane (10kDa-PSf) that had similar alginic acid retention of ~77 – 82% and permeability of 21.9 – 22.6 $L \cdot m^{-2} \cdot h^{-1} \cdot bar^{-1}$ (**Table 5-1**). The fouling tests were carried out with a feed solution at an elevated alginic acid concentration (1 g/L) as a stress test at pH of 6 and 8. At the above pH range, carboxylic acid (the dominant functional group of both alginic acid and PAA having pK_a of ~3 – 5 [228-230]), is expected to be nearly fully deprotonated and hence negatively charged [231]. However, the charges on alginic and PAA layers are expected to be screened at high salinity [232]. Therefore, the degree of association of alginic acid with the tethered PAA layer would be expected to be similar to that with the native PSf membrane. Indeed, flux decline for the SNS-PAA-PSf membrane at pH 6 and 8, after filtration for 2 h, was only about 2% lower than the flux decline observed for the 10kDa-PSf membrane (**Figures 5-1 and 5-2**).

Table 5-1. UF membrane performance.

Membrane	$L_{p,0}$ ($L \cdot m^{-2} \cdot h^{-1} \cdot bar^{-1}$)	Alginic acid rejection (%)†	$L_p/L_{p,0}$‡ Alginic acid solution pH	
			pH 6	pH 8
SNS-PAA-PSf	22.1 – 24.1	80.7 – 81.7	0.90	1.00
10kDa-PSf	21.9 – 22.6	77.3 – 81.9	0.49	0.68

†Alginic acid rejection was quantified by UV absorbance at 220 nm using feed solution of 1 g/L alginic acid in DI water containing 35 g/L NaCl at pH 6 and 8.
‡Permeability recovery ratio determined after performing a membrane backwash for 2 min at permeate flux of ~44 $L \cdot m^{-2} \cdot h^{-1}$.

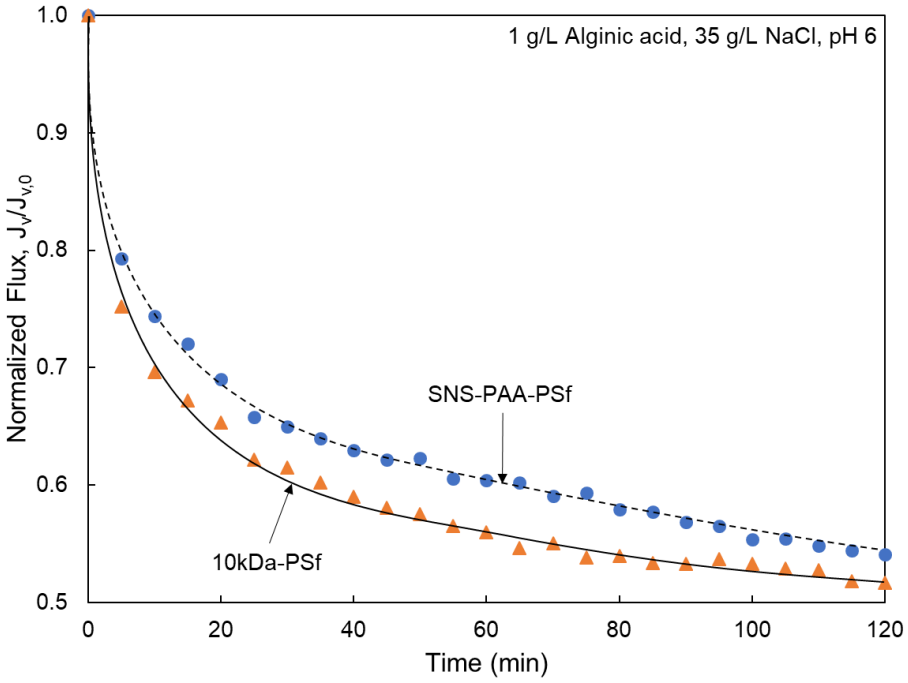

Figure 5-1. Permeate flux decline during filtration of saline alginic acid solution at pH 6 with (a) SNS-PAA-PSf membrane (synthesized at $[M]_0$ = 20 vol% for 1 h post PSf surface activation with He/O_2 plasma) and (b) 10kDa-PSf membrane.

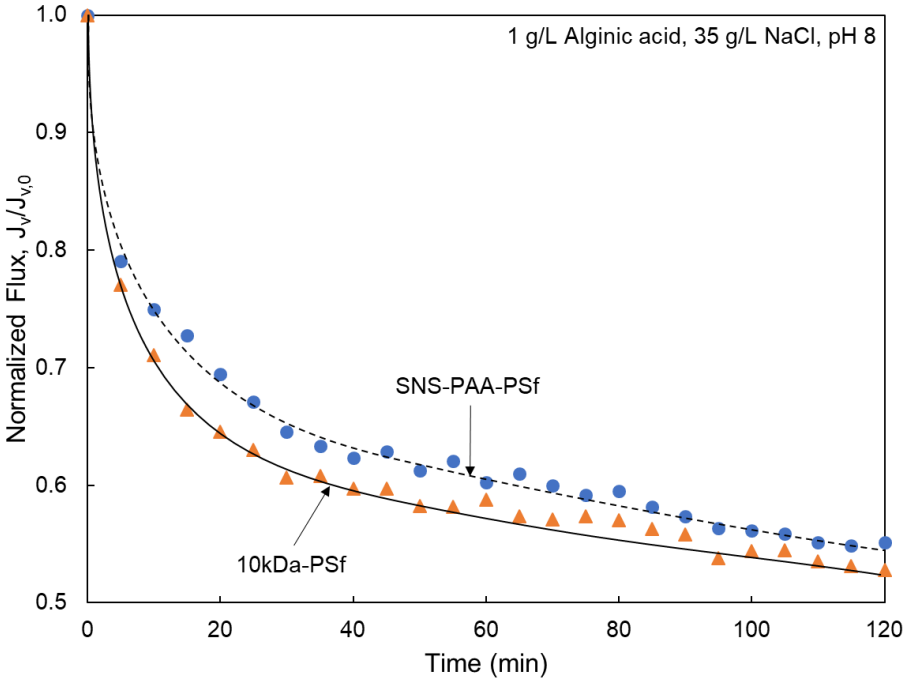

Figure 5-2. Permeate flux decline during filtration of saline alginic acid solution at pH 8 with (a) SNS-PAA-PSf membrane (synthesized at $[M]_0$ = 20 vol% for 1 h post PSf surface activation with He/O_2 plasma) and (b) 10kDa-PSf membrane.

The above results indicate that the tethered PAA layer did not provide significant improvement in terms of membrane fouling resistance. However, upon backwash with DI water, permeability recovery post fouling of the SNS-PAA-PSf membrane by alginic acid at pH of 6 and 8 was ~90% and 100%, respectively (**Table 5-1**). In contrast, backwashing the 10kDa-PSf membrane after fouling with alginic acid at pH 6 and 8, led to permeability recovery of merely ~49% and ~68%, respectively. The greater effectiveness of permeability recovery for the fouled SNS-PAA-PSf membrane upon DI water backwash is attributed to swelling of the PAA chains. These chains are somewhat collapsed (against the PSf surface) in the salt solution and it is conjectured that their swelling in DI water, as indicated via the AFM-FS analysis (**Section 3.3.4**), assists in removal of the foulant layer. It is noted that the difference in captive bubble (CB) contact angle for the PAA surfaces in the salt solution and DI water (**Table 3-6** in **Section 3.3.5**) was marginal (~2%) at pH 8 and ~31% higher for the latter at pH 6, but the surfaces remained hydrophilic (i.e., CB contact angle ~29 – 38°).

The above results suggest that the tethered PAA layer, whose swelling is affected by feed water salinity, could impart unique cleaning function to membranes used for filtration of high salinity water. Once the collapsed layer of tethered chains is fouled, exposure of the membrane surface to low salinity water should swell the chains and aid in removal of the foulant layer. While the above results are encouraging, additional studies are needed over a wider range of foulants in order to evaluate the effectiveness of membrane cleaning imparted by tethered hydrophilic polymer chains.

5.3.2 RO membrane fouling and cleaning efficiency

Reduced fouling (organic and biological) and mineral scaling propensities, as well as increased membrane cleaning effectiveness, for SNS-PA membranes with tethered hydrophilic

polymer layers, have been previously demonstrated via laboratory tests using laboratory PFRO systems [15-17]. Therefore, it is expected that the present SNS-PAA-PA membranes would display similar behavior. This was indeed confirmed via a simple fouling test for a SNS-PAA-PA1 membrane (#6 in **Table 4-1**; **Chapter 4**) which had a similar B (0.26 $L \cdot m^{-2} \cdot h^{-1}$) and a higher L_p relative to SW30 (**Figure 5-3**). As illustrated in **Figure 5-3**, filtration of the BSA solution (in an aqueous 32 g/L NaCl at pH 6.4, over 24 hours) resulted in the greatest flux reduction for the SW30 membrane (49%), followed by 27% and 10% for the Base-PA1 and SNS-PAA-PA1 membranes, respectively. Flushing the fouled membranes with DI water provided the highest L_p recovery (94%) for the SNS-PAA-PA1 membrane, followed by SW30 and Base-PA1 for which L_p recovery was 92% and 80%, respectively (**Figure 5-3**).

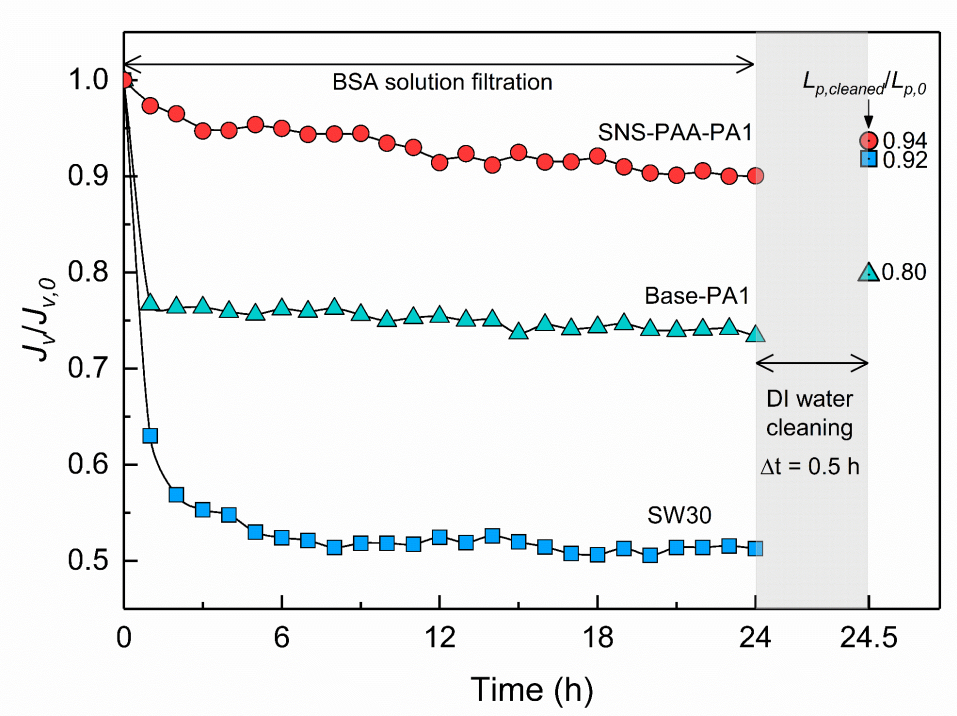

Figure 5-3. Permeate flux decline during filtration of BSA solution (salinity of 32 g/L NaCl at pH 6.4) and water permeability coefficient recovery after DI water cleaning for SNS-PAA-PA1 (#6 in **Table 4-1**), Base-PA1, and SW30 membranes.

Some studies have suggested that increased surface roughness could lead to a greater degree of fouling [233, 234]. It is noted that although the root-mean-square (RMS) surface roughness of the SNS-PAA-PA1 membrane (72.9 nm) was lower than that of SW30 (93.8 nm), it was somewhat higher than for the Base-PA1 membrane (67.6 nm) (**Figure 5-4**). Yet, the SNS-PAA-PA1 membrane exhibited the lowest degree of fouling relative to both the SW30 and Base-PA1 membranes.

Water contact angle measurements (**Table 5-2**) were lowest for the SNS-PAA-PA1 membrane (19.9°), followed by SW30 (22.4°) and Base-PA1 (28.4°) indicating that the first two membranes were of similar levels of hydrophilicity, with Base-PA1 being somewhat less hydrophilic. The above results are consistent with XPS elemental analysis indicating an increasing oxygen/carbon ratio in the same order of decreasing water contact angle. However, it is questionable whether the above differences would have accounted for the differences in the fouling tendency observed for the above three membranes. It is postulated, that the significantly lower flux decline due to BSA fouling observed for the SNS-PAA-PA1 membrane may be attributed to both screening of the underlying PA surface by the tethered PAA layer and their partial Brownian motion [16, 17]; the latter is also likely to account for the ability to restore membrane permeability via DI water cleaning [17]. Similarly, flux recovery after DI water cleaning achieved for the SW30 membrane may also be attributed to this membrane's hydrophilic poly(vinyl alcohol) surface layer [83, 214]. Finally, it is emphasized that for all of the tested membranes, membrane permeability restoration should be feasible via chemical cleaning as per the protocol described in [17].

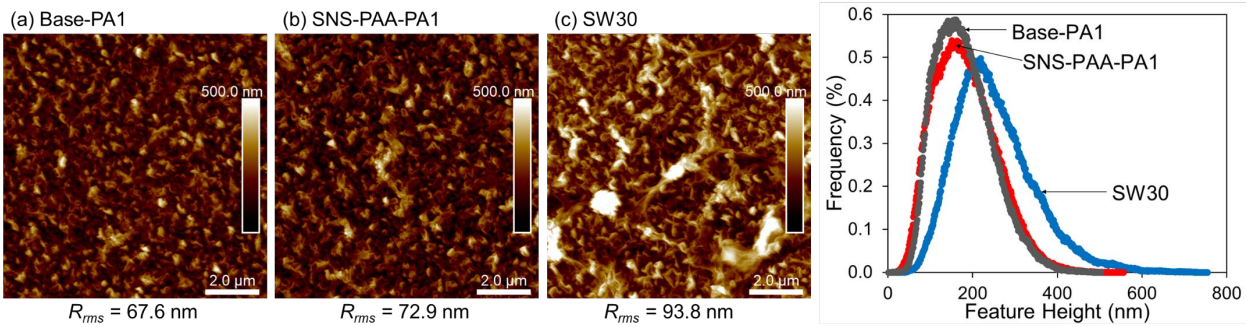

Figure 5-4. AFM 2-D images for (a) Base-PA1, (b) SNS-PAA-PA1 (#6 in **Table 4-1**), and (c) SW30 membranes (obtained as dry surfaces in air) with their respective feature height distributions.

Table 5-2. Elemental surface compositions and water contact angles for Base-PA1, SNS-PAA-PA1[†] and SW30 membranes.

Membrane	C (%)	O (%)	N (%)	O/C ratio	Water contact angle (°)
Base-PA1	77.2	11.8	11.1	0.16	28.4
SNS-PAA-PA1[†]	74.1	16.2	9.7	0.22	19.9
SW30	76.5	15.2	8.3	0.20	22.4

[†]SNS-PAA-PA1 membrane (#6 in **Table 4-1; Section 4.3.1**) was synthesized via surface activation with He plasma (*PSS* distance = 10 mm, $N = 2$) followed by AA graft polymerization carried out at $[M]_0$ = 20 vol% and initial monomer solution pH of 6 for 1 h at 70°C; Elemental surface compositions were obtained via XPS. Sessile drop contact angle measurements were taken with 2 µL DI water drops. The reported contact angles are averaged values based on measurements at 5 locations for each sample (**Section 5.2.4**).

5.4 Conclusions

Membrane fouling reduction by surface tethered PAA layers was assessed by UF and RO membrane fouling tests performed with SNS-PAA-PSf UF and SNS-PAA-PA RO membranes using alginic acid and bovine serum albumin as model foulants. It was shown that flux decline for the SNS-PAA-PSf membrane due to alginic acid fouling was only 2% lower than the flux decline observed for the native PSf membrane of a similar molecular weight cutoff and water permeability. However, cleaning (i.e., foulant removal) from the SNS-PAA-PSf surface was effective by washing with non-saline (deionized) water. Fouling stress tests with alginic acid revealed 90 – 100% restoration of SNS-PAA-PSf UF permeability relative to only 50 – 70% permeability

recovery for the native PSf membrane.

Fouling stress tests with bovine serum albumin (as a model foulant) confirmed fouling reduction and increased SNS-PAA-PA1 membrane cleaning efficiency achievement with the tethered hydrophilic polymer layers consistent with previous studies. The SNS-PAA-PA1 membrane had lower fouling resistance than both the SWRO and the base Base-PA1 membranes and could be cleaned with a DI water flush at a level comparable to that of SW30, with a higher level of water permeability coefficient recovery of both membranes relative to the base BWRO (Base-PA1) membrane. The present study suggests that surfaces with tethered hydrophilic polymers can be effectively cleaned provided that such layers will swell when exposed to a suitable cleaning solvent.

Chapter 6. Scaled-up Membrane Surface Nano-structuring with Tethered Poly(acrylic acid) Layers

6.1 Overview

Surface modification is a popular approach for mitigating fouling of polyamide (PA) thin film composite (TFC) reverse osmosis (RO)/nanofiltration (NF) membranes. However, scalability of membrane surface modification approaches that are suitable for producing commercial-scale spiral wound elements is seldomly reported in the literature. To date, scalability of membrane surface modification has been only demonstrated for *in situ* surface modification of commercial spiral wound PA RO/NF membrane elements via redox-initiated graft polymerization [61, 218, 235-238]. In the above approach an aqueous solution of vinyl monomer (e.g., polyethylene glycol ester of methacrylate (PEGMA), 2-hydroxyethyl methacrylate (HEMA), glycidyl methacrylate (GMA)) containing a redox initiator pair (e.g., potassium persulfate and potassium metabisulfite) was circulated through the RO membrane modules [61, 218, 235, 236] (**Table 6-1**). It was reported that *in situ* modification of a spiral wound LPRO element, via redox-initiated graft polymerization of GMA, could improve element performance to a comparable level of a commercial BWRO membrane element. For example, it was reported that the redox-initiated graft polymerization of GMA carried out with a spiral wound LPRO element (Dow XLE) increased salt rejection (from 98% to 99.5 – 99.8%) and boric acid rejection (from 50% to 68 – 74%) but at the cost of 24 – 61% water permeability reduction relative to the base Dow XLE element (L_p^{XLE} = 4.9 $L \cdot m^{-2} \cdot h^{-1} \cdot bar^{-1}$) (element performance testing was with feed water containing 1 g/L NaCl and 5 mg/L boric acid) [61].

In another approach surface of polyamide membranes in spiral wound RO elements (Dow TW30-1812) was coated with polydopamine by contacting the membrane surfaces with dopamine

solutions through the RO modules [237, 238]. The polydopamine (PD) modified RO element was further modified by covalently attaching Jeffamine (i.e., a block copolymer consisting of poly(ethylene glycol) and poly(propylene glycol)). The resulting PD-g-Jeffamine modified element could achieve a slightly increased salt rejection (evaluated with 250 mg/L NaCl feed water) of 96.9%, but at a significantly reduced L_p (by ~53%) relative to the native TW30 element (L_p^{TW30} = 1.65 $L \cdot m^{-2} \cdot h^{-1} \cdot bar^{-1}$, R_o^{TW30} = 96.5%). A negligible L_p reduction (1%) after a 24 h filtration of a silicone surfactant/soybean oil/water mixture (includes 250 mg/L NaCl) reported for the PD-g-Jeffamine modified element was attributed to the hydrophilic poly(ethylene glycol) groups present in Jeffamine resisting surface adsorption of oily foulants. In contrast, filtration of the same surfactant/oil/water mixture over a 24 h period resulted in a significant L_p reduction (56%) for the native TW30 element. However, it is noted that the initial permeate flux for the PD-g-Jeffamine modified membrane element was ~53% lower relative to the native TW30 element; hence, the fouling propensities for the above membranes were evaluated at different initial fouling rates. Moreover, long-term stability of the polydopamine coating layer is questionable given that polydopamine leaching from the PD modified elements has been reported to occur. The above studies demonstrated that the membrane surface modifications can be performed within commercial-scale spiral wound modules. However, the membrane elements can be only modified batchwise; thus, these approaches are not suitable for implementing in the PA TFC manufacturing process.

In contrast to the above, membrane surface nano-structuring (SNS) via atmospheric pressure plasma-induced graft polymerization (APPIGP) can be easily implemented in the downstream process of PA TFC flat sheet membrane manufacturing. Therefore, the SNS-PA sheets can be produced prior to fabrication of spiral wound elements. In APPIGP, atmospheric

pressure plasma (APP) is utilized to treat membrane surfaces to generate surface active sites, followed by surface-initiated free radical graft polymerization of vinyl monomers to synthesize surface tethered polymer layers [15-17]. APP surface treatment is particularly appealing since it can, in principle, be scaled up to treat large membrane surfaces [199], unlike LPP sources that require vacuum chambers. Unlike low pressure plasma, APP is operated in ambient air, thus the plasma treatment step can be easily scaled-up to treat a large membrane surface as required for construction of spiral wound elements. Moreover, the synthesized polymer layers are covalently attached to the membrane surface and thus provide stable membrane performance over a long period of time (**Section 4.3.2**).

Table 6-1. Summary of studies that conducted membrane surface modification in spiral wound NF/RO elements.

Reference	Base spiral wound membrane element used for membrane surface modification	Membrane Surface Modification Technique
[235]	Hydranautics SWC2-2521 (SWRO)	Redox-initiated surface graft polymerization of polyethylene glycol ester of methacrylate (PEGMA) was performed by filtering a PEGMA solution containing redox initiators (potassium persulfate and potassium metabisulfite) through the base membrane element at a rate of 600 mL/min for 30 min.
[239]	Dow NF70-2540, NF90-2540, NF 200-2540, and NF270-2540 (NF)	Redox-initiated surface graft polymerization of 2-hydroxyethyl methacrylate (HEMA) was carried out by filtering a HEMA solution containing ethylene glycol dimethacrylate (cross-linker) and redox-initiator pairs (potassium persulfate and sodium or potassium metabisulfite) through the base spiral wound elements at a rate of 0.3 L/min for 15 min – 1 h.
[61]	Dow XLE-2540 (LPRO)	Redox-initiated surface graft polymerization of glycidyl methacrylate (GMA) was carried out by filtering GMA solutions containing redox initiators (sodium persulfate and potassium metabisulfite) through the base RO membrane element at 20-30°C at 15 bar and 100% recovery for 35 min. Subsequently, the modified membrane element was thoroughly rinsed with deionized water for 24 h.
[218, 236]	Hydranautics ESPA1-2521 (LPRO)	Redox-initiated surface graft polymerization of glycidyl methacrylate (GMA) was carried out by filtering a feed water containing GMA and Triton X-100 (nonionic surfactant) through the base RO membrane element at a feed pressure of 20 bar for 5 min at a crossflow velocity of 1.8 cm/s and a permeate recovery of 30-40%. Subsequently, an aqueous solution containing N'N-methylenebis(acrylamide) (cross-linker) and redox-initiators (potassium sulfate and potassium metabisulfite) were added to the

		feed water to start the membrane surface modification, which was carried out at 24°C for 30 minutes. The modified membrane element was then rinsed with deionized water for 24 h.
[237]	Dow FilmTec TW30-1812	A dopamine solution was circulated through the base membrane element at ~1 L/min using a peristaltic pump at room temperature for 30 min. Then, the element was rinsed by circulating deionized water at the same flow rate for ~1 h. Subsequently, an aqueous Jeffamine solution was circulated through the element at 50°C for 30 min, followed by deionized water circulation through the element at room temperature for 1 h to rinse the modified element.
[238]	Hydranautics SWC3	Spiral wound membrane element was filled with a dopamine solution and gently rolled back and forth to contact the active side of the membrane with the dopamine solution for 1 h during which fresh oxygen was introduced into the element every 10 min in order to polymerize dopamine. The modified element was then flushed with deionized water.

In the present study the scale-up potential of APPIGP was evaluated by fabricating large SNS-PAA-PA flat sheet membranes (30” x 24”) that are suitable for fabricating commercial scale spiral wound membrane elements (2.5” in outer diameter and 21” in length). The scaled-up synthesis of the SNS-PAA-PA membrane sheets was accomplished by utilizing an APP source mounted on an XYZ robot capable of scanning a large membrane sheet area, followed by graft polymerization in a custom-made reactor designed for the large membrane sheet. Uniformity of the SNS-PAA-PA membrane sheets, synthesized via the scaled-up membrane SNS approach, was evaluated by testing water and salt permeability coefficients of eighteen ~2” x 4” membrane coupons extracted from the 30” x 24” SNS-PAA-PA membrane sheet area. The performance of the SNS-PAA-PA membrane coupons was compared to a commercial seawater reverse osmosis (Dow SW30) flat sheet membrane coupons. Finally, the fabrication process of 2.5 x 21” spiral wound RO elements with the synthesized SNS-PA membrane sheets is described.

6.2 Experimental

6.2.1 Materials and reagents

Flat sheet polyamide based TFC membranes, supplied by Toray Membrane USA Inc. (Poway, CA), were utilized as base membranes onto which tethered PAA layers were synthesized. The synthesized SNS-PAA-PA membrane sheets were compared to flat sheet membranes extracted from a popular commercial spiral wound element for seawater desalination (Dow Filmtec SW30-2514). Helium (99.999%) gas for plasma generation and treatment and nitrogen (99.5%) gas, used for drying polyamide membrane surfaces and purging monomer solutions during graft polymerization, were obtained from Airgas (Los Angeles, CA). Acrylic acid (99%) was obtained from Sigma-Aldrich (St. Louis, MO), and sodium chloride (≥ 99.0%) and sodium hydroxide solution (50% w/w) were obtained from Fisher Scientific (Chino, CA). Solution pH was measured with an Oakton pH 110 meter (Oakton Instruments, Vernon Hills, IL). The ultra-pure deionized (DI) water was produced using a Milli-Q filtration system (Millipore Corp., San Jose, CA).

6.2.2 Base membrane sheet preparation

PA TFC brackish water reverse osmosis (BWRO) flat sheet membrane rolls that had water permeability coefficient and salt permeability coefficient of 3.0 $L \cdot m^{-2} \cdot h^{-1} \cdot bar^{-1}$ and 0.15 $L \cdot m^{-2} \cdot h^{-1}$ (evaluated following the protocol described in **Appendix B**) were supplied by Toray Membrane USA Inc. (Poway, CA) and utilized as base membranes onto which the tethered PAA layers were synthesized. Base PA membrane sheets (31” x 25” each) were freshly cut from the roll and fully immersed in DI water for a day prior to use. Following the immersion period, a given membrane sheet was mounted onto an aluminum plate (31” x 25” x 0.2”) following the protocol described in

Appendix A.3 in order to keep the membrane sheet flat during the SNS process. Subsequently, the active side of the base membrane sheet was thoroughly dried by blowing nitrogen over the membrane surface. Visual inspection was made of each membrane sheet in order to ensure that there were no apparent membrane defects (e.g., scratches, discoloration, pinholes, etc.).

6.2.3 Scaled-up plasma surface activation

Plasma surface activation of each base PA membrane sheet was accomplished with an APP system, which consisted of a plasma controller (Atomflo^{TM} 500), a coolant control module, a 3-inch linear source head (produces 79 mm x 0.4 mm beam), and a XYZ scanning robot (Surfx Technologies LLC, Redondo Beach, CA) as illustrated in **Figure 6-1**. Helium plasma, which was selected for PA surface activation, was generated at a helium flow rate of 45 L/min and radio frequency (RF) power of 150 W. The XYZ scanning robot was used to translate the plasma head over the base membrane surface at a speed of 100 mm/s. The base PA membrane surface was treated with helium plasma at a plasma source-substrate separation (*PSS*) distance of 10 mm for 2 sequential scans, which were determined to be optimal plasma treatment conditions (**Section 4.3**). The plasma treatment of 30" x 24" base membrane sheet (details provided in **Appendix A.3.3**), performed at the above treatment conditions, was accomplished in about 5 minutes per membrane sheet.

6.2.4 Scaled-up graft polymerization

6.2.2.1 Scaled-up graft polymerization system

Surface graft polymerization for the 30" x 24" base PA membrane sheets was carried out post plasma surface activation using the reactor system depicted in **Figure 6-2**. The reactor system

consisted of a high density polyethylene (HDPE) container (32” x 26” x 2), which was utilized as a vessel to carry out the graft polymerization reaction, a peristaltic pump (EW-77600-62 and EW07594-10, Cole-Parmer, Vernon Hills, IL), and an immersion circulation water bath (Cole-Parmer; Vernon Hills, IL), which were connected via segments of stainless steel pipe and Tygon tubing to form a closed loop system in which the monomer solution was circulated during graft polymerization. Two manifolds installed at short ends of the reaction vessel served for inlet and outlet of the monomer solution, which was circulated throughout the reactor system via the peristaltic pump. The reactor inlet was constructed from spray nozzle manifolds (Part # 3404K78) connected to 11 flat spray nozzles (Part # 2491K24), both purchased from McMaster-Carr (Santa Fe Springs, CA). The reactor outlet manifold was constructed with 11 segments of stainless steel 316 pipes (¼” ID) and pipe compression fittings. Temperature of the monomer solution inside the reaction vessel was kept constant at 70°C during the graft polymerization reaction period controlled by circulating the monomer solution through a coil immersed in the heated water bath and a pipe heating cable (Part #3631K22, McMaster-Carr; Santa Fe Springs, CA), which was wrapped around the stainless steel pipe line that connected ends of the reactor vessel inlet manifold. A three-way diverting valve was installed between the reactor outlet and peristaltic pump in order to introduce the monomer solution to the reactor prior to initiation of graft polymerization.

6.2.2.2 Graft polymerization procedure

Graft polymerization of acrylic acid (AA) onto the base PA membrane sheet was carried out at the optimized conditions of initial AA monomer concentration of 20 vol%, initial AA monomer solution pH 6, graft polymerization temperature of 70°C, and 1 h graft polymerization period. The above reaction conditions were shown be the most effective at reducing the membrane

salt permeability coefficient (**Chapter 4**). The above conditions were also selected since the resulting SNS-PAA-PA membrane, which was synthesized using Base-PA2 membrane was shown to have salt permeability coefficient that was lower by 45% and water permeability coefficient greater by 16% relative to a popular commercial SWRO membrane (i.e., Dow SW30) (**Chapter 4**). Detailed scale-up SNS-PAA-PA membrane synthesis procedures are provided in **Appendix A.3**.

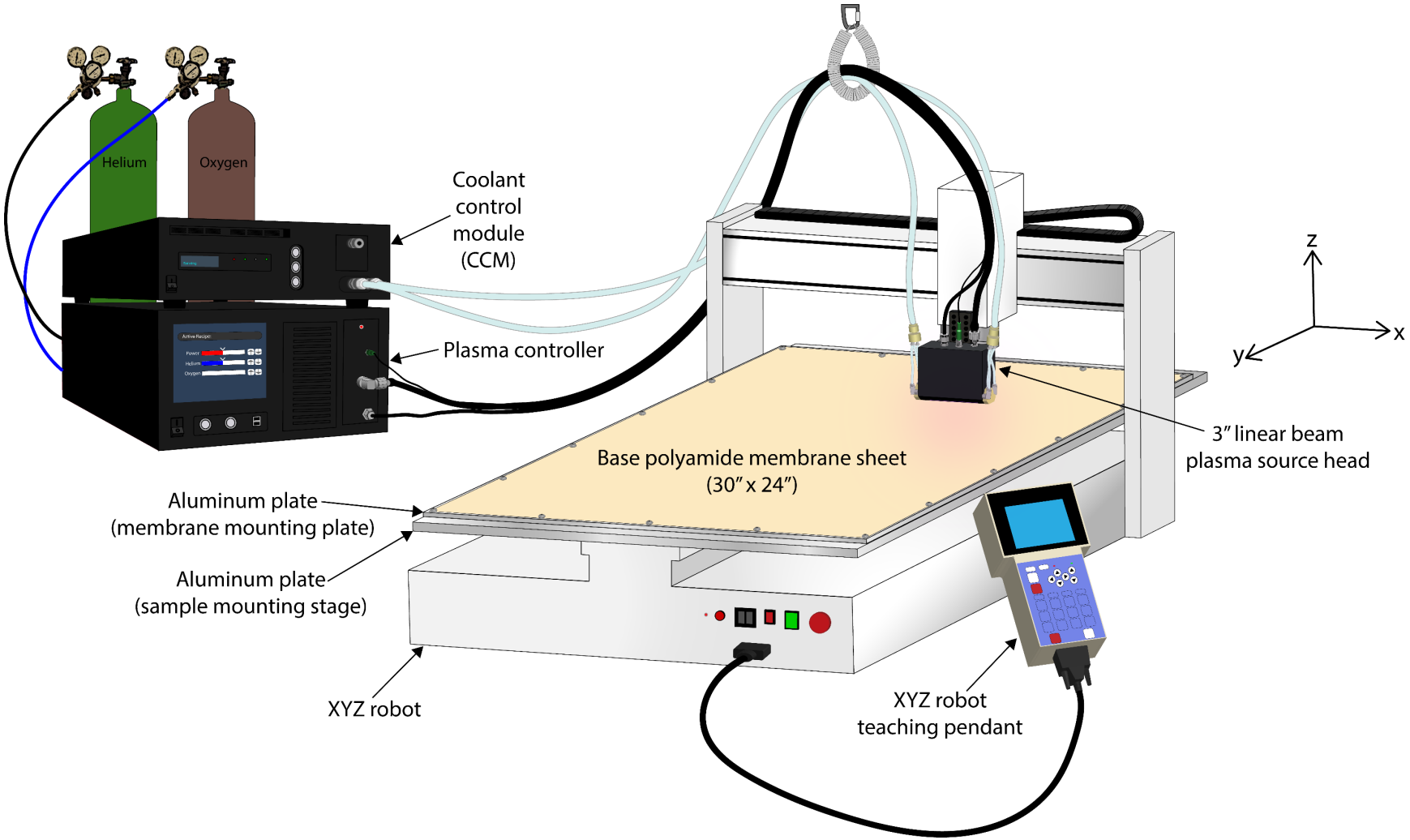

Figure 6-1. Atmospheric pressure plasma system with an XYZ robot (the plasma source head moves in the x- and z-directions, and the aluminum plates move in the y-direction only).

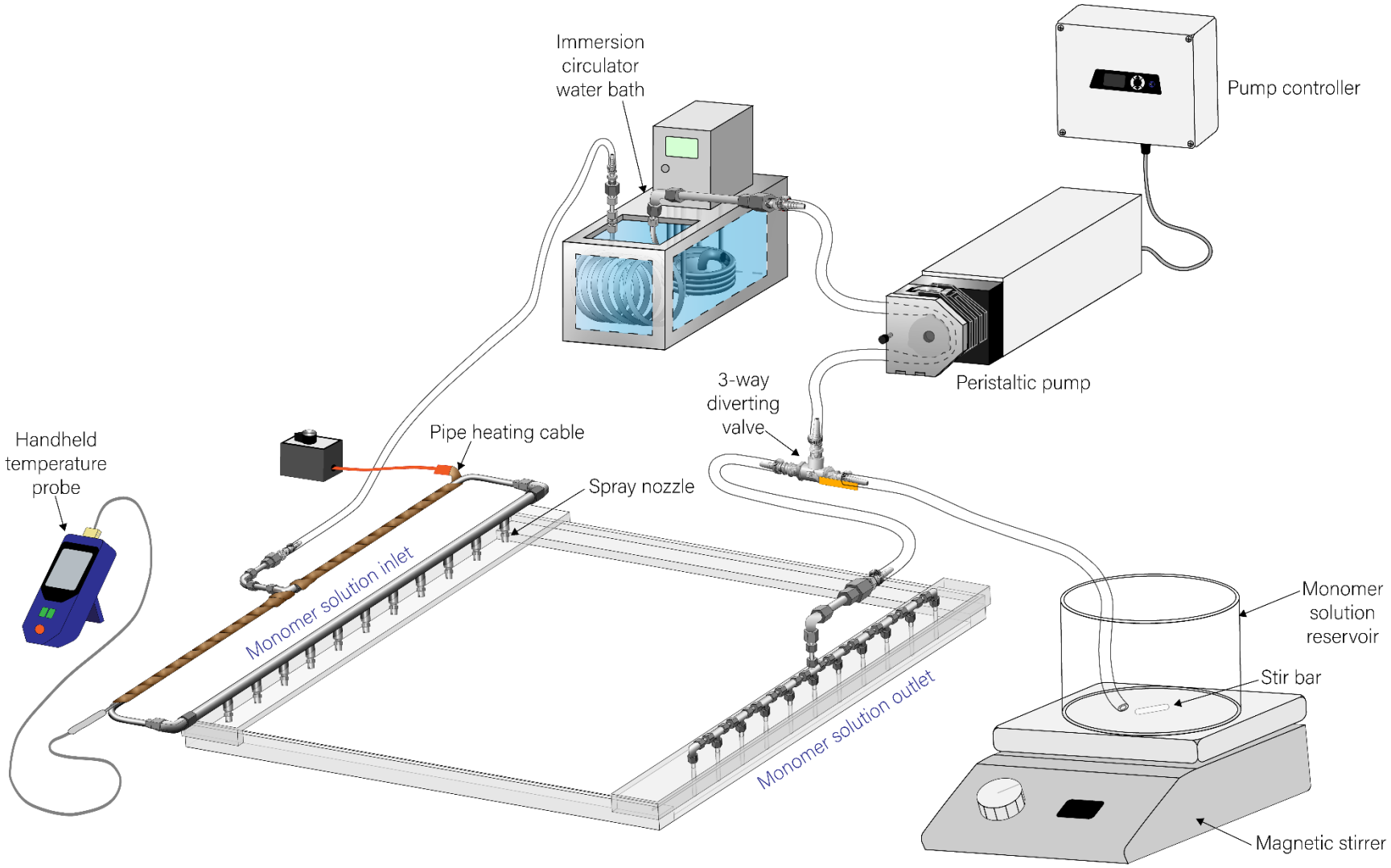

Figure 6-2. Scaled-up membrane graft polymerization system (details of the reactor configuration is shown in **Figure 6-3**).

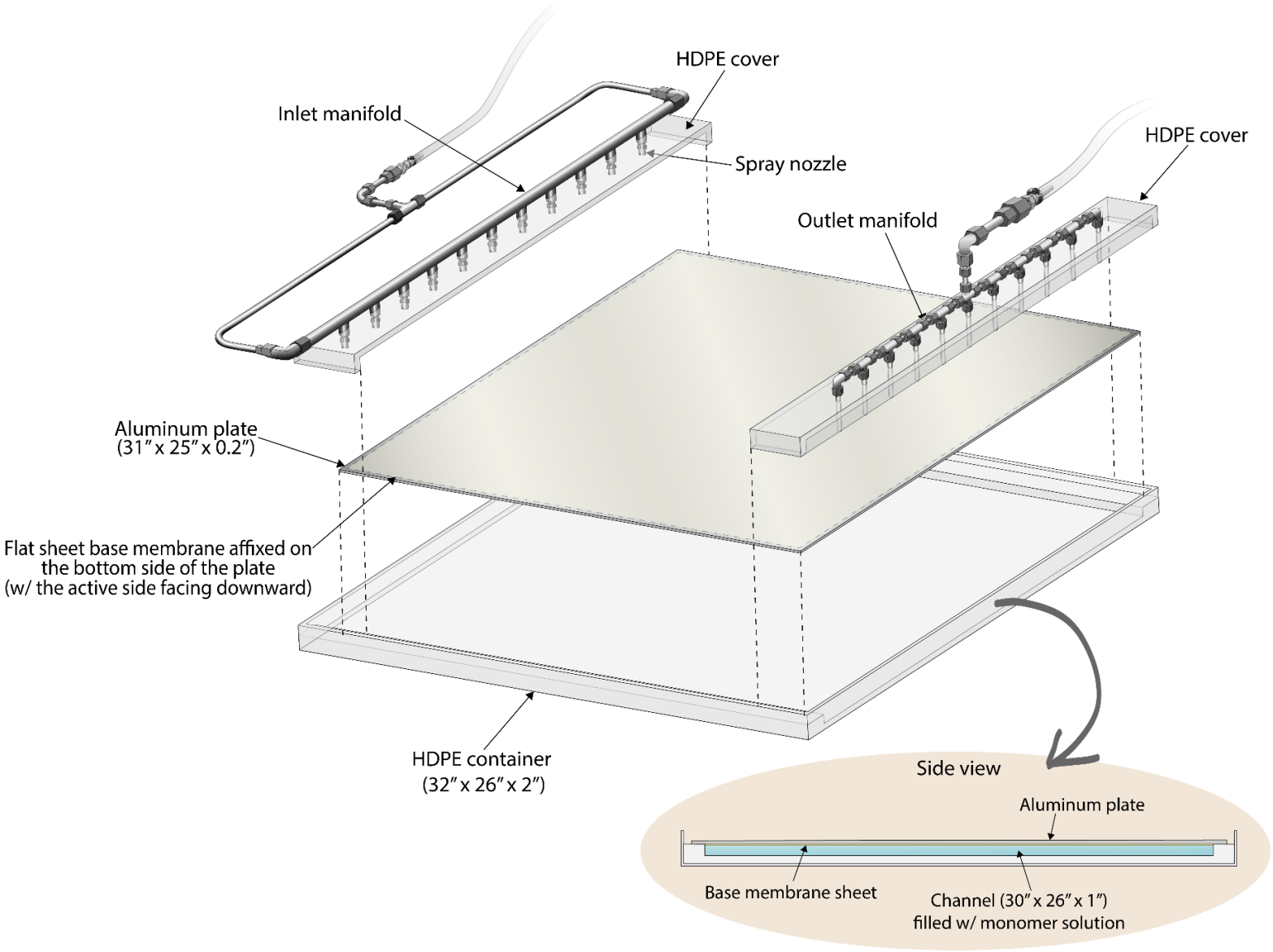

Figure 6-3. Exploded view of the scaled-up graft polymerization reactor in **Figure 6-2**.

6.2.5. Membrane performance evaluation

The uniformity of membrane surface nano-structuring over the large SNS-PAA-PA flat sheet membrane (30" x 24") was initially evaluated by testing the performance of eighteen membrane coupons (size of each coupon is about 4.4" x 2.2") extracted from the large membrane sheet using a CF042 steel rule die (Sterlitech Corp., Kent, WA) following the procedure described in **Appendix A.2.1**. Performance of the membrane coupons was evaluated in terms of water permeability coefficient (L_p), salt permeability coefficient (B), and intrinsic salt rejection (R_i), using the laboratory plate-and-frame RO (PFRO) membrane test system and membrane performance evaluation protocol described in **Appendix B.1-B.2**. Membrane performance in terms of L_p, B, and R_i was also evaluated for flat sheet membrane coupons extracted from a commercial spiral wound element (Dow Filmtec SW30-2514) for a baseline comparison.

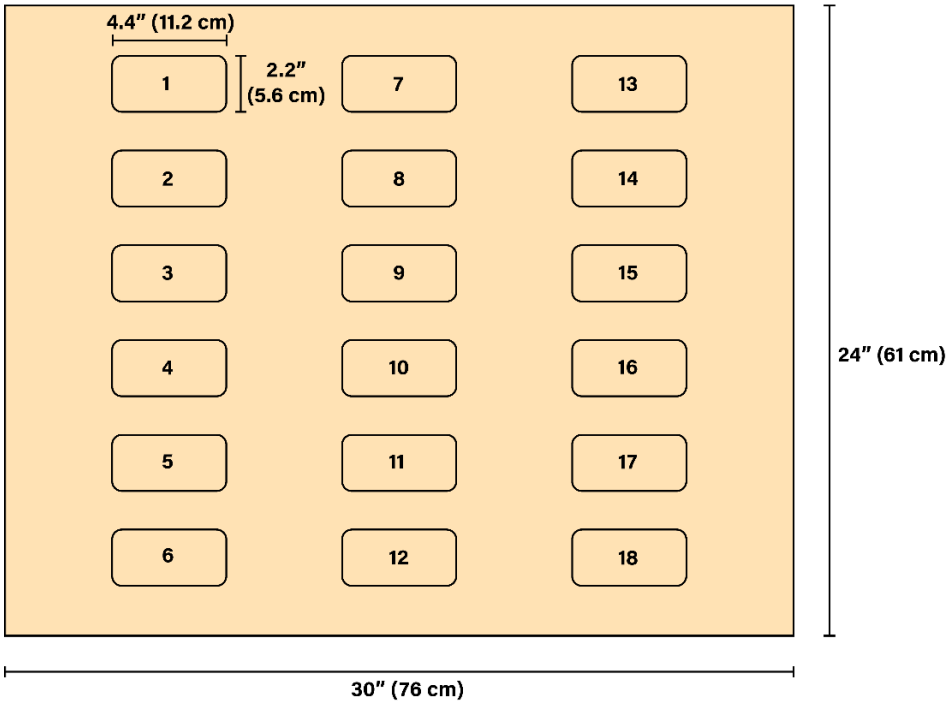

Figure 6-4. Locations of the eighteen individual membrane coupons (each is 4.4" x 2.2") extracted from the large SNS-PAA-PA membrane sheet (30" x 24") for testing membrane uniformity.

6.3. Results and Discussion

6.3.1 Uniformity of scaled up membrane sheet

Uniformity of the synthesized SNS-PAA-PA membrane sheet was assessed by evaluating the performance of 18 membrane coupons extracted from the membrane sheet. As shown in **Figure 6-5**, the average L_p, B, and R_i for the membrane coupons were 2.00 ± 0.21 L·m^{-2}·h^{-1}·bar^{-1}, 0.16 ± 0.02 L·m^{-2}·h^{-1}, and 99.5 ± 0.1%, respectively, indicating that the surface nano-structuring was uniform over the above membrane sheet area. Compared to the SW30 membrane (L_p^{SW30} = 1.6 ± 0.08 L·m^{-2}·h^{-1}·bar^{-1}, B^{SW30} = 0.26 L·m^{-2}·h^{-1}, R_i^{SW30} = 99.2%), the SNS-PAA-PA membrane had ~25% greater L_p and ~37% lower B.

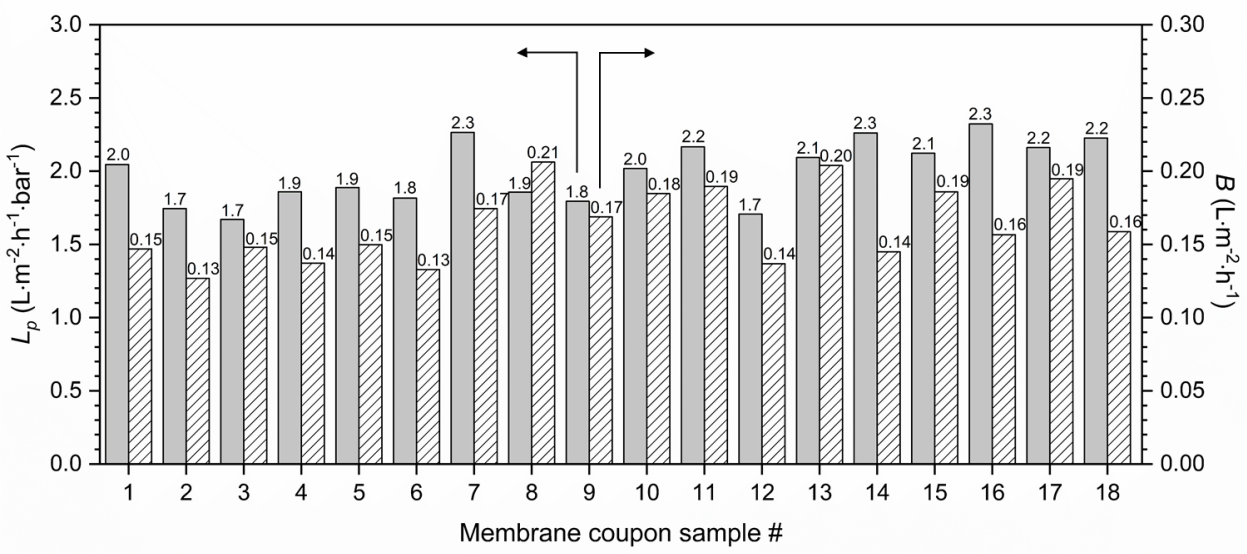

Figure 6-5. Water permeability coefficient (L_p) and salt permeability coefficient (B) for eighteen membrane coupon samples tested for uniformity of membrane SNS over the 30" x 24" membrane sheet area.

6.3.2 Fabrication of spiral wound membrane elements

Spiral wound elements (2.5” outer diameter and 21” in length) were fabricated at Toray Membrane USA Inc. (Poway, CA) from the synthesized large SNS-PAA-PA membrane sheets. Each spiral wound element was constructed of two 30.75” x 21” membrane leaves, and each membrane leaf was assembled by gluing a sandwich of two sheets of SNS-PAA-PA membrane glued together back-to-back with a sheet of porous permeate flow material (i.e., permeate carrier/spacer made of Tricot, 0.01” thick) inserted in-between. After gluing, the active membrane area per membrane sheet was 27.75” x 15.5” (~3 ft^2). Two membrane leaves, separated by a sheet of feed spacer (0.028” thick), were then wrapped around a central permeate collection tube (**Figure 6-6**).

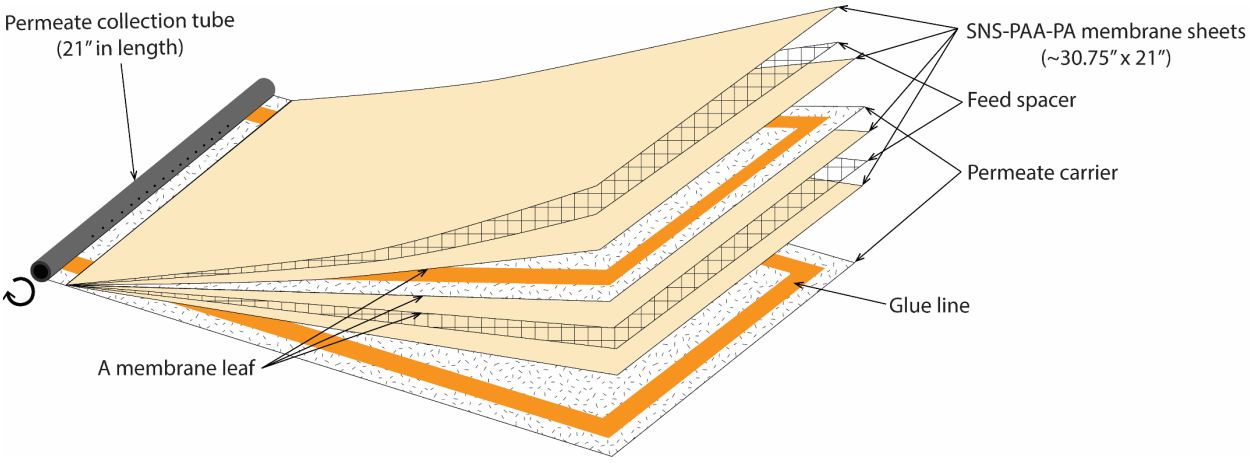

Figure 6-6. Assembly of a spiral wound element using the SNS-PAA-PA membrane sheets.

The freshly rolled membrane sheets were then encased inside a fiberglass shell with each end capped with an anti-telescoping device to avoid mechanical deformation of the rolled membrane sheets (telescoping). The final products of the spiral wound elements fabricated with the SNS-PAA-PA membrane sheets are shown in **Figure 6-7**. These spiral-wound membrane elements are prototypes that are suitable for use in small RO seawater desalination systems.

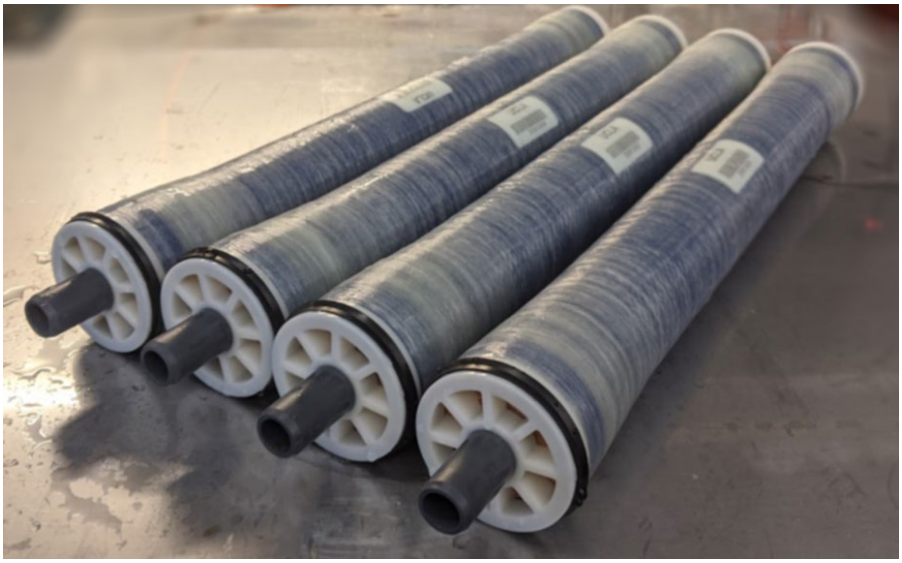

Figure 6-7. Spiral wound SNS-PAA-PA membrane elements.

6.4 Conclusions

Membrane surface nano-structuring via atmospheric pressure plasma-induced graft polymerization was scaled up to synthesize ~30" x 24" SNS-PAA-PA membrane sheets suitable for construction of commercial-scale spiral wound elements. Initial laboratory testing of small membrane coupons (~2" x 4") extracted from the 30" x 24" SNS-PAA-PA membrane sheet demonstrated that the synthesized membranes were uniform and having water permeability coefficient (L_p) and salt permeability coefficient (B) of 2.00 ± 0.21 $L \cdot m^{-2} \cdot h^{-1} \cdot bar^{-1}$, 0.16 ± 0.02 $L \cdot m^{-2} \cdot h$. Compared to the SW30 membrane ($L_p^{SW30} = 1.6 \pm 0.08$ $L \cdot m^{-2} \cdot h^{-1} \cdot bar^{-1}$, $B^{SW30} = 0.26$ $L \cdot m^{-2} \cdot h^{-1}$, $R_i^{SW30} = 99.2\%$), the SNS-PAA-PA membrane had ~25% greater L_p and ~37% lower B. It was shown that the synthesized SNS-PAA-PA membrane sheets could be successfully used to fabricate commercial-scale spiral wound elements (2.5" diameter and 21" length).

Appendix A. Membrane Surface Nano-structuring via APPIGP

A.1 Atmospheric Pressure Plasma (APP) System

A.1.1 APP system description

The Atomflo^{TM} 500 APP system utilized for base membrane surface activation consisted of the of a coolant control module (CCM), a plasma controller, and a plasma source head, which were used with an XYZ robot (**Figure A-1**).

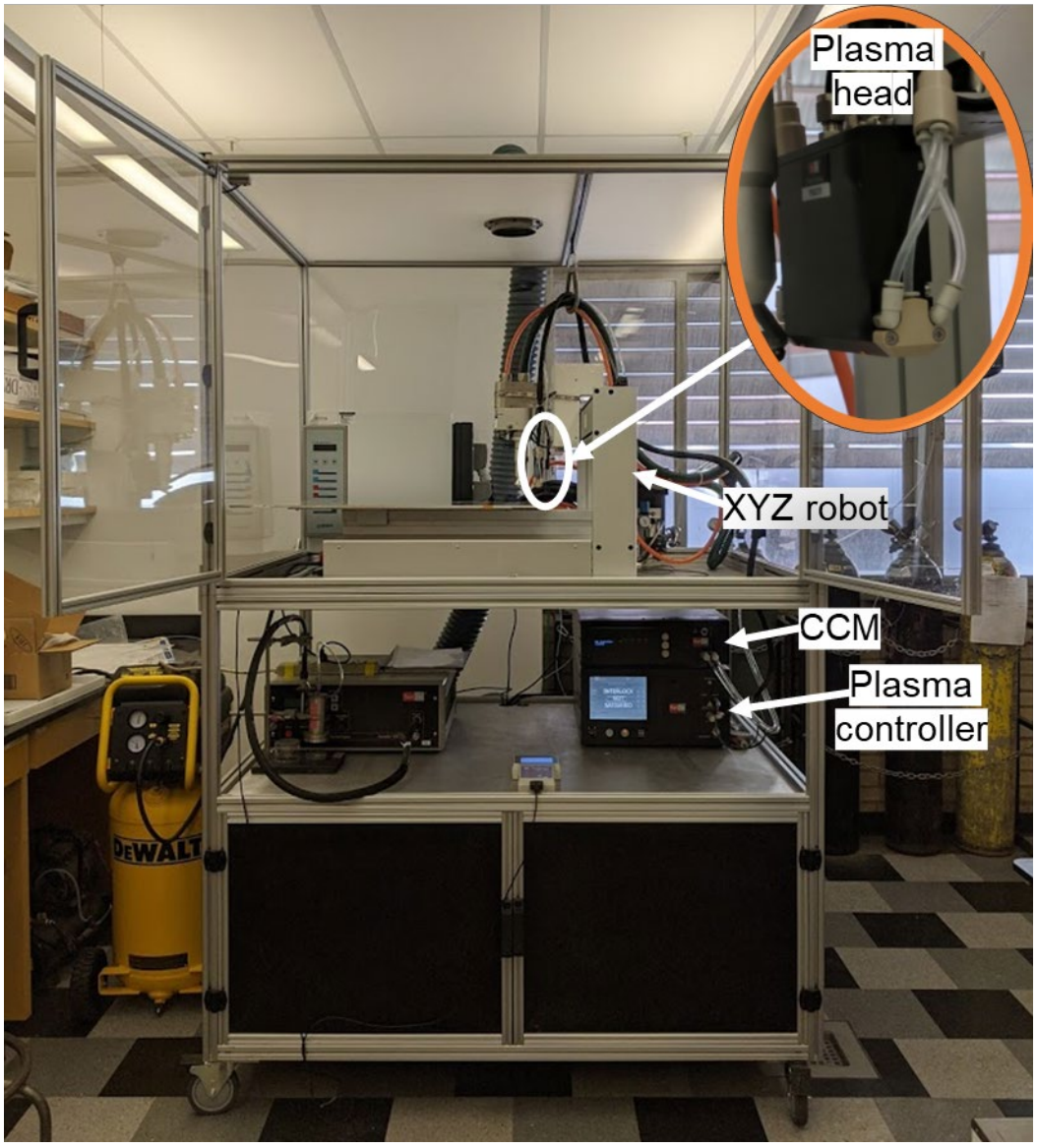

Figure A-1. The atmospheric pressure plasma system.

The plasma controller used to generate an APP plasma (**Figure A-2**) contained a variable power, 27.12 MHz radio frequency (RF) generator, and auto-tuning matching network, and a gas delivery system. The APP system was optimized to generate a plasma using helium as the main plasma gas used alone or with a secondary process gas (e.g., oxygen). The CCM was used to circulate deionized water through a plasma head in order to stabilize the temperatures of the plasma head and the plasma discharge.

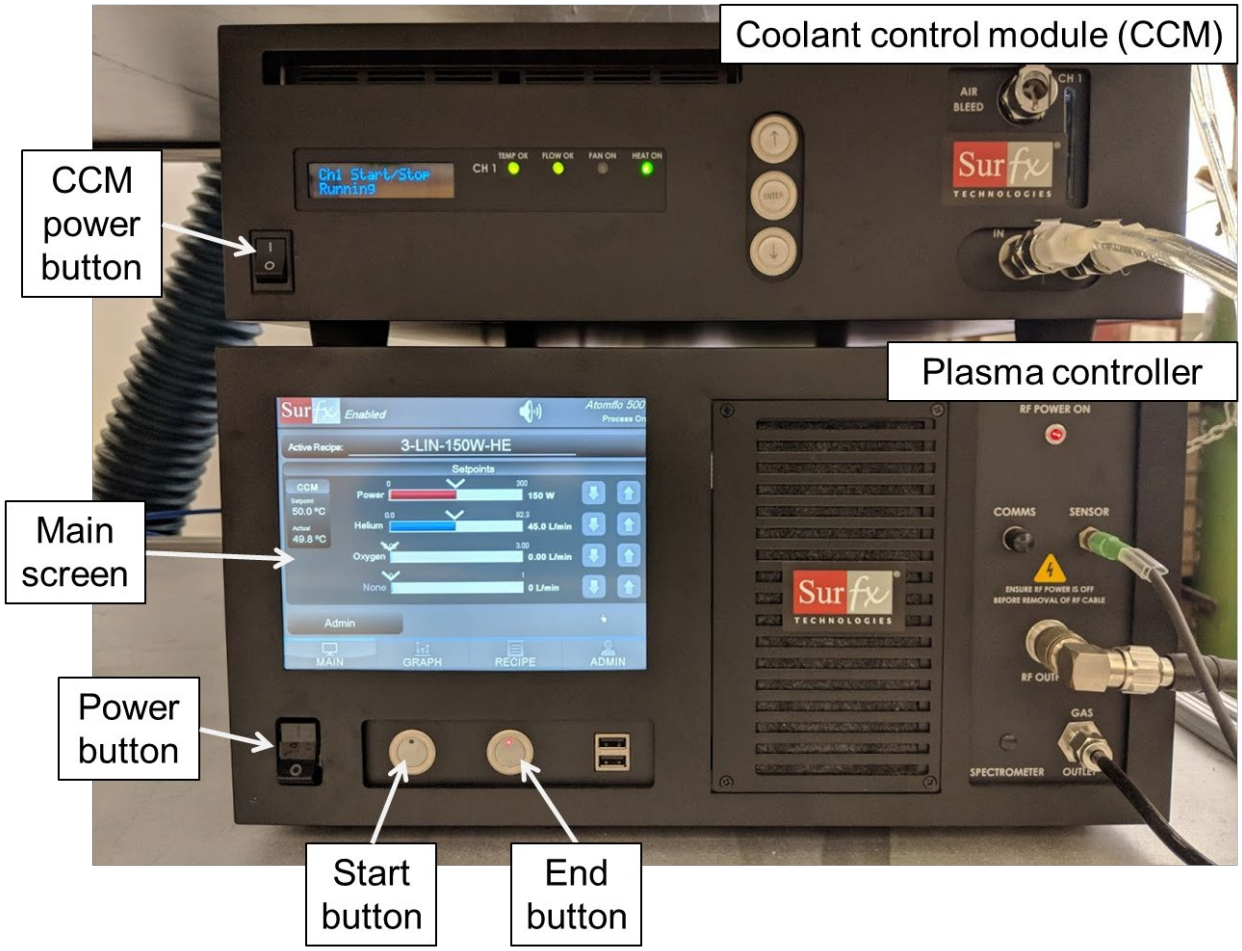

Figure A-2. The front view of the Atomflo^{TM} 500 system.

A.1.2 APP system operation

1. Turn on the power switch of the coolant control module (CCM) and click ‘Enter’ button three times to initiate heating the water in the CCM system (**Figure A-3**). It will take ~9 min to reach the temperature setpoint (i.e., 50.0°C).

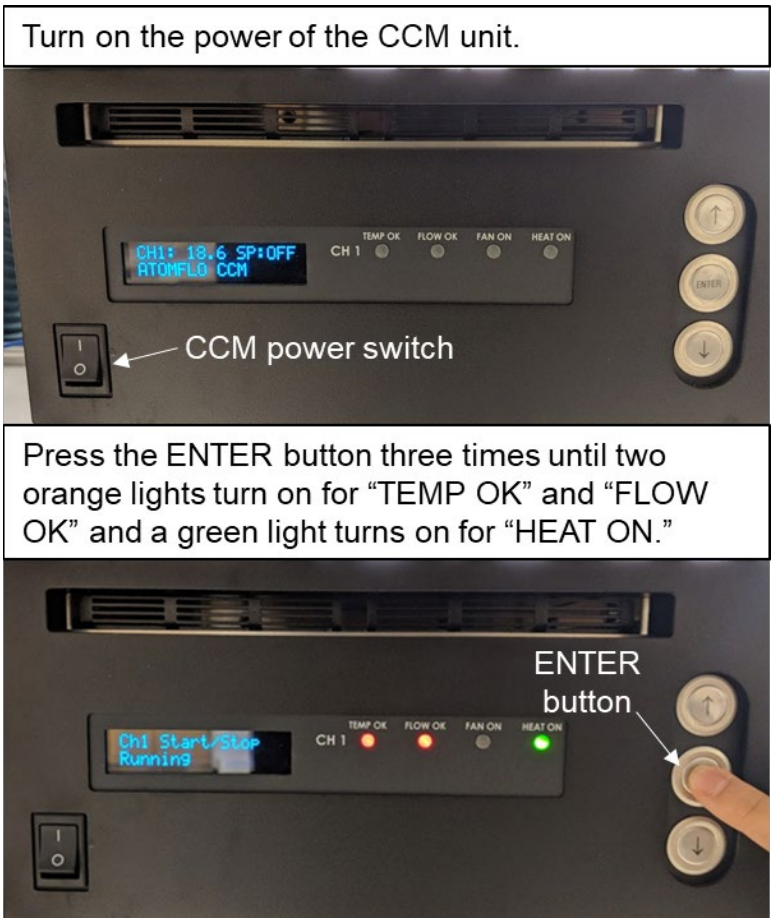

Figure A-3. Startup steps for the coolant control module.

2. Turn on the power switch of the plasma controller after the CCM is powered on (**Figure A-4**). It takes about 2 minutes for the system to boot (Note: The CCM must be powered on before the plasma controller is powered on).

Figure A-4. Atomflo^{TM} 500 system during booting.

3. Open helium (99.99% purity) and oxygen (99.999% purity) gas cylinders that are connected to the plasma controller. The outlet gauges of the pressure regulators for the above gas cylinders should be set to 45 psi.

4. The system is ready when the actual temperature (as indicated on the front touchpad screen of the controller) is above 47°C. It is also indicated by three green lights at the front on the CCM (**Figure A-5**).

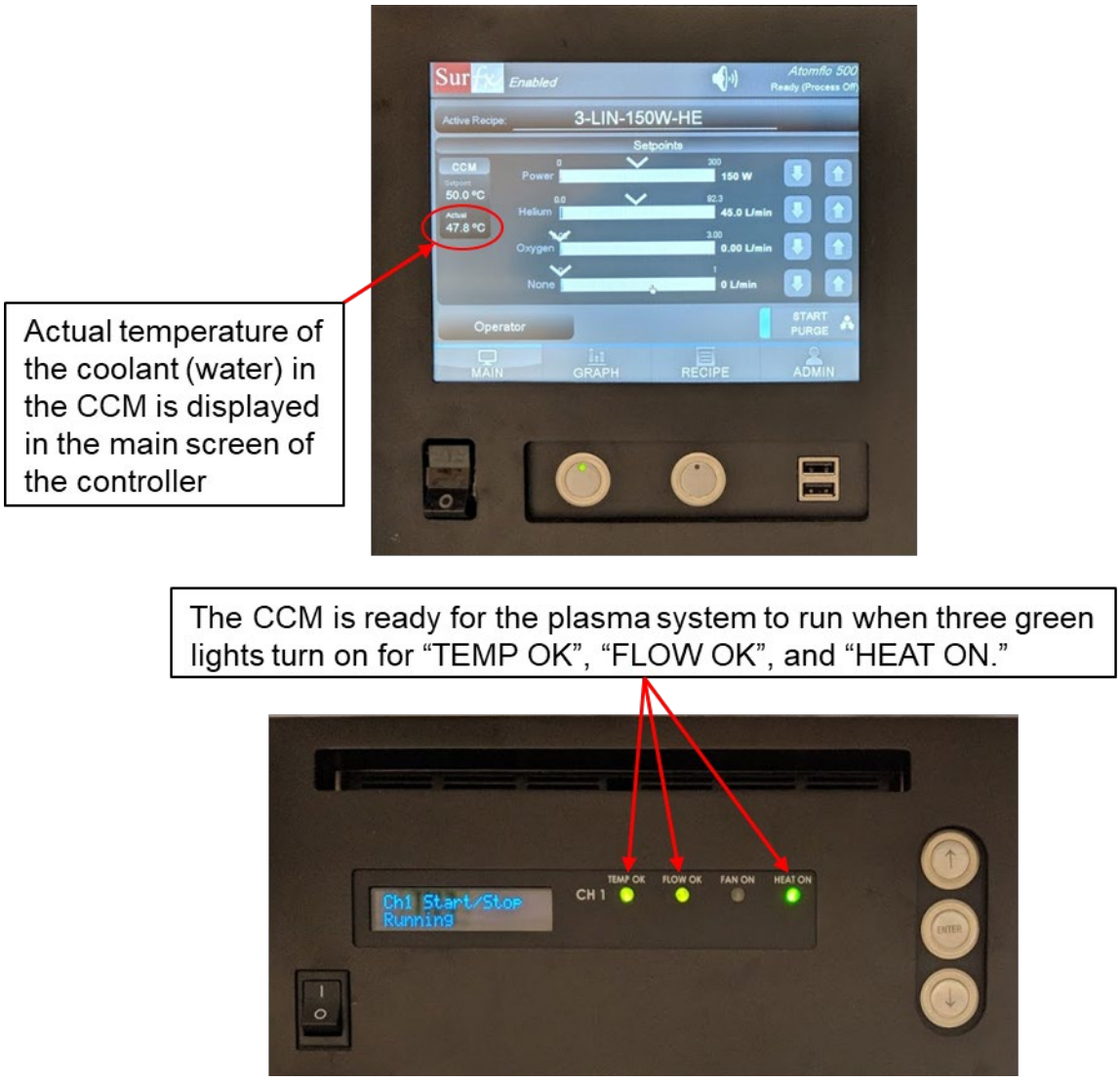

Figure A-5. The controller main screen and CCM and the front display of the CCM when the system is ready.

5. Check if the name of the current active recipe displayed on the controller main screen is correct (**Figure A-6**). The recipe defined setpoints for RF power and gas flow rates should be also displayed on the main screen. For example, RF power and He flow rate setpoints for the ‘3-LIN-150W-HE’ recipe is 150W and 45 L/min, respectively. Active recipe can be changed or customized by accessing the admin mode. Change the user access type from

'Operator' to 'Admin.' Selecting 'Admin' will prompt a keypad to enter PIN (i.e., 1234) (**Figure A-7**).

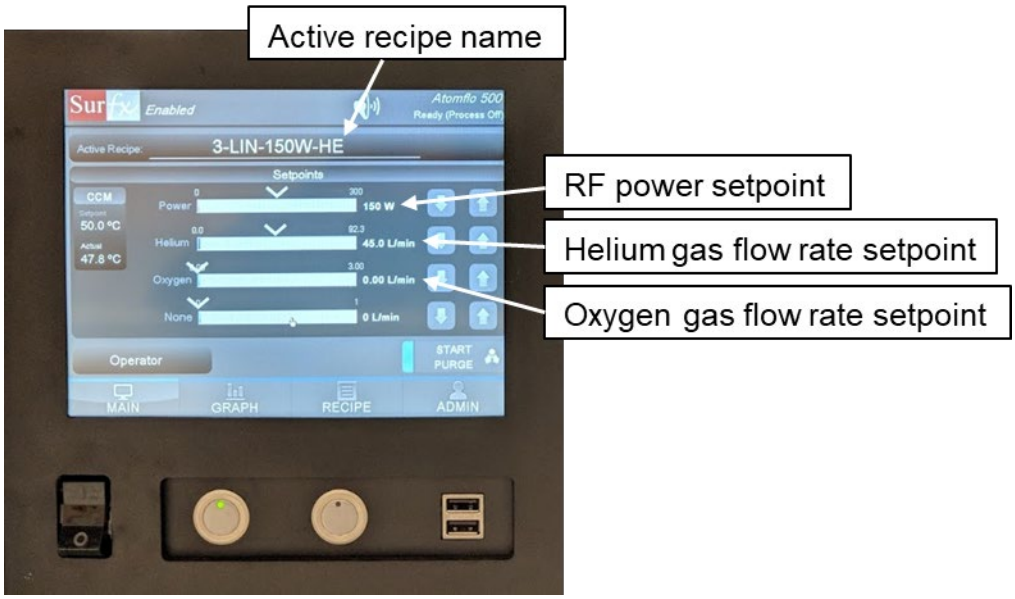

Figure A-6. The active recipe defined plasma operating parameters (RF power and gas flow rates) shown on the controller main screen.

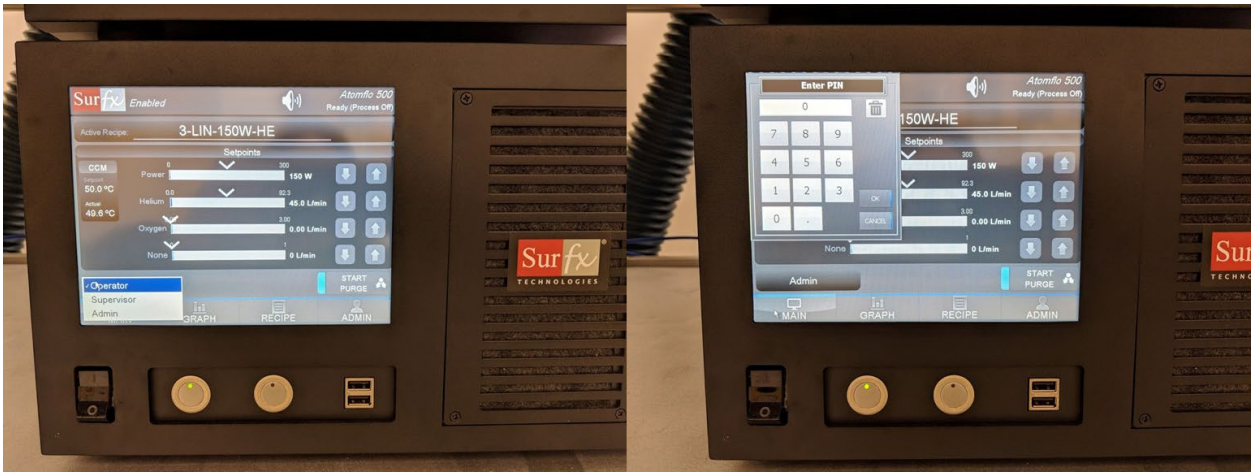

Figure A-7. Changing the user type from 'Operator' (default) to 'Admin' will prompt a PIN pad.

6. the 'START PURGE' on the display. This will purge the plasma system with the connected gas(es) (i.e., helium and oxygen).

7. Turn on the plasma by pressing the START button of the plasma controller (**Figure A-2**). The system will start the tuning process (lasts ~45 s) and display 'Process ON' on the main screen when the plasma is running (**Figure A-8**).

8. Press the controller STOP button (**Figure A-2**) to terminate the plasma process.

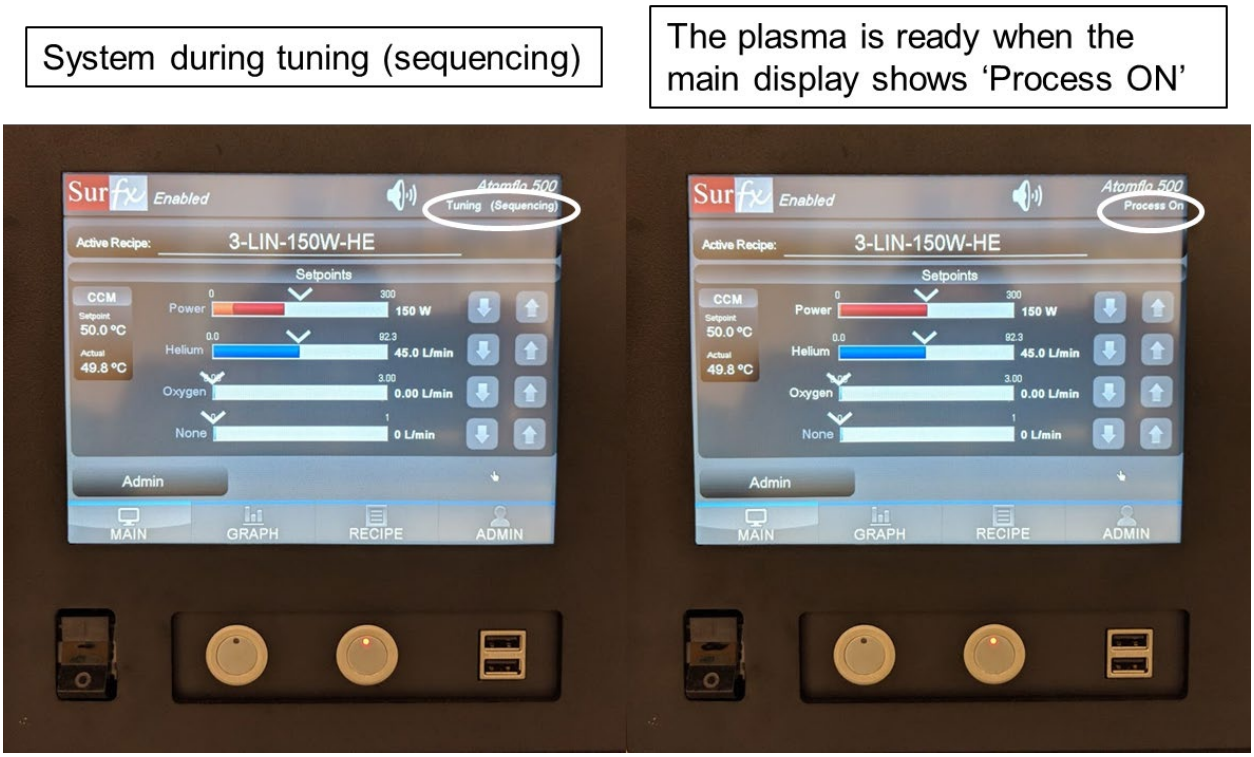

Figure A-8. The controller main screen during system tuning (*left*) and when the plasma system is operating (*right*).

A.2 Membrane Surface Nano-structuring Procedures for PA Membrane Coupons

A.2.1 Base polyamide membrane coupon preparation

Extract a membrane coupon (4.4” x 2.2” or 11.2 cm x 5.6 cm) from a base polyamide membrane flat sheet using a CF042 steel rule die (Sterlitech Corp.; Kent, WA) shown in **Figure A-9** and steps shown in **Figure A-10**. Place the die over a membrane sheet affixed onto a flat surface, and pound down on each corner of the die with a mallet. Use scissors to cut along the delineated outline (produced from the die) with the exception of two tabs at one of the long edges of the membrane coupon. Use a hole puncher (0.25” diameter) to punch two holes at the center of short edges. Store the membrane coupon fully immersed in DI water for at least a day prior to use.

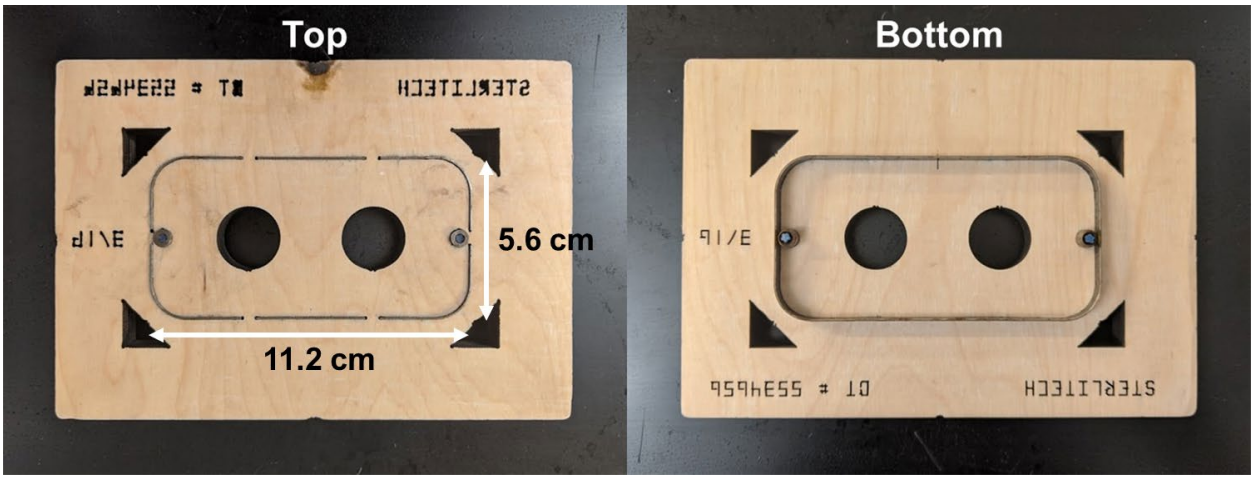

Figure A-9. Top and bottom views of the CF042 steel rule die used to cut ~4” x 2” membrane coupons from flat sheet membrane rolls.

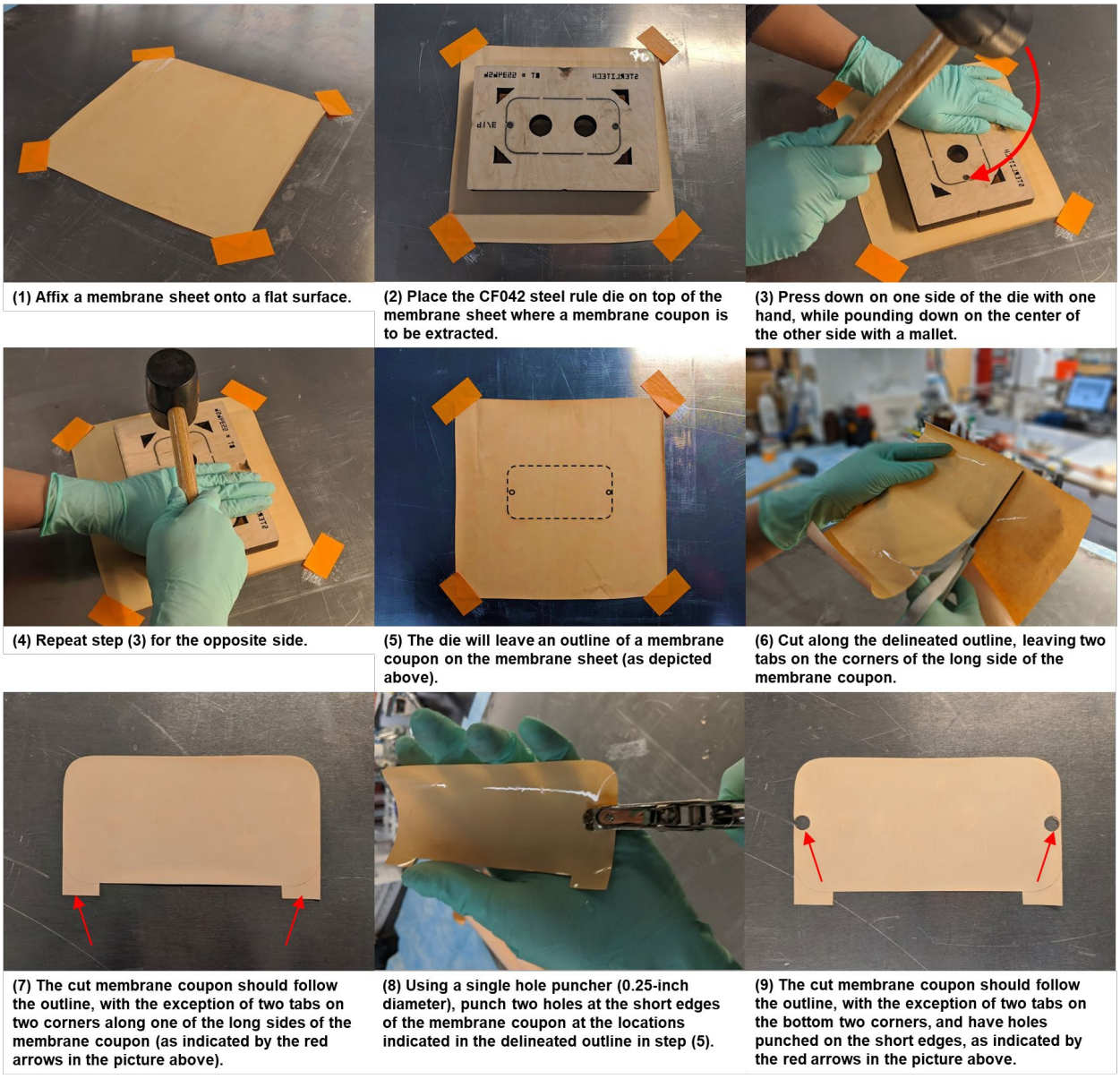

Figure A-10. Steps to extract a 4” x 2” membrane coupon from a flat sheet membrane using a CF042 steel rule die (It is noted that step (7) was omitted for the membrane coupons extracted to test uniformity of the SNS-PAA-PA membrane sheet in **Chapter 6**).

A.2.2 APP surface activation for membrane coupons

1. Rinse the membrane coupon sample surface under DI water for ~30 s and blow dry with nitrogen using a PTFE nitrogen/drying gun (International Polymer Solutions Inc.; Irvine, CA) for ~1 – 2 min until the membrane surface is completely dry.
2. Affix the dried base membrane coupon onto the aluminum plate of the XYZ robot as shown in **Figure A-11**.
3. Run the APP system (following the protocol provided in **Appendix A.1.2**) and execute an XYZ robot program to achieve the desired number of sequential plasma surface scans for the base membrane coupon at a preset separation distance between the plasma source and the membrane surface.

   Note: The robot can be programmed by inputting addresses, i.e., sets of xyz coordinates to be executed by the robot system using the XYZ robot teaching pendant (see the manual). The plasma head moves in the x- and z-directions, while the aluminum plate (used as a stage for sample mounting) moves in the y-direction. The aluminum plate can be moved back and forth (relative to the plasma head while stationary) in the y-direction to achieve sequential plasma surface scans (**Figure A-12**).

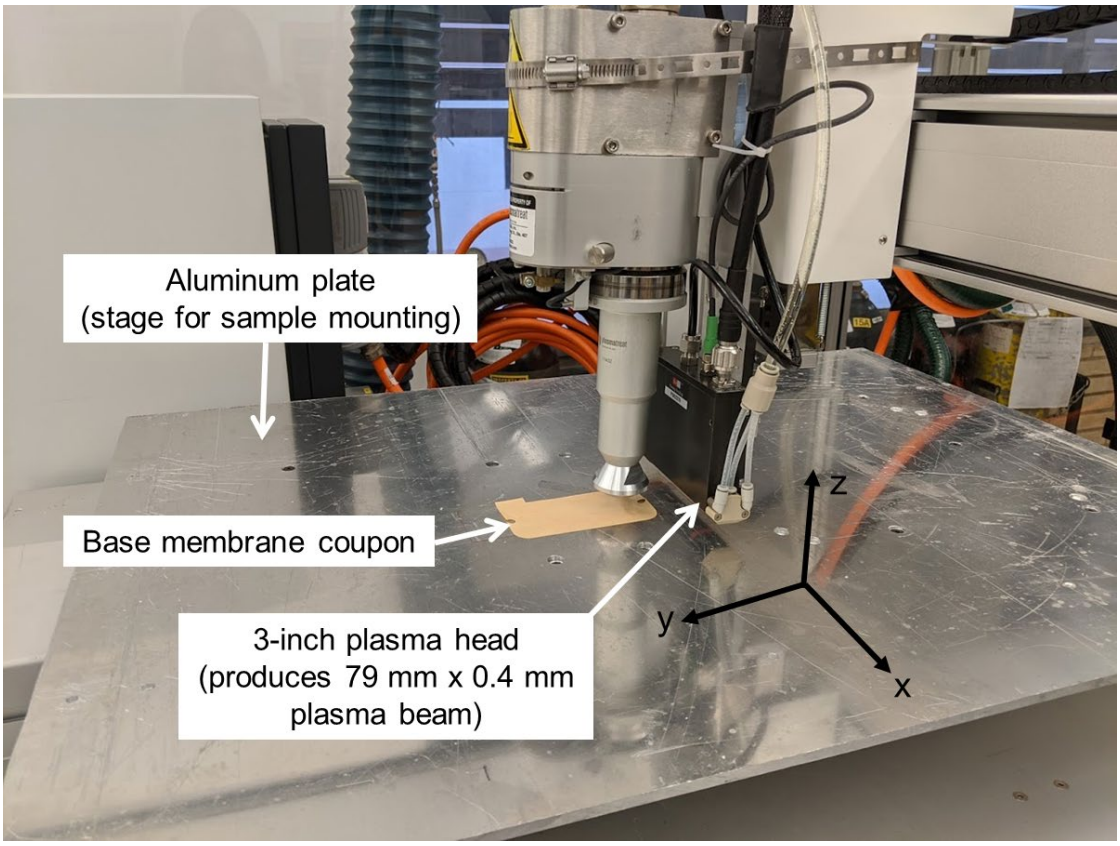

Figure A-11. APP surface activation of small membrane coupons performed using the XYZ robot.

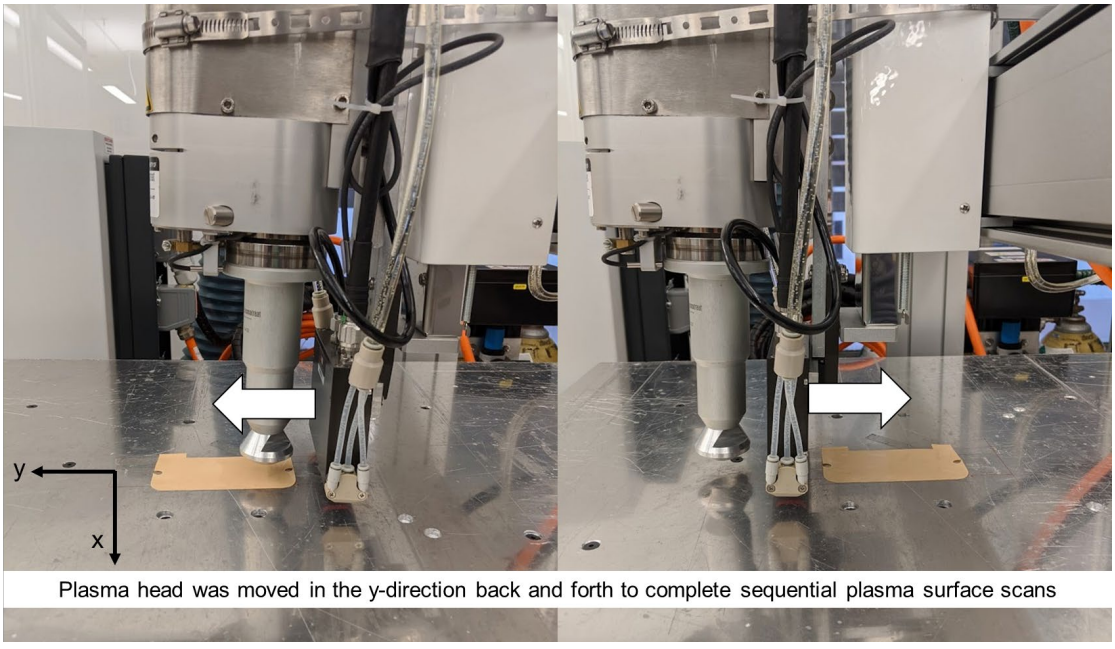

Figure A-12. Illustration of sequential plasma surface scans for small base membrane coupons.

A.2.3 Graft polymerization

1. Prepare an aqueous acrylic acid (AA) monomer solution (of a total volume of 100 mL) in a glass jar (235 mL capacity, Part #42235T55; McMaster-Carr, Santa Fe Springs, CA) using acrylic acid and DI water. Typically, AA graft polymerization was carried out with solutions of 10 – 30 vol% initial AA concentrations, which have pH in the range of ~1.7 – 2.0. Adjust the solution pH as needed by adding sodium hydroxide.
2. Following surface plasma treatment as described in **Section A.2.2**, briefly rinse the plasma treated membrane coupon sample surface under DI water stream (i.e., ~5 s). Then, wrap the membrane coupon around a Teflon PTFE rod (1-3/8" diameter, cut to ~4.25" in length) (Part #8546K27; McMaster-Carr, Santa Fe Springs, CA), and slide a PTFE o-ring (Part #9559K42; McMaster-Carr, Santa Fe Springs, CA) over the two tabs of the membrane coupon to affix the membrane onto the rod (**Figure A-13**).

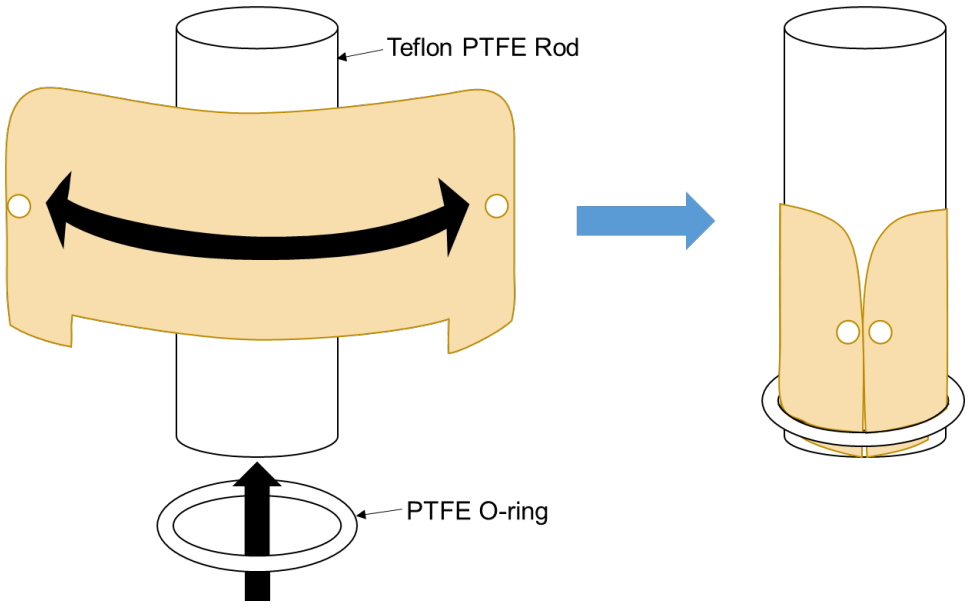

Figure A-13. Illustration of membrane coupon wrapping and affixing onto a PTFE rod for graft polymerization.

3. Place the membrane wrapped rod in the monomer containing jar. The membrane coupon should be fully immersed in the monomer solution. Screw on the jar lid (which is connected to a thin tubing loop (with small holes poked with needles) that is connected to a nitrogen source). Turn on the nitrogen source and check that there is a stream of nitrogen bubbles as shown in **Figure A-14**.

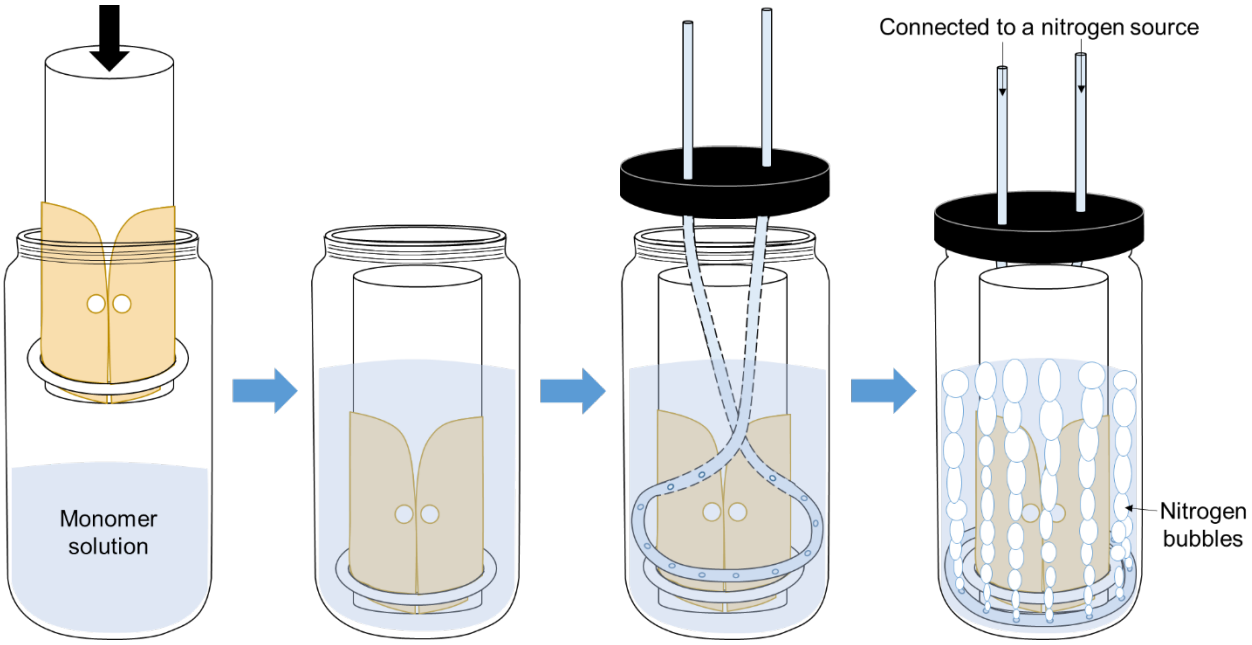

Figure A-14. Illustration of graft polymerization vessel setup suitable for small membrane coupons (4" x 2").

4. Immerse the jar containing the membrane wrapped rod and nitrogen line in a temperature-controlled water bath to initiate graft polymerization (**Figure A-15**). Leave the jar in the water bath for the duration of the graft polymerization reaction (typically 0.5 – 2 h).
5. Terminate the graft polymerization by disposing the monomer solution in a designated waste container and rinse the membrane coupon surface thoroughly under a DI water stream for ~1 min and store the membrane coupon in DI water until use.

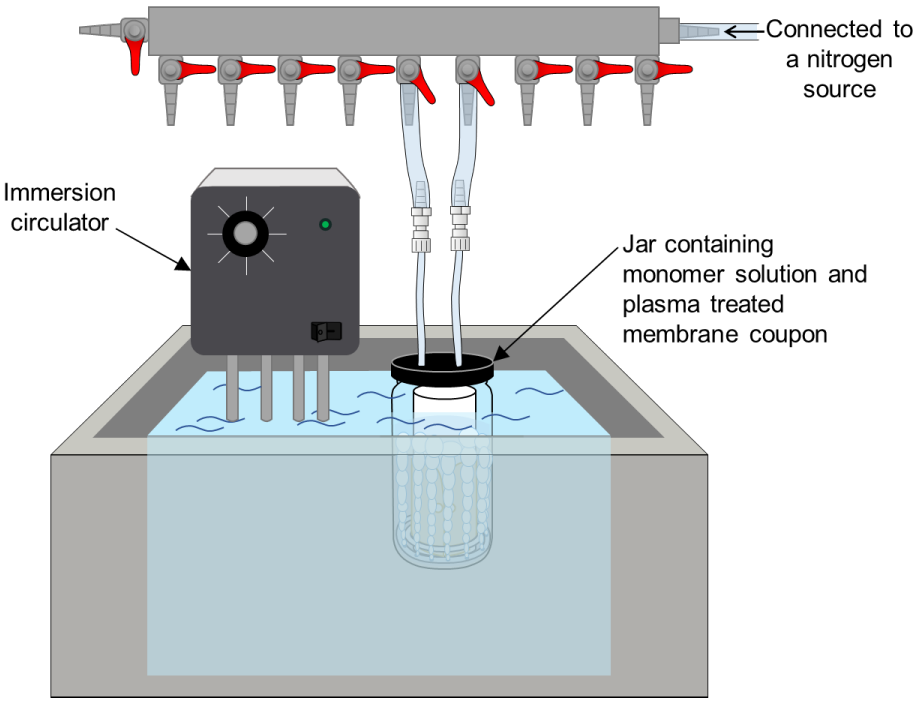

Figure A-15. Immersion circulator water bath and nitrogen purging system used for graft polymerization of small membrane coupons.

A.3 Scaled-up Membrane Surface Nano-structuring Procedures

A.3.1 Base polyamide membrane sheet preparation

1. Cut a base membrane flat sheet sample of the size of the base aluminum plate (31” x 25”) from a roll. Keep the cut membrane sheet fully immersed in DI water (**Figure A-16**) for a day prior to use.

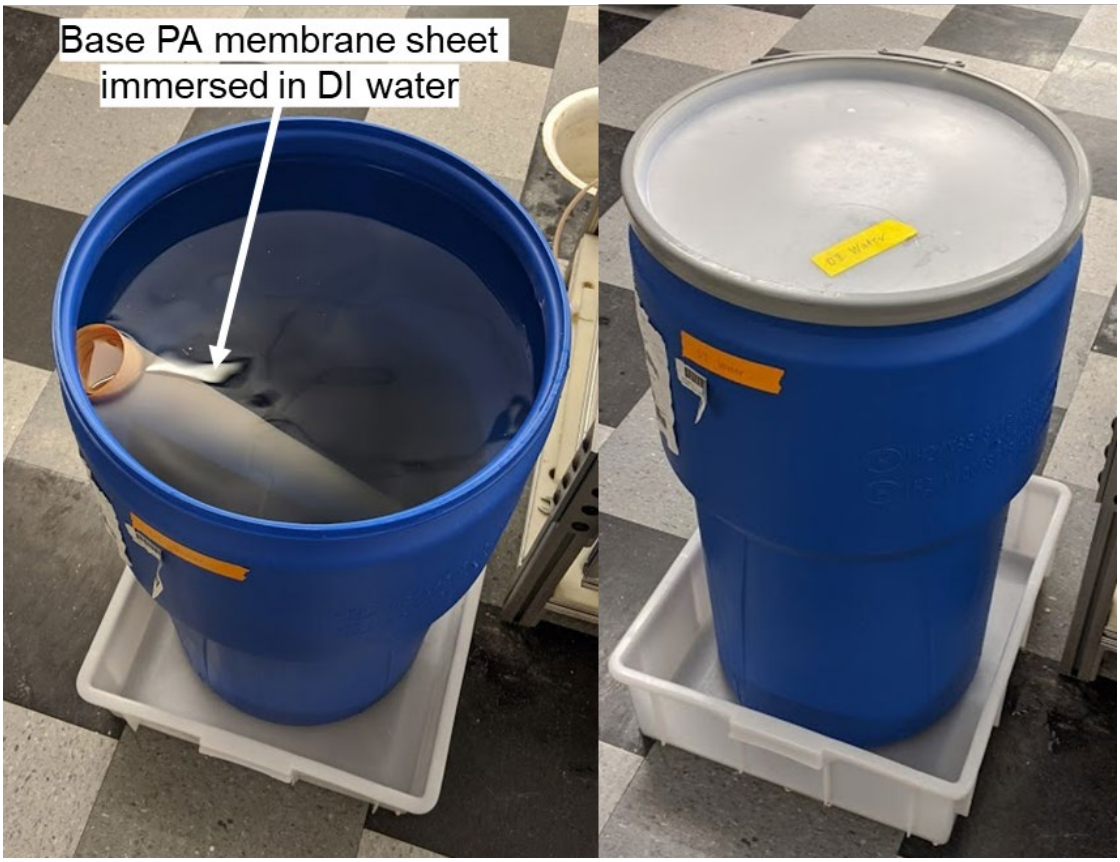

Figure A-16. Base PA membrane sheet stored in deionized water inside a covered container to avoid light exposure.

2. On the following day, take out the base membrane sheet from storage in DI water. Mount the sheet onto the base aluminum plate with the active side facing up. Cut away any excess membrane sheet along the plate edges.

3. Thoroughly dry the active sides of the membrane by blowing nitrogen with a PTFE nitrogen/drying gun (International Polymer Solutions Inc.; Irvine, CA) (**Figure A-17**).

Figure A-17. (a) Drying of the base PA membrane sheet via blowing nitrogen. The base PA membrane sheet: (b) before and (c) after drying with nitrogen.

A.3.2 Monomer solution preparation and graft polymerization system setup

1. Turn on the immersion circulator water bath and fill the water bath reservoir with DI water. Set the temperature to 95°C (it takes about an hour to reach 95°C).

2. Prepare 2.8 L of acrylic acid (AA) and 2 L of sodium hydroxide (50% w/w NaOH) separately in graduate cylinders as shown in **Figure A-18**. Prepare 0.1 L of NaOH (50% w/w NaOH) in a separate graduate cylinder. Seal the top of graduate cylinders with strips of Parafilm.

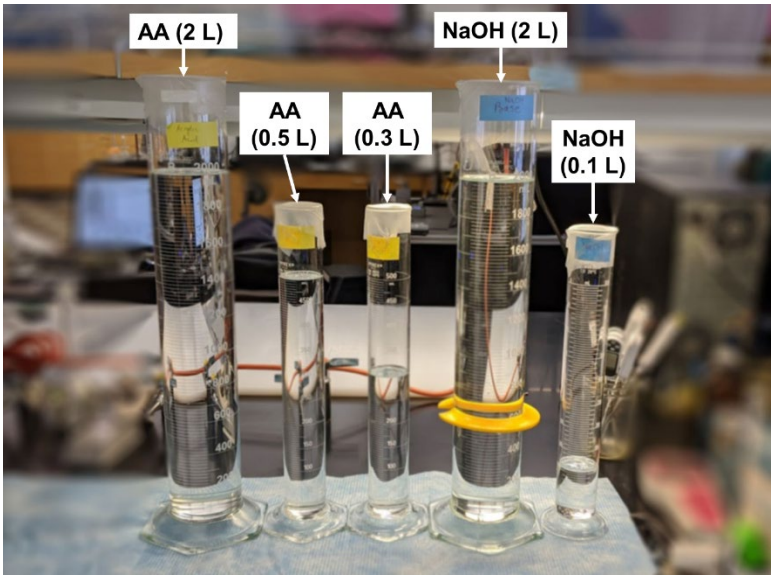

Figure A-18. Acrylic acid and sodium hydroxide prepared in graduate cylinders.

3. Set up a small laboratory table or cart containing three magnetic stir plates, next to the reactor. Place a stainless steel container on top of two small stir plates; and place a plastic container (i.e., the polypropylene pitcher, 10 L capacity) on top of the large stir plate (**Figure A-19**). Also, place stir bars inside each container.

4. Add 4.2 L of DI water to each container. Place the nitrogen purge line (constructed of a 1/16" ID, 1/8" OD PTFE tubing that have ~1 mm diameter holes (spaced few inches apart)

that were produced with a needle) inside each container as shown in **Figure A-19**. Connect the tubing to a nitrogen gas cylinder to deliver nitrogen bubbles in the waters.

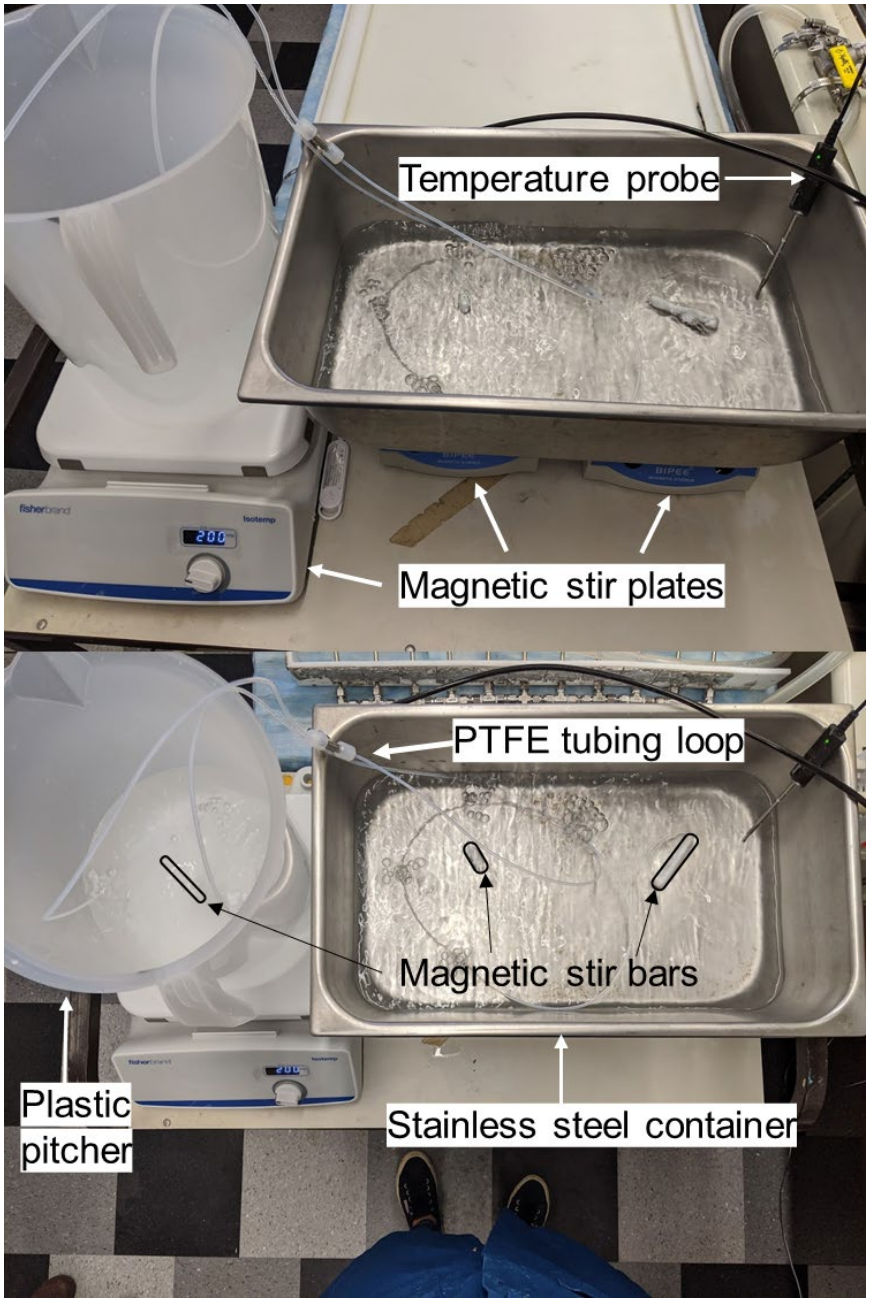

Figure A-19. Instruments used to prepare monomer solution for the scaled-up graft polymerization process.

5. Transfer 2.8 L of AA (prepared in Step 2) into 4.2 L DI water in the stainless steel container to prepare an AA solution (total volume of 7.0 L) while purging nitrogen in the AA solution.
6. Remove the nitrogen purging line segment place from inside the plastic container and transfer 2 L of NaOH (prepared in Step 2) to the DI water in the plastic container to prepare an NaOH solution (total volume of 6.2 L).
7. Remove the nitrogen line from the AA solution in the stainless steel container. Transfer the NaOH solution in the plastic container into the AA solution in the stainless steel container slowly while mixing. This should lead to a rise in the monomer solution temperature close to 70°C.
8. Check the AA solution pH with an Oakton pH 110 meter (Oakton Instruments, Vernon Hills, IL). Slowly transfer additional (~500 mL) of NaOH (50% w/w NaOH), from 0.1 L of NaOH prepared in a separate graduate cylinder in Step 2, to the AA solution to adjust the final solution pH of 6.

A.3.3 Scaled-up membrane surface activation with atmospheric pressure plasma

Surface activation of the base polyamide membrane sheet was performed with two sequential scans of helium APP (He flow rate of 45 mL/min; RF power = 150 W) using the XYZ robot (**Figure 6.1; Section 6.2**) at a speed of 100 mm/s and plasma source-substrate separation (*PSS*) distance of 10 mm. Since the length of the base membrane sheet (30" x 24") was longer than the working range of the XYZ robot (24" x 24"), two plasma treatment sequences (which the XYZ robot was programmed to perform) were employed to treat the entire membrane sheet area as illustrated in **Figure A-20**. First, a 23.6" x 24" area of the base membrane sheet was treated by the plasma source which travelled along the path indicated in **Figure A-20** (Plasma Treatment Sequence #1), resulting in the 23.6" x 24" area being treated via two plasma scans. Subsequently, the base membrane sheet was rotated 180°, and the remaining untreated area of 6.3" x 24" was treated by the plasma source travelling along the path indicated in **Figure A-20** (Plasma Treatment Sequence #2). The above treatment resulted in the entire base membrane sheet area (24" x 30") being treated by 2 plasma scans. The entire process of the base membrane plasma surface treatment took about 5 minutes (per 30" x 24" membrane sheet).

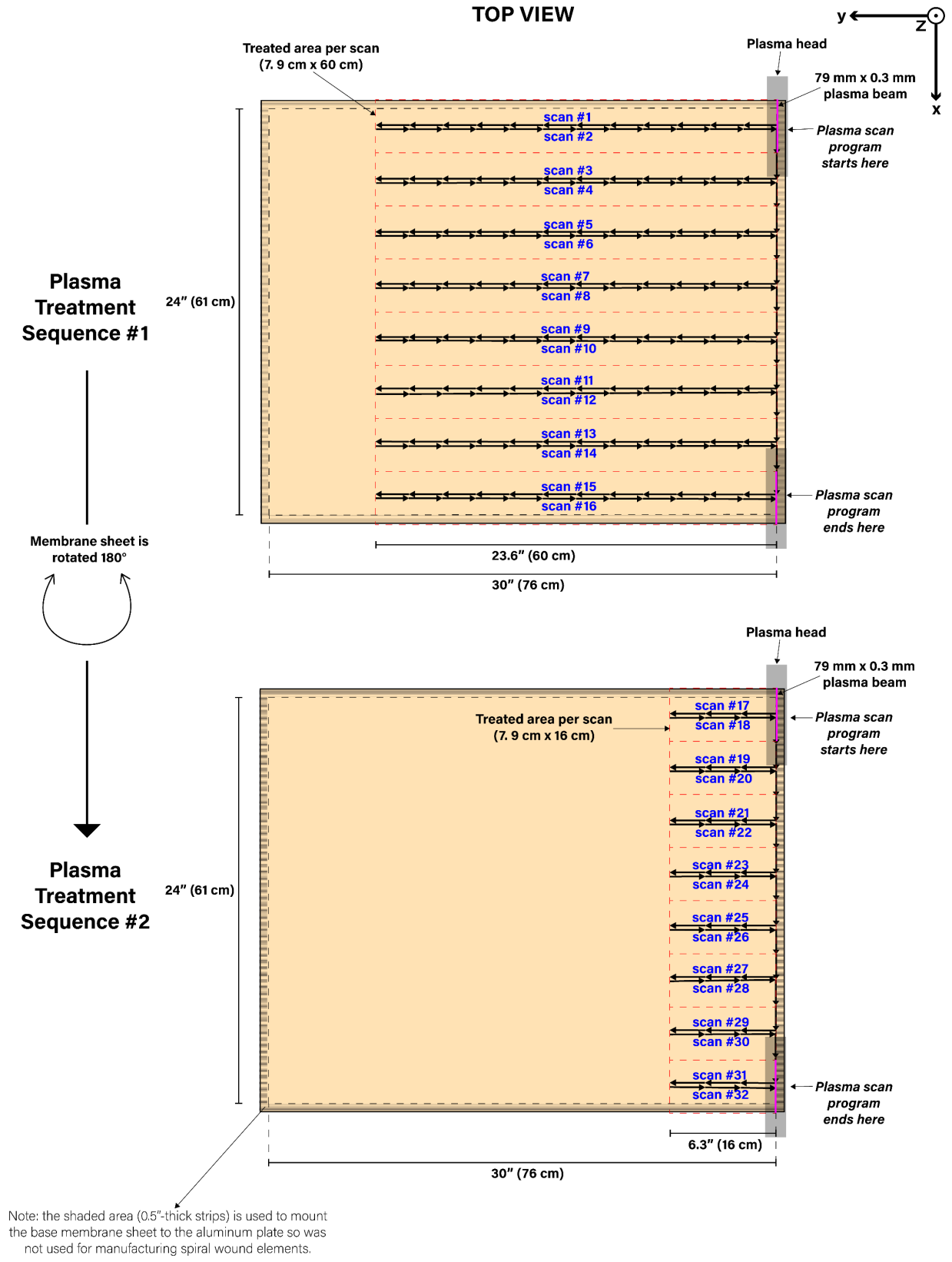

Figure A-20. Illustration of the paths taken by plasma surface treatment scans performed using the XYZ scanning robot.

A.3.4 Scaled-up membrane surface nano-structuring procedures

The timeline of the scaled-up membrane surface nano-structuring procedures is shown in **Table A-1**. The entire process can be divided into two phases, each started with a new timer (t_1 and t_2). In Phase I, the base PA membrane plasma surface activation and preparation of the AA monomer solution were carried out (i.e., Task 1 through 5). In Phase II, graft polymerization reaction was carried out for 1 hour. It is noted that Task 1 (1-1 through 1-4) and Task 2 were executed simultaneously by two persons in order to minimize delay between the plasma treatment and graft polymerization steps.

Table A-1. Scaled-up membrane surface nano-structuring procedures.

<table>
<tr><th colspan="2">Elapsed Time[1] (minutes)</th><th colspan="2">Tasks</th></tr>
<tr><td rowspan="7">Phase I. Plasma surface activation & monomer solution prep</td><td colspan="3">Complete tasks outlined in Sections A.3.1 and A.3.2 (up to Step 4).</td></tr>
<tr><td>t_1=0-1</td><td>Task 1-1: Start a timer (t_1=0). Set the cable heater control dial to 100%.[2]</td><td rowspan="4">Task 2: Plasma surface activation of base PA membrane sheet (30” x 24”) as described in Section A.3.3</td></tr>
<tr><td>t_1=1-3</td><td>Task 1-2: Transfer 2.8 L AA to 4.2 L DI water (in stainless steel container) to make an AA solution (7.0 L total volume) while purging the solution with nitrogen (Step 5 of Section A.3.2).[3]</td></tr>
<tr><td>t_1=3-4</td><td>Task 1-3: Remove the nitrogen purging line from the plastic container. Transfer 2 L of NaOH to the plastic container containing 4.2 L DI water to make a NaOH solution of 6.2 L total volume (Step 6 of Section A.3.2).[4]</td></tr>
<tr><td>t_1=4-6</td><td>Task 1-4: Remove the nitrogen purging line from the AA solution prepared in the stainless steel container. Transfer the prepared NaOH solution in the plastic container into the AA solution slowly (Step 7 of Section A.3.2).</td></tr>
<tr><td>t_1=6–7</td><td colspan="2">Task 3: Place the membrane sheet in the reactor as shown in Figure A-21.</td></tr>
<tr><td>t_1=7–10</td><td colspan="2">Task 4: Add additional NaOH (~500 mL) into the monomer solution slowly (while mixing the solution and monitoring the solution pH with a pH meter) to make the final solution pH to 6 ±0.05 (Step 8 of Section A.3.2).[5]</td></tr>
</table>

	t_1=10–15	**Task 5:** Set the 3-way valve handle to Position #1 and transfer the finalized monomer solution into the reactor using the peristaltic pump (**Figure A-21**).[6] After the transferring all the monomer solution, set the valve handle to Position #2 to start circulating the monomer solution in the reactor system (**Figure A-22**).
Phase II. Graft polymerization	t_2=0	**Task 6:** Start a new timer (t_2=0) and start logging the monomer solution temperature data via a temperature probe placed at the exit of the reactor (**Figure A-22**).
	t_2=20–30	**Task 7:** When the temperature of the monomer solution at the reactor outlet reaches 70 ± 0.2°C (after 20-30 min as shown in **Figure A-23**), change the temperature setpoint for the immersion circulator-water bath to 75°C and change the cable heater control dial to 35% in order to maintain the monomer solution temperature inside the reactor ~70°C for the rest of the graft polymerization period (i.e., 1 hour).
	t_2=60	**Task 8:** Terminate the graft polymerization reaction by pumping out the monomer solution from the reactor and take out the membrane sheet from the reactor and thoroughly rinse the membrane sheet under DI water stream. Store the synthesized SNS-PAA-PA membrane sheets in DI water.

Notes:

[1] Indicated times (in minutes) are elapsed time since the beginning of Phase I and Phase II.

[2] About 10 minutes prior to pumping the monomer solution into the reactor, set the cable heater control dial to 100% (the percentage of time that the heater cycles on). Monitor the temperature of the pipe wrapped in the cable heater using a temperature probe. After 10 minutes, the temperature reading should be close to ~160-180°C. Longer heating (> 10 – 15 minutes) without cycling water in the reactor system may result in overheating of the cable.

[3] The prepared AA monomer solution has pH ~1.55.

[4] The addition of the NaOH to the DI water rises the solution temperature to ~40°C.

[5] The temperature of the final AA monomer solution (after addition of the prepared NaOH solution to the AA solution) should be about ~72°C (which is close to the temperature at which graft polymerization reaction is performed).

[6] Pumping the finalized monomer solution (total volume of ~13.25 L) takes about 4 minutes (i.e., 4 minutes and 16 seconds). After pumping in all of 13.3 L of monomer solution into the reactor system, change the valve position so that the solution circulates within the reactor system.

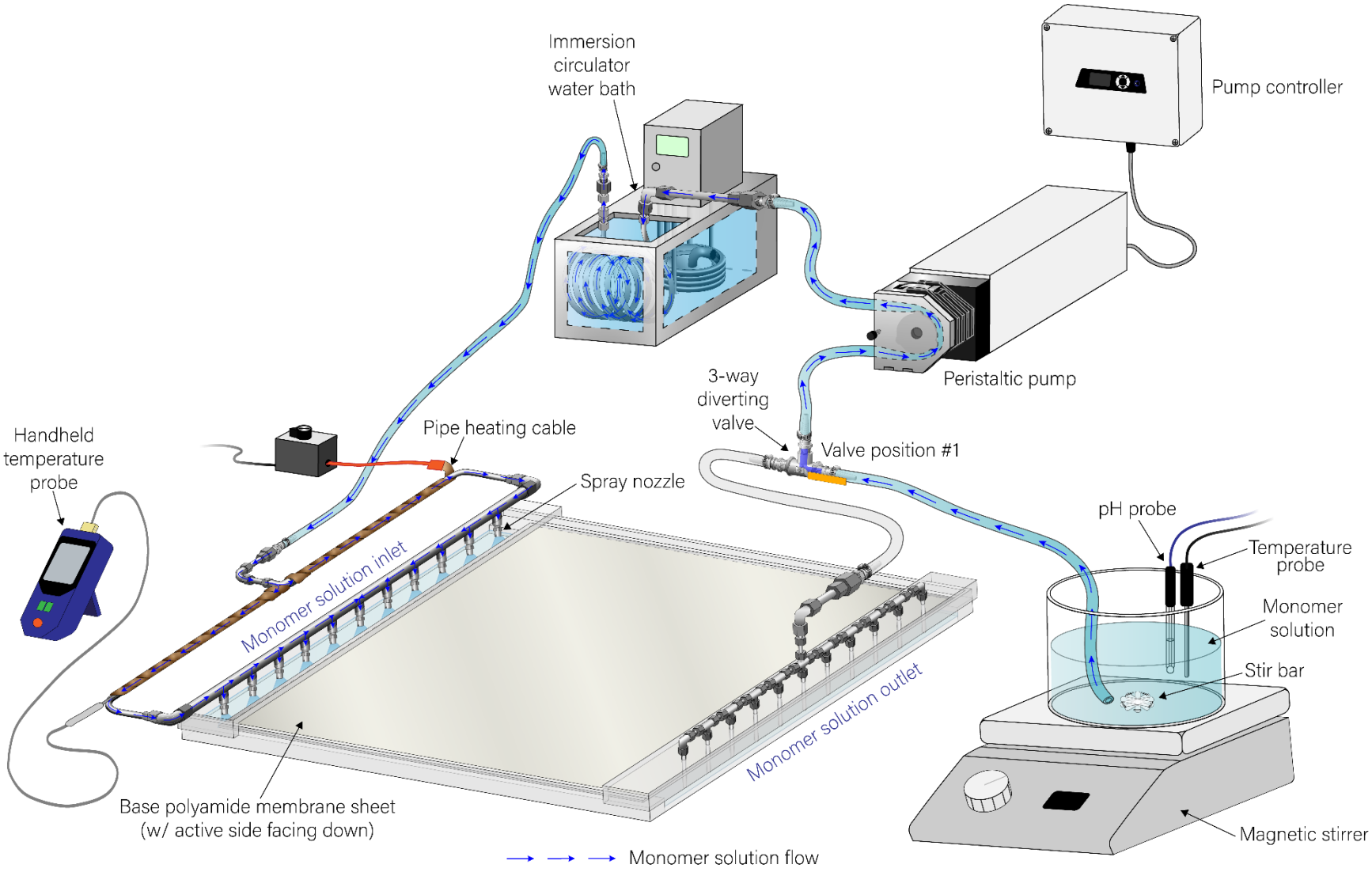

Figure A-21. Illustration of monomer solution introduction into the graft polymerization reactor.

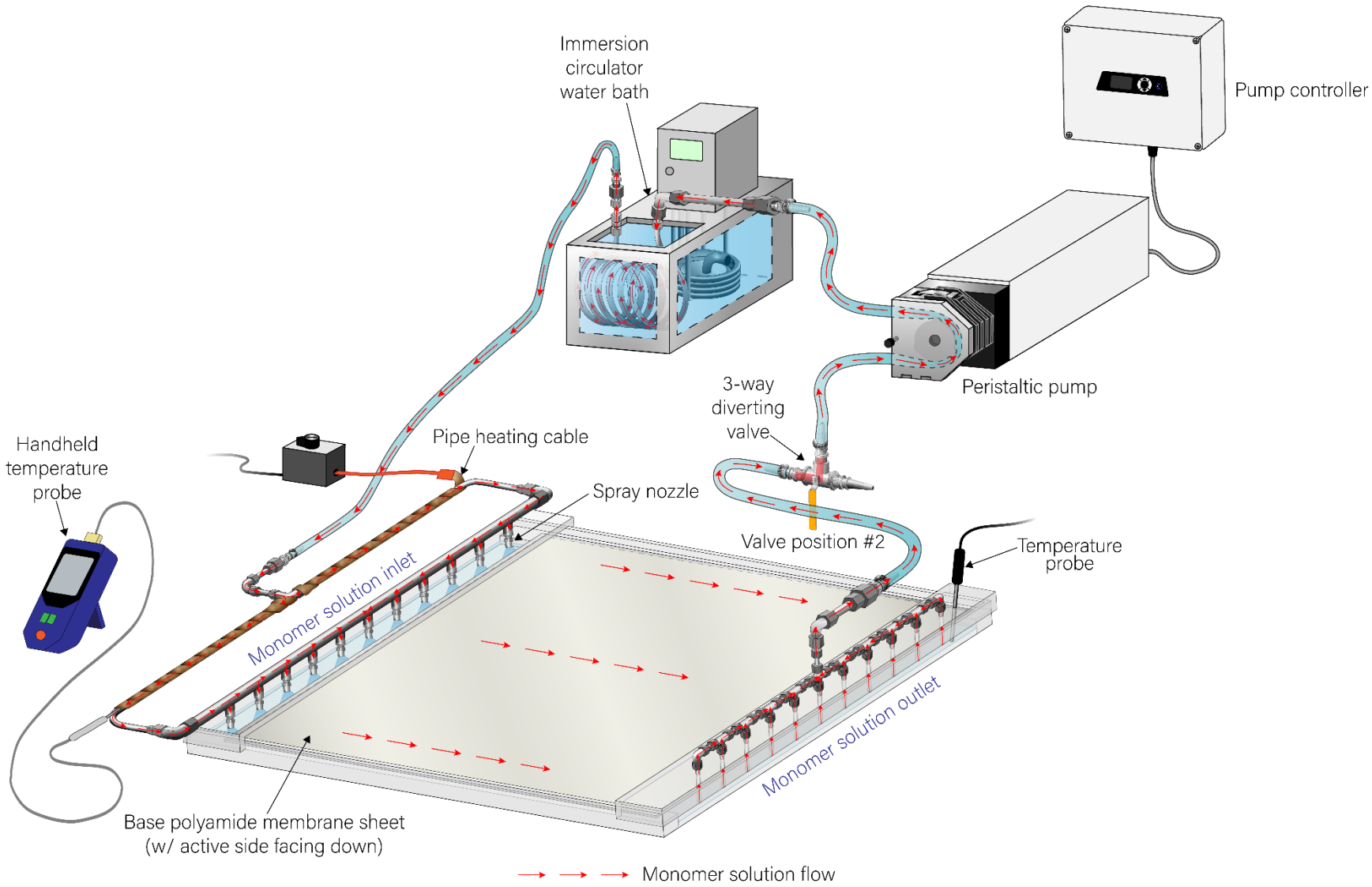

Figure A-22. Illustration of monomer solution circulation within the reactor system during graft polymerization.

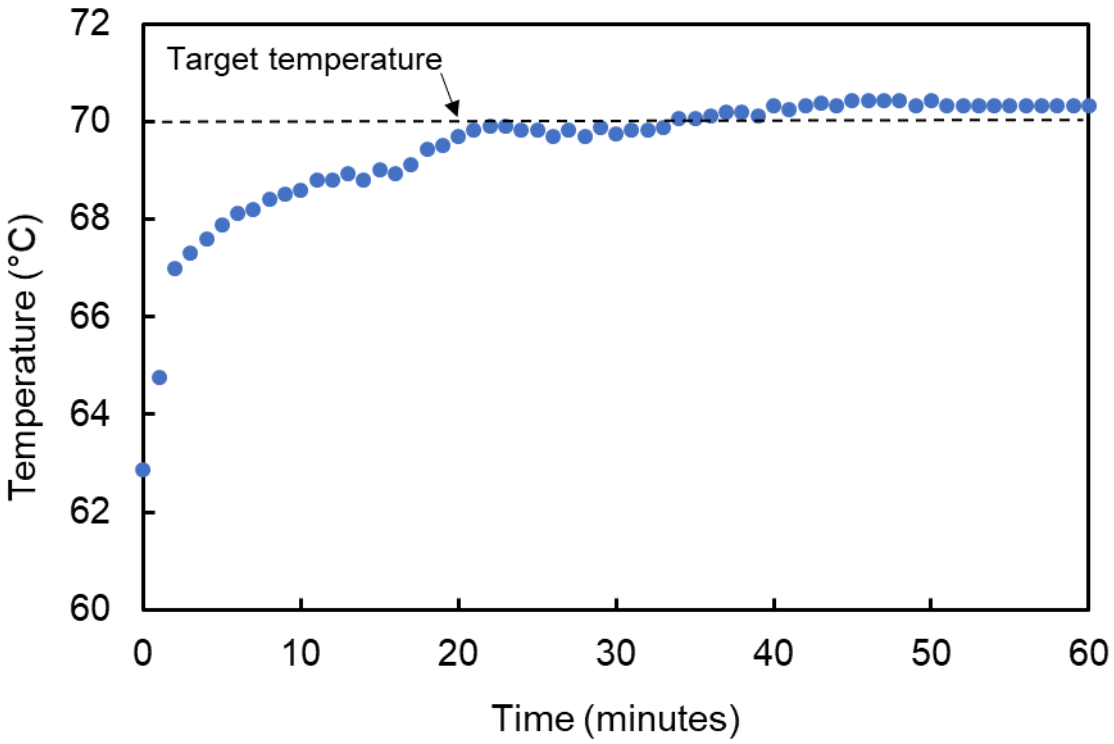

Figure A-23. A typical temperature profile of the AA monomer solution inside the reactor (measurement taken at the reactor outlet) during graft polymerization period of 1 h.

Appendix B. Membrane Performance Evaluation

B.1 Laboratory Plate-and-Frame RO (PFRO) Membrane Test System

Membrane performance evaluation and fouling tests were conducted using a laboratory plate-and-frame RO (PFRO) membrane recirculation unit (**Figure B-1**), which consisted of a cross flow cell (CF042D; Sterlitech Corp., Kent, WA) having an active membrane area of 42 cm^2. The flow channel, fitted with a channel spacer (CF042 Low Foulant Spacer; Sterlitech Corp., Kent, WA), had dimensions of 8.5 cm (L) x 3.9 cm (W) x 0.08 cm (H). The feed water stream to the PFRO unit was delivered by a positive displacement pump (Hydra-Cell; Wanner Engineering Inc., Minneapolis, MN) interfaced with a variable frequency drive (VFD) (L100-004MFU2; Hitachi Ltd., Japan). Transmembrane pressure was adjusted using a back-pressure valve (MCJ-050AB-3-1335G4Y; Hanbay Inc., Virginia Beach, VA) at the RO unit concentrate exit, along with the pump VFD, and monitored via a pressure transmitter (Model A-10; WIKA Instrument LP, Lawrenceville, GA). A refrigerated bath circulator (RTE-221, NESLAB Instruments Inc., Newington, NH) with a cooling coil was used to maintain a constant temperature (20.0 ± 0.2°C) feed solution, monitored with a temperature probe (Go!Temp; Vernier Software & Technology, Beaverton, OR).

The PFRO retentate and permeate flow rates were monitored with a liquid flow sensor (Model 101-7; McMillan, Georgetown, TX) and a digital liquid flow meter (Model 5025000; GJC Instruments Ltd., UK), respectively. Permeate and feed conductivities were monitored with an online sensor (Conductivity Probe; Vernier Software & Technology, Beaverton, OR) and a handheld conductivity probe (CON 6+; Oakton Instruments, Vernon Hills, IL), respectively. The measured conductivities were converted to NaCl salt concentrations using correlations derived based on simulation results from a multi-electrolyte thermodynamic simulator (OLI Systems, Inc., Morris Plains, NJ).

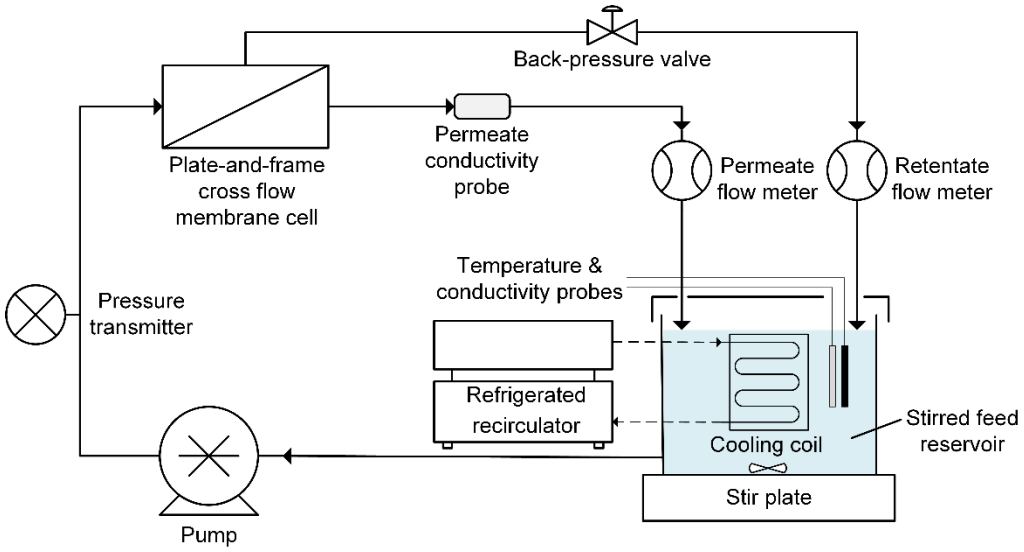

Figure B-1. Laboratory plate-and-frame reverse osmosis (PFRO) membrane test system.

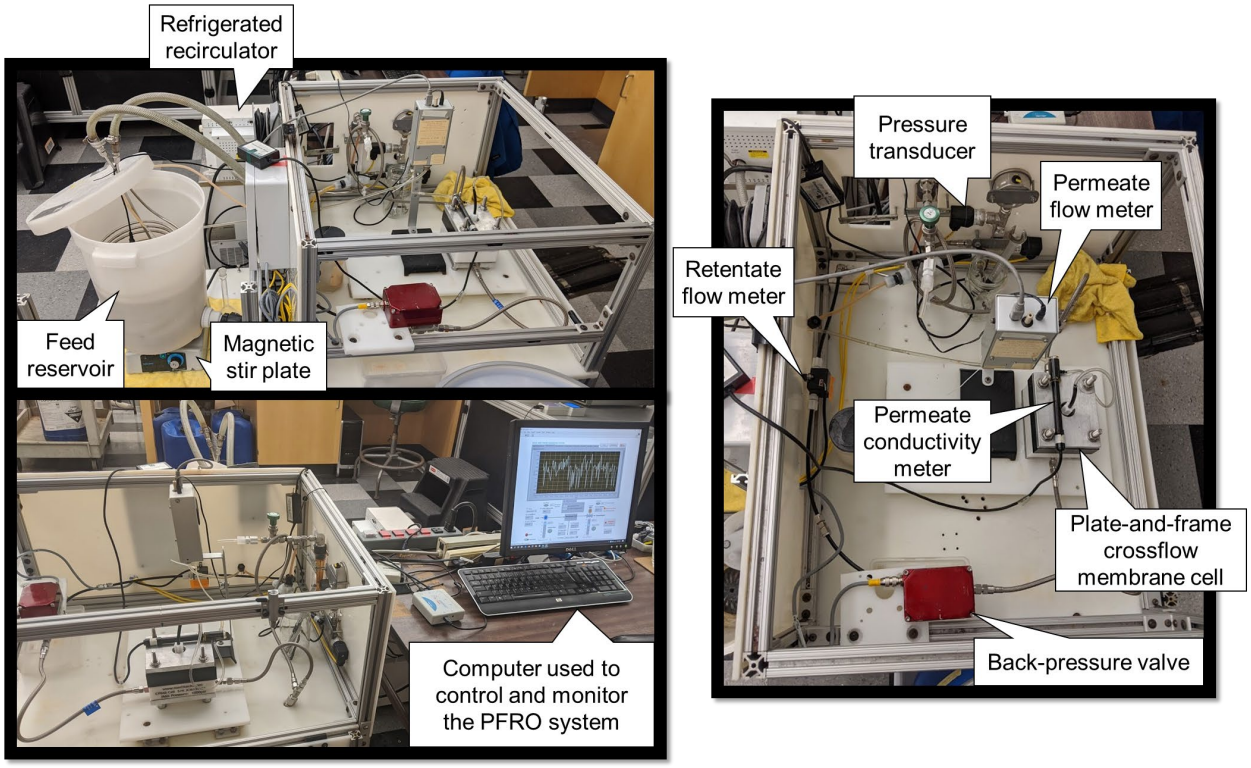

Figure B-2. Photos of the laboratory PFRO system.

B.2 Operation of the PFRO System

1. Place 10 L of fresh DI water in the feed reservoir. Place a stir bar in the feed reservoir and turn on the stir plate placed under the feed reservoir. Set the refrigerated recirculator temperature to 18.3°C (to keep the feed temperature at 20.0 ± 0.2 °C when operating at pressure in the range of ~600 – 850 psi). The temperature of the feed solution can be monitored using a temperature probe (Go!Temp, Vernier Software & Technology) connected to a Vernier Logger Lite desktop program.
2. Load a membrane coupon (cut to 4.4" x 2.2" via the procedure described in **Appendix A.2.1**) into the membrane cell (CF042D, Sterlitech Corporation). Fit a custom-made nylon shim of thickness 0.062" and a 31 mil (0.031") thick spacer (CF042 Low Foulant Spacer, Sterlitech Corporation) inside the membrane channel in order to have the final membrane cell crossflow channel height to exactly match the spacer thickness (i.e., 0.031") The membrane coupon should sit perfectly flat on the spacer and cover the inner o-ring but does not extend outside of the outer o-ring in order to prevent water leakage during filtration at high pressure. Assemble the membrane cell as shown in **Figure B.3**.
3. Open a custom-made LabVIEW program named 'PFM System 1.0.lvproj' from the connected desktop. From the Project Explorer window, double click 'PFM System 1.0.vi' to open the main system control window. Also, open 'DI-Conductivity-Labquest.vi' and 'DI-PermeateFlow.vi' for monitoring the permeate conductivity and permeate flow rate, respectively. Click 'Run' (arrow sign) for all three windows.
4. From the main program window, click 'Activate Pump' and 'Activate Valve'. Also click the toggle switch 'PT Range' to have a message appear on the screen 'High Pressure Mode'. This allows for the feed pressure reading above 300 psi.

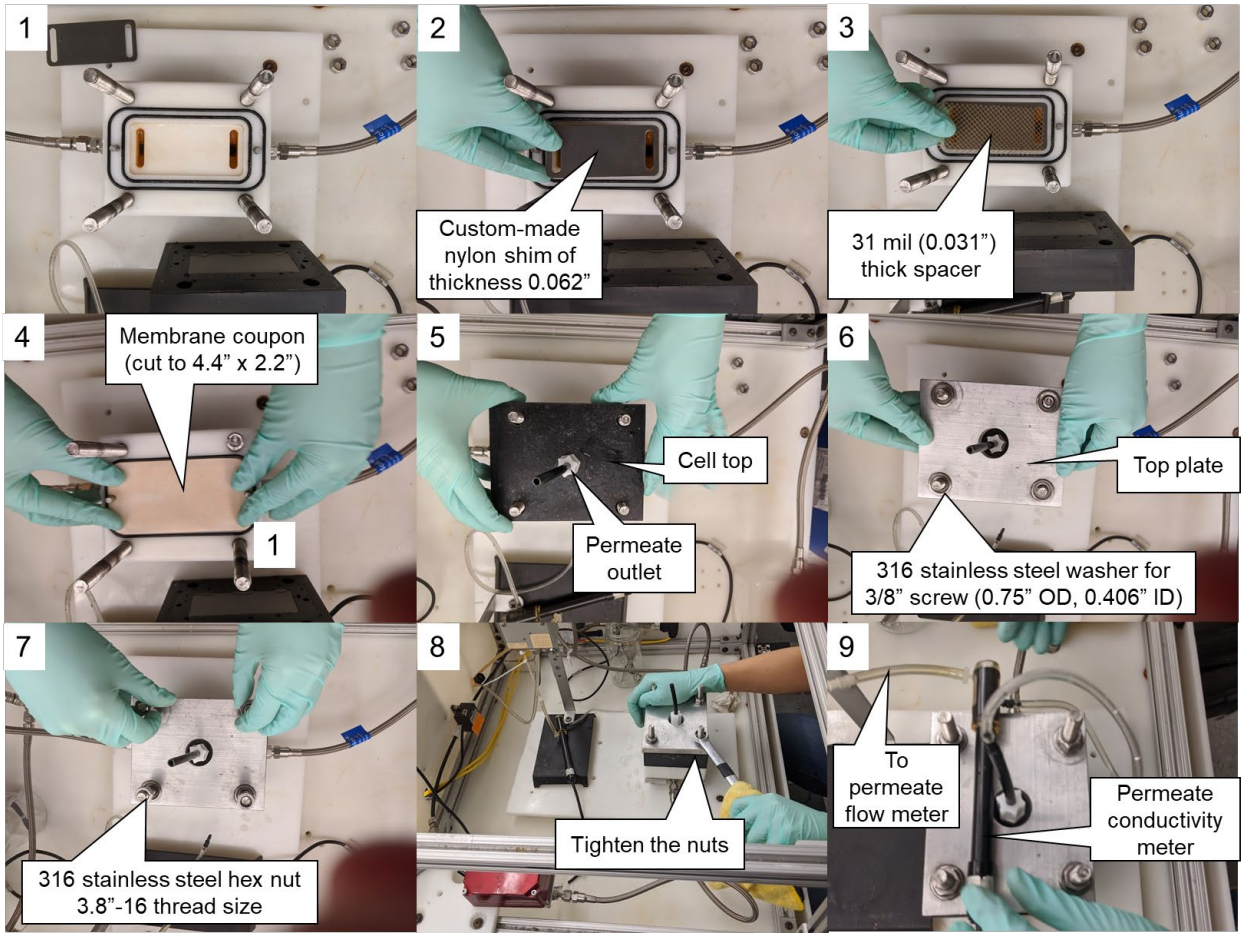

Figure B-3. Steps to set up the plate-and-frame RO membrane cell with a membrane coupon.

5. Increase the Pump Speed (%) until the retentate flow sensor reads ~900 mL/min (equivalent crossflow velocity ~49 cm/s). Click ‘Auto Pump’ to fix the crossflow velocity.
6. Decrease the Valve Opening (%) value (initially at 100%) slowly to increase the feed pressure to ~850 psi. Click ‘Auto Valve’ once the feed pressure reading is close to 850 psi.
7. Proceed with the membrane compaction at 850 psi for 24 hours to allow for the permeate flow reading to stabilize. Record the permeate flow rate value at 850 psi. Sequentially, reduce the feed pressure to ~800 psi, ~700 psi, ~600 psi, and ~500 psi. Record the stabilized permeate flow rate for each operating pressure. Convert the permeate flow rates to fluxes (in $L \cdot m^{-2} \cdot h^{-1}$) using the membrane cell active area (42 cm^2). Plot the permeate flux (in $L \cdot m^{-}$

$^{2}\cdot h^{-1}$) vs. feed pressure (in bar) and obtain a linear regression. Obtain the membrane permeability value ($L\cdot m^{-2}\cdot h^{-1}\cdot bar^{-1}$) from the slope of the linear regression line.

8. Click 'Activate Pump' and 'Activate Valve' to stop the DI water filtration (or set the pump speed and valve opening to zero).

9. Empty out the DI water in the feed tank. Place 320 grams of NaCl and 10 L of fresh DI water in the feed container to prepare a 32 g/L NaCl aqueous solution. Place a stir bar in the feed reservoir and turn on the stir plate placed under the feed reservoir to mix the solution. The conductivity of the 32 g/L NaCl feed solution should be close to 51,000 μS at 20°C. Click 'Options' tab from the main control window and click the button for 'Manual Input Feed Conductivity.' Type 51,000 in the box under CT-1 (uS) Manual Input to set the feed conductivity manually (if the concentration is outside of the range of the currently installed feed conductivity meter) (**Figure B-4**). Use the same the refrigerated recirculator temperature setpoint as in Step 1 to keep the feed solution temperature at 20.0 ± 0.2°C.

10. Click 'Activate Pump' and 'Activate Valve' again and increase the Pump Speed (%) until the retentate flow sensor reads ~900 mL/min (equivalent crossflow velocity of ~49 cm/s). Click 'Auto Pump' to fix the crossflow velocity.

11. Decrease the Valve Opening (%) value slowly to increase the feed pressure to ~800 psi. Click 'Auto Valve' once the feed pressure reading is close to 800 psi. Filter the salt solution for 24 h to attain stabilized permeate flow rate and permeate conductivity values.

12. Change the feed pressure by changing the Valve Opening (%) to set the permeate flow rate to ~2.37 mL/min, which corresponds to permeate flux of ~20 $gallon\cdot ft^{-2}\cdot day^{-1}$ or 34 $L\cdot m^{-2}\cdot h^{-1}$. Allow for the permeate flow rate to stabilize (~20 – 30 min) and record the permeate

concentration. Calculate the observed and intrinsic salt rejection values as well as salt permeability value (*B*) (See **Section 4.2.3**).

13. Click 'Activate Pump' and 'Activate Valve' to turn off the pump and set the retentate valve opening to 100% (the default system value).

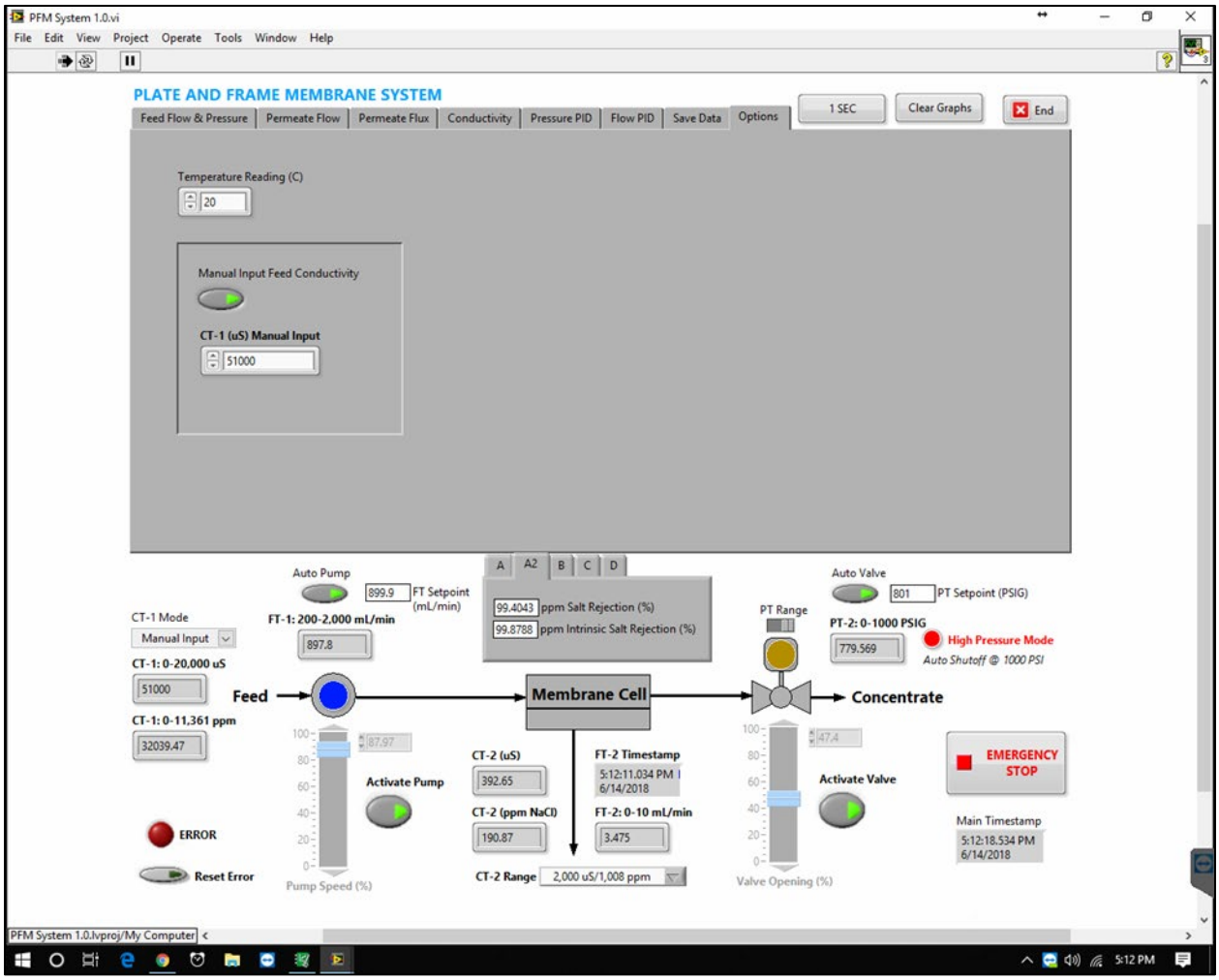

Figure B-4. The main user interface of the custom-made LabView program used to control the PFRO system.

B.3 Determination of the Feed-side Mass Transfer Coefficient

Determination of the feed-side mass transfer coefficient (k) should be carried out following membrane compaction and saline water (i.e., 32 g/L NaCl) filtration as described in **Appendix B.2** in order to ensure that the membrane tested is conditioned. At a fixed retentate flow rate, change the Valve Opening to set the feed pressure to the desired value (in the range of ~500 – 850 psi). Let the system stabilized for ~30 min before recording the permeate flux and permeate conductivity at the fixed crossflow velocity and feed pressure. Determine observed salt rejection (R_o) at various permeate fluxes (in the range of 15 – 30 gal·ft^{-2}·day^{-1} or 25 – 50 L·m^{-2}·h^{-1}). Using the combined equation from the Film Theory and solution-diffusion model (i.e., $\ln\left(J_v \frac{1-R_o}{R_o}\right) = \ln B + \frac{J_v}{k}$), the feed-side mass transfer coefficient and salt permeability coefficient (B) can be simultaneously determined by plotting J_v vs. $\ln\left(J_v \frac{1-R_o}{R_o}\right)$ to obtain the slope (i.e., $1/k$) and the intercept (i.e., ln B).

References

1. Gude, V.G., Desalination and water reuse to address global water scarcity, Reviews in Environmental Science and Bio/Technology 16 (2017) 591-609.

2. Cohen, Y., R. Semiat, and A. Rahardianto, A perspective on reverse osmosis water desalination: Quest for sustainability, AIChE Journal 63 (2017) 1771-1784.

3. Voutchkov, N., Energy use for membrane seawater desalination - current status and trends, Desalination 431 (2018) 2-14.

4. Gu, H., A. Rahardianto, L.X. Gao, P.D. Christofides, and Y. Cohen, Ultrafiltration with self-generated RO concentrate pulse backwash in a novel integrated seawater desalination UF-RO system, Journal of Membrane Science 520 (2016) 111-119.

5. Badruzzaman, M., N. Voutchkov, L. Weinrich, and J.G. Jacangelo, Selection of pretreatment technologies for seawater reverse osmosis plants: A review, Desalination 449 (2019) 78-91.

6. Wolf, P.H., S. Siverns, and S. Monti, UF membranes for RO desalination pretreatment, Desalination 182 (2005) 293-300.

7. Galloway, M. and J. Mahoney, Ultrafiltration for seawater reverse osmosis pretreatment, Membrane Technology 2004 (2004) 5-8.

8. Prihasto, N., Q.F. Liu, and S.H. Kim, Pre-treatment strategies for seawater desalination by reverse osmosis system, Desalination 249 (2009) 308-316.

9. Li, S., S.G.J. Heijman, J.Q.J.C. Verberk, G.L. Amy, and J.C. van Dijk, Seawater ultrafiltration fouling control: Backwashing with demineralized water/SWRO permeate, Separation and Purification Technology 98 (2012) 327-336.

10. Hilal, N., M. Khayet, and C.J. Wright, Membrane modification : technology and applications. 2012, Boca Raton: Taylor & Francis. xviii, 492 p.

11. Ulbricht, M., Advanced functional polymer membranes, Polymer 47 (2006) 2217-2262.

12. Gohil, J.M. and P. Ray, A review on semi-aromatic polyamide TFC membranes prepared by interfacial polymerization: Potential for water treatment and desalination, Separation and Purification Technology 181 (2017) 159-182.

13. Goh, P.S., W.J. Lau, M.H.D. Othman, and A.F. Ismail, Membrane fouling in desalination and its mitigation strategies, Desalination 425 (2018) 130-155.

14. Werber, J.R., A. Deshmukh, and M. Elimelech, The critical need for increased selectivity, not increased water permeability, for desalination membranes, Environmental Science & Technology Letters 3 (2016) 112-120.

15. Kim, M.-M., N.H. Lin, G.T. Lewis, and Y. Cohen, Surface nano-structuring of reverse osmosis membranes via atmospheric pressure plasma-induced graft polymerization for reduction of mineral scaling propensity, Journal of Membrane Science 354 (2010) 142-149.

16. Lin, N.H., M.M. Kim, G.T. Lewis, and Y. Cohen, Polymer surface nano-structuring of reverse osmosis membranes for fouling resistance and improved flux performance, Journal of Materials Chemistry 20 (2010) 4642-4652.

17. Varin, K.J., N.H. Lin, and Y. Cohen, Biofouling and cleaning effectiveness of surface nanostructured reverse osmosis membranes, Journal of Membrane Science 446 (2013) 472-481.

18. Currie, E.P.K., A.B. Sieval, G.J. Fleer, and M.A.C. Stuart, Polyacrylic acid brushes: Surface pressure and salt-induced swelling, Langmuir 16 (2000) 8324-8333.

19. Zhang, H.N. and J. Ruhe, Swelling of poly(methacrylic acid) brushes: influence of monovalent salts in the environment, Macromolecules 38 (2005) 4855-4860.

20. Zhang, T.C., Environmental and Water Resources Institute (U.S.). Membrane Technology Task Committee., and American Society of Civil Engineers., Membrane technology and environmental applications. 2012, Reston, VA: American Society of Civil Engineers. xii, 742 p.

21. Huang, H., K. Schwab, and J.G. Jacangelo, Pretreatment for Low Pressure Membranes in Water Treatment: A Review, Environmental Science & Technology 43 (2009) 3011-3019.

22. Singh, N., Z. Chen, N. Tomer, S.R. Wickramasinghe, N. Soice, and S.M. Husson, Modification of regenerated cellulose ultrafiltration membranes by surface-initiated atom transfer radical polymerization, Journal of Membrane Science 311 (2008) 225-234.

23. Van Der Bruggen, B., C. Vandecasteele, T. Van Gestel, W. Doyen, and R. Leysen, A review of pressure-driven membrane processes in wastewater treatment and drinking water production, Environmental Progress 22 (2003) 46-56.

24. Jacangelo, J.G., R.R. Trussell, and M. Watson, Role of membrane technology in drinking water treatment in the United States, Desalination 113 (1997) 119-127.

25. Costa, A.R., M.N. de Pinho, and M. Elimelech, Mechanisms of colloidal natural organic matter fouling in ultrafiltration, Journal of Membrane Science 281 (2006) 716-725.

26. Kubota, N., T. Hashimoto, and Y. Mori, Microfiltration and Ultrafiltration, in Advanced Membrane Technology and Applications. 2008, John Wiley & Sons, Inc. p. 101-129.

27. Cheryan, M. and M. Cheryan, Ultrafiltration and microfiltration handbook. 1998, Lancaster, Pa.: Technomic Pub. Co. xvii, 527 p.

28. Zeman, L.J. and A.L. Zydney, Microfiltration and ultrafiltration : principles and applications. 1996, New York: Marcel Dekker. xix, 618 p.

29. Frenkel, V.S., Y. Cohen, G. Cummings, A. Rahardianto, S. Surawanvijit, and J. Thompson, New Techniques for Real-Time Monitoring of Membrane Integrity for Virus Removal: Pulsed-Marker Membrane Integrity Monitoring System. 2014: WateReuse Research Foundation.

30. American Water Works Association. and Knovel (Firm), Microfiltration and ultrafiltration membranes for drinking water, in AWWA manual M53. 2005, American Water Works Association,: Denver, CO. p. xxii, 257 p.

31. EPA, Low pressure membrane filtration for pathogen removal: application, implementation, and regulatory issues, EPA 815-C-01-001 (April 2001)

32. Madaeni, S.S., A.G. Fane, and G.S. Grohmann, Virus removal from water and wastewater using membranes, Journal of Membrane Science 102 (1995) 65-75.

33. Clever, M., F. Jordt, R. Knauf, N. Räbiger, M. Rüdebusch, and R. Hilker-Scheibel, Process water production from river water by ultrafiltration and reverse osmosis, Desalination 131 (2000) 325-336.

34. Pearce, G.K., UF/MF Membrane Water Treatment: Principles and Design. 2011: Water Treatment Academy.

35. Ghayeni, S.B.S., S.S. Madaeni, A.G. Fane, and R.P. Schneider, Aspects of microfiltration and reverse osmosis in municipal wastewater reuse, Desalination 106 (1996) 25-29.

36. Rosberg, R., Ultrafiltration (new technology), a viable cost-saving pretreatment for reverse osmosis and nanofiltration - A new approach to reduce costs, Desalination 110 (1997) 107-113.

37. Li, Q., S. Mahendra, D.Y. Lyon, L. Brunet, M.V. Liga, D. Li, and P.J.J. Alvarez, Antimicrobial nanomaterials for water disinfection and microbial control: Potential applications and implications, Water Research 42 (2008) 4591-4602.

38. Gu, H. (2017). Mitigation of mineral scaling and fouling of RO desalination via self-adaptive operation. UCLA. ProQuest ID: Gu_ucla_0031D_16350. Merritt ID: ark:/13030/m5wx2djn. Retrieved from https://escholarship.org/uc/item/9pf7n8fp

39. Kimura, K., Y. Hane, Y. Watanabe, G. Amy, and N. Ohkuma, Irreversible membrane fouling during ultrafiltration of surface water, Water Research 38 (2004) 3431-3441.

40. Fan, L.H., J.L. Harris, F.A. Roddick, and N.A. Booker, Influence of the characteristics of natural organic matter on the fouling of microfiltration membranes, Water Research 35 (2001) 4455-4463.

41. Flemming, H.C., G. Schaule, T. Griebe, J. Schmitt, and A. Tamachkiarowa, Biofouling - the Achilles heel of membrane processes, Desalination 113 (1997) 215-225.

42. Hyun, J., H. Jang, K. Kim, K. Na, and T. Tak, Restriction of biofouling in membrane filtration using a brush-like polymer containing oligoethylene glycol side chains, Journal of Membrane Science 282 (2006) 52-59.

43. Sutzkover, I., D. Hasson, and R. Semiat, Simple technique for measuring the concentration polarization level in a reverse osmosis system, Desalination 131 (2000) 117-127.

44. Baker, R.W., Reverse Osmosis, in Membrane Technology and Applications. 2004, John Wiley & Sons, Ltd. p. 191-235.

45. Geise, G.M., H.B. Park, A.C. Sagle, B.D. Freeman, and J.E. McGrath, Water permeability and water/salt selectivity tradeoff in polymers for desalination, Journal of Membrane Science 369 (2011) 130-138.

46. Lee, J., C.M. Doherty, A.J. Hill, and S.E. Kentish, Water vapor sorption and free volume in the aromatic polyamide layer of reverse osmosis membranes, Journal of Membrane Science 425 (2013) 217-226.

47. Freger, V., Nanoscale heterogeneity of polyamide membranes formed by interfacial polymerization, Langmuir 19 (2003) 4791-4797.

48. Kamada, T., T. Ohara, T. Shintani, and T. Tsuru, Controlled surface morphology of polyamide membranes via the addition of co-solvent for improved permeate flux, Journal of Membrane Science 467 (2014) 303-312.

49. Fujioka, T., N. Oshima, R. Suzuki, S.J. Khan, A. Roux, Y. Poussade, J.E. Drewes, and L.D. Nghiem, Rejection of small and uncharged chemicals of emerging concern by reverse osmosis membranes: The role of free volume space within the active skin layer, Separation and Purification Technology 116 (2013) 426-432.

50. Lin, L., R. Lopez, G.Z. Ramon, and O. Coronell, Investigating the void structure of the polyamide active layers of thin-film composite membranes, Journal of Membrane Science 497 (2016) 365-376.

51. Kosutic, K., L. Kastelan-Kunst, and B. Kunst, Porosity of some commercial reverse osmosis and nanofiltration polyamide thin-film composite membranes, Journal of Membrane Science 168 (2000) 101-108.

52. Zhang, H. and G.M. Geise, Modeling the water permeability and water/salt selectivity tradeoff in polymer membranes, Journal of Membrane Science 520 (2016) 790-800.

53. Kim, S.H., S.Y. Kwak, and T. Suzuki, Positron annihilation spectroscopic evidence to demonstrate the flux-enhancement mechanism in morphology-controlled thin-film-composite (TFC) membrane, Environmental Science & Technology 39 (2005) 1764-1770.

54. Werber, J.R., S.K. Bull, and M. Elimelech, Acyl-chloride quenching following interfacial polymerization to modulate the water permeability, selectivity, and surface charge of desalination membranes, Journal of Membrane Science 535 (2017) 357-364.

55. Geise, G.M., D.R. Paul, and B.D. Freeman, Fundamental water and salt transport properties of polymeric materials, Progress in Polymer Science 39 (2014) 1-42.

56. Wong, M.C.Y., L. Lin, O. Coronell, E.M.V. Hoek, and G.Z. Ramon, Impact of liquid-filled voids within the active layer on transport through thin-film composite membranes, Journal of Membrane Science 500 (2016) 124-135.

57. Ghosh, A.K., B.H. Jeong, X.F. Huang, and E.M.V. Hoek, Impacts of reaction and curing conditions on polyamide composite reverse osmosis membrane properties, Journal of Membrane Science 311 (2008) 34-45.

58. Lind, M.L., D.E. Suk, T.V. Nguyen, and E.M.V. Hoek, Tailoring the structure of thin film nanocomposite membranes to achieve seawater RO membrane performance, Environmental Science & Technology 44 (2010) 8230-8235.

59. Lee, T.H., M.Y. Lee, H.D. Lee, J.S. Roh, H.W. Kim, and H.B. Park, Highly porous carbon nanotube/polysulfone nanocomposite supports for high-flux polyamide reverse osmosis membranes, Journal of Membrane Science 539 (2017) 441-450.

60. Choi, W., J.E. Gu, S.H. Park, S. Kim, J. Bang, K.Y. Baek, B. Park, J.S. Lee, E.P. Chan, and J.H. Lee, Tailor-Made Polyamide Membranes for Water Desalination, ACS Nano 9 (2015) 345-355.

61. Bernstein, R., S. Belfer, and V. Freger, Improving performance of spiral wound RO elements by in situ concentration polarization-enhanced radical graft polymerization, Journal of Membrane Science 405 (2012) 79-84.

62. Liu, C., Y.Q. Guo, J.M. Zhang, B. Tian, O.K. Lin, Y.W. Liu, and C.H. Zhang, Tailor-made high-performance reverse osmosis membranes by surface fixation of hydrophilic macromolecules for wastewater treatment, RSC Advances 9 (2019) 17766-17777.

63. Zhao, Y.L., L. Dai, Q.F. Zhang, and S.B. Zhang, Surface modification of polyamide reverses osmosis membrane by phosphonic acid group with improved performance, Journal of Applied Polymer Science 136 (2019) 46931.

64. Xie, W., G.M. Geise, B.D. Freeman, H.S. Lee, G. Byun, and J.E. McGrath, Polyamide interfacial composite membranes prepared from m-phenylene diamine, trimesoyl chloride and a new disulfonated diamine, Journal of Membrane Science 403 (2012) 152-161.

65. Khorshidi, B., T. Thundat, B.A. Fleck, and M. Sadrzadeh, A Novel Approach Toward Fabrication of High Performance Thin Film Composite Polyamide Membranes, Scientific Reports 6 (2016)

66. Nadler, R. and S. Srebnik, Molecular simulation of polyamide synthesis by interfacial polymerization, Journal of Membrane Science 315 (2008) 100-105.

67. Jegal, J., S.G. Min, and K.H. Lee, Factors affecting the interfacial polymerization of polyamide active layers for the formation of polyamide composite membranes, Journal of Applied Polymer Science 86 (2002) 2781-2787.

68. Jin, Y. and Z.H. Su, Effects of polymerization conditions on hydrophilic groups in aromatic polyamide thin films, Journal of Membrane Science 330 (2009) 175-179.

69. Khan, M.T., C.L.D. Manes, C. Aubry, L. Gutierrez, and J.P. Croue, Kinetic study of seawater reverse osmosis membrane fouling, Environmental Science & Technology 47 (2013) 10884-10894.

70. Goosen, M.F.A., S.S. Sablani, H. Ai-Hinai, S. Ai-Obeidani, R. Al-Belushi, and D. Jackson, Fouling of reverse osmosis and ultrafiltration membranes: A critical review, Separation Science and Technology 39 (2004) 2261-2297.

71. Bar-Zeev, E., U. Passow, S.R.V. Castrillon, and M. Elimelech, Transparent Exopolymer Particles: From Aquatic Environments and Engineered Systems to Membrane Biofouling, Environmental Science & Technology 49 (2015) 691-707.

72. Zhang, Q.F., C.C. Zhang, J.L. Xu, Y. Nie, S.H. Li, and S.B. Zhang, Effect of poly(vinyl alcohol) coating process conditions on the properties and performance of polyamide reverse osmosis membranes, Desalination 379 (2016) 42-52.

73. Louie, J.S., I. Pinnau, I. Ciobanu, K.P. Ishida, A. Ng, and M. Reinhard, Effects of polyether-polyamide block copolymer coating on performance and fouling of reverse osmosis membranes, Journal of Membrane Science 280 (2006) 762-770.

74. Sagle, A.C., E.M. Van Wagner, H. Ju, B.D. McCloskey, B.D. Freeman, and M.M. Sharma, PEG-coated reverse osmosis membranes: Desalination properties and fouling resistance, Journal of Membrane Science 340 (2009) 92-108.

75. Zhou, Y., S. Yu, C.J. Gao, and X.S. Feng, Surface modification of thin film composite polyamide membranes by electrostatic self deposition of polycations for improved fouling resistance, Separation and Purification Technology 66 (2009) 287-294.

76. Xu, J., X.S. Feng, and C.J. Gao, Surface modification of thin-film-composite polyamide membranes for improved reverse osmosis performance, Journal of Membrane Science 370 (2011) 116-123.

77. Kwon, Y.N., S. Hong, H. Choi, and T. Tak, Surface modification of a polyamide reverse osmosis membrane for chlorine resistance improvement, Journal of Membrane Science 415 (2012) 192-198.

78. Nikkola, J., X. Liu, Y. Li, M. Raulio, H.L. Alakomi, J. Wei, and C.Y. Tang, Surface modification of thin film composite RO membrane for enhanced anti-biofouling performance, Journal of Membrane Science 444 (2013) 192-200.

79. Yu, S.C., G.H. Yao, B.Y. Dong, H.W. Zhu, X.Y. Peng, J. Liu, M.H. Liu, and C.J. Gao, Improving fouling resistance of thin-film composite polyamide reverse osmosis membrane by coating natural hydrophilic polymer sericin, Separation and Purification Technology 118 (2013) 285-293.

80. Ni, L., J.Q. Meng, X.G. Li, and Y.F. Zhang, Surface coating on the polyamide TFC RO membrane for chlorine resistance and antifouling performance improvement, Journal of Membrane Science 451 (2014) 205-215.

81. Saeki, D., T. Tanimoto, and H. Matsuyama, Prevention of bacterial adhesion on polyamide reverse osmosis membranes via electrostatic interactions using a cationic phosphorylcholine polymer coating, Colloids and Surfaces a-Physicochemical and Engineering Aspects 443 (2014) 171-176.

82. Choi, H., Y. Jung, S. Han, T. Tak, and Y.N. Kwon, Surface modification of SWRO membranes using hydroxyl poly (oxyethylene) methacrylate and zwitterionic carboxylated polyethyleneimine, Journal of Membrane Science 486 (2015) 97-105.

83. Tang, C.Y.Y., Y.N. Kwon, and J.O. Leckie, Effect of membrane chemistry and coating layer on physiochemical properties of thin film composite polyamide RO and NF membranes I. FTIR and XPS characterization of polyamide and coating layer chemistry, Desalination 242 (2009) 149-167.

84. Lee, J.H., J.Y. Chung, E.P. Chan, and C.M. Stafford, Correlating chlorine-induced changes in mechanical properties to performance in polyamide-based thin film composite membranes, Journal of Membrane Science 433 (2013) 72-79.

85. Miller, D.J., D.R. Dreyer, C.W. Bielawski, D.R. Paul, and B.D. Freeman, Surface modification of water purification membranes, Angewandte Chemie, International Edition 56 (2017) 4662-4711.

86. Hurwitz, G., G.R. Guillen, and E.M.V. Hoek, Probing polyamide membrane surface charge, zeta potential, wettability, and hydrophilicity with contact angle measurements, Journal of Membrane Science 349 (2010) 349-357.

87. Ishigami, T., K. Amano, A. Fujii, Y. Ohmukai, E. Kamio, T. Maruyama, and H. Matsuyama, Fouling reduction of reverse osmosis membrane by surface modification via layer-by-layer assembly, Separation and Purification Technology 99 (2012) 1-7.

88. Wang, Y., Z. Wang, X.L. Han, J.X. Wang, and S.C. Wang, Improved flux and anti-biofouling performances of reverse osmosis membrane via surface layer-by-layer assembly, Journal of Membrane Science 539 (2017) 403-411.

89. Chan, E.P., W.D. Mulhearn, Y.R. Huang, J.H. Lee, D. Lee, and C.M. Stafford, Tailoring the Permselectivity of Water Desalination Membranes via Nanoparticle Assembly, Langmuir 30 (2014) 611-616.

90. Ma, W., A. Soroush, T.V.A. Luong, G. Brennan, M.S. Rahaman, B. Asadishad, and N. Tufenkji, Spray- and spin-assisted layer-by-layer assembly of copper nanoparticles on thin-film composite reverse osmosis membrane for biofouling mitigation, Water Research 99 (2016) 188-199.

91. Martin, T.P., K.K.S. Lau, K. Chan, Y. Mao, M. Gupta, A.S. O'Shaughnessy, and K.K. Gleason, Initiated chemical vapor deposition (iCVD) of polymeric nanocoatings, Surface & Coatings Technology 201 (2007) 9400-9405.

92. Yang, R., J.J. Xu, G. Ozaydin-Ince, S.Y. Wong, and K.K. Gleason, Surface-tethered zwitterionic ultrathin antifouling coatings on reverse osmosis membranes by initiated chemical vapor deposition, Chemistry of Materials 23 (2011) 1263-1272.

93. Ozaydin-Ince, G., A. Matin, Z. Khan, S.M.J. Zaidi, and K.K. Gleason, Surface modification of reverse osmosis desalination membranes by thin-film coatings deposited by initiated chemical vapor deposition, Thin Solid Films 539 (2013) 181-187.

94. Matin, A., H.Z. Shafi, Z. Khan, M. Khaled, R. Yang, K. Gleason, and F. Rehman, Surface modification of seawater desalination reverse osmosis membranes: Characterization studies & performance evaluation, Desalination 343 (2014) 128-139.

95. Shafi, H.Z., Z. Khan, R. Yang, and K.K. Gleason, Surface modification of reverse osmosis membranes with zwitterionic coating for improved resistance to fouling, Desalination 362 (2015) 93-103.

96. Shafi, H.Z., M. Wang, K.K. Gleason, and Z. Khan, Synthesis of surface-anchored stable zwitterionic films for inhibition of biofouling, Materials Chemistry and Physics 239 (2020) 121971.

97. Yang, R., H. Jang, R. Stocker, and K.K. Gleason, Synergistic prevention of biofouling in seawater desalination by zwitterionic surfaces and low-level chlorination, Advanced Materials 26 (2014) 1711-1718.

98. Van Wagner, E.M., A.C. Sagle, M.M. Sharma, Y.H. La, and B.D. Freeman, Surface modification of commercial polyamide desalination membranes using poly(ethylene glycol) diglycidyl ether to enhance membrane fouling resistance, Journal of Membrane Science 367 (2011) 273-287.

99. Kang, G.D., M. Liu, B. Lin, Y.M. Cao, and Q. Yuan, A novel method of surface modification on thin-film composite reverse osmosis membrane by grafting poly(ethylene glycol), Polymer 48 (2007) 1165-1170.

100. Wei, X.Y., Z. Wang, J. Chen, J.X. Wang, and S.C. Wang, A novel method of surface modification on thin-film-composite reverse osmosis membrane by grafting hydantoin derivative, Journal of Membrane Science 346 (2010) 152-162.

101. Xu, J., Z. Wang, L.L. Yu, J.X. Wang, and S.C. Wang, A novel reverse osmosis membrane with regenerable anti-biofouling and chlorine resistant properties, Journal of Membrane Science 435 (2013) 80-91.

102. Xu, J., Z. Wang, J.X. Wang, and S.C. Wang, Positively charged aromatic polyamide reverse osmosis membrane with high anti-fouling property prepared by polyethylenimine grafting, Desalination 365 (2015) 398-406.

103. Wu, J.H., Z. Wang, Y. Wang, W.T. Yan, J.X. Wang, and S.C. Wang, Polyvinylamine-grafted polyamide reverse osmosis membrane with improved antifouling property, Journal of Membrane Science 495 (2015) 1-13.

104. Kang, G.D., H.J. Yu, Z.N. Liu, and Y.M. Cao, Surface modification of a commercial thin film composite polyamide reverse osmosis membrane by carbodiimide-induced grafting with poly(ethylene glycol) derivatives, Desalination 275 (2011) 252-259.

105. Staros, J.V., R.W. Wright, and D.M. Swingle, Enhancement by *N*-hydroxysulfosuccinimide of water-soluble carbodiimide-mediated coupling reactions, Analytical Biochemistry 156 (1986) 220-222.

106. Sehgal, D. and I.K. Vijay, A method for the high-efficiency of water-soluble carbodiimide-mediated amidation, Analytical Biochemistry 218 (1994) 87-91.

107. Hu, Y.T., K. Lu, F. Yan, Y.L. Shi, P.P. Yu, S.C. Yu, S.H. Li, and C.J. Gao, Enhancing the performance of aromatic polyamide reverse osmosis membrane by surface modification via covalent attachment of polyvinyl alcohol (PVA), Journal of Membrane Science 501 (2016) 209-219.

108. Liu, M.H., Q. Chen, L.Z. Wang, S.C. Yu, and C.J. Gao, Improving fouling resistance and chlorine stability of aromatic polyamide thin-film composite RO membrane by surface grafting of polyvinyl alcohol (PVA), Desalination 367 (2015) 11-20.

109. An, J.-C., A. Weaver, B. Kim, A. Barkatt, D. Poster, W.N. Vreeland, J. Silverman, and M. Al-Sheikhly, Radiation-induced synthesis of poly(vinylpyrrolidone) nanogel, Polymer 52 (2011) 5746-5755.

110. Bernstein, R., S. Belfer, and V. Freger, Bacterial Attachment to RO Membranes Surface-Modified by Concentration-Polarization-Enhanced Graft Polymerization, Environmental Science & Technology 45 (2011) 5973-5980.

111. Wei, X.Y., Z. Wang, Z. Zhang, J.X. Wang, and S.C. Wang, Surface modification of commercial aromatic polyamide reverse osmosis membranes by graft polymerization of 3-allyl-5,5-dimethylhydantoin, Journal of Membrane Science 351 (2010) 222-233.

112. Saeki, D., T. Tanimoto, and H. Matsuyama, Anti-biofouling of polyamide reverse osmosis membranes using phosphorylcholine polymer grafted by surface-initiated atom transfer radical polymerization, Desalination 350 (2014) 21-27.

113. Ngo, T.H.A., D.T. Tran, and C.H. Dinh, Surface photochemical graft polymerization of acrylic acid onto polyamide thin film composite membranes, Journal of Applied Polymer Science 134 (2017)

114. Teng, M.Y., K.R. Lee, D.J. Liaw, Y.S. Lin, and J.Y. Lai, Plasma deposition of acrylamide onto novel aromatic polyamide membrane for pervaporation, European Polymer Journal 36 (2000) 663-672.

115. Wang, J., Z. Wang, J.X. Wang, and S.C. Wang, Improving the water flux and bio-fouling resistance of reverse osmosis (RO) membrane through surface modification by zwitterionic polymer, Journal of Membrane Science 493 (2015) 188-199.

116. Belfer, S., Y. Purinson, R. Fainshtein, Y. Radchenko, and O. Kedem, Surface modification of commercial composite polyamide reverse osmosis membranes, Journal of Membrane Science 139 (1998) 175-181.

117. Rana, H.H., N.K. Saha, S.K. Jewrajka, and A.V.R. Reddy, Low fouling and improved chlorine resistant thin film composite reverse osmosis membranes by cerium(IV)/polyvinyl alcohol mediated surface modification, Desalination 357 (2015) 93-103.

118. Cheng, Q.B., Y.P. Zheng, S.C. Yu, H.W. Zhu, X.Y. Peng, J. Liu, J.Q. Liu, M.H. Liu, and C.J. Gao, Surface modification of a commercial thin-film composite polyamide reverse osmosis membrane through graft polymerization of N-isopropylacrylamide followed by acrylic acid, Journal of Membrane Science 447 (2013) 236-245.

119. Meng, J.Q., Z. Cao, L. Ni, Y.F. Zhang, X.Y. Wang, X. Zhang, and E.H. Liu, A novel salt-responsive TFC RO membrane having superior antifouling and easy-cleaning properties, Journal of Membrane Science 461 (2014) 123-129.

120. Bernstein, R., S. Beller, and V. Freger, Surface Modification of Dense Membranes Using Radical Graft Polymerization Enhanced by Monomer Filtration, Langmuir 26 (2010) 12358-12365.

121. Lewis, G.T. and Y. Cohen, Controlled Nitroxide-Mediated Styrene Surface Graft Polymerization with Atmospheric Plasma Surface Activation, Langmuir 24 (2008) 13102-13112.

122. Liu, C.H., J. Lee, J. Ma, and M. Elimelech, Antifouling thin-film composite membranes by controlled architecture of zwitterionic polymer brush layer, Environmental Science & Technology 51 (2017) 2161-2169.

123. Yang, Z., D. Saeki, and H. Matsuyama, Zwitterionic polymer modification of polyamide reverse-osmosis membranes via surface amination and atom transfer radical polymerization for anti-biofouling, Journal of Membrane Science 550 (2018) 332-339.

124. Lewis, G.T., G.R. Nowling, R.F. Hicks, and Y. Cohen, Inorganic surface nanostructuring by atmospheric pressure plasma-induced graft polymerization, Langmuir 23 (2007) 10756-10764.

125. Hara, Y., K. Ooka, N. Zettsu, and K. Yamamura, Relationship between peroxide radical species on plasma-treated PFA surface and adhesion strength of PFA/electroless copper-plating film, Current Applied Physics 12 (2012) S38-S41.

126. Moses, K.J. and Y. Cohen, Wettability of terminally anchored polymer brush layers on a polyamide surface, Journal of Colloid and Interface Science 436 (2014) 286-295.

127. Hung, L.-Y., S.J. Lue, and J.-H. You, Mass-transfer modeling of reverse-osmosis performance on 0.5–2% salty water, Desalination 265 (2011) 67-73.

128. Yip, N.Y. and M. Elimelech, Performance limiting effects in power generation from salinity gradients by pressure retarded osmosis, Environmental Science & Technology 45 (2011) 10273-10282.

129. Fortin, N. and H.-A. Klok, Glucose Monitoring Using a Polymer Brush Modified Polypropylene Hollow Fiber-based Hydraulic Flow Sensor, ACS Applied Materials & Interfaces 7 (2015) 4631-4640.

130. Abu-Lail, N.I., M. Kaholek, B. LaMattina, R.L. Clark, and S. Zauscher, Micro-cantilevers with end-grafted stimulus-responsive polymer brushes for actuation and sensing, Sensors and Actuators B-Chemical 114 (2006) 371-378.

131. Song, L.J., J. Zhao, H.W. Yang, J. Jin, X.M. Li, P. Stagnaro, and J.H. Yin, Biocompatibility of polypropylene non-woven fabric membrane via UV-induced graft polymerization of 2-acrylamido-2-methylpropane sulfonic acid, Applied Surface Science 258 (2011) 425-430.

132. Gajda, M. and M. Ulbricht, Capillary pore membranes with grafted diblock copolymers showing reversibly changing ultrafiltration properties with independent response to ions and temperature, Journal of Membrane Science 514 (2016) 510-517.

133. Liu, H.L., Y.Y. Li, K. Sun, J.B. Fan, P.C. Zhang, J.X. Meng, S.T. Wang, and L. Jiang, Dual-Responsive Surfaces Modified with Phenylboronic Acid-Containing Polymer Brush To Reversibly Capture and Release Cancer Cells, Journal of the American Chemical Society 135 (2013) 7603-7609.

134. Alarcon, C.D.H., S. Pennadam, and C. Alexander, Stimuli responsive polymers for biomedical applications, Chemical Society Reviews 34 (2005) 276-285.

135. Kochkodan, V. and N. Hilal, A comprehensive review on surface modified polymer membranes for biofouling mitigation, Desalination 356 (2015) 187-207.

136. Kang, G.D. and Y.M. Cao, Development of antifouling reverse osmosis membranes for water treatment: A review, Water Research 46 (2012) 584-600.

137. Keating, J.J., J. Imbrogno, and G. Belfort, Polymer brushes for membrane separations: A review, ACS Applied Materials & Interfaces 8 (2016) 28383-28399.

138. Eshet, I., V. Freger, R. Kasher, M. Herzberg, J. Lei, and M. Ulbricht, Chemical and Physical Factors in Design of Antibiofouling Polymer Coatings, Biomacromolecules 12 (2011) 2681-2685.

139. Birkner, M. and M. Ulbricht, Ultrafiltration membranes with markedly different pH- and ion-responsivity by photografted zwitterionic polysulfobetain or polycarbobetain, Journal of Membrane Science 494 (2015) 57-67.

140. Zhu, L.P., B.K. Zhu, L. Xu, Y.X. Feng, F. Liu, and Y.Y. Xu, Corona-induced graft polymerization for surface modification of porous polyethersulfone membranes, Applied Surface Science 253 (2007) 6052-6059.

141. Wu, T., P. Gong, I. Szleifer, P. Vlcek, V. Subr, and J. Genzer, Behavior of surface-anchored poly(acrylic acid) brushes with grafting density gradients on solid substrates: 1. Experiment, Macromolecules 40 (2007) 8756-8764.

142. Lego, B., W.G. Skene, and S. Giasson, Swelling Study of Responsive Polyelectrolyte Brushes Grafted from Mica Substrates: Effect of pH, Salt, and Grafting Density, Macromolecules 43 (2010) 4384-4393.

143. Emin, C., E. Kurnia, I. Katalia, and M. Ulbricht, Polyarylsulfone-based blend ultrafiltration membranes with combined size and charge selectivity for protein separation, Separation and Purification Technology 193 (2018) 127-138.

144. Mahmoudi, N., L. Reed, A. Moix, N. Alshammari, J. Hestekin, and S.L. Servoss, PEG-mimetic peptoid reduces protein fouling of polysulfone hollow fibers, Colloids and Surfaces, B: Biointerfaces 149 (2017) 23-29.

145. Nady, N., M.C.R. Franssen, H. Zuilhof, M.S.M. Eldin, R. Boom, and K. Schroen, Modification methods for poly(arylsulfone) membranes: A mini-review focusing on surface modification, Desalination 275 (2011) 1-9.

146. Wang, J., H.J. Sun, X.L. Gao, and C.J. Gao, Enhancing antibiofouling performance of polysulfone (PSf) membrane by photo-grafting of capsaicin derivative and acrylic acid, Applied Surface Science 317 (2014) 210-219.

147. Moses, K.J., S. Kim, M. Bilal, and Y. Cohen, Tethered hydrophilic polymers layers on a polyamide surface, Journal of Applied Polymer Science 135 (2018)

148. Goodman, D., J.N. Kizhakkedathu, and D.E. Brooks, Evaluation of an atomic force microscopy pull-off method for measuring molecular weight and polydispersity of polymer brushes: Effect of grafting density, Langmuir 20 (2004) 6238-6245.

149. Yamamoto, S., Y. Tsujii, and T. Fukuda, Atomic force microscopic study of stretching a single polymer chain in a polymer brush, Macromolecules 33 (2000) 5995-5998.

150. Sharma, S., S. Lavender, J. Woo, L.H. Guo, W.Y. Shi, L. Kilpatrick-Liverman, and J.K. Gimzewski, Nanoscale characterization of effect of L-arginine on Streptococcus mutans biofilm adhesion by atomic force microscopy, Microbiology-Sgm 160 (2014) 1466-1473.

151. Schutze, A., J.Y. Jeong, S.E. Babayan, J. Park, G.S. Selwyn, and R.F. Hicks, The atmospheric-pressure plasma jet: a review and comparison to other plasma sources, IEEE Transactions on Plasma Science 26 (1998) 1685-1694.

152. Gonzalez, E., M.D. Barankin, P.C. Guschl, and R.F. Hicks, Remote atmospheric-pressure plasma activation of the surfaces of polyethylene terephthalate and polyethylene naphthalate, Langmuir 24 (2008) 12636-12643.

153. Gonzalez, E., M.D. Barankin, P.C. Guschl, and R.F. Hicks, Ring Opening of Aromatic Polymers by Remote Atmospheric-Pressure Plasma, Ieee Transactions on Plasma Science 37 (2009) 823-831.

154. Decker, C. and A.D. Jenkins, Kinetic approach of oxygen inhibition in ultraviolet- and laser-induced polymerizations, Macromolecules 18 (1985) 1241-1244.

155. Beamson, G. and D. Briggs, High resolution XPS of organic polymers : the Scienta ESCA300 database. 1992, Chichester England ; New York: Wiley. 295 p.

156. Andrade, J.D., R.N. King, D.E. Gregonis, and D.L. Coleman, Surface Characterization of Poly(Hydroxyethyl Methacrylate) and Related Polymers .1. Contact-Angle Methods in Water, Journal of Polymer Science, Part C: Polymer Symposia (1979) 313-336.

157. Güleç, H.A., K. Sarıogˇlu, and M. Mutlu, Modification of food contacting surfaces by plasma polymerisation technique. Part I: Determination of hydrophilicity, hydrophobicity and surface free energy by contact angle method, Journal of Food Engineering 75 (2006) 187-195.

158. Roudman, A.R. and F.A. DiGiano, Surface energy of experimental and commercial nanofiltration membranes: effects of wetting and natural organic matter fouling, Journal of Membrane Science 175 (2000) 61-73.

159. Stuart, M.A.C., W.M. de Vos, and F.A.M. Leermakers, Why surfaces modified by flexible polymers often have a finite contact angle for good solvents, Langmuir 22 (2006) 1722-1728.

160. Owens, D.K. and R.C. Wendt, Estimation of the surface free energy of polymers, Journal of Applied Polymer Science 13 (1969) 1741-1747.

161. Kaelble, D.H., Dispersion-Polar Surface Tension Properties of Organic Solids, Journal of Adhesion 2 (1970) 66-&.

162. Lévy, R. and M. Maaloum, Measuring the spring constant of atomic force microscope cantilevers: thermal fluctuations and other methods, Nanotechnology 13 (2002) 33.

163. Sonnenberg, L., J. Parvole, O. Borisov, L. Billon, H.E. Gaub, and M. Seitz, AFM-based single molecule force spectroscopy of end-grafted poly(acrylic acid) monolayers, Macromolecules 39 (2006) 281-288.

164. AL-Baradi, A., M.R. Tomlinson, Z.Y.J. Zhang, and M. Geoghegan, Determination of the molar mass of surface-grafted weak polyelectrolyte brushes using force spectroscopy, Polymer 67 (2015) 111-117.

165. Nash, M.A. and H.E. Gaub, Single-molecule adhesion of a stimuli-responsive oligo(ethylene glycol) copolymer to gold, ACS Nano 6 (2012) 10735-10742.

166. de Vos, W.M., P.M. Biesheuvel, A. de Keizer, J.M. Kleijn, and M.A.C. Stuart, Adsorption of the protein bovine serum albumin in a planar poly(acrylic acid) brush layer as measured by optical reflectometry, Langmuir 24 (2008) 6575-6584.

167. Vagharchakian, L. and S. Henon, Adsorption of poly(acrylic acid) at an oppositely charged Langmuir film: Surface-tension, ellipsometry, and elasticity measurements, Langmuir 19 (2003) 7989-7994.

168. Wang, S.Y., K.M. Chen, Y.S. Xu, X.J. Yu, W.H. Wang, L. Li, and X.H. Guo, Protein immobilization and separation using anionic/cationic spherical polyelectrolyte brushes based on charge anisotropy, Soft Matter 9 (2013) 11276-11287.

169. Bornmann, L., How to analyze percentile citation impact data meaningfully in bibliometrics: The statistical analysis of distributions, percentile rank classes, and top-cited papers, Journal of the American Society for Information Science and Technology 64 (2013) 587-595.

170. Thompson, J., A. Rahardianto, S. Kim, M. Bilal, R. Breckenridge, and Y. Cohen, Real-time direct detection of silica scaling on RO membranes, Journal of Membrane Science 528 (2017) 346-358.

171. Sanchis, M.R., O. Calvo, O. Fenollar, D. Garcia, and R. Balart, Surface modification of a polyurethane film by low pressure glow discharge oxygen plasma treatment, Journal of Applied Polymer Science 105 (2007) 1077-1085.

172. Van Deynse, A., P. Cools, C. Leys, R. Morent, and N. De Geyter, Influence of ambient conditions on the aging behavior of plasma-treated polyethylene surfaces, Surface and Coatings Technology 258 (2014) 359-367.

173. Hopkins, J. and J.P.S. Badyal, XPS and atomic force microscopy of plasma-treated polysulfone, Journal of Polymer Science, Part A: Polymer Chemistry 34 (1996) 1385-1393.

174. Dietz, P., P.K. Hansma, K.H. Herrmann, O. Inacker, and H.D. Lehmann, Atomic-Force Microscopy of Synthetic Ultrafiltration Membranes in Air and under Water, Ultramicroscopy 35 (1991) 155-159.

175. Suvorova, A.I., I.S. Tyukova, A.L. Suvorov, N.N. Malysheva, and A.V. Okhokhonin, Hydrophilic nature and sorption-diffusion properties of nanocomposite hybrid polysulfone films, Russian Chemical Bulletin 61 (2012) 555-562.

176. Dell'Orto, E.C., A. Vaccaro, and C. Riccardi, Morphological and chemical analysis of PP film treated by Dielectric Barrier Discharge, Journal of Physics: Conference Series 550 (2014)

177. Guimond, S. and M.R. Wertheimer, Surface degradation and hydrophobic recovery of polyolefins treated by air corona and nitrogen atmospheric pressure glow discharge, Journal of Applied Polymer Science 94 (2004) 1291-1303.

178. Kostov, K.G., T.M.C. Nishime, A.H.R. Castro, A. Toth, and L.R.O. Hein, Surface modification of polymeric materials by cold atmospheric plasma jet, Applied Surface Science 314 (2014) 367-375.

179. Greenwood, O.D., J. Hopkins, and J.P.S. Badyal, Non-isothermal O-2 plasma treatment of phenyl-containing polymers, Macromolecules 30 (1997) 1091-1098.

180. O'Hare, L.A., J.A. Smith, S.R. Leadley, B. Parbhoo, A.J. Goodwin, and J.F. Watts, Surface physico-chemistry of corona-discharge-treated poly(ethylene terephthalate) film, Surface and Interface Analysis 33 (2002) 617-625.

181. Strobel, M., J. V, C.S. Lyons, M. Ulsh, M.J. Kushner, R. Dorai, and M.C. Branch, A comparison of corona-treated and flame-treated polypropylene films, Plasmas and Polymers 8 (2003) 61-95.

182. Yeung, C., A.C. Balazs, and D. Jasnow, Lateral Instabilities in a Grafted Layer in a Poor Solvent, Macromolecules 26 (1993) 1914-1921.

183. Koutsos, V., E.W. van der Vegte, and G. Hadziioannou, Direct view of structural regimes of end-grafted polymer monolayers: A scanning force microscopy study, Macromolecules 32 (1999) 1233-1236.

184. Siqueira, D.F., K. Kohler, and M. Stamm, Structures at the Surface of Dry Thin-Films of Grafted Copolymers, Langmuir 11 (1995) 3092-3096.

185. Ayres, N., S.G. Boyes, and W.J. Brittain, Stimuli-responsive polyelectrolyte polymer brushes prepared via atom-transfer radical polymerization, Langmuir 23 (2007) 182-189.

186. Jackson, N.E., B.K. Brettmann, V. Vishwanath, M. Tirrell, and J.J. de Pablo, Comparing Solvophobic and Multivalent Induced Collapse in Polyelectrolyte Brushes, Acs Macro Letters 6 (2017) 155-160.

187. Hugel, T., M. Grosholz, H. Clausen-Schaumann, A. Pfau, H. Gaub, and M. Seitz, Elasticity of single polyelectrolyte chains and their desorption from solid supports studied by AFM based single molecule force spectroscopy, Macromolecules 34 (2001) 1039-1047.

188. Moh, L.C.H., M.D. Losego, and P.V. Braun, Solvent Quality Effects on Scaling Behavior of Poly(methyl methacrylate) Brushes in the Moderate- and High-Density Regimes, Langmuir 27 (2011) 3698-3702.

189. Dammer, U., O. Popescu, P. Wagner, D. Anselmetti, H.J. Guntherodt, and G.N. Misevic, Binding Strength between Cell-Adhesion Proteoglycans Measured by Atomic-Force Microscopy, Science 267 (1995) 1173-1175.

190. Butt, H.-J., Measuring electrostatic, van der Waals, and hydration forces in electrolyte solutions with an atomic force microscope, Biophysical Journal 60 (1991) 1438-1444.

191. Butt, H.J., B. Cappella, and M. Kappl, Force measurements with the atomic force microscope: Technique, interpretation and applications, Surface Science Reports 59 (2005) 1-152.

192. Israelachvili, J.N., Intermolecular and Surface Forces, 3rd Edition, Intermolecular and Surface Forces, 3rd Edition (2011) 1-674.

193. Pashley, R.M., Hydration Forces between Mica Surfaces in Aqueous-Electrolyte Solutions, Journal of Colloid and Interface Science 80 (1981) 153-162.

194. Yoshikawa, C., A. Goto, Y. Tsujii, T. Fukuda, K. Yamamoto, and A. Kishida, Fabrication of high-density polymer brush on polymer substrate by surface-initiated living radical polymerization, Macromolecules 38 (2005) 4604-4610.

195. Kobayashi, M., Y. Terayama, H. Yamaguchi, M. Terada, D. Murakami, K. Ishihara, and A. Takahara, Wettability and Antifouling Behavior on the Surfaces of Superhydrophilic Polymer Brushes, Langmuir 28 (2012) 7212-7222.

196. Liu, Z.M., Z.K. Xu, L.S. Wan, J. Wu, and M. Ulbricht, Surface modification of polypropylene microfiltration membranes by the immobilization of poly(N-vinyl-2-pyrrolidone): a facile plasma approach, Journal of Membrane Science 249 (2005) 21-31.

197. Kim, S., Y. Cohen, K.J. Moses, S. Sharma, and M. Bilal, Polysulfone surface nano-structured with tethered polyacrylic acid, Applied Surface Science 470 (2019) 411-422.

198. Moses, K.J., S. Kim, M. Bilal, and Y. Cohen, Tethered hydrophilic polymers layers on a polyamide surface, Journal of Applied Polymer Science 135 (2018) 46843.

199. Cohen, Y., M.-M. Kim, G.T. Lewis, and N.H. Lin, Fouling and scaling resistant nano-structured reverse osmosis membranes, U.S. Patent, Editor.

200. Zhu, L., W.H. Teng, H.L. Xu, Y. Liu, Q.R. Jiang, C.X. Wang, and Y.P. Qiu, Effect of absorbed moisture on the atmospheric plasma etching of polyamide fibers, Surface and Coatings Technology 202 (2008) 1966-1974.

201. Li, Y.S., J. Sun, L. Yao, F. Ji, S.J. Peng, Z.Q. Gao, and Y.P. Qiu, Influence of Moisture on Effectiveness of Plasma Treatments of Polymer Surfaces, Journal of Adhesion Science and Technology 26 (2012) 1123-1139.

202. Maruf, S.H., D.U. Ahn, A.R. Greenberg, and Y.F. Ding, Glass transition behaviors of interfacially polymerized polyamide barrier layers on thin film composite membranes via nano-thermal analysis, Polymer 52 (2011) 2643-2649.

203. Reis, R., L.F. Dumee, B.L. Tardy, R. Dagastine, J.D. Orbell, J.A. Schutz, and M.C. Duke, Towards enhanced performance thin-film composite membranes via surface plasma modification, Scientific Reports 6 (2016) 29206.

204. Reis, R., L.F. Dumee, A. Merenda, J.D. Orbell, J.A. Schutz, and M.C. Duke, Plasma-induced physicochemical effects on a poly(amide) thin-film composite membrane, Desalination 403 (2017) 3-11.

205. Fricke, K., H. Steffen, T. von Woedtke, K. Schroder, and K.D. Weltmann, High Rate Etching of Polymers by Means of an Atmospheric Pressure Plasma Jet, Plasma Processes and Polymers 8 (2011) 51-58.

206. Scott, R.A. and N.A. Peppas, Kinetic study of acrylic acid solution polymerization, AIChE Journal 43 (1997) 135-144.

207. Kabanov, V.A. and D.A. Topchiev, Characteristic features of the radical polymerizations of ionized monomers, Polymer Science U.S.S.R. 13 (1971) 1486-1512.

208. Bartels, C., R. Franks, S. Rybar, M. Schierach, and M. Wilf, The effect of feed ionic strength on salt passage through reverse osmosis membranes, Desalination 184 (2005) 185-195.

209. Synytska, A., E. Svetushkina, N. Puretskiy, G. Stoychev, S. Berger, L. Ionov, C. Bellmann, K.J. Eichhorn, and M. Stamm, Biocompatible polymeric materials with switchable adhesion properties, Soft Matter 6 (2010) 5907-5914.

210. Pontié, M., H. Dach, J. Leparc, M. Hafsi, and A. Lhassani, Novel approach combining physico-chemical characterizations and mass transfer modelling of nanofiltration and low pressure reverse osmosis membranes for brackish water desalination intensification, Desalination 221 (2008) 174-191.

211. Zouhri, N., M. Igouzal, M. Larif, M. Hafsi, M. Taky, and A. Elmidaoui, Prediction of salt rejection by nanofiltration and reverse osmosis membranes using Spiegler-Kedem model and an optimisation procedure, Desalination and Water Treatment 120 (2018) 41-50.

212. Lyster, E. and Y. Cohen, Numerical study of concentration polarization in a rectangular reverse osmosis membrane channel: Permeate flux variation and hydrodynamic end effects, Journal of Membrane Science 303 (2007) 140-153.

213. Asadollahi, M., D. Bastani, and S.A. Musavi, Enhancement of surface properties and performance of reverse osmosis membranes after surface modification: A review, Desalination 420 (2017) 330-383.

214. Widjaya, A., T. Hoang, G.W. Stevens, and S.E. Kentish, A comparison of commercial reverse osmosis membrane characteristics and performance under alginate fouling conditions, Separation and Purification Technology 89 (2012) 270-281.

215. Louie, J.S., I. Pinnau, and M. Reinhard, Effects of surface coating process conditions on the water permeation and salt rejection properties of composite polyamide reverse osmosis membranes, Journal of Membrane Science 367 (2011) 249-255.

216. Wang, X.Y., E. Duitsman, N. Rajagopalan, and V.V. Namboodiri, Chemical treatment of commercial reverse osmosis membranes for use in FO, Desalination 319 (2013) 66-72.

217. Ben-David, A., R. Bernstein, Y. Oren, S. Belfer, C. Dosoretz, and V. Freger, Facile surface modification of nanofiltration membranes to target the removal of endocrine-disrupting compounds, Journal of Membrane Science 357 (2010) 152-159.

218. Baransi-Karkaby, K., M. Bass, S. Levchenko, S. Eitan, and V. Freger, Facile modification of reverse osmosis membranes by surfactant-assisted acrylate grafting for enhanced selectivity, Environmental Science & Technology 51 (2017) 2347-2354.

219. Werber, J.R., C.O. Osuji, and M. Elimelech, Materials for next-generation desalination and water purification membranes, Nature Reviews Materials 1 (2016) 16018.

220. Lu, X., X. Feng, Y. Yang, J. Jiang, W. Cheng, C. Liu, M. Gopinadhan, C.O. Osuji, J. Ma, and M. Elimelech, Tuning the permselectivity of polymeric desalination membranes via control of polymer crystallite size, Nature Communications 10 (2019) 2347.

221. Van Wagner, E.M., A.C. Sagle, M.M. Sharma, and B.D. Freeman, Effect of crossflow testing conditions, including feed pH and continuous feed filtration, on commercial reverse osmosis membrane performance, Journal of Membrane Science 345 (2009) 97-109.

222. Masse, A., O. Arab, V. Sechet, P. Jaouen, M. Pontie, N.E. Sabiri, and S. Plantier, Performances of dead-end ultrafiltration of seawater: from the filtration and backwash efficiencies to the membrane fouling mechanisms, Separation and Purification Technology 156 (2015) 512-521.

223. Resosudarmo, A., Y. Ye, P. Le-Clech, and V. Chen, Analysis of UF membrane fouling mechanisms caused by organic interactions in seawater, Water Research 47 (2013) 911-921.

224. Zhao, M., X. Zhang, Y. Li, and W. Chang, A New Spectrophotometry Method for the Determination of Aniline in Environmental Water Samples, Analytical Letters 33 (2000) 3067-3075.

225. Arnamwong, S., P. Suksabye, and P. Thiravetyan, Using kaolin in reduction of arsenic in rice grains: effect of different types of kaolin, pH and arsenic complex, Bulletin of Environmental Contamination and Toxicology 96 (2016) 556-561.

226. Asatekin, A., S. Kang, M. Elimelech, and A.M. Mayes, Anti-fouling ultrafiltration membranes containing polyacrylonitrile-graft-poly (ethylene oxide) comb copolymer additives, Journal of Membrane Science 298 (2007) 136-146.

227. Becht, N.O., D.J. Malik, and E.S. Tarleton, Evaluation and comparison of protein ultrafiltration test results: Dead-end stirred cell compared with a cross-flow system, Separation and Purification Technology 62 (2008) 228-239.

228. Draget, K.I., G.S. Braek, and O. Smidsrod, Alginic acid gels: the effect of alginate chemical composition and molecular weight, Carbohydrate Polymers 25 (1994) 31-38.

229. Chen, H. and Y.L. Hsieh, Enzyme immobilization on ultrafine cellulose fibers via poly(acrylic acid) electrolyte grafts, Biotechnology and Bioengineering 90 (2005) 405-413.

230. Gao, K., L.T. Kearney, and J.A. Howarter, Planar phase separation of weak polyelectrolyte brushes in poor solvent, Journal of Polymer Science, Part B: Polymer Physics 55 (2017) 370-377.

231. Lee, S. and M. Elimelech, Relating organic fouling of reverse osmosis membranes to intermolecular adhesion forces, Environmental Science & Technology 40 (2006) 980-987.

232. Zazouli, M.A., S. Nasseri, and M. Ulbricht, Fouling effects of humic and alginic acids in nanofiltration and influence of solution composition, Desalination 250 (2010) 688-692.

233. Vrijenhoek, E.M., S. Hong, and M. Elimelech, Influence of membrane surface properties on initial rate of colloidal fouling of reverse osmosis and nanofiltration membranes, Journal of Membrane Science 188 (2001) 115-128.

234. Li, Q.L., Z.H. Xu, and I. Pinnau, Fouling of reverse osmosis membranes by biopolymers in wastewater secondary effluent: Role of membrane surface properties and initial permeate flux, Journal of Membrane Science 290 (2007) 173-181.

235. Belfer, S., J. Gilron, Y. Purinson, R. Fainshtain, N. Daltrophe, M. Priel, B. Tenzer, and A. Toma, Effect of surface modification in preventing fouling of commercial SWRO membranes at the Eilat seawater desalination pilot plant, Desalination 139 (2001) 169-176.

236. Baransi-Karkaby, K., M. Bass, and V. Freger, In Situ Modification of Reverse Osmosis Membrane Elements for Enhanced Removal of Multiple Micropollutants, Membranes 9 (2019)

237. McCloskey, B.D., H.B. Park, H. Ju, B.W. Rowe, D.J. Miller, and B.D. Freeman, A bioinspired fouling-resistant surface modification for water purification membranes, Journal of Membrane Science 413 (2012) 82-90.

238. Miller, D.J., X.F. Huang, H. Li, S. Kasemset, A. Lee, D. Agnihotri, T. Hayes, D.R. Paul, and B.D. Freeman, Fouling-resistant membranes for the treatment of flowback water from hydraulic shale fracturing: A pilot study, Journal of Membrane Science 437 (2013) 265-275.

239. Belfer, S., R. Fainshtain, Y. Purinson, J. Gilron, M. Nystrom, and M. Manttari, Modification of NF membrane properties by in situ redox initiated graft polymerization with hydrophilic monomers, Journal of Membrane Science 239 (2004) 55-64.